MINISTRY OF EDUCATION AND TRAINING

HCM CITY UNIVERSITY OF TECHNOLOGY AND EDUCATION

---oo0oo---

DANG MINH PHUNG

DEVELOPMENT AND OPTIMIZATION OF COMPLIANT POSITIONING STAGES APPLIED FOR NANOINDENTATION TESTING DEVICE

PH.D. THESIS

MAJOR: MECHANICAL ENGINEERING

CODE: 9520103

HCM City, December 2022

MINISTRY OF EDUCATION AND TRAINING

HCM CITY UNIVERSITY OF TECHNOLOGY AND EDUCATION

--- oOo ---

DANG MINH PHUNG

DEVELOPMENT AND OPTIMIZATION OF COMPLIANT POSITIONING STAGES APPLIED FOR NANOINDENTATION TESTING DEVICE

MAJOR: MECHANICAL ENGINEERING

CODE: 9520103

Supervisor 1: Assoc. Prof. Dr. Le Hieu Giang

Supervisor 2: Dr. Dao Thanh Phong

Reviewer 1:

Reviewer 2:

Reviewer 3:

HCM City, December 2022

BỘ GIÁO DỤC VÀ ĐÀO TẠO
TRƯỜNG ĐẠI HỌC SƯ PHẠM KỸ THUẬT
THÀNH PHỐ HỒ CHÍ MINH

Số: 109a/QĐ-ĐHSPKT

CỘNG HÒA XÃ HỘI CHỦ NGHĨA VIỆT NAM
Độc lập – Tự do – Hạnh phúc

Tp. Hồ Chí Minh, ngày 16 tháng 02 năm 2017

QUYẾT ĐỊNH

Về việc đổi tên luận án và người hướng dẫn nghiên cứu sinh khóa 2015
HIỆU TRƯỞNG TRƯỜNG ĐẠI HỌC SƯ PHẠM KỸ THUẬT TP. HỒ CHÍ MINH

Căn cứ Quyết định số 118/2000/QĐ-TTg ngày 10 tháng 10 năm 2000 của Thủ tướng Chính phủ về việc thay đổi tổ chức của Đại học Quốc gia TP. Hồ Chí Minh, tách Trường Đại học Sư phạm Kỹ thuật TP. Hồ Chí Minh trực thuộc Bộ Giáo dục và Đào tạo;

Căn cứ Quyết định số 70/2014/QĐ-TTg ngày 10/12/2014 của Thủ tướng Chính phủ về ban hành Điều lệ trường Đại học;

Căn cứ Thông tư số 10/2009/TT-BGDĐT ngày 07/5/2009 của Bộ Giáo dục và Đào tạo về việc Ban hành Qui chế đào tạo trình độ tiến sĩ;

Căn cứ Thông tư số 05/2012/TT-BGDĐT ngày 15/02/2012 của Bộ Giáo dục và Đào tạo về việc sửa đổi, bổ sung một số điều của Quy chế đào tạo trình độ tiến sĩ ban hành kèm theo Thông tư số 10/2009/TT-BGDĐT ngày 07/5/2009 của Bộ trưởng Bộ Giáo dục và Đào tạo;

Xét nhu cầu công tác và khả năng cán bộ;

Xét đề nghị của Trưởng phòng Đào tạo,

QUYẾT ĐỊNH

Điều 1: Đổi tên đề tài luận án tiến sĩ cho:

Nghiên cứu sinh : ***Đặng Minh Phụng***

Ngành : Kỹ thuật cơ khí Khoá: ***2015 – 2018***

Tên luận án mới : ***Phát triển và tối ưu hóa các bộ định vị sử dụng cơ cấu mềm cho thiết bị kiểm tra độ cứng vật liệu***

Người HD thứ nhất (HD chính): ***PGS.TS Lê Hiếu Giang***

Người HD thứ hai : ***TS. Đào Thanh Phong***

Thời gian thực hiện : ***05/10/2015 đến 05/10/2018***

Điều 2: Giao cho Phòng Đào tạo quản lý, thực hiện theo đúng Qui chế đào tạo trình độ tiến sĩ của Bộ Giáo dục & Đào tạo đã ban hành.

Điều 3: Trưởng các đơn vị: phòng Đào tạo, khoa quản ngành, phòng KHTC và các Ông (Bà) có tên ở Điều 1 chịu trách nhiệm thi hành quyết định này.

Quyết định có hiệu lực kể từ ngày ký.

Nơi nhận:
- BGH (để chỉ đạo);
- Như điều 3;
- Lưu: VT, SĐH (3b).

KT. HIỆU TRƯỞNG
PHÓ HIỆU TRƯỞNG

TRƯỜNG ĐẠI HỌC SƯ PHẠM KỸ THUẬT TP. HỒ CHÍ MINH

PGS. TS Lê Hiếu Giang

LÝ LỊCH KHOA HỌC

I. LÝ LỊCH SƠ LƯỢC

Họ và tên: ĐẶNG MINH PHỤNG Giới tính: NAM

Ngày, tháng, năm sinh: 29/06/1983 Nơi sinh: Bình Dương

Quên quán: Bình Dương Dân tộc: Kinh

Học vị cao nhất: Thạc Sỹ Kỹ thuật

Đơn vị công tác: Trường Đại học Sư Phạm Kỹ thuật Thành phố Hồ Chí Minh

Chỗ ở riêng hoặc địa chỉ liên lạc: D302, chung cư C2, Đường D1, P. Hiệp Phú, Tp. Thủ Đức, Tp. HCM.

Điện thoại liên hệ: 0906814944 Email: phungdm@hcmute.edu.vn

II. QUÁ TRÌNH ĐÀO TẠO

1. Đại học:

- Hệ đào tạo: Chính qui
- Nơi đào tạo: Trường Đại học Sư phạm Kỹ thuật TP. HCM
- Ngành học: Cơ khí chế tạo máy
- Năm tốt nghiệp: 2007

2. Sau đại học

- Hệ đào tạo: Chính qui
- Nơi đào tạo: Trường Đại học Sư phạm Kỹ thuật Tp. HCM
- Thạc sĩ chuyên ngành: Kỹ thuật cơ khí
- Năm tốt nghiệp: 2009

III. QUÁ TRÌNH CÔNG TÁC

- Từ 6/2007 đến 8/2007: Kỹ sư thiết kế - Công ty TNHH TM & XD Nội Lực.
- 10/2007 đến 9/2009: Giảng viên, Khoa Cơ khí, Trường Cao đẳng Công Thương Tp. HCM.
- 10/2009 - nay: Giảng viên, Bộ môn Công nghệ Chế tạo máy, Khoa Cơ khí Chế tạo máy, Trường Đại học Sư phạm Kỹ thuật Tp. HCM.

IV. LĨNH VỰC CHUYÊN MÔN

- Công nghệ chế tạo máy, đo lường cơ khí.
- Thiết kế, chế tạo máy nông nghiệp và máy CNC.
- Cơ cấu mềm.
- Bộ định vị chính xác.
- Tối ưu hóa thiết kế và gia công cơ khí.

V. CÁC CÔNG TRÌNH ĐÃ CÔNG BỐ

Số TT	NỘI DUNG
1	**Minh Phung Dang, Hieu Giang Le**, Nguyen Thanh Duy Tran, Ngoc Le Chau, **Thanh-Phong Dao**, Optimal design and analysis for a new 1-DOF compliant stage based on additive manufacturing method for testing medical specimens, Symmetry, Volume 14, Issue 6, 06/2022. (**SCIE – Q2**)
2	**Minh Phung Dang**, **Hieu Giang Le**, Minh Nhut Van, Ngoc Le Chau, **Thanh-Phong Dao**, Modeling and optimization for a new compliant 02-DOF stage for locating bio-materials sample by an efficient approach of kinetostatic analysis-based method and neural network algorithm, Computational Intelligence and Neuroscience, Volume 2022, Article ID 6709464. (**SCIE – Q1**)
3	**Minh Phung Dang, Hieu Giang Le**, Ngoc Le Chau, **Thanh-Phong Dao**, Optimization for a flexure hinge using an effective hybrid approach of fuzzy logic and moth-flame optimization algorithm, Mathematical Problems in Engineering, Volume 2021, Article ID 6622655, 18 pages, Feb-2021. (**SCIE – Q2**)
4	**Minh Phung Dang**, **Hieu Giang Le**, Ngoc N. Trung Le, Ngoc Le Chau, **Thanh-Phong Dao**, Multiresponse Optimization for a Novel Compliant Z-Stage by a Hybridization of Response Surface Method and Whale Optimization Algorithm, Mathematical Problems in Engineering, Volume 2021, Article ID 9974230, 18 pages, ISSN 1024-123X, April 2021. **(SCIE – Q2)**
5	**Minh Phung Dang, Hieu Giang Le**, Ngoc Le Chau, **Thanh-Phong Dao**, A Multi-Objective Optimization Design for a New Linear Compliant Mechanism, Journal of Optimization and Engineering, 10.1007/s11081-019-09469-8, 2020. (**SCIE – Q2**)
6	**Minh Phung Dang**, **Thanh-Phong Dao**, Ngoc Le Chau, **Hieu Giang Le**, Effective Hybrid Algorithm of Taguchi Method, FEM, RSM, and Teaching Learning-Based Optimization for Multiobjective Optimization Design of a Compliant Rotary Positioning Stage for Nanoindentation Tester, Mathematical Problems in Engineering, 1563-5147, 2018. (**SCIE – Q2**).

Số TT	NỘI DUNG
7	Ngoc Le Chau, **Hieu Giang Le, Thanh-Phong Dao**, **Minh Phung Dang**, and Van Anh Dang, Efficient Hybrid Method of FEA-Based RSM and PSO Algorithm for Multi-Objective Optimization Design for a Compliant Rotary Joint for Upper Limb Assistive Device, Mathematical Problems in Engineering, 2587373, 2019. (**SCIE – Q2**).
8	Ngoc Le Chau, **Minh Phung Dang**, Chander Prakash, Dharam Buddhi, **Thanh-Phong Dao**, Structural optimization of a rotary joint by hybrid method of FEM, neural-fuzzy and water cycle-moth flame algorithm for robotics and automation manufacturing, Robotics and Autonomous Systems (2022): 104199. (**SCIE – Q1**).
9	**Minh Phung Dang**, **Hieu Giang Le**, Thu Thi Dang Phan, Ngoc Le Chau, and **Thanh-Phong Dao**, Design and Optimization for a New XYZ Micropositioner with Embedded Displacement Sensor for Biomaterial Sample Probing Application." Sensors 22, no. 21 (2022): 8204. (**SCIE – Q1**).
10	Duc Nam Nguyen, **Minh Phung Dang**, Shyh-Chour Huang, **Thanh-Phong Dao**, Computational optimization of a steel A-36 monolithic mechanism by bonobo algorithm and intelligent model for precision machining application, International Journal on Interactive Design and Manufacturing (IJIDeM) (2022): 1-11. **(Scopus, ESCI – Q2)**
11	Nguyen, Duc Nam, **Minh Phung Dang**, Tan Thang Nguyen, and **Thanh-Phong Dao**, Intelligent computation modeling and analysis of a gripper for advanced manufacturing application, International Journal on Interactive Design and Manufacturing (IJIDeM) (2022): 1-11. **(Scopus, ESCI – Q2)**
12	Duc Nam Nguyen, **Minh Phung Dang**, Saurav Dixit, **Thanh-Phong Dao**, A design approach of bonding head guiding platform for die to wafer hybrid bonding application using compliant mechanism, International Journal on Interactive Design and Manufacturing (IJIDeM) (2022): 1-12. **(Scopus, ESCI – Q2)**
13	**Minh Phung Dang**, **Thanh-Phong Dao, Hieu Giang Le**, Ngoc Thoai Tran, Development and analysis for a New Compliant XY Micropositioning Stage applied for Nanoindentation Tester System, Applied Mechanics and Materials, 1662-7482, Vol. 894, pp 60-71, 2019.
14	**Minh Phung Dang, Thanh-Phong Dao, Hieu Giang Le**, Optimal Design of a New Compliant XY Micropositioning Stage for Nanoindentation Tester Using Efficient Approach of Taguchi Method, Response Surface Method and NSGA-II,

Số TT	NỘI DUNG
	4th International Conference on Green Technology and Sustainable Development (GTSD), IEEE, 2018.
15	Nhat Linh Ho**, Thanh-Phong Dao, Minh Phung Dang, Hieu Giang Le**, Tan Thang Nguyen, Manh Tuan Bui, Design and Analysis of a Displacement Sensor-Integrated Compliant Micro-gripper Based on Parallel Structure, The first International Conference on Material, Machines and Methods for Sustainable Development, Da Nang, Vietnam, 978-604-95-0502-7.
16	**Minh Phung Dang,** Nhat Linh Ho, Ngoc Le Chau, **Thanh Phong Dao, Hieu Giang Le**, A hybrid mechanism based on beetle-liked structure and multi-lever amplification for a compliant micropositioning platform, The Xth National Mechanics Conference, Ha Noi, Vietnam, 978-604-913-719-8, 2017.

TP. HCM, ngày 27 tháng 12 năm 2022

Nghiên cứu sinh

Đặng Minh Phụng

ORIGINALITY STATEMENT

I, Dang Minh Phung, confirm that this dissertation is my own work, done under the guidance of Assoc. Prof. Dr. Le Hieu Giang and Dr. Dao Thanh Phong to my great knowledge.

The data and achieved results stated in the dissertation are honest and have not been published elsewhere.

Ho Chi Minh City, December 2022

Dang Minh Phung

ACKNOWLEDGMENTS

To begin, I would like to express my heartfelt gratitude to my two main supervisors, **Assoc. Prof. Le Hieu Giang** and **Dr. Dao Thanh Phong**, from the Faculty of Mechanical Engineering, Ho Chi Minh City University of Technology and Education, and the Institute for Computational Science, Ton Duc Thang University, respectively. From the very first day of my Ph.D. study, my supervisors always show their kindness and enthusiasm to help me in my life and support me in writing international papers in English as well as doing research. Moreover, my advisors have given me helpful advice in my life in order to balance my research and teaching, as well as provide me with professional knowledge to conduct my research in the compliant mechanism field.

Secondly, I would like to thank my colleagues in the compliant research group at Institute for Computational Science, Ton Duc Thang University, as well as my colleagues and great students at the Ho Chi Minh City University of Technology and Education's Faculty of Mechanical Engineering, for their help in developing my research. Thirdly, I would like to thank the Ho Chi Minh City University of Technology professors who gave me great advice in correcting my thesis and showing appropriate developing directions in my research field. Fourthly, I would like to thank the Vietnam National Foundation for Science and Technology Development (NAFOSTED, No. 107.01-2019-14) and HCMC University of Technology and Education in Vietnam for financial support under Grant No. T2019-05TĐ, T2019-06TĐ, T2020-60TĐ, T2020-61TĐ, T2021-10TĐ, T2021-11TĐ, T2022-86, and T2022-87.

Finally, I would like to express my gratitude to my family for their encouragement, support, and patience: my parents, my wife, my younger brother, two younger sisters, my daughters, and my son.

Dang Minh Phung

ABSTRACT

This thesis presents the development and optimization for flexure hinge, 01-DOF positioning stages, XY positioning stages, and a rotary stage for a nanoindentation testing device.

Firstly, a new hybrid multi-response optimization approach was developed by combination of the Taguchi method (TM) with response surface methodology (RSM), fuzzy logic reasoning, and Moth-Flame optimizer is developed to select and optimize a new flexure joint. The elliptical hinge is chosen to integrate into the positioners in the nanoindentation device. The attained results were of $10.94*10^{-5}$ mm for the rotation axis shift, 2.99 for the safety factor and $52.006*10^{-3}$ rad for the angle deflection. The elliptic hinge is then integrated into the indenter for driving and specimen locating positioners.

Secondly, three design alternatives of new 01-DOF positioning stage are developed. A four-lever displacement intensification structure and beetle-liked configuration are proposed for the first stage. A two-lever displacement amplifier, flexure shift mechanism, and parallel guiding mechanism are designed for the second stage. A six-lever amplifier and parallel guiding mechanism are devoted for the third stage. The advanced adaptive neuro-fuzzy inference system was coupled with teaching learning-based optimization algorithm to improve the quality characteristics of the first 01-DOF stage. Another methodology combining the TM, RSM, weight factor computation technique, and Whale optimization algorithm was also offered for optimizing the second 01-DOF stage. Furthermore, the pseudo-rigid-body model and Lagrange method were used for modeling the third 01-DOF stage. The Firefly algorithm was then used to advance the important response of the third positioner. For the 1st stage, the safety factor was 1.5141 and the displacement was 2.4065 mm. For the 2nd stage, the output Z-displacement was 436.04 μm and the safety factor was 2.224. For the 3rd stage, the result achieved 176.957 Hz for the first natural frequency.

Finally, three new design alternatives for locating specimens were developed, including two XY positioning stages and a rotary positioning stage. In particular, the first XY stage included a four-lever displacement amplifier and guiding parallel guiding based on a zigzag-based flexure spring. Following that, an eight-lever displacement intensification structure with elliptic hinges and parallel guiding via a zigzag-based flexure spring was integrated into the second XY stage. Eventually, the rotary stage included a four-lever displacement amplifier, the profile's beetle leg, cartwheel hinge, and a rotation platform based on three leaf flexure hinges. Furthermore, an offered optimization approach combining the TM, RSM, and nondominated sorting genetic algorithm II was proposed for optimizing the key variables of the first compliant X-positioner for improving the quality responses of the stages mentioned above. Then, a neural network algorithm was used to optimize the main parameters of the second XY-positioner for improving the output characteristics of the second X-positioner. Moreover, to optimize the rotary stage's main factors, an offered integration optimization approach of the TM, RSM, weight factor computation technique according to signal to noise, and TLBO algorithm was developed. For the 1st 2-DOF stage, the displacement was 3.862 mm and the first natural was 45.983 Hz. For the 2nd 2-DOF stage, the frequency of stage was 112.0995 Hz. For the rotary stage, the safety factor was 1.558 and the displacement was about 2.096 mm.

Additionally, Wilcoxon's rank signed analysis as well as Friedman analysis were exploited to benchmark the effectiveness of the offered hybrid method to other optimizers. ANOVA was also used to figure out the significant contributions of the main input factors to output characteristics. The physical prototypes are manufactured and experimentally verified the predicted results.

CONTENTS

List of Abbreviations

Abbreviation	*Full name*
CAD	Computer aided design

FEA	Finite element analysis
FEM	Finite element Method
TM	Taguchi method
RSM	Response surface methodology
GA	Genetic algorithm
NSGA-II	Nondominated Sorting Genetic Algorithm II
TLBO	Teaching learning-based optimization algorithm
ANFIS	Adaptive neuro-fuzzy inference system
MEMS	Microelectromechanical systems
DOF	Degree of freedom
PEA	Piezoelectric actuator
AR	Amplification ratio
ANOVA	Analysis of Variance
PRBM	Pseudo-rigid-body model
PSO	Particle swarm optimization
DE	Differential evolutionary
S/N	Signal to Noise
MF	Membership function
MFO	Moth flame optimization algorithm
ASO	Atom search optimization
CPP	Compliant positioning Platform
WEDM	Wire electrical discharged machining
WOA	Whale optimization algorithm
CSA	Cuckoo search algorithm
LAM	Lever amplification mechanism
CRPS	Compliant rotary positioning stage
CPP	compliant positioning platform
AEDE	Adaptive elitist differential evolution
NNA	Neural network algorithm

SEM	Scanning electron microscope
TEM	Transmission electron microscope
PZT	Piezoelectric actuator
LAM 1	Lever displacement amplifier of 1st floor
LAM 2	Lever displacement amplifier of 2nd floor
LAM 3	Lever displacement amplifier of 3rd floor
MDLD	Modified displacement lever magnifier
1-DOF	One degree of freedom
2-DOF	Two degrees of freedom
3-DOF	Three degrees of freedom
RMSE	Root mean squared error
WF	Weight factor
FA	Firefly algorithm

Nomenclature

Symbol	*Explanation of symbol*
K_C	Rigidity of the right circular hinge
K_E	Rigidity of elliptic hinge
K_L	Rigidity of rectangular hinge
f	First natural frequency
σ	Stress
σ_y	The yield strength of the material
E	Young's modulus
ε	Strain
N	Sum of the experiments
k	Quantity of input parameters

W_i	Weight factor of every characteristic function i_{th}.
m_{OF}	The number of response functions
e	The decoupling error
l_1	Length of division AO_1
l_2	Length of division O_1B
$l_{1'}$	Length of division JO_2
$l_{2'}$	Length of division O_2C
l_3	Length of division O_4H
l_4	Length of division HI
l_5	Length of division EO_3
l_6	Length of division O_3G
A	Magnification proportion
δ_{in}	Input displacement
$K^c_{\theta zMz}$	Rotation rigidity produced by the torque of a right circular joint
$K^c_{\theta yMy}$	Linear rigidity generated by the axial force of a right circular joint
$K^c_{\delta xFx}$	Bending rigidity created by the lateral force of a right circular joint
$K^l_{\theta zMz}$	Rotation rigidity generated by the torque of a rectangular joint
$K^l_{\theta yMy}$	Linear rigidity generated by the axial force of a rectangular joint
$\Delta\theta$	Variable angle generated by the torque of a rectangular joint
$M^l_{\theta zMz}$	Bending moments of a rectangular joint
$K^e_{\theta zMz}$	Rotation rigidity generated by the torque of an elliptic joint
$K^e_{\theta yMy}$	Linear rigidity generated by the axial force of an elliptic joint
$K^e_{\delta_X F_X}$	Bending rigidity produced by lateral force of an elliptic joint
E	Elastic modulus of a suggested material
b	Thickness of a right circular joint
r	Radius of a right circular joint

t	Minimum width of a circular/elliptic joint
l	Length of a compliant joint
a	Width of a compliant joint
a_x	Major axis of an elliptic compliant joint
a_y	Minor axis of an elliptic compliant joint
β_X	Dimensionless parameter demonstrating the joint geometry ax
β_y	Dimensionless parameter demonstrating the joint geometry ay
$\in$	Multiplication parameter of the proportion of major to minor axes
$f(\beta_y)$	The dimensionless compliance factor based on β_y
$f(\beta_x)$	The dimensionless compliance factor based on β_X
K_{in}	Input rigidity of the micromanipulator
F_{in}	Input force of the micromanipulator
F_{O3y}	The force is operating at point O_3 in the y-direction
F_{Ey}	Force is operating at point E in the y-direction
F_{Gy}	Force is operating at point G in the y-direction
M_{O3t}	Bending moments at point O_3
M_{Gt}	Bending moments at point G
M_{Et}	Bending moments at point E
K_{O3x}	Lateral bending rigidity by the force FO_3y
δ_4	Deformation based on drift of 4th beam
K_{Gy}	The G point's output rigidity of the hybrid amplifier
θ_4	Angle variable is generated by the torque of 4th beam
K_{O3t}	Rotation rigidity of point O_3
K_{Gt}	Rotation rigidity of point G
K_{Et}	Rotation rigidity of point E
λ_4	Intensification proportion of 4th beam

K_{in4}	Input rigidity of 4th beam
F_{Hy}	Force operating at point H in y-direction
F_{Iy}	Force operating at a point I in y-direction
F_{O4y}	Force operating at point O_4 in y-direction
M_{O4t}	Bending moments at point O_4
M_{It}	Bending moments at point I
M_{Ht}	Bending moments at point H
δ_3	Deformation generated by drift of 3rd beam
θ_3	Angle variable is generated via the torque of 3rd beam
K_{O4x}	Lateral bending rigidity by the force FO_4y
K_3	Output stiffness at point I
K_{O4t}	Rotation rigidity of point O_4
K_{It}	Rotation rigidity of point I
K_{Ht}	Rotation rigidity of point H
λ_3	Magnification proportion of the amplifier of 3rd beam
K_{in3}	Input rigidity of 3rd beam
F_{O2y}	Force operating at point O_2 in y-direction
F_{Cy}	Force operating at point C in y-direction
F_{Jy}	Force operating at point J in y-direction
M_{O2t}	Bending moments at point O_2
M_{Jt}	Bending moments at point J
M_{Ct}	Bending moments at point C
δ_2	Deformation based on drift of 2nd beam
θ_2	Variable angle generated by the torque of 2nd beam
K_{O2x}	Lateral bending rigidity via force FO_2y
K_2	Output rigidity at point E

K_{O2t}	Rotation rigidity of point O_2
K_{Ct}	Rotation rigidity of point C
K_{Jt}	Rotation rigidity of point J
λ_2	Mechanism amplification proportion of 2nd beam
K_{in2}	Input rigidity of 2nd beam
F_{O1y}	Force operating at point O_1 in y-direction
F_{Ay}	Force operating at point A in y-direction
F_{By}	Force operating at point B in y-direction
M_{O1t}	Bending moment at point O_1
M_{Bt}	Bending moment at point B
M_{At}	Bending moment at point A
δ_1	Deformation based on drift of 1st beam
θ_1	Angle variable generated by the torque of 1st beam
K_{O1x}	Lateral bending rigidity by force FO_1y
K_1	Output rigidity integrating points A and B
K_{12}	Output rigidity integrating 1st beam and 2nd beam
K_{13}	Output rigidity integrating 1st beam and 3rd beam
K_{y12}	Integration rigidity between 1st beam and 2nd beam
K_{y13}	Integration rigidity between 1st beam and 3rd beam
K_{O1t}	Rotation rigidity of point O_1
K_{Bt}	Rotation rigidity of point B
K_{At}	Rotation rigidity of point A
λ_1	Proportion of the amplification mechanism of 1st beam
k_{in1}	Input rigidity of 1st beam
$K_{\theta zMz}^{l7}$	Rigidity generated by the torque of a rectangular joint l_7

$K_{\theta yMy}^{l7}$	Linear rigidity generated by the axial force of a rectangular joint l_7
$K_{\theta zMz}^{l8}$	Rigidity generated by the torque of a rectangular joint l_8
$K_{\theta zMz}^{l9}$	Rigidity generated by the torque of a rectangular joint l_9
K_{b3}	Output rigidity integrating $K_{\theta zMz}^{l9}$ and double $K_{\theta zMz}^{c}$
ω_1	Rotation angle of a rectangular joint l_8
ω_2	Rotation angle of a rectangular joint l_7
ω_3	Rotation angle of a rectangular joint l_9
α_1	Rotation angle of compliant joint of the amplifier of 4th beam
β_1	Rotation angle of compliant joint of the amplifier of 3rd beam
γ_1	Rotation angle of compliant joint of the amplifier of 2nd beam
ε_1	Rotation angle of compliant joint of the amplifier of 1st beam
d_{out}	Output displacement
d_{in}	Input displacement
E_p	Potential energy inside compliant joints
K_{out}	Output rigidity of a micromanipulator
K_N	Integration rigidity of a micromanipulator in one direction
K_a	Integration stiffness of $K_{\theta yMy}^{l7}$
σ_y	Yield strength of the offered material
s	Safety factor
$f(\beta)$	Compliance parameter of a right circular joint
β	Dimensionless geometry parameter of a right circular joint
T	Total kinetic energy of the offered positioner
T_{η_1}	Kinetic energy of y-directions
T_{η_2}	Kinetic energy of x-directions
T_i	Kinetic energy of the element in a micromanipulator (i= m_1 to mb_3)

η_1	Coordinate exploited to express the movement of y-directions
η_2	Coordinate exploited to express the movement of x-directions
K_{out}	Output rigidity of a micromanipulator
K_N	Integration rigidity of a micromanipulator in one direction
K_a	Integration stiffness of $K_{\theta yMy}^{l7}$
σ_y	Yield strength of the proposed material
k_c	Concentration parameter of a right circular joint
$f(\beta)$	Compliance parameter of a right circular joint
β	Dimensionless geometry parameter of a right circular joint

List of Figures

List of Tables

CHAPTER 1 INTRODUCTION

Chapter 1 introduces background and motivation, purposes and objects, contributions, objectives, research methods, scientific and practical significance, thesis objectives, and scopes of the thesis.

1.1. Background and motivation

Nanoindentation is a standard and effective method to research the mechanical properties of materials at a small scale with minimal sample preparation. The technique is ideal for studying thin films or low material volume. In addition to hardness and elastic modulus, nanoindentation gives valuable insight into materials' creep, fracture, and fatigue properties. Using the size effect in miniaturized samples also studies the plastic behavior of quasi-brittle materials. By combining ultra-high load and displacement resolutions with in-situ SEM observation, the nanoindentation tester can measure the mechanical properties of specific submicron-scale microstructural features.

The nanoindentation tester is designed to measure hardness, elastic modulus, and creep. It is able to be utilized for specifying the distinctive features of organic, inorganic, hard, and soft materials. This method is extremely effective for characterizing the mechanical properties of biomaterials, permitting measurement of properties at small length scales that can be utilized to check or model micro/macroscale behavior. Different mechanical properties can be measured by selecting suitable tip geometries and checking protocols [1]. It is possible to conduct an indentation measurement in less than 3 minutes with no requirement of thermal stability using the distinctive top surface referring method. Accordingly, a locating procedure should be highly precise. Materials of soft and hard types from biological cell, material science, biomechanics, tissue, semiconductor nanomaterial, electronics, micro-electromechanical systems, and optics can be examined [2–4].

Currently, many labor accidents, occupational diseases, and traffic accidents have happened in Vietnam and in the world. Therefore, there is a need to use artificial joints such as artificial knee joint (Fig. 1.1(a)), artificial knee joints integrated with piezoelectric actuator (PZT) (Fig. 1.1(b)), and different artificial joints. An artificial joint is a prosthetic

joint, fabricated by various materials such as alloy, ceramic and plastic, which is implanted for replacing an injured or diseased natural joint. Firstly, the aforementioned joints are usually fabricated by 3D printing or CNC machining methods. Secondly, they are finished by grinding or polishing to achieve a good surface quality. In addition, finished components should be coated with a suitable material to improve the quality characteristics of artificial joints. Finally, before leaving the factory to put it into practical use, the aforementioned joints need to be tested for mechanical properties and durability. Therefore, the micro/nanoindentation testing device is potentially essential applied to develop for checking the mechanical properties of the coating material layer of artificial joints. Especially, the nanoindentation tester has been applied for checking the mechanical properties of animal bone (Fig. 1.2a) and thin film (Fig. 1.2b).

Figure 1.1. Potential compliant mechanism applications for nanoindentation testing device: (a) artificial knee joint [5], (b) artificial knee joint integrated PZT [6].

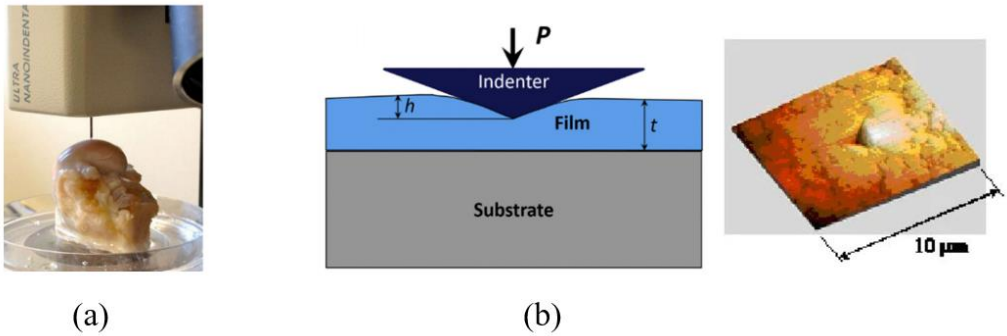

Figure 1.2. Potential compliant mechanism applications for nanoindentation tester system: (a) animal bone, and (b) thin film [7,8].

Multiple microscopes are used during the indentation process for recording the picture

of the specimen before and after the indenting test for checking the displacement versus load curve while a specimen is brought facing the microscope. An accurate positioner is required for locating the specimen so as to attain nice image excellence. It follows that the compliant positioner is an essential structure for the nanoindentation testing device. The existing system is difficult to achieve extreme location accurateness due to the use of servo motors, ball screws, and rigid joints in commercialization. This results in adverse consequences such as abrasion, wear, and backlash.

Flexure positioners are developed for overcoming the drawbacks of traditional technologies in order to improve system resolution because of key advantages such as monolithic configuration, no wear, light weight, free backlash, no friction, low price, free lubricant, high exactness, and miniature configuration.

Based on the compactness of compliant mechanisms [9,10], Huang et al. developed a modular miniaturization nanoindentation device, as illustrated in Fig. 1.3, with the working travel in x and y directions of 12 μm for location positioning and the z direction of 40 μm for indenter [11]. However, this study only concentrated on the design of the 01-DOF stage for driving the indenter. This design was developed for checking soft specimens. Meanwhile, the Z-output displacement should be improved for checking the mechanical properties of harder specimens.

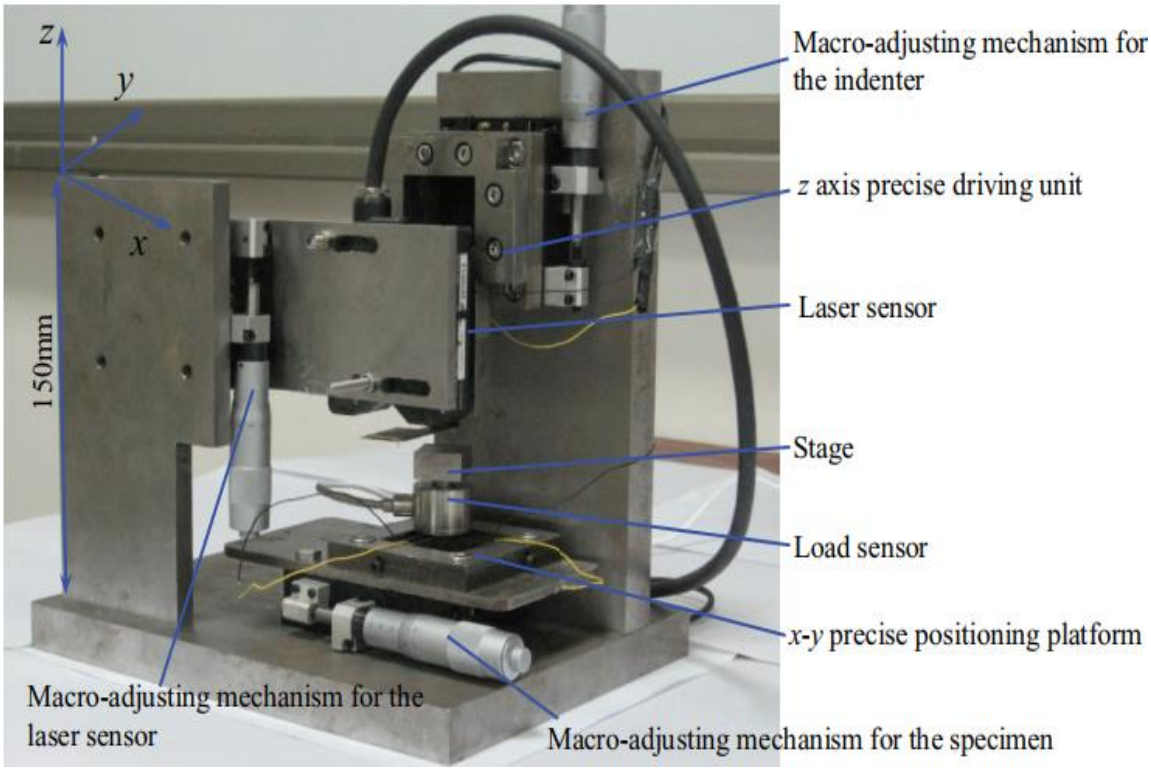

Figure 1.3. A modular miniaturization nanoindentation device [11].

In particular, in situ nanoindentation was applied in the field of implants (e.g., bone, teeth, femur, and prosthetics) [1,12]. However, the mechanical components, (e.g., machine base, shaft, bush, gear, cam, sliding rail, ball screw, and ball nut) have existing restrictions, such as clearance, friction, wear, and vibration. Consequently, these mechanical devices are complicated for obtaining a precise motion or positioning.

In addition, a compact structure is a recent tendency in designing a new in-situ nanoindentation tester in order to reduce energy consumption. Especially, in situ nanoindentation often requires many force and displacement feedback sensors to achieve a precise positioning capability. In such in situ nanoindentation applications, the two main modules consist of an indenter driving stage and a bio-material sample locating stage. However, the existing stages continue to have a slow response speed, indicating a low resonant frequency. Due to their large size, they are difficult to install positioners in in-situ nanoindentation with a transmission electron microscope (TEM) or a scanning electron microscope (SEM). Hence, a new structural design of the stage with a faster response speed is in high demand.

Many designs for in situ nanoindentation in SEM/TEM have been developed over the last two decades. A survey on SEM in situ nanoindentation was thoroughly investigated, taking into account the mechanical and electrical properties of nanomaterials [13]. The nanomechanical properties of micro/nano-materials were observed through in situ nanoindentation in SEM [14].

Particularly for the nanoindentation tester, with reference to the compactness of the compliant mechanism, Rabe et al. [15] developed an SEM nano scratch instrument with the indenter driving stage stroke of 20 μm, as illustrated in Fig. 1.4. An indenter driving stage stroke of 11.44 μm was developed by Huang et al. [9].

Additionally, Huang et al. developed another stage with 40 μm. Besides, Zhao et al. developed an indenter driving stage with 15 μm. In practical applications, a nanoindentation device is desired to achieve excellent locating precision, high operating travel, and high material strength.

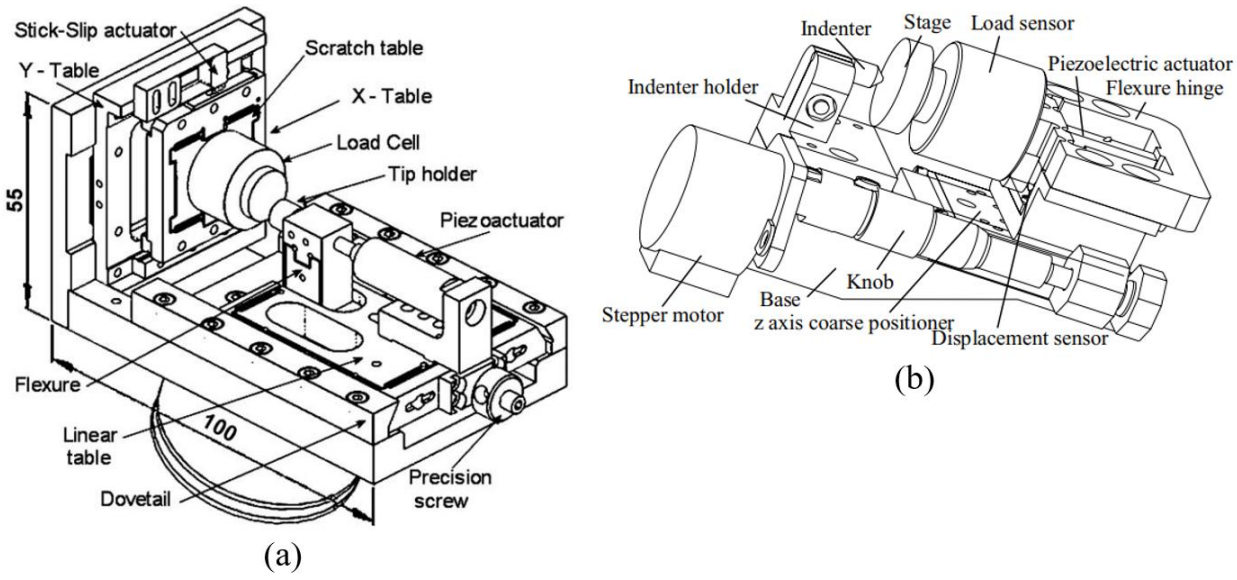

Figure 1.4. Basic application of nanoindentation tester system: (a) nanoscratching device [15], (b) in-situ nanoindentation device inside the SEM [9].

In summary, the above-mentioned designs only focused on the 1-DOF compliant stages for driving the indenter. A full design of the nanoindentation device should include the 1-DOF stages for the indenter driver and 2-DOF/3-DOF stages for specimens positioning. However, the previous studies have not a full development for a nanoindentation device yet. Moreover, the existing designs are difficult to integrate into the nanoindentation device for indenting and checking various specimens, especially bio-specimens (as shown in Figs. 1.1-1.2) due to their disadvantages, such as a small working stroke, a high parasitic motion error and a small stiffness. Therefore, the author chooses this thesis, namely, "*Development and optimization of compliant positioning stages applied for nanoindentation testing device"*.

1.2. Proposed nanoindentation device

In testing the mechanical properties of materials, a nanoindentation tester is applied to assess the hardness, and elastic modulus of material samples such as bones, joints, porcelain teeth, and thin-walled plates in electronics and packaging technology. Nowadays, numerous methods for testing strength or mechanical properties of materials have been proposed, such as tesnsile test, torsional test, fatigue test, fracture mechamics test, compressive test, and creep test. Especially in testing hardness properties of materials, a few common methods include Brinell, Vicker, Rockwell, and Berkovich. To monitor the mechnical properties of thin-thickness material samples in Figs. 1.1-1.2, a new

nanoindentation device based on Berkovich principle is proposed in this thesis, as given in Fig. 1.5. To increase the positioning accuracy of indenter and sample driver, compliant mechanism is chosen to develop the indenter and sample positioners.

As illustrated in Fig. 1.5, the indenter (1) will be guided to the specimen. Then, the material sample is positioned on a positioning table (2). The positioning table moves the sample into close proximity to the indenter. The interest in the aforementioned measurement technique is how to control in-situ nanoindentation online. Furthermore, how to adjust the force and stroke of the puncture head (1) in a variety of a few micrometers to several hundred micrometers to suit different material samples is a problem to be solved. Moreover, the material sample positioner (2) must achieve an accurate working stroke with a variety from a few micrometers or hundreds of micrometers.

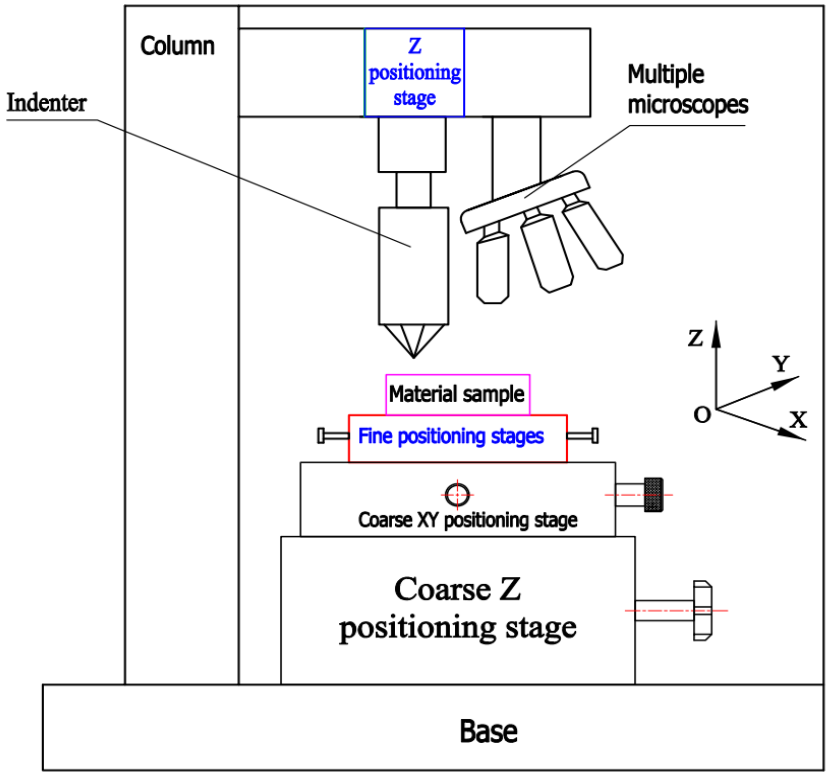

Figure 1.5. Suggested model for indentation positioning system

Recently, the trend is that nanoindentation devices are increasingly required to be more compact and have higher accuracy. More specifically, a material hardness tester (micro/nano indentation tester) is often adopted for measuring the hardness, elastic modulus and different mechanical properties of material samples. The nanoindentation tester is expected to be integrated into SEM or TEM to directly monitor the deformation process, geometric morphology and damage of material samples. This is named as an in

situ nanoindentation process. However, such an integration is still limited. Therefore, the development of compact devices with high precision to integrate into the scanning electron microscope to ensure both mechanical testing and observation of the geometry of the deformation process and material damage is necessary for future research and development. Compared with the traditional structures, the compliant mechanism is of interest for various applications such as biomedical, robotics, micromechanics, force and displacement measurement devices, and precision positioning tables. However, the application of the compliant mechanism for developing in-situ nanoindentation equipment is relatively restricted.

In this thesis, the proposed nanoindentation device is potential to be applied for testing artificial joints, animal bone and thin film (as depicted in Figs. 1.1-2). In order to ensure a good positioning system, this thesis suggests new designs of one degree of freedom (DOF) positioners to 3-DOF positioners using compliant mechanisms with symmetrical structures and parallel structures. In terms of working functions, the positioners must achieve the following characteristics: (i) amplify the large output displacement to widen the working stroke, (ii) reduce parasitic motion error to increase positioning accuracy, (iii) a high natural frequency to accelerate device response and avoid vibration resonance; and (iv) a long life to ensure long-term working capability.

1.3. Purposes and objects of the thesis

The purpose of this thesis is to develop the compliant positioning stages applied for the nanoindentation testing device. In this thesis, the research objects include as follows: (i) Flexure hinge with multi-performances, (ii) 01-DOF positioning stages for driving indenter, (iii) 02-DOF positioning stages and 03-DOF positioning stage for locating the specimens.

1.4. Objectives of the thesis

The objectives of the thesis are to:

- Analyze, evaluate as well as select suitable flexure hinges which will be integrated into compliant positioning stages in nanoindentation tester system.
- Develop three new design alternatives of compliant 01-DOF stages for driving indenter.
- Develop the 02-DOF stages and 03-DOF positioning stage applied for locating the specimens.

- Establish mathematical equations to describe static, kinetostatic, and dynamic behaviors of the proposed stages for evaluating the behaviors of the stages.
- Establish a finite element analysis-based computational simulation program to simulate the behavior of the stages.
- Develop integrated optimization algorithms and intelligent calculation methods for optimizing the main factors of the positioning stages for improving the positioning stages' output characteristics.
- Compare and verify analytical calculation results with simulation results and optimal results.

1.5. Scopes

The scopes of this thesis demonstrate are as follows:

- Development of a new hybrid method for evaluating and selecting a suitable flexure hinge integrated for compliant stages.
- Design, analysis and optimization of passive 01-DOF passive positioning Z-stages, passive XY compliant positioning stage, and rotary compliant positioning stage.
- Development of hybrid displacement amplifiers with suitable flexure hinges integrated into new compact positioning stages for in situ nanoindentation tester.
- Development of compact above-mentioned positioning stages to fulfill quality characteristics such as small parasitic motion, high stiffness and suitable output displacement for in situ nanoindentation testing device.

1.6. Research methods

The research methods list as follows:

- The theory of compliant mechanisms is used to develop compliant positioning stages.
- The pseudo-rigid-body model (PRBM) method, kinetostatic analysis-based method and Lagrange method are built to establish analytical modeling to analyze static, dynamic and kinetostatic behaviors of the proposed stages.
- The behaviors of the proposed stages are analyzed using the finite element method.
- New hybrid optimization approaches are developed to enhance the quality characteristics of the proposed stages.

1.7. Scientific and practical significance of the thesis

1.7.1 Scientific significance

The scientific significance of the thesis covers as follows

- Develop an effective approach for evaluating and choosing suitable flexure hinges integrated compliant positioning stages.
- Contribute new structures of compliant positioning stages for driving the indenter and locating the specimens in a nanoindentation testing device as well as a precise positioning system.
- Describe and predict static and dynamic behaviors of the proposed stages based on the PRBM method, kinetostatic analysis-based method and the Lagrange method.
- Develop new hybrid optimization approaches for enhancing the quality characteristics of the proposed stages as well as applying them to engineering fields.
- Provide basic approaches for design, analysis, and optimization for the compliant positioning stages.

1.7.2. Practical significance

The scientific significance of the thesis covers as follows.

- The proposed positioners can be applied for a nanoindentation testing device as well as a precise positioning system.
- The cost of proposed positioners can be significantly reduced due to the advantages of compliant mechanisms such as no friction, no wear, minimal assembly, and no lubrication.

1.8. Contributions

In this thesis, the key contributions are covered as follows:

Initially, a new multi-response optimization design approach is developed to optimize the elliptic flexure hinge. The presented framework method is an integration approach of the Taguchi method (TM), fuzzy logic reasoning, response surface method, and moth flame optimization (MFO) algorithm. Exploiting Wilcoxon and Friedman tests, the efficiency of the offered methodology is superior to other methods, such as the atom search optimization (ASO) algorithm and genetic algorithm (GA). In this study, the elliptic hinge is employed for positioners in a nanoindentation testing device.

Secondly, three new design alternatives of 01-DOF positioning stages are proposed for driving the indenter.

- The four-lever displacement intensification structure and beetle-like structure are used to integrate the first 01-DOF stage. A combination of the advanced ANFIS and TLBO

is proposed for handling the multi-criteria optimization problem. The TM is devoted to optimize the ANFIS predicting accuracy.

- The second design is built according to a two-lever displacement amplifier, a flexure shifted structure, and a parallel guiding structure. An offered hybrid optimization approach that combines the TM, RSM, weight factor computation technique, and Whale optimization algorithm (WOA) was presented for optimizing the quality attributes of the second design alternative of a 01-DOF stage. The effectiveness of the offered combination methodology is confirmed using FEA and experimental results.
- The third 01-DOF stage design is based on a six-lever amplifier and parallel guiding mechanism. The PRBM method and the Lagrange method are developed to build the equations of statistics and dynamics which can calculate the displacement amplification ratio the first natural frequency. Later, the Firefly algorithm is exploited for optimizing the main parameters for advancing the quality features of the proposed positioner.

Finally, three new design alternatives are proposed for locating material samples in nanoindentation testing device as well as precise positioning system.

- The first compliant XY stage is based on four-lever displacement amplifier and guiding parallel guiding according to zigzag-based flexure spring. An integration optimization methodology combining TM, RSM, and NSGA-II was offered for conducting the multi-objective design problem.
- The second design of rotary stage iss based on the profile's beetle leg, cartwheel hinge and rotation platform based on three leaf flexure hinges. A new hybrid optimization approach of TM, RSM, weight factor quantifying technique, and teaching learning-based optimization (TLBO) algorithm is developed for optimizing the quality characteristics of the compliant rotary stage. Wilcoxon's rank signed analysis as well as Friedman analysis are employed for statistical comparison.
- The second 02-DOF stage is built with a displacement intensification mechanism with eight levers, elliptic joints, and a parallel guiding mechanism. The kinetostatic analysis-based method and Lagrange method are developed to formulate the dynamic equation. Later on, the neural network algorithm is utilized for optimizing the main parameters for advancing the quality characteristic of the offered positioner.

1.9. Outline of thesis

- Chapter 1 introduces the background and motivation, purposes and objects of the thesis, thesis objectives, scopes, research methods, scientific and practical significance of the thesis, contributions, and outline of the thesis.
- Chapter 2 presents a theoretical basis for compliant mechanisms, compliant positioning stages, displacement amplification mechanisms, nanoindentation tests, the statistical analysis, modeling methods of compliant mechanisms, optimization methodologies applied for designing, analytical modeling, and optimization of proposed compliant stages.
- Chapter 3 focuses on the evaluation and analysis of four common flexure hinges. This chapter, in particular, proposes a new effective optimization approach that combines the TM, fuzzy logic, RSM, and MFO algorithm for optimizing the main input parameters of an elliptic compliant joint. According to the consequences of analysis and optimization, the elliptical hinge as well as other flexure hinges such as the leaf hinge and circular hinge are integrated into compliant positioners to locate and indent material samples in a nanoindentation testing device.
- Chapter 4 presents three design alternatives for indenting the specimens in nanoindentation testing device. Each design has its own advantages and disadvantages. To be more specific, the first design alternative presents the design of the 01-DOF stage inspired by the profile of the beetle leg, as well as an effective hybrid optimization approach of RSM and advanced ANFIS for improving output responses. The second design alternative shows a 01-DOF stage with a four-lever intensification structure, a flexure hinge shifted layout structure, a zigzag-based compliant spring driving structure, and a symmetrical six-rectangular joints-based parallel driving structure, as well as an effective approach of the TM, RSM, weight factor computation technique, and Whale optimization algorithm. The third design alternative presents the design of 01-DOF stage based on symmetric six-lever displacement intensification structure combined elliptical flexure hinges and symmetrical six rectangular joint parallel driving structure. Furthermore, analytical modelling was established based on the PRBM method and Lagrange method to quickly identify the initial characteristics of the stage.
- Chapter 5 presents three design alternatives locating the specimens in nanoindentation testing device. The first design alternative of an XY stage is designed according to the four-lever amplification mechanism and parallel guiding mechanism using zigzag-based flexure

hinge. In addition, an integration methodology of TM, RSM and NSGA-II is applied for optimizing the quality responses. The second design alternative of an XY stage is designed according to the eight-lever amplification mechanism integrated elliptic hinges and parallel guiding mechanism. The kinetostatic analysis-based method and Lagrange method are proposed to build dynamic structure modeling for evaluating rapidly the initial quality characteristic of the proposed second 02-DOF stage. In the third design alternative, in order to reduce a number of actuators, the positioner is designed according to four-lever displacement intensification structure, the parallel guiding mechanism inspired from the profile's beetle leg, the compliant cartwheel hinge and rotary platform. Furthermore, an effective hybrid approach of TM, RSM, and weight factor computation technique according to signal to noise and TLBO algorithm is upgraded for optimizing the design variables to advance the output characteristics of the offered positioner.

- Chapter 6 presents achieved results of proposed 01-DOF compliant positioning stages, rotary compliant positioning stage, and XY stages intended to apply for nanoindentation tester as well as precise positioning stage. To improve the distinctive features of the compliant stages, various efficient hybrid optimization approaches for enhancing the characteristics of the compliant positioning platforms were proposed. This chapter also recommends the proposed solutions for the development of compliant stages as follows:

- Develop more compliant positioning stages intended to apply for in situ nanoindentation testing device and precise positioning system.
- Develop more compliant positioning stages inspired from profile of animals for precise positioning system.
- Develop new optimal approaches for enhancing compliant stages and compliant mechanism.
- Fabricate and test the quality characteristics of the proposed compliant positioning stages.

CHAPTER 2 LITERATURE REVIEW AND BASIS THEORY

Chapter 2 represents the literature review and theoretical basis of compliant mechanisms, compliant positioning stages, displacement amplification mechanisms, nanoindentation testing device, statistical analysis, modeling methods of compliant mechanism, and optimization methodologies applied for designing, analytical modeling, and optimization of the proposed compliant stages.

2.1. Compliant mechanisms

2.1.1. Compliant mechanism and applications

The compliant mechanism has been defined in the field of mechanical engineering as a flexible or flexure-based mechanism that transmits force, moment, and motion through the process of elastic deformation. This mechanism achieves some or all of its motion through the relative flexibility of its components, rather than solely through the rigid-body joints. These structures can be monolithic (one piece) or jointless. There are numerous benefits to compliant mechanisms, including no friction, low cost, no wear, compact structure, and monolithic material. As a result of the benefits of compliant mechanisms, they are now widely used in a variety of fields such as commonly used devices, medicine, micro-electromechanical systems (MEMS), and robotics.

a. Daily life

There are a large number of common devices using compliant mechanisms because of their flexibility, as demonstrated in Fig. 2.1.

Figure 2.1. Popular flexure-based amenities [16].

b. Medicine

The compliant mechanism has merits because of its monolithic structure, no wear, no friction, and no lubrication. It is suitable for the internal environment of the body. Consequently, compliant mechanisms have been researched for using the medical area, as depicted in Fig. 2.2.

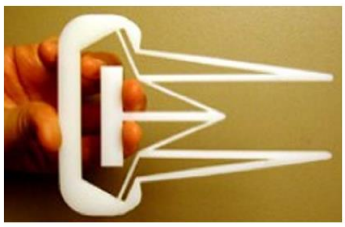

(a)

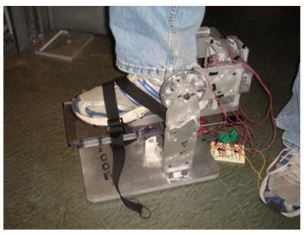

(b)

Figure 2.2. Applications of compliant mechanisms in medicine: (a) Prototype of the compliant gripper [17], (b) Prototype ankle rehabilitation device in use [18].

Furthermore, as shown in Fig. 2.3, compliant mechanisms have been widely used in the bio-robotics industry, as has the application of a flexure-based 2-DOF ankle-foot system for a motivated human arm bio-robot, as shown in Fig. 2.4.

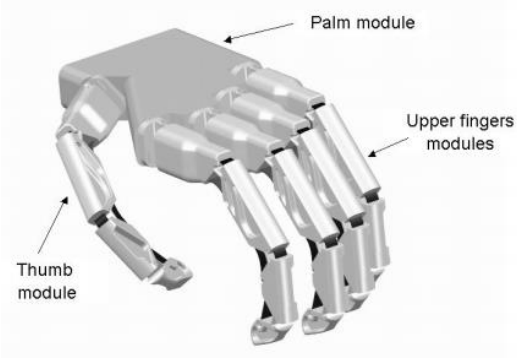

Figure 2.3. Robotic hands based on the compliant mechanism [19].

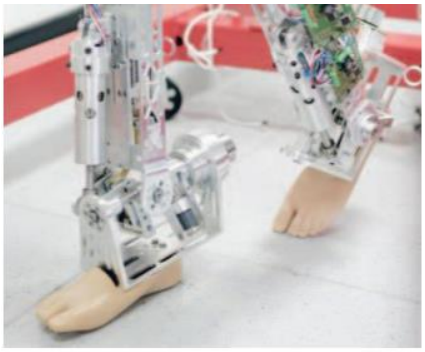

Figure 2.4. The 2-DOF ankle-foot system based on the compliant mechanism [20].

c. Micro-electromechanical systems

Micro-electromechanical systems (MEMS) is a technological process for developing equipment or systems integrating electrical and mechanical components. MEMS elements can be manufactured using combined circuit (IC) batch handling methods and a variety in size [a few micrometers, millimeters]. Based on the benefits of small size, compliant

mechanism is the suitable choice for application. Fig. 2.5 illustrates a MEMS device based on compliant mechanisms.

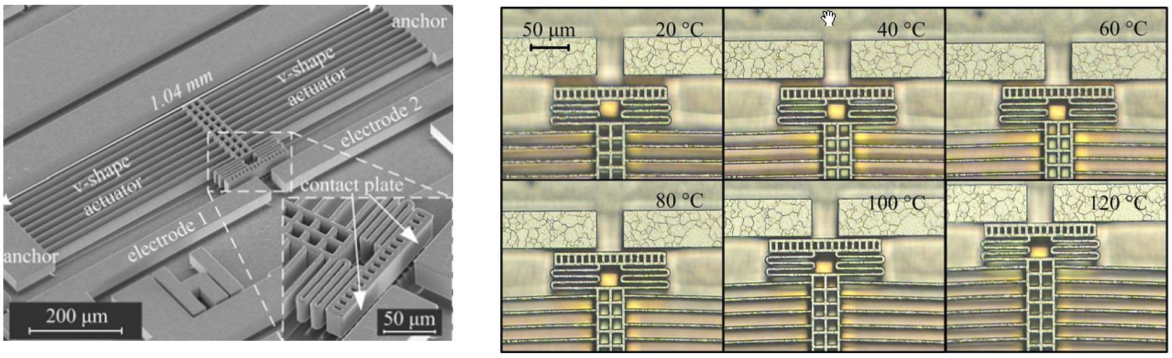

Figure 2.5. Applications of compliant mechanisms in MEMS [21]: A temperature triggered MEMS switch.

However, the compliant mechanism applications for nanoindentation indentation testing device have less been investigated. Therefore, in this research, new compliant positioning structures are developed for the nanoindentation indentation tester system as well as precise positioning system.

2.1.2. Flexure hinges

In the field of compliant mechanisms, flexure hinges are extensively exploited and have a wide range of applications. A flexure hinge is a mechanical element that supports the relative rotation of rigid elements based on its bending ability rather than traditional rotary hinges [22]. Many different types of flexible hinges have been researched and improved in previous studies. Lobontiu et al. [23] suggested precise compliance formulas for calculating symmetrical corner-rounded flexure hinges. Likewise, various types of flexure hinges have been investigated and studied. For example, a concise presentation to the classification of flexure hinges according to their operational principles as well as related geometry constructions has been provided. Flexure hinges are generally classified into two types: original flexure hinges and complicated flexure hinges. [24,25], as illustrated in Fig. 2.6. A single axis flexure hinge, in particular, has a rectangular cross-section with an unchanging width and changeable height. The shapes of their cross-sections are used to classify these flexure hinges. The two examples are notch-type flexure hinges (shown in Fig. 2.7) and complicated hinges (shown in Fig. 2.8). More specifically, notch-type flexure hinges have been extensively exploited in precise macro/micro/nano positioning structures. Circular flexure hinges [26], corner-rounded flexure hinges [27], V shape flexure hinges

[28], elliptical flexure hinges [29], parabolic flexure hinges and hyperbolic flexure hinges [30] are examples of this type of flexure hinge.

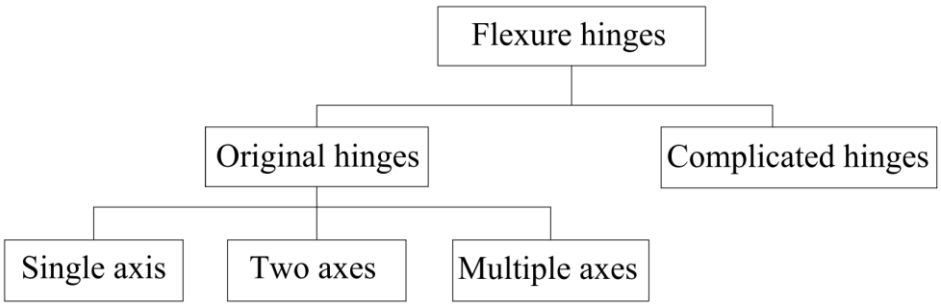

Figure 2.6. Key categories of flexure hinge.

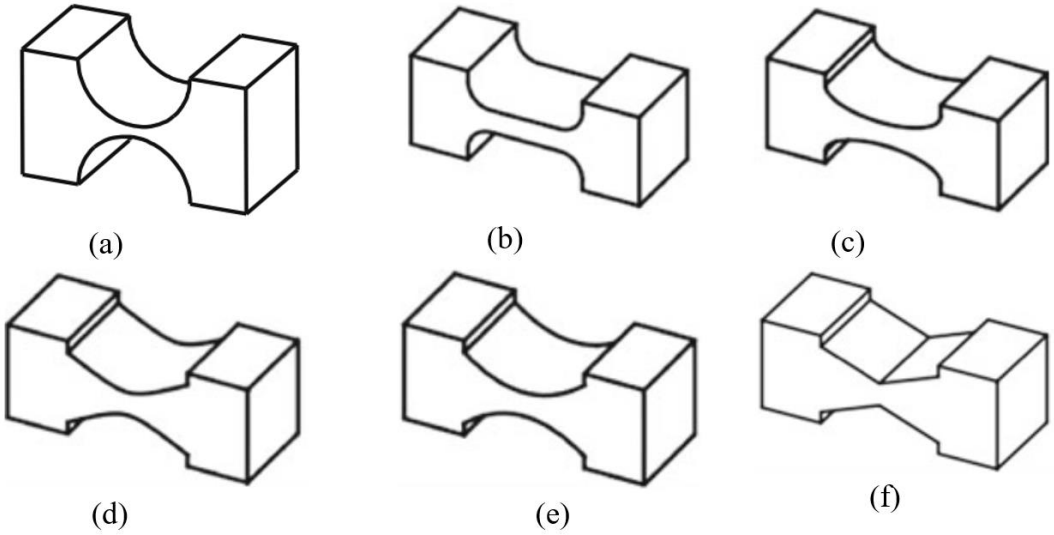

Figure 2.7. Notch-type compliant joint [31]: (a) right circular joint, (b) corner-rounded joint, (c) elliptic joint, (d) hyperbolic joint, (e) parabolic joint, (f) V-shaped joint.

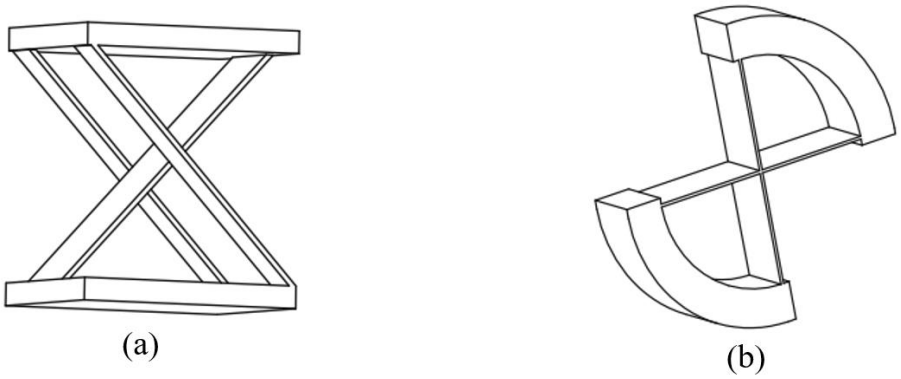

Figure 2.8. Complicated hinges [32]: (a) Cross axis hinge, (b) Cartwheel hinge.

Each kind of flexure hinge has its own scope of usage, depending on its structure and operating range. Nowadays, flexure hinges, especially notch-type flexure hinges are widely used in many fields, especially in positioning stages and MEMS systems. Meanwhile, the evaluation, choice and integration of various flexure hinges based on the merits of flexure hinges into positioners applied in nanoindentation testing device has been less investigated. Therefore, in this thesis, an effective approach is proposed for evaluating and selecting appropriate flexure hinges to facilitate the integration into proposed compliant positioners.

2.1.3. Actuators

There are four kinds of actuators which are widely utilized for designing micro-/nano-positioning stages [33,34]. Their working principles such as electrostatic, electromagnetic, piezoelectric and electrothermal effects are considered as criteria for the classification. As the introduced actuators are able to satisfy the stroke requirement with the range from sub-nanometer to centimeter scale, these four types of actuators [35] are extensively adopted for the compliant micro-/nano positioning platforms. In this research, piezoelectric actuator (PEA or PZT), as illustrated in Fig. 2.9 is proposed for using in generating the input displacement of the stages. Currently, stack-based PEA is primarily exploited for actuation because it is made up of multi-layers of piezoelectric material offering a sufficient output force and working travel. Furthermore, the easiness of utilization causes PEA the most extensively exploited actuator in precise micro-/nano-positioning systems.

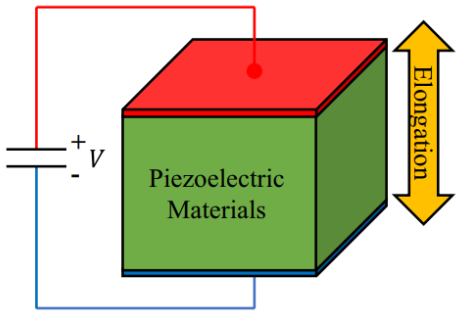

Figure 2.9. Piezoelectric actuator.

The ability to generate force up to a kilonewton grade is the most significant advantage of PEA. It also has a high sub-nanometer-scale resolution and response speed, which aids in precision manipulation implementation. However, because the capacity of the PEA changes during operation, the input voltage-output displacement relationship exhibits severe hysteresis. For better precision control, controller designers must investigate the

modeling of PEA hysteresis. [36]. Furthermore, because PEA's tensile strength is much lower than its compressive strength, preloaded PEA is a resolution to evade destruction. A suitable preload is offered for warranting that PEA maintains its effective dynamic characteristics. Hence, the stage must incorporate a preload-adjustable design.

PEA actuator is used in this thesis for the proposed stages due to its advantages such as high stiffness, high response, and large output force.

2.2. Previous compliant positioning stages

In general, compliant positioning stage structures [37] are classified into three main kinds of serial structure, parallel structure, and serial-parallel structure, as demonstrated in Fig. 2.10 (a-c), respectively.

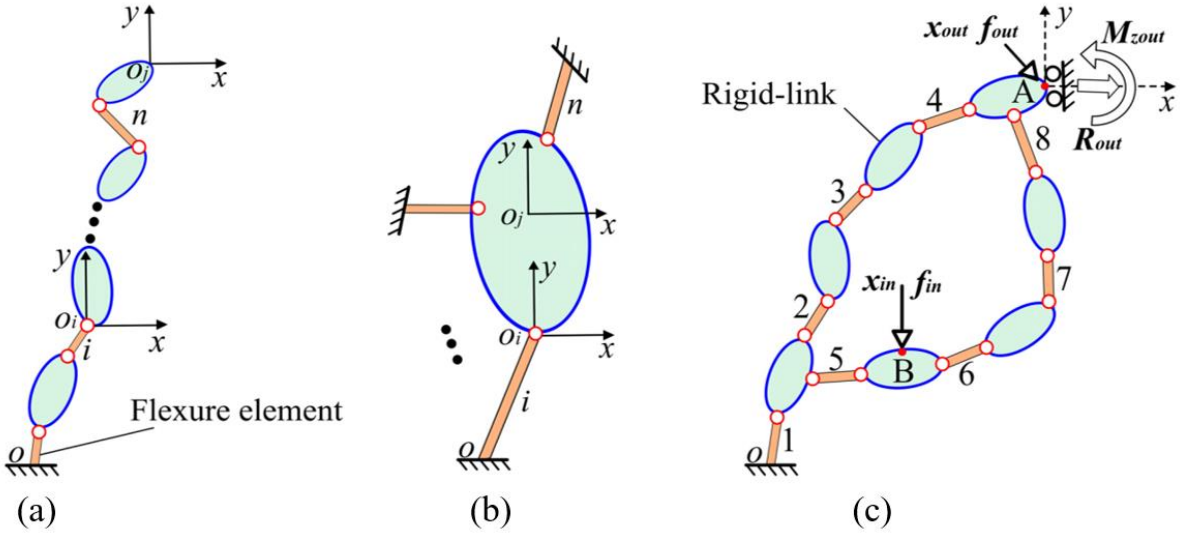

Figure 2.10. Kinds of compliant positioning stage structures [37]: (a) serial, (b) parallel, and (c) serial-parallel.

In order to execute various complex actions, the micro/nano positioner requires more degrees of freedom (DOF). Three crucial diagrams for the design of a multi-DOF platform include serial diagram, parallel diagram and serial-parallel diagram [35].

2.2.1. Serial diagram design

The serial diagram is the most basic approach for creating a multi-DOF platform, requiring a series connection between one positioner's fixed end and another stage's output end. As a result, the serial positioners can be exploited modularly; for example, several 1-DOF stages can be combined to form an XY, XYZ, or large travel 1-DOF positioner. Furthermore, the serial positioner is simple for building as a stacked mechanism decreasing

planar dimension and enrich miniaturization. Finally, the serial diagram is suggested for building compliant positioners that demand high modularity or suppleness to fit various purposes. Specifically, Xu [38] proposed a dual-stage 1-DOF positioning stage, as illustrated in Fig. 2.11, by serially connecting the VCM-driven and PEA-driven platforms, with a resolution of 500 nm and a stroke of over 10 mm. Lee et al. [39] proposed a serial XY positioner with a stacked mechanism and a workspace area of 80 × 80 μm^2. Liu et al. [40] developed a planar serial XY stage using an embedded mechanism. It has a 50 nm resolution as well as a working space of 41.6 × 42.9 μm^2. Pinskier et al. [41] created a 02-DOF serial platform with a working space of 39.1 × 42.1 μm^2 by combining two modular 1-DOF positioners in a stack.

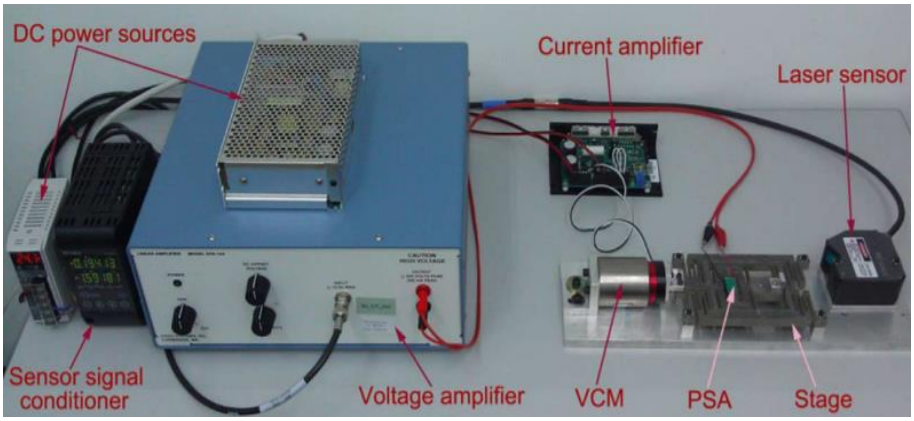

Figure 2.11. A compliant dual-platform nano-positioning platform [38].

Meanwhile, as with a multi-DOF serial stage, each stage's positioning error is accumulated and expressed in the final output. Alternatively, differences in loading between levels will result in varying dynamic performances at each stage. To overcome these drawbacks, a feedback control system should be used.

2.2.2. Parallel diagram structure

A multi-input system that concurrently connects the output ends of various connections and pairs the output movement could be used to advance compliant parallel platforms. Another approach is to use decoupling structures as connectors to link the output ends of various positioners. These structures are exploited for decreasing the coupling influence or to separate the output movement of a stage's different axes. The issue of integrating multiple single-input single-output systems could be solved thanks to this outstanding feature.

By utilizing a symmetrical structure, the parallel diagram could offer greater stiffness, rapider response, no accumulated error, and identical dynamic characteristics on each axis when compared to the serial diagram. This diagram is typically used in applications requiring great dynamic characteristic.

Existing studies about the parallel positioner mainly put their focus on three main types of stages such as XY stage [42], XYθ stage [43], and XYZ stage [44] due to their high versatility. Specifically, Lai et al. [45] proposed a decoupled parallel micro-positioning XY stage that achieved the resonant frequencies of the loaded positioner at 2 kg and 5 kg with 105 Hz and 68 Hz, correspondingly. Tian et al. developed a compliant XY positioning platform that achieved a workspace range in excess of 8 x 8 μm with a stiffness of 4.97 N/mm, the first-order natural frequency of 231 Hz, and a low cross-axis coupling ratio (less than 0.6%). Ding et al. [46] proposed an XYθ stage integrated one-lever displacement amplifier that achieved a displacement amplification ratio of 3.27. Zhang et al. [47] proposed a new flexure-based XYZ parallel nano-positioner that achieved the overall stage size of 68.5mm × 68.5mm × 68.5mm, the displacement amplification ratio of 9.31, and high percentage cross axis errors of 0.7% and 0.8%.

2.2.3. Serial-parallel diagram design

Because both serial and parallel diagrams have benefits and drawbacks, the serial-parallel diagram is regarded as a harmony option for reducing design difficulties and achieving more reliable characteristics. In general, the serial-parallel diagram has more stiffness than the serial diagram as well as requires a superior working space than the parallel diagram. The serial-parallel diagram is commonly used in building design structure when three or more degrees of freedom are required. There are numerous studies on the serial-parallel stage utilizing rigid mechanisms [48,49], but only a few on the compliant mechanism. Based on many benefits such as simple structure, high system stability, low assembly error, and good dynamic performance, Tang et al. [50] proposed the XYZ serial-parallel positioning platform that integrated two-axis flexure hinges. Cai et al. [51] constructed a 6-DOF compliant platform by serially connecting two balancing 3-DOF parallel stages.

Moreover, compliant mechanisms have been widely utilized in the micro-/nano-positioning stage, as illustrated in Figs. 2.12-21. Specifically, Quan Zhang et al. [52] developed compliant 02-DOF stage integrated bridge displacement amplifier for precise positioning system, as illustrated in Fig. 2.12. The authors utilized an integration of the

elastic beam theory and Castigliano's second theorem for modeling bridge amplification proportion. The experimental results revealed that the magnification proportions for the X and Y axes are 5.83 as well as 5.71, correspondingly, the platform's working space is 174.9x171.3 (μm), and the parasitic motion error is less than 3%.

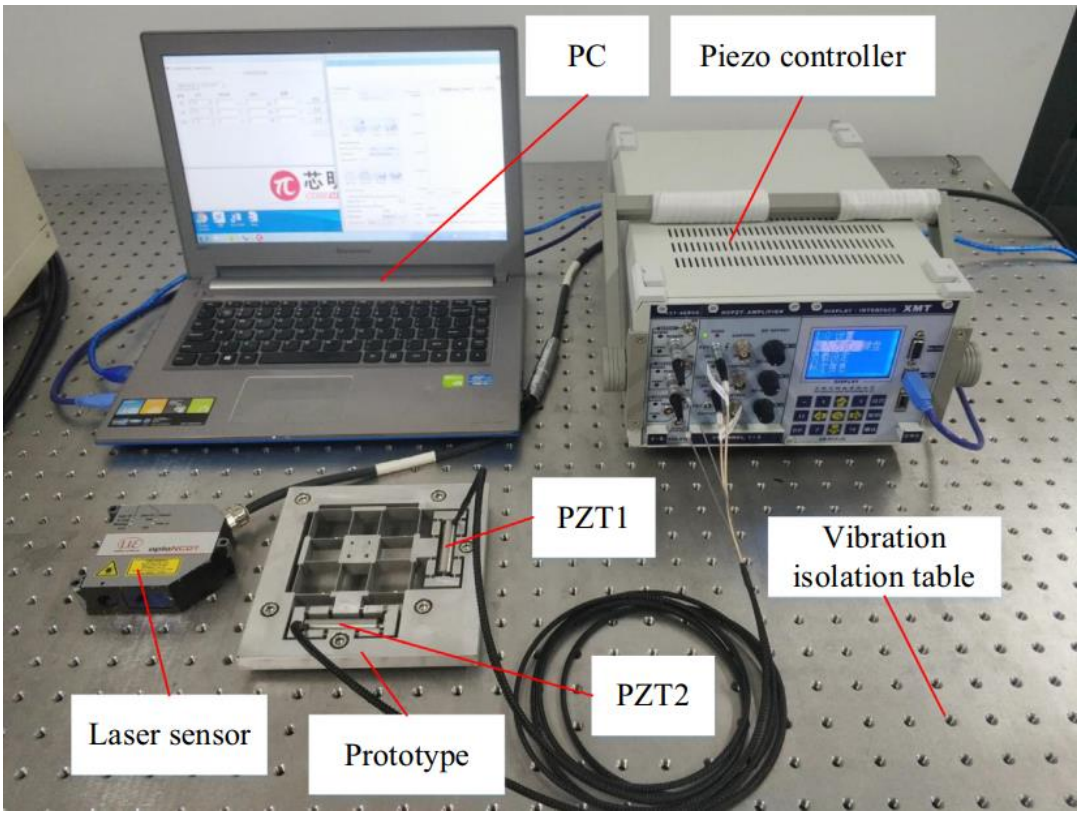

Figure 2.12. A compliant 02-DOF positioning stage integrated bridge displacement amplifier [52].

More specifically, Wu-Le Zhu et al. [53] introduced a XY stage which integrated a hybrid compliant displacement amplifier of Scott–Russell structure as well as a half-bridge structure applied for precise positioning system, as illustrated in Fig. 2.13. An analytical model was built to express the platform's output response behavior. The results of the experiment revealed that the magnification proportions in the X, Y-directions are 5.2 and 5.4, respectively. The experimental natural frequencies in the X as well as Y axes were 570 and 585 Hz, correspondingly. Furthermore, the parasitic motion error was reduced by 1%.

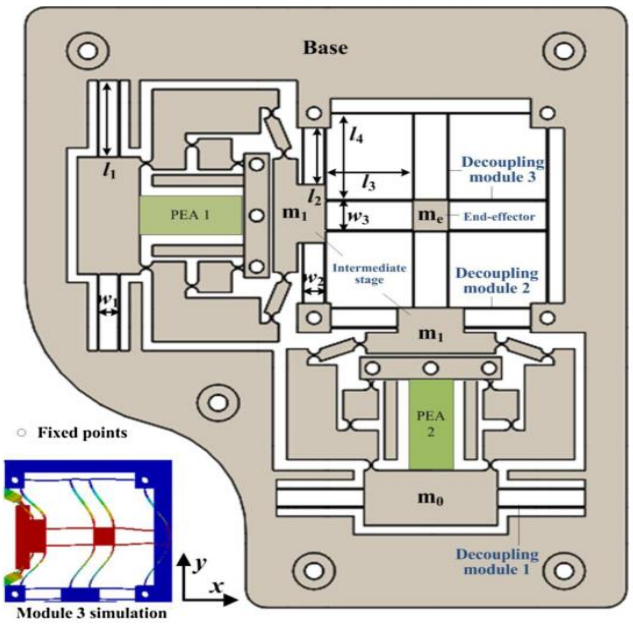

Figure 2.13. A compliant XY nano-positioning stage integrated Scott-Russell and a half bridge displacement amplifier with fully decoupled kinematics [53].

In addition, as shown in Fig. 2.14, Jinqiang Gan et al. [54] created a compliant 3-DOF XYZ stage integrated Z-formed compliant joints and bridge displacement. The bi-direction motion in the Z-direction is created by reversing the arrangement of the Z-shaped compliant joints based on the X, Y-direction motions. Based on the energy method, compliance matrix approach as well as force balance rule, an analytical model was established. The simulated results showed that the mean travels of the stage based on the X, Y, and Z directions denote ±125.58 μm, ±126.37 μm, as well as ±568.45 μm, correspondingly. The first natural frequencies of three modes are 247.3 Hz, 270.2 Hz, and 271.7 Hz, correspondingly. Meanwhile, the stage's strokes in reference to the X, Y, and Z-directions can be not the same.

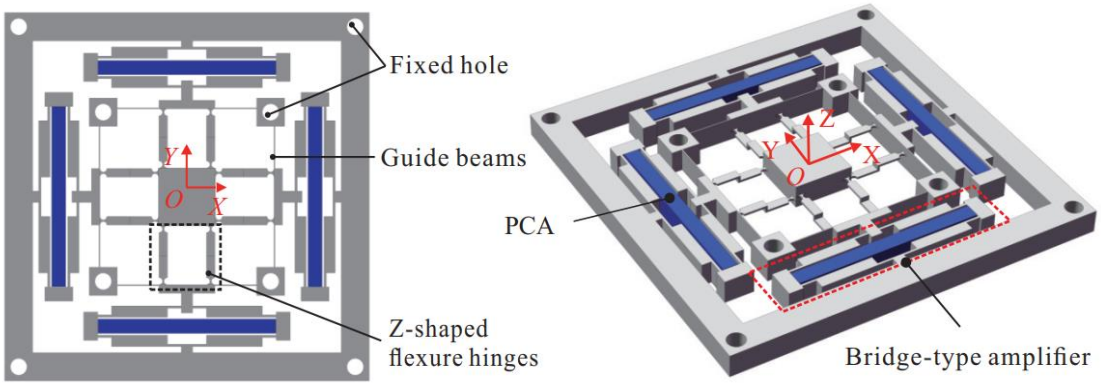

Figure 2.14. A 3-DOF XYZ bi-directional movement stage according to Z-shaped flexure hinges [54].

Moreover, Xu developed a rotary stage according to multi-segment compound radial flexures, as illustrated in Fig. 2.15. The simulation and experimental consequences illustrate that the stage can achieve rotation positioning with a resolution better than 20 μrad over a variety of 10.953°.

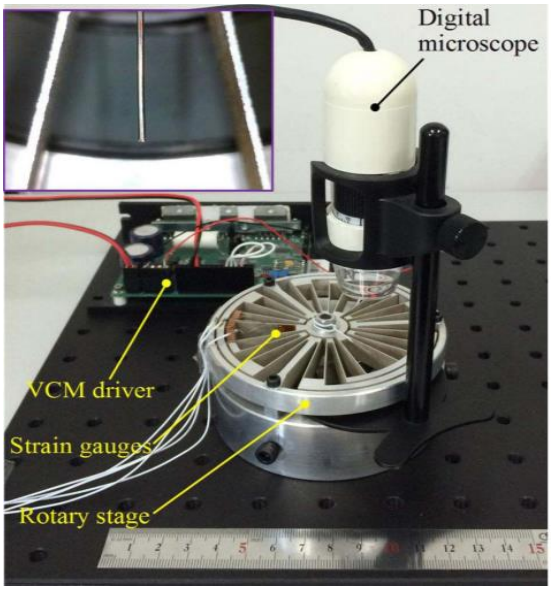

Figure 2. 15. A model with a large-range compliant rotation positioning platform [55].

More specifically, Xu [56] proposed a novel compliant multi-stroke micro-positioning XY stage or a precise positioning system. S. Polit and J. Dong [57] developed the monolithic XY stage integrated flexure leaf and right circular hinges with a stroke of 15 μm. Dao and Huang [58] proposed a new compact compliant XY stage using two-lever amplifier integrated leaf hinges with a displacement amplification ratio of 2. Sharing similar characteristics with other purposes, the indentation device also demands a high stroke and a great safety factor for performing different positioning duties.

In the past few years, many studies have been conducted on a large working stroke. Specifically, several researchers focused on the exploitation of various amplification mechanisms. Ling et al. [59] proposed improved mathematical models of the displacement amplification ratio for rhombus-kind and bridge-kind magnification structure to enhance the forecast precision. Yong et al. [60] developed the compliant XY stage integrated single-lever amplifier for fast nanoscale positioning. Kim et al. [61] employed a double displacement amplification structure integrated cartwheel hinges for a compliant 3-DOF positioner. Zhu et al. [53] developed a displacement amplifier for the 2-DOF nano-positioning stage that combines a Scott-Russell structure and a half-bridge structure.

Unlike previous studies, which were inspired by beetle motion's high flexibility, the proposed platform in this thesis is designed to achieve a minor decoupling error. Following that, an innovative multiple lever deformation intensification mechanism was combined within the positioner to produce a long working stroke. Conversely, it is problematic to attain a large displacement while also ensuring good safety factor through a design procedure. In addition, two output characteristics are in conflict with each other. As a result, balancing them requires a multi-criteria optimization trouble.

In the literature review, the aforementioned studies have conducted passive designs and active controllers to track exactly the trajectory, displacement, and positions of platforms. However, the mentioned-above positioning systems have still obstacles that are difficult to be applied for the nanoindentation tester. The obstacles can be listed such as small output displacement, high parasitic motion error, low natural frequency, and complex structure.

Therefore, this thesis proposes a few new positioning platforms for use in nanoindentation tests. Based on the merits and demerits of three main kinds of positioning structures, in this thesis, the serial-parallel design diagram was the main structure for developing compliant passive positioners to achieve large working stroke, high stiffness, and small parasitic motion.

2.3. Displacement amplification mechanisms

An amplifier is a middle member enhancing the input signal's magnitude. In the compliant mechanism field, amplifiers are widely utilized to amplify the amplitude of input signals such as force, displacement, velocity, acceleration, and torque as well as rotational systems. In recent years, compliant mechanisms have been also utilized to design displacement amplifiers using for micro-actuator applications, MEMS, especially in the positioning stages in order to amplify input displacement.

There are many ways to design a displacement amplifier. Meanwhile, most are based on traditional structures, as illustrated in Fig. 2.16 such as lever mechanism [62–64], Scott-Russell [65–68], the four-bar mechanism [69,70], the double-rocker mechanism and the parallelogram mechanism [71], bridge type mechanism [72,73], rhombus-type mechanism [74] and distributed compliance-type [75].

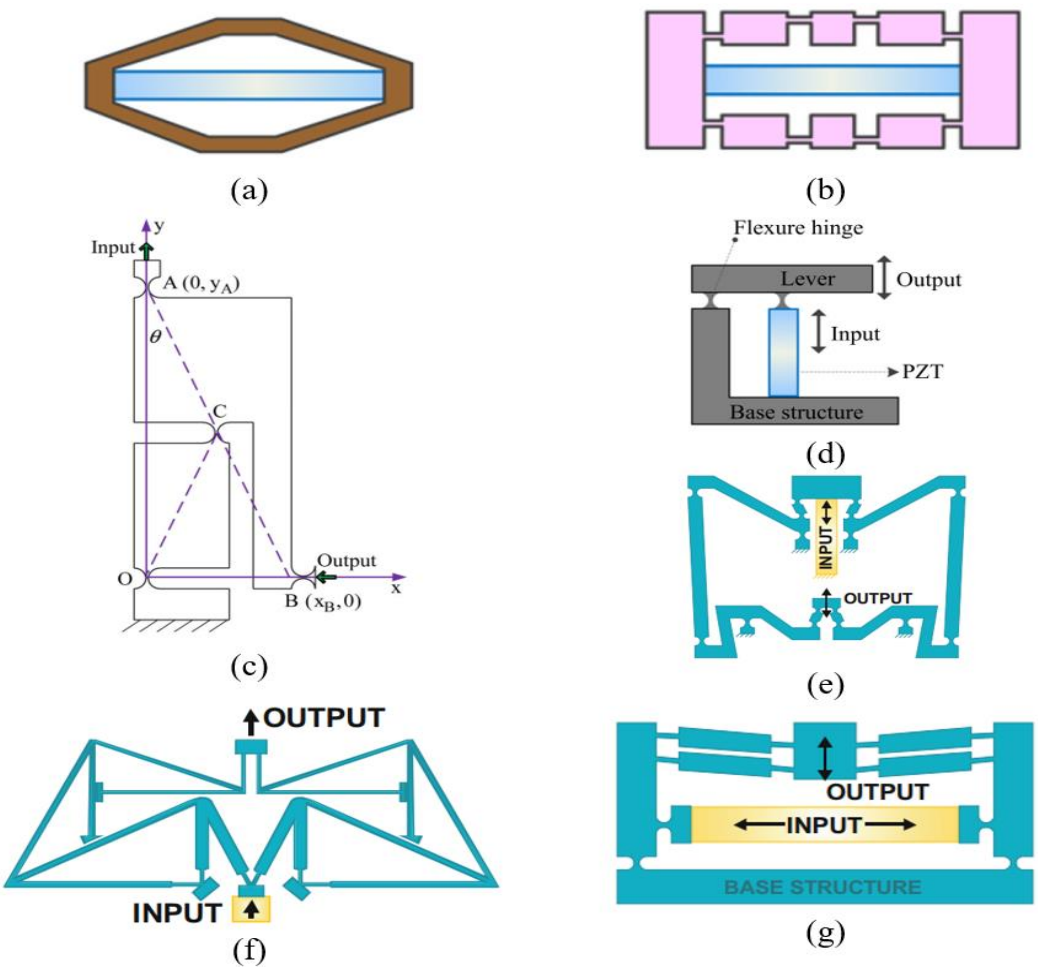

Figure 2.16. Several kinds of compliant displacement amplifiers [74], (a) Rhombus-type [74], (b) Bridge-type [74], (c) Scott-Russell [67], (d) Lever-type [74], (e) Tensural-type [76,77], (f) 20:1 stroke [76,78], (g) Symmetric five bar mechanism [76,79].

The design flow chart for major processes and components of compliant micro-/nano-positioning stages was proposed [35], as illustrated in Fig. 2.17.

Although displacement amplifiers have been well developed, they still have demerits such as small displacement amplification ratio, high parasitic motion error, and small stiffness. Therefore, several new hybrid amplifiers are developed to improve displacement amplification ratio and reduce parasitic motion error. Specifically, in this research, multi-lever amplification mechanisms are proposed and integrated into 1-DOF positioning stages, 2-DOF positioning stage, and rotary stage in order to achieve large working stroke. In addition, other hybrid displacement amplifiers are considered to integrate into proposed stages.

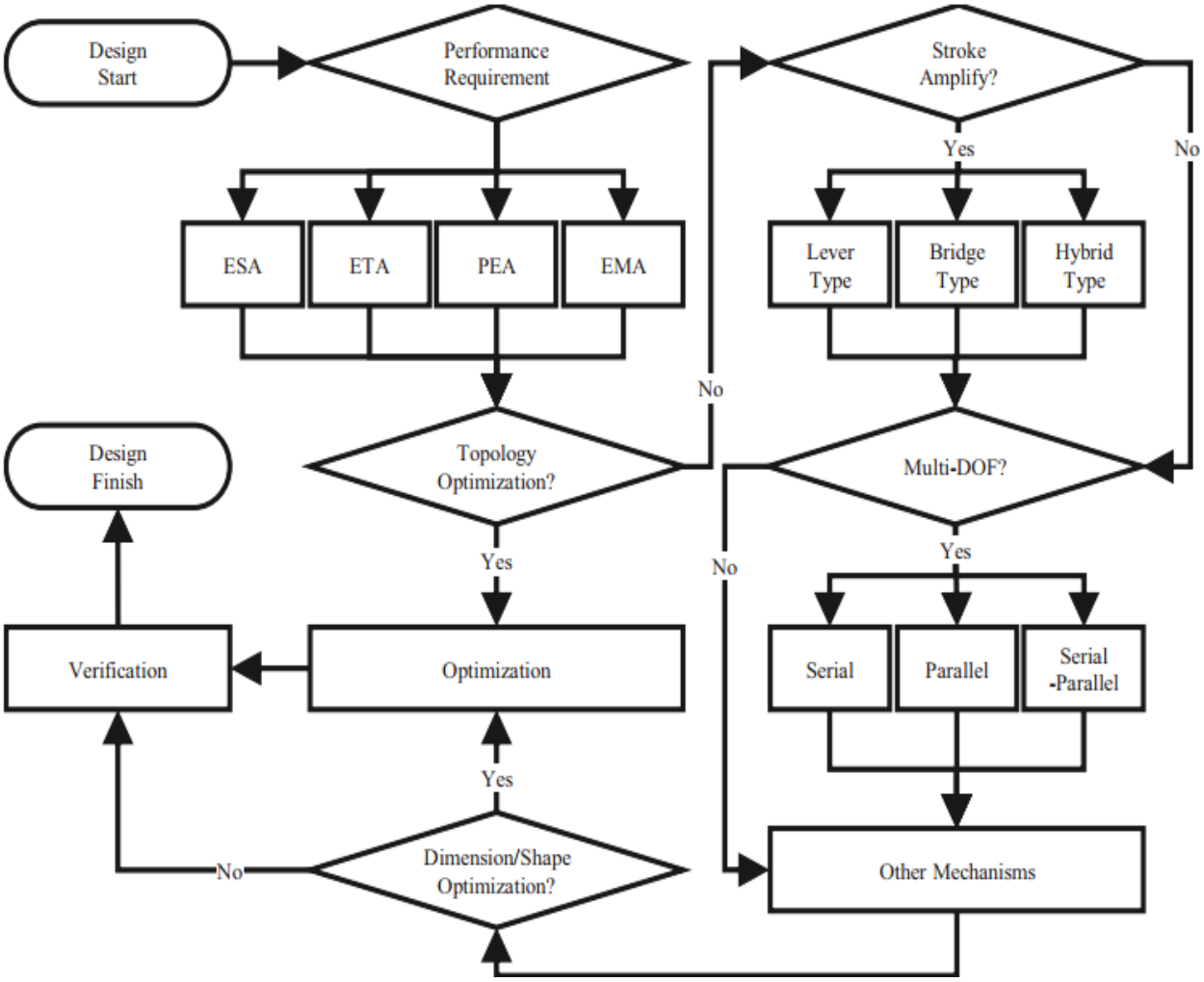

Figure 2.17. Design flow chart for compliant positioning platforms [35].

2.4. Nanoindentation analysis

In the nanoindentation analysis [80], the indenter is placed on the surface of the specimen, as illustrated in Fig. 2.20, generating both elastic and plastic deformation of the material. The feature which differentiates the nanoindentation tests from macro-indentation or micro-indentation analysis is that the displacement h and the load L in the nanoindentation machines is checked continuously with high level of accuracy. Details are presented in Fig. 2.18. In the nanoindentation procedure, the indenter moves into the specimen until a predefined maximum load L_{max} is attained with the corresponding penetration depth is h_{max}. Then, when the indenter is removed from the specimen, the process of monitoring the unloading displacement takes place until the achievement of the zero load happens and the measurement of ultimate or residual penetration depth h_f finishes. The slope of the unloading curve's upper portion ($S= dL/dh$) is defined as the elastic contact stiffness.

Berkovich and cube corner are the two main types of shapes in nanoindentation. The Berkovich indenter has a three-sided pyramid with a face angle of 65.3 to the indentation vertical direction and the same area-to-depth function as a Vickers indenter. The cube corner denotes a three-sided pyramid or, more accurately, the corner of a cube.

In nanoindentation, the formula $H = L/A_{pml}$ is applied to calculate the material's hardness, where A_{pml} is the projected area of contact at the maximal load. While the maximum load varies in a range [few μN, 200 mN] as well as in a range [few nm, roughly few μm] for penetrations. Therefore, as the indented area outcomes are extremely minor (nanometer or few micrometers size), it is almost impossible to use optical microscopy like in macro- and micro-indentation tests. The only method for detecting such a tiny area is to employ a SEM although it is not really practical. Conversely, solutions to solve the issue of computing the space straight from the load – unload curve have been suggested.

Oliver and Pharr introduced a method in 1990s that precisely computed H as well as E from indentation load-deformation data with no prerequisite for a microscope for measuring the deformed area. The first step in this technique is to fit the unloading part of the load-displacement data to the elastic contact theory's power-law relation:

$$L = \beta(h - h_f)^m \tag{2.1}$$

where b and m represent for empirically defined fitting factors and h_f for the final deformation after entire unloading, also defined from the curve fit, as indicated in Fig. 2.19. The analysis continues with the second step of determining the contact stiffness through the process of differentiation of the unloading curve fit, and evaluation of consequence at the point of penetration's maximum depth, $h = h_{max}$. This gives

$$S = \left(\frac{dL}{dh}\right)_{h=h_{\max}} = \beta m(h_{\max} - h_f)^{m-1} \tag{2.2}$$

The final step in Oliver and Parr's method is to specify the interaction depth h_c for an elastic interaction which should be lower than the whole depth of penetration. Supposing that pileup is insignificant, an elastic model indicates that the sum of sink-in h_s, as illustrated in Fig. 2.18a, is provided by

$$h_s = \varepsilon L_{\max} / S \tag{2.3}$$

where ε denotes a constant depending on the indenter's geometry. In reference to empirical inspection with Berkovich as well as cube-corner indenters, the worth ε= 0.75 has converted the worth exploited to analyze.

The contact depth is approximated as follows

$$h_c = h_{\max} - h_s = h_{\max} - \varepsilon L_{\max} / S \tag{2.4}$$

It was noted that the correction for h_c does not apply when there is material pileup around an indent. As a result, using a SEM or an atomic force microscope (AFM) to inspect the residual impression is beneficial.

The more details about indentation hardness measurements at Macro/Micro/Nano-scale can be read in Ref. [80].

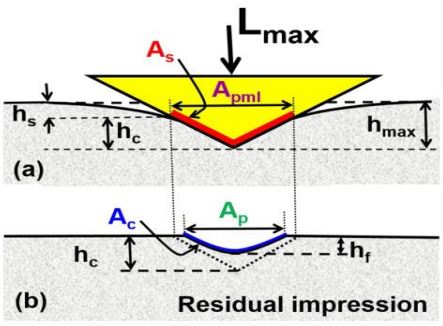

Figure 2.18. (a): Elasto-plastic deformation at the maximal utilized load [80] L_{max}; (b): plastic deformation after discharging the load.

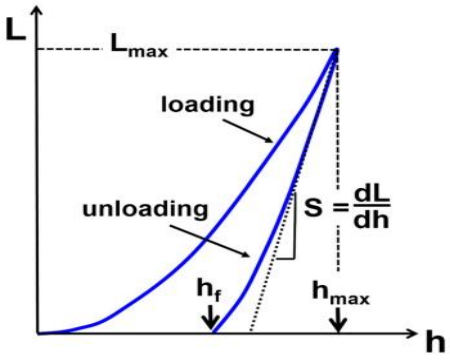

Figure 2.19. Load–unload during nanoindentation [80].

In previous studies, based on the compact merits of compliant mechanism, the researchers developed the 01-DOF stages for driving the indenter with small output displacement [9,11,15]. Unlike previous studies, in the thesis, the author will develop the nanoindentation testing device with 01-DOF stages with different output displacements to adapt various specimens and 02-DOF stages as well as rotary stage for locating the specimens integrated into the nanoindentation testing device, as illustrated in Fig. 1.5.

2.5. Modeling methods of compliant mechanisms

Many analytical approaches for kinetostatic and dynamic modeling of flexure-based structures [81] have been developed in recent years, including the PRBM [82,83], compliance matrix method [84], elastic beam theory [85], two-port dynamic stiffness model [86], Ryu's method [87], and beam constraint model [88]. The analytical approaches mentioned above have made consequential progress in building mechanical designs of

flexure-based structures. More information can be found in reference [81]. In addition, there is a development and application of approximate methods for analyzing the behaviors of compliant mechanisms, which will be presented in later.

2.5.1. Pseudo-rigid-body model method

The PRBM method is useful for obtaining and assessing the main characteristics of a compliant structure. The PRBM primarily applied to three kinds of compliant members: fixed-free beams, short compliant pivots, and fixed-guided beams [89,90]. The pseudo-rigid-body model of a fixed-free flexure beam is shown in Fig. 2.20. A torsional spring as well as two rigid-link bars decouple the beam into a joint. The kinematic trajectory of rigid-link structures approximates its deflection path, while the force-deflection association is estimated by the spring that denotes the stiffness of the pivot. The main problem is determining the location of the feature pivot and the spring stiffness. The specified process is to use for optimization strategies to estimate the tip trajectory (a, b) and slope θ of the pseudo-rigid-body model subjected to external loads (F, M) with respect to the precise continuum model [16]. More information on the PRBM method can be found in ref. [16].

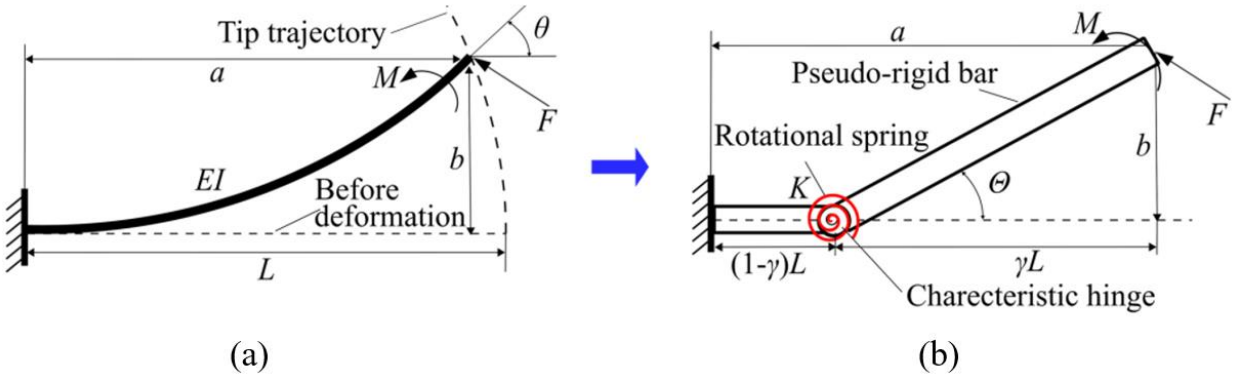

Figure 2.20. Mechanical representation of compliant beams with large deflections [81]: (a) Large-deflection beam continuum model and (b) matching pseudo-rigid-body.

The main advantage of the PRBM method is to rapidly achieve the primary suitable design with the initial design variables and output responses. Therefore, in this thesis, the PRBM method is proposed for forming an analytical calculation model of a compliant 1-DOF and 2-DOF stages.

2.5.2. Lagrange-based Methods

As shown in Fig. 2.27, flexure-based structures are extended to apply for excessive speed [91] and excessive frequency [92]. Finally, for compliant mechanisms, Lagrange-based

dynamic modeling approaches [93,94] have been used. Specifically, the methods can be generally classified into three major types, as indicated in Fig. 2.21. For the dynamic analysis of flexure-based structures, some advanced modeling methods for modeling of compliant mechanisms [95,96] are currently proposed. More information on Lagrange's method can be found in ref. [81].

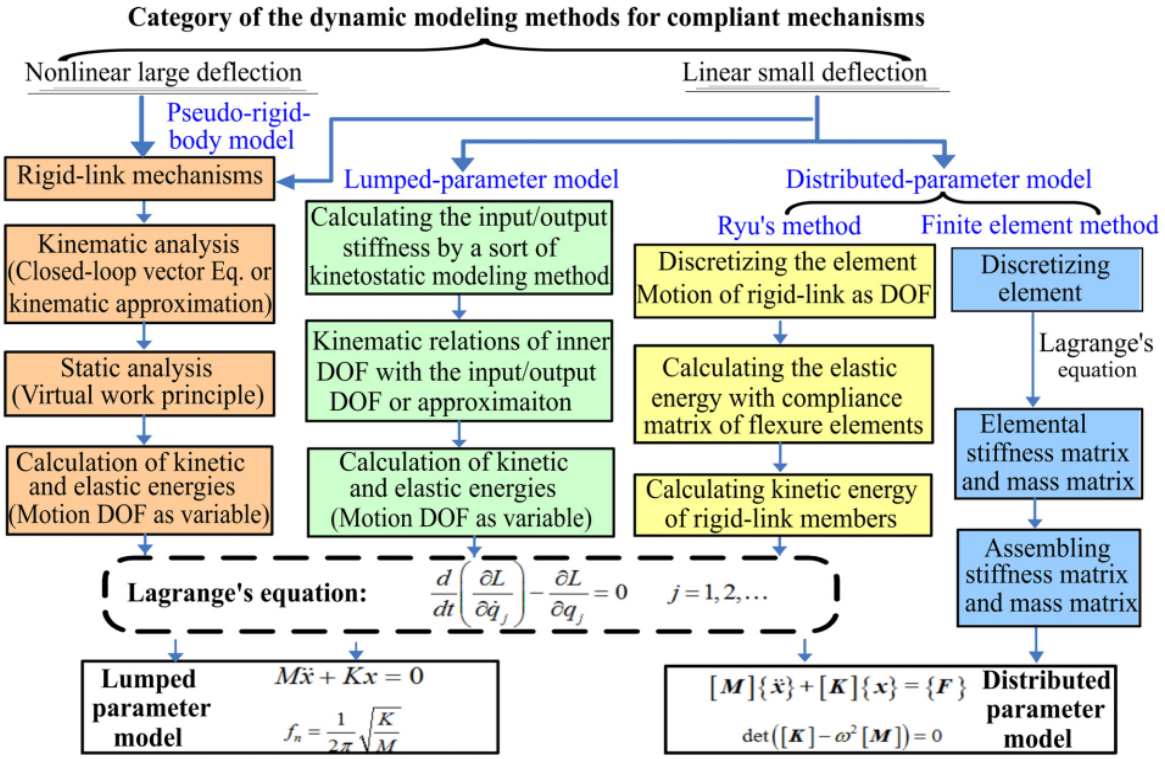

Figure. 2.21. Flexure-based structure modeling according to Lagrange's technique [81].

Based on the benefits of Lagrange's method, Pseudo-rigid-body model method integrated with Lagrange's method for forming analytical model of a compliant 01-DOF stage and 02-DOF stage will be applied in this thesis.

2.5.3. Approximation-based modeling method

2.5.3.1. Response surface methodology-based approximation modeling method

Response surface methodology (RSM) is a set of statistical and mathematical techniques exploited to advance and optimize design processes. It is also useful in the process of designing, developing and formulating new products, as well as enhancing or improving the existing product designs. In this research, the simulated experimentations are collected by RSM and FEM. In addition, these simulated data are also automatically generated by combining RSM and FEM. Initially, a 3D model is created in the FEM. Later on, a number

of simulation experiments are launched with the use of the RSM [97,98]. The estimated consequences for the output characteristics are regained using finite element analysis (FEA). In general, central composite design (CCD) is a common method to generate the number of experiments. Particularly, a number of experiments are specified by following formula.

$$N = 2^{(k-f)} + 2k + n_c, \tag{2.5}$$

where N denoted the sum of the design points, k denoted the number of input parameters, f denoted the factorial number, and $n_c = 1$ denoted the number of duplicates at the center point of the construction area.

In addition, the number of experiments can be determined by other methods such as full factorial design of experiment, Taguchi method or Box–Behnken design (BBD). In particular, CCD, TM, or BBD is preferred because it provides the sufficiently necessary number of experiments.

Based on simulated experimentations, datasets are collected. Later on, response surface methodology (RSM) is a mathematical model is formulated as follows [100].

$$y = \beta_0 + \sum_{v=1}^{N} \beta_v x_v + \sum_{v=1}^{N} \beta_{vv} x_v^2 + \varepsilon \tag{2.6}$$

where y denotes the predicted output parameter, x denotes the design variable, N is the number of design variables, β_v (v = 0, 1, 2,…, N) are regression coefficients, β_{vv} denotes quadratic coefficients; and ε denotes the model error.

In this thesis, the RMS is applied to approximate simple behaviors. In addition, more complex behaviors are presented in following method, namely, adaptive neuro-fuzzy inference system.

2.5.3.2. Adaptive neuro-fuzzy inference system-based approximation modeling method

Artificial neural networks are human neuron-based modeling methods, whereas fuzzy logic is an inaccurate reasoning method that allows for linguistic modeling of the human reasoning procedure. The adaptive neuro-fuzzy inference system (ANFIS) is the result of combining an artificial neural network and fuzzy logic to reap the benefits of both methods [99,100]. One of the executions of a first order Sugeno fuzzy inference system is the ANFIS model. The following rules have been established:

$$\text{if } x_1 \text{ is } A_1 \text{ and } x_2 \text{ is } A_2, \text{ then } y = p \times x_1 + q \times x_2 + r \tag{2.7}$$

in which x_1 and x_2 denote inputs for A_1 and A_2 term set, y is the output, p, q, r are constants. The ANFIS's structure comprises five-layer feed-forward neural network. These layers' specifics are supplied.

(1) Input fuzzification is carried out by Layer 1, also referred to as the layer of fuzzy membership, to ascertain the membership levels of each input in accordance with the provided fuzzy membership function. For this layer's outputs, use the following formula:

$$M_1^i = \mu A_i(x) \tag{2.8}$$

where x denotes input to node i, as well as A_i denotes a linguistic tag correlated with this node function. M_1^i is A_i's membership function.

(2) Layer 2 is the regulation, which is a rule node that collects input from the corresponding fuzzification nodes and determines the regulation's firing strength. In layer 2, every node is a circular node symbolized Π and each node output demonstrates a regulation's firing strength which is defined as:

$$w_i = \mu A_i(x) \times \mu A_i(y) \ldots i = 1, 2, 3, \ldots, N \tag{2.9}$$

(3) In Layer 3, which is known as the standardized layer, the proportion of the firing strength of a particular regulation to the sum of the firing strengths of all regulations is computed. In layer 3, each node is a circular node named N. The *ith* node specifies the proportion of the *ith* regulations firing strength to the totality of all regulation's firing strengths, in which $\overline{w}$ denotes the standardized firing strength of regulations.

$$\overline{w} = \frac{w_i}{w_1 + w_2 + w_3, \ldots, + w_n}, \; i = 1, \; 2, 3, \; \ldots, N \tag{2.10}$$

(4) Layer 4, known as the defuzzification layer, receives primary inputs and gives the consequential factors of the principle. In layer 4, each node i denotes a square node as:

$$M_1^i = \overline{w}_i f_i(px + qy, \ldots, r), \; i = 1, \; 2, 3, \; \ldots, N \tag{2.11}$$

where $\overline{w}_i$ denotes the output of layer 3 and p, q, r denote factor sets.

(5) Layer 5 is a single node that calculates the whole output as the total of all incoming signals below:

$$M_5^i = \sum_i \bar{w}_i f_i \frac{\sum_i w_i f_i}{w_i} \tag{2.12}$$

A least squares algorithm is typically integrated with a gradient descent algorithm in ANFIS training. In every epoch of the algorithm's combination progression, there are two types of passes: forward passes and backward passes. In terms of the forward pass, the ANFIS is almost always given a training set of inputs, and neuron outputs are identified on a layer-by-layer basis. The least squares algorithm was used to compute the resulting parameters. The ANFIS [101] frequently employs common membership functions such as Gaussian, sigmoidal, triangular, trapezoidal, and bell kinds. ANFIS employs five network layers to execute the following fuzzy inference steps, as demonstrated in Fig. 2.22: (1) input fuzzification, (2) fuzzy set database construction, (3) fuzzy regulation base structure, (4) decision making, and (5) output defuzzification.

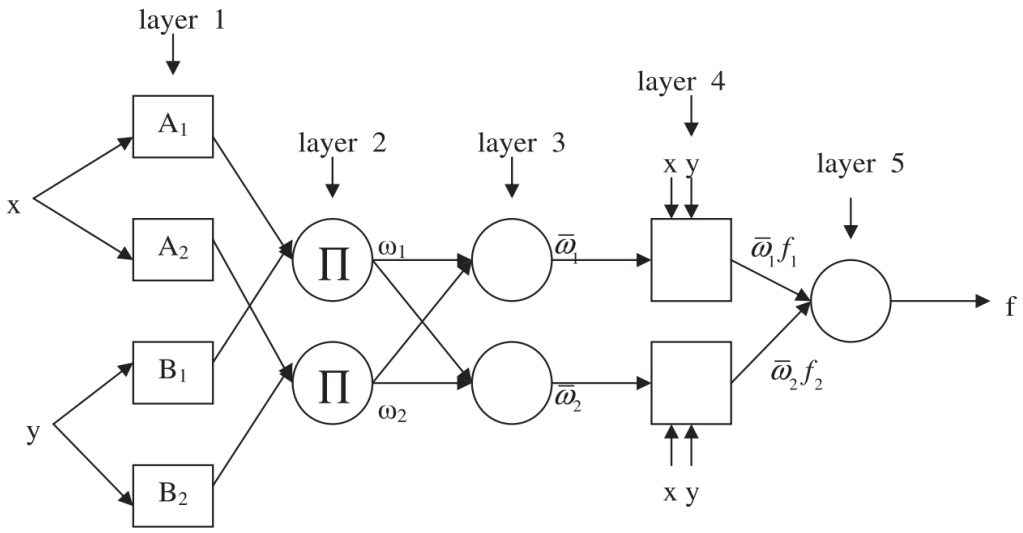

Figure 2.22. Structure of ANFIS [102].

Basically, compliant mechanisms do not have specific kinematic joints, and this results in a coupling of kinematic and mechanical behaviors. Therefore, simple structure can be analyzed via using the mentioned-above analytical methods. On the contrary, for a more complex structure, e.g., series-parallel structure mechanisms, the analytical methods can lead a wrong prediction of complicated behaviors. As a result, in this thesis, the ANFIS is utilized to approximate more complex behaviors. i.e., the behaviors have a high nonlinearity, which are difficult to build the analytical equations.

2.6. Statistical analysis

2.6.1. Analysis of variance

The sensitivity of design parameters can be analyzed by using analysis of variance (ANOVA) to present important contributions of each design factor on the quality deformation and the safety factor of the positioner. Based on these results, the design space of each design parameter can be refined. This process helps for optimal process which is faster in convergent speed and time. Sensitivity is the influence of a parameter (the independent variable) on another parameter (the dependent variable), both of which may be either continuous or discrete. Other possible methods to calculate the sensitivity are Modal method, differential method, RSM and ANOVA, matrix perturbation method and Nelson method. ANOVA [103] is a statistical analysis tool that divides monitored aggregate variability in a data set into two categories: systematic parameters and random parameters. Random factors have no statistical influence on the given data set, whereas systematic parameters do. In a regression study, the ANOVA test is used for determining the effects of design variables on output responses.

The formula in F-test in ANOVA is calculated as follow:

$$F=\frac{MST}{MSE} \tag{2.13}$$

where F(F-test) symbolizes the ANOVA coefficient, MST symbolizes the mean sum of squares according to treatment, and MSE symbolizes the average sum of squares according to error.

2.6.2. Wilcoxon and Friedman

The Friedman test is a non-parametric statistical check proposed by Milton Friedman [104]. Similar to the parametric repeated measures ANOVA, it is employed to find dissimilarities in treatments across multi-check efforts. More details can be read in Refs. [104]. The Wilcoxon signed-rank test [105] is a non-parametric statistical hypothesis check utilized either to check the position of a set of specimens or to compare the positions of two populations utilizing a set of matched specimens. When employed to check the position of a set of specimens, it assists the similar aim as the one-specimen Student's t-check. The more details can be read in Ref. [105].

2.7. Optimization methodologies

Structural factor design plays essential role in establishing a compliant positioning platforms, because it dominates the key performances of the stage such as strength, stiffness, decoupling characteristic or deflection shape. An optimization structure can ensure the strength as well as reliability of the structure and enhance the working effectiveness of the compliant stages such as workspace and material usage.

Objective functions must be efficiently established in order to achieve a reliable optimization design. FEA and mathematical modeling are two key approaches used in mechanical design to evaluate performance prior to prototype fabrication.

There are three key kinds of optimal methods for mechanical design optimization such as dimension optimization, shape optimization, and topology optimization. In general, in the mechanical structure designing field, topology optimization is performed at the starting phase while the dimension and shape optimization are usually implemented the next phase. In this section, various optimal methodologies are presented.

In particular, when it comes to dimension and shape optimization, the dimension of the structures has a meaningful effect on the responses of the stages. An optimal process should be used to reinforce quality responses for selecting the best worth of the dimensions so as to advance the proficiency of a structure. After identifying optimization problems such as optimal objectives, design variables, and constraints, optimal approaches to carry out the optimal procedure should be proposed. Non-heuristic and heuristic algorithms are the two types of optimal approaches.

2.7.1. Non-Heuristic Algorithms

Non-heuristic algorithms comprise mathematical algorithms (gradient descent, Newton's method) and statistical methods (response surface method, grey relational analysis). Therefore, the algorithms have been employed to solve the design optimal issue. For example, Dao et al. [106] proposed hybrid approach of the RSM, entropy measurement technique, TM as well as grey relational analysis for optimizing two quality responses of 02-DOF platform. Lai et al. [45] applied the "fmincon" function supplied via MATLAB so as to optimize the output response of a 02-DOF platform. Jiang et al. [107] identified the input coupling degree (ICD) to assess the decoupling characteristic of the stage first, and next exploited the "fmincon" function to optimize the ICD. Kim et al. [108], as well as Lee et al. [109] utilized the sequential quadratic programming technique to optimize the

quality responses.

2.7.2. Heuristic Algorithm

To achieve better the optimization results within a reasonable time limit and appropriate resource cost, heuristic algorithms are a suitable selection. Li et al. [110] exploited particle swarm optimization (PSO) to improve the quality of positioning platforms. Lin et al. [111] and Liu et al. [112] used a Genetic Algorithm to maximize the natural frequency of the positioning platforms. Furthermore, Tian et al. [113] optimized the natural frequency exploiting both PSO and GA, and the same consequences were obtained with the same values. Therefore, two algorithms are reliable for solving optimization problems in engineering. In optimal problems, the Taguchi method and response surface methodology are known as one of the easiest algorithms to use and are good algorithms. However, TM and RSM have limitations that are only optimal for a single objective, so the optimal results may not be as real. Meanwhile, in population search algorithms such as GA [114], Differential Evolution (DE) [115], and PSO [116]. Optimal analysis results are more accurate. However, the search process is quite time-consuming and this reduces the efficiency of work and increases costs.

From the above-mentioned statement, to increase the efficiency of work, shorten the analysis time, reduce costs, etc. In addition, the new optimization algorithms will include the merits of the algorithm that makes it. This new algorithm is called hybridization. So, hybridization optimization algorithms have received a lot of attention from scientists. Therefore, in this thesis, several new optimization algorithms based on combinations of available optimization algorithms need to be proposed and developed for optimizing the quality responses of the proposed stages. In particular, in this thesis, new hybrid approaches of TM, RSM, fuzzy logic, weight factor technique according to signal to noise, ANFIS, and new algorithms such as Teaching Learning-Based Optimization Algorithm [117], Moth Flame Optimization [118], and Whale Optimization Algorithm [119], the Firefly Algorithm (FA) [120], and Neural Network Algorithm (NNA) [121] were proposed for optimizing the main parameters to improve the response quality of the proposed stages.

2.8. Conclusions

In this chapter, the aforementioned scientific theoretical basis illustrates the foundation for the development of the thesis contents in subsequent chapters. This thesis concentrated on

the creation of new structures for compliant positioning stages for nanoindentation testing device and hybrid optimization approaches for enhancing the quality characteristics of proposed compliant stages.

Based on the analysis of basic theories, the analytical methods is critically accurate for modeling the small and midlle deformation while the soft computing methods (Artifical neural network, fuzzy logic, ANFIS) are capable of modeling the complex nonlinear behaviors. In oder to overcome such these limitations, this thesis will combine of statistical methods (TM, RSM) with fuzzy logic, and metaheuristic optimization algorithm to solve the multi-response problem for the flexure hinge. Besides, the PRBM and Lagrange principle to establish the statics, kionestatics, and dynamics for positioners. Additionally, statistic techqniues will be coupled with ANFIS and metaheuristic optimizers to handle the optimization design for positioners.

CHAPTER 3 ANALYSIS, EVALUATION, AND SELECTION OF A FLEXURE HINGE FOR COMPLIANT POSITIONING STAGES

This chapter examines and analyzes four common flexure hinges. This chapter, in particular, proposes an innovative proficient integrated optimal approach for optimizing the design parameters of an elliptical flexure hinge that incorporates the TM, the RSM, fuzzy logic, and the MFO. According to the outcomes of the analysis and optimization, the elliptical hinge and other flexure hinges, such as the leaf hinge and circular hinge, are integrated into flexure-based positioning stages in the proposed nanoindentation testing device, as shown in Fig. 1.5, for locating and indenting material samples in the nanoindentation testing device as well as in the precise positioning system.

3.1. Background and motivation

The most important components of compliant mechanisms are flexure hinges. Instead of using a conventional rotation joint, a flexure hinge uses a mechanical component to flex in order to give relative rotation between stiff components [122]. Normally, the quality of a compliant stage is determined by the flexure hinge's characteristics. Currently, there have been many flexure hinges applied for precise positioning system such as circular flexure hinges with small rotation axis shift [26], corner-filleted flexure hinges with large angular deflection [27], V shape flexure hinges [28], parabolic flexure hinges and hyperbolic flexure hinges [30]. Each flexure hinge has certain merits such as high accuracy, large stroke and small rotation axis shift, but it is difficult to have all the merits simultaneously. To address this issue, an effective optimization approach for the analysis, evaluation, and selection of a suitable flexure hinge to achieve multi-characteristics such as a minor rotary direction shift, a great safety factor, as well as a high angular deflection was applied in a nanoindentation testing device for indenting and locating specimens was developed in this study. As shown in Fig. 1.5, the proposed flexure hinge with multi-characteristics is combined into an XY-stage for positioning thin material specimens as well as bio-specimens, and a Z-stage for guiding the indenter in a nanoindetation testing device.

It is known that the flexure hinge's three mentioned qualities are resisted together. Nowadays, simulataneously solving three objectives is critically difficult task. Therefore,

this study introduces a new method of integration optimization to suggest solutions for this problem so as to instantaneously stabilize the output responses. The method was developed via an efficacious consolidation of the TM, fuzzy logic, the RSM, and the MFO algorithm with the purpose of solving a three-objective optimization problem of the flexure hinge, including accuracy, computing speed, and cost reduction. The purpose of fuzzy logic is combine three objectives into a single objective. From that, it is more easy to handle a single objective optimization problem.

The primary goals of this chapter are to present the evaluation and selection of an appropriate compliant joint so as to apply in a nanoindentation tester. In this research, a combined optimal approach based on the TM, fuzzy logic, the RSM, and the MFO algorithm was proposed for simultaneous optimization of the three flexure hinge performances regarding safety factor, rotation axis shift and angular deflection. The Taguchi and detasFlex software were used to collect numerical experimental datasets. To remove unit variances, three objective functions were converted into signal to noises. Following that, the fuzzy modeling was used for interpolating 3 target formulas to a single combined target formula. The RSM was used to formulate the fuzzy modeling's integrated regression equation. Finally, the MFO algorithm was exploited to optimize the main geometric factors of the flexure hinge. The sensitivity of input variables was assessed using ANOVA to determine their effects as well as the validation of the optimal consequences was also conducted.

3.2. Technical requirements of flexure hinges for nanoindentation tester

In order to achieve large working travel, small parasitic motion error with compact structure, the compliant positioners will be used suitable flexure hinges integrated into compact amplifiers. As a result, the three main technical characteristics of a suitable flexure hinge integrated into flexure-based positioning stages are minor rotary direction shift, great safety factor, as well as high angular deflection.

- A rotation axis shift of less than 0.00012 was desired.
- A safety factor greater than 2 was desired.
- An angular deflection greater than 0.052 was desired.

3.3. Proposed optimization methodology

As shown in Fig. 3.1, a flowchart depicts a new proficient optimal approach that integrates the TM, the RSM, the fuzzy logic, the MFO. Dang et al. offered this proposed hybrid approach [123]. The parameters of the flexure hinge show a high level of sensitivity to the three mentioned features in the field of flexure-based mechanisms. A novel approach is introduced for the optimization of the significant geometric factors of the proposed flexure hinge to concurrently satisfy three aforementioned technical demands. The proposed approach in this study consists of four major phases below: (i) Identify the optimization issue and choose the compliant joint, (ii) Generate a fuzzy model, (iii) Form the combined regression formula using the RSM, and (iv) Run the optimal trouble using the MFO algorithm.

Phase (i): *Identification of the optimization issue and selection of a flexure hinge.*

The three flexure hinge qualities mentioned above are identified in accordance with the requirements of a nanoindentation tester. DestasFlex software [124] evaluates four common flexure hinges. Design variables and goal functions are established. Data is collected using an integration of the TM as well as the detasFlex Software. So as to remove unit effects, three aforementioned responses are computed for obtaining signal to noises (*S/N*).

Phase (ii): *Fuzzy modeling*

This process results in the introduction of fuzzy modeling in this study to incorporate three aforementioned responses into one target function by the interpolation. The fuzzy modeling process consists of a knowledge base, fuzzing procedure, inference engine, and defuzzification procedure. Details can be demonstrated succinctly in Ref. [100].

To begin, the fuzzification process fuzzifies the *S/N* proportions using membership functions (MFs). Following that, the implication operating mechanism executes a proper response based on fuzzy principles. Defuzzification, in the end, converts a fuzzy worth into a combined objective function (Z).

Main step 1: Fuzzification procedure

Real values are converted into linguistic parameters during the fuzzification process. Furthermore, expertise-based regulations were developed, and the membership functions (MF) of the fuzzy sets are identified. The implication operating mechanism is according to

a set of pre-established rules, which allows the designer to use practical experience to reach a high level of exactness for the management system.

Main step 2: Defuzzification progression

Defuzzication converts the fuzzy inference system's (FIS) output to a true worth, a nonfuzzy worth (*Z*), which is an integration of 3 fitness formulas into one target formula. The centroid approach is used to convert in this process. The regression equation was developed according to the combined objective function to link input parameters and the combined objective function. In this chapter, the outputs of the system are calculated using the centroid technique to perform the FIS algorithm modeling, and Mamdani insinuation is used for defuzzification. The Gaussian MFs are suggested in this study for both design variables and responses for establishing fuzzy sets according to primary data. MFs have the range [0,1], and they can express the way a variable coincides with a fuzzy set. The Gaussian membership function can be identified as follows:

$$\mu_A\left(x,c,\sigma\right)=e^{-\frac{1}{2}(\frac{x-c}{\sigma})^2}, \tag{3.1}$$

where c and σ define the Gaussian MF; c represents the MF's center as well as σ denotes the MF's width.

Phase (iii): Form a combined regression equation.

The consequences of three quality responses and input parameters after the defuzzification process and the interpolation of the integrated regression equation (*Z*) were employed for the establishment of relationship between the input factors and the combined function. If this equation meets the requirement of reliability, its use in the next optimization process will be approved.

Phase (iv): Optimize design variables via MFO

The MFO algorithm was developed for solving a variety of engineering problems [118]. MFO, as shown in Tab. 3.1, randomly places moths in the solution space before calculating each moth's fitness worth (i.e., positioning place) and assigning the greatest location by flame. Afterward, notifying the locations of moths is based on a helical traveling formulation to attain superior points connected by a flame, advancing the most recent and perfect particular points, and duplicating the previous strategies (i.e., advancing the instant locations of the moths and generating latest positions) until the evaluation targets are met.

More literature on the MFO algorithm's features and applications can be found [118]. Table 3.1 also shows the primary setting factors for this algorithm.

Table 3.1 MFO algorithm initialization parameters

Factor	Overall worth
Agents	30-50
Moths	10-30
Maximum reiterations	100-10000

This MFO algorithm is divided into three sub-steps, which are as follows.

Substep 1: Creating the first Moth population

Each moth moves in 1-D, 2-D, 3-D, or super-dimensional space. A primary matrix of moths is expressed below.

$$M = \begin{bmatrix} m_{1,1} & m_{1,2} & \dots & \dots & m_{1,d} \\ m_{2,1} & m_{2,2} & \dots & \dots & m_{2,d} \\ . & . & . & . & . \\ . & . & . & . & . \\ . & . & . & . & . \\ m_{n,1} & m_{n,2} & \dots & \dots & m_{n,d} \end{bmatrix}, \tag{3.2}$$

where n as well as d denote the quantity of moths and the quantity of dimensions in a solution region. Furthermore, the fittingness numbers for full moths are warehoused in an array as follows:

$$OM = \begin{bmatrix} OM_1 \\ OM_2 \\ . \\ . \\ . \\ OM_n \end{bmatrix}. \tag{3.3}$$

Flames are considered as rest aspects in the MFO algorithm. The following array describes the flames in the D-dimension space that are being tracked by their aptness formulation vector:

$$F = \begin{bmatrix} F_{1,1} & F_{1,2} & \ldots & \ldots & F_{1,d} \\ F_{2,1} & F_{2,2} & \ldots & \ldots & F_{2,d} \\ . & . & . & . & . \\ . & . & . & . & . \\ . & . & . & . & . \\ F_{n,1} & F_{n,2} & \ldots & \ldots & F_{n,d} \end{bmatrix}. \tag{3.4}$$

$$OF = \begin{bmatrix} OF_1 \\ OF_2 \\ . \\ . \\ . \\ OF_n \end{bmatrix}. \tag{3.5}$$

It has been noted that the two resolves are produced by moths and flames. The way they are handled as well as upgraded in every repetition demonstrates a difference between them. In fact, though the flames have the best position for moths, the moths are real enquiry agents that move around the exploration zone. In particular, flames are referred as flags dropped by moths while exploring the exploration area. Consequently, each moth examines the flame and advances its solution if it obtains a superior location. This mechanism will never discard a moth's best solution.

Substep 2: Advancing positions of Moths

MFO combines three various functions to perform universal optimization of optimal issues. These formulations are referred to as:

$$MFO = (I, P, T). \tag{3.6}$$

where *I* denotes the moths' primary haphazard locations. This function is written as follows:

$$I : \varnothing \rightarrow \{M, OM\}. \tag{3.7}$$

The P function depicts moth mobility in the search space. This function obtains the matrix M and eventually returns its advanced version.

$$P : M \rightarrow M. \tag{3.8}$$

The T function denotes the accomplishment of the investigation procedure. True if the appraisal condition is met; false if the appraisal condition is not met.

$$T : M \to \{true, false\}. \tag{3.9}$$

The I function formulation is used to carry out the random distribution.

$$M(i, j) = (ub(i) - lb(j)) * rand() + lb(j), \tag{3.10}$$

where *lb* as well as *ub* represent the lower as well as upper limits of input parameters. As previously stated, the moths fly in the enquiry region in a mark route.

When a logarithmic helix is used, several situations can arise. To begin, the primary point of helix should begin with the moth. Second, the flame's position should be the helix's ending point. Finally, the fluctuation of spiral variety should not exceed the searching area. Consequently, the MFO algorithm's logarithmic helix is defined as:

$$S(M_i, F_j) = D_i \,.\, e^{bt} \,.\, \cos(2\pi t) + F_j, \tag{3.11}$$

in which D_i, *b* as well as *t* represent the i-th moth gap for the j-th flame, an unchanging worth for defining the shape of the logarithmic spiral, and an arbitrary number between -1 and 1. The D factor is calculated as following formula:

$$D_i = \left| F_j - M_i \right|, \tag{3.12}$$

where M_i , F_j as well as D_i demonstrate the i-th moth, the j-th flame as well as the gap of the i-th moth for the j-th flame, correspondingly.

The spiral route of the moth close to the flame in the inquiry space ensures the equilibration of exploitation and exploration in MFO. Furthermore, to avoid getting caught in the entrapments of domestic optimization, the optimal solutions are maintained in every repetition and the moths fly encircling the flames in order for each moth flying near the closest flame using the OF and OM matrices.

Substep 3: Apprising the quantity of flames

This section focuses on the improvement of MFO algorithm's exploitation, for example, advancing the positions of moths in various spaces in the investigation area may result in the reduction of exploitation chance of the most potential resolutions. As a result, lowering the number of flames offers a solution in reference to as follows:

$$flame\ no = round(N - l * \frac{N - l}{T}), \tag{3.13}$$

in which *N*, *l*, as well as *T* denote the maximum quantity of flames, the existing number of repetitions and the maximal quantity of repetitions, correspondingly. More specific information can be found in the previous study [118].

in which *N*, *l*, as well as *T* denote the maximum quantity of flames, the present number of repetitions, and the maximum number of repetitions, correspondingly. Detailed information is provided in Ref. [118].

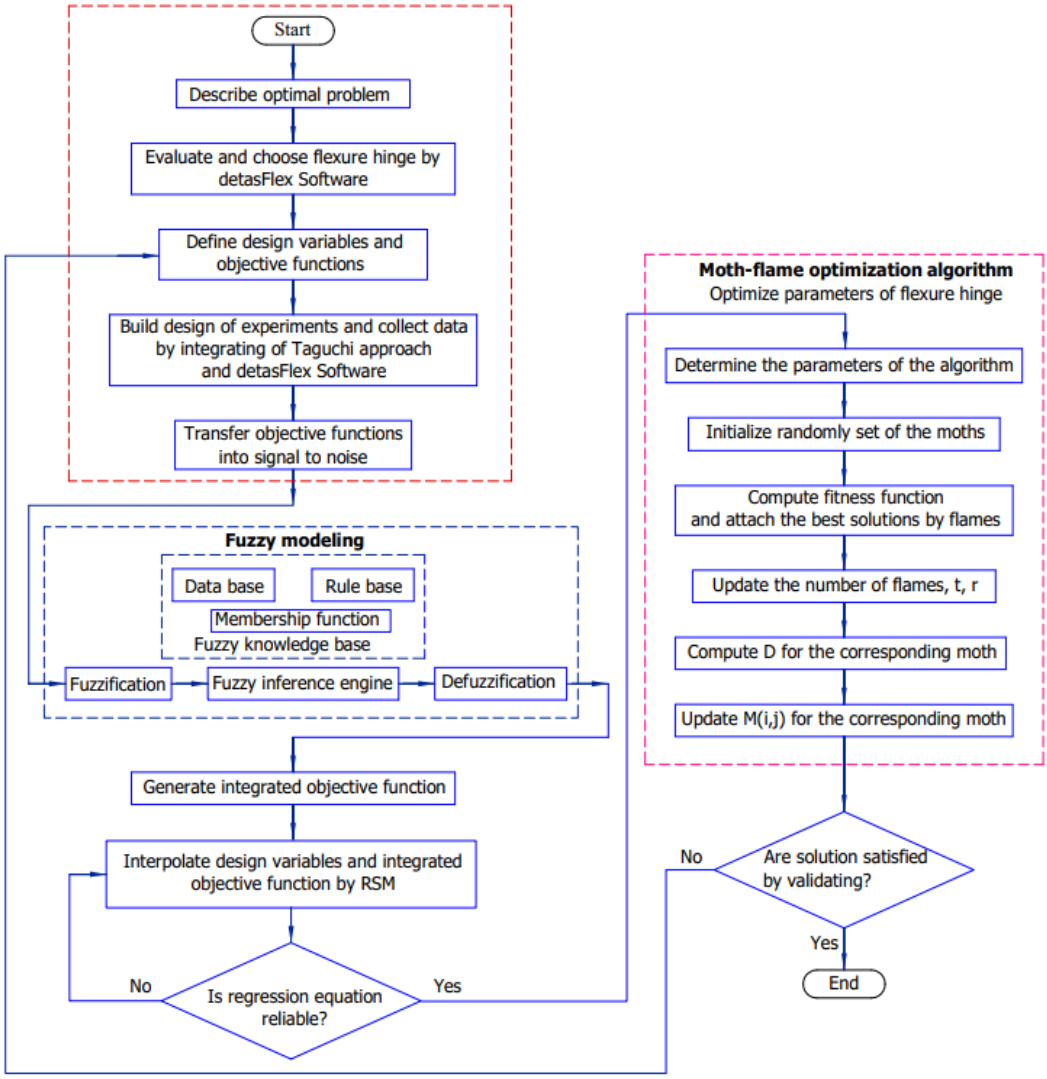

Figure 3.1. Flow diagram for developed optimization methodology.

The hybrid approach of TM, fuzzy logic, RSM, and MFO algorithm was offered in this study for optimization of the selected flexure hinge's three quality responses. Every target function is consigned a weight factor in general. Meanwhile, in this study, the fuzzy modeling phase promotes the interpolation of three target formulas into one combined target formula and the automatic assigning of the weight factor for every objective function. Furthermore, personal experience with fuzzy modeling of mechanical engineers

can be significant for use. Accordingly, this hybrid approach for solving complex optimization problems is effective, fast, and accurate.

It can be seen that the distinction between the novel method and the previously proposed one is clear. To begin with, a combined optimal approach of Taguchi method, fuzzy logic, RSM, and MFO algorithm is offered to conduct the optimization of the three flexure hinge performances concurrently. Afterward, three target formulas are converted to signal to noises to eliminate unit discrepancies. Following that, fuzzy modeling interpolates three objective functions into a single combined target formula. The RSM is used to formulate the combined regression equation of the fuzzy modeling. In this study, employment of the fuzzy modeling leads to an ignorance of the weight factor.

3.4. Results and discussion

3.4.1. Assessment and collection for flexure-based joint

The main goal of this chapter aims to find an appropriate compliant joint for incorporating into flexure-based positioning stages in the nanoindentation testing device. Three essential evaluation standards are rotary direction shift, safety factor, and maximum angular deflection when looking for a suitable flexure hinge. Figure 3.2 depicts four types of popular compliant joints which are utilized in accurate positioners and devices, such as right circular joint, corner-rounded joint, elliptic joint, and power function joint (power of 2). The primary geometric factors with similar values for proposed hinges (H=10 mm, h= 0.5 mm, L_1= 10 mm, L_2= 10 mm, w= 5 mm) were chosen with the similar dimensional specifications for comparing the main characteristics such as safety factor, angular deflection and rotation axis shift. Furthermore, each of the four suggested flexure hinges had the similar left affixed constraint and free end with the similar value of primary input deflection angle ($\varphi = 1^0$). As shown in Fig. 3.3, the rotary axis shift, v, is the gap of the initial central spot C to the targeted center point C' with an unchangeable gap of L_2 during the motion (affixed central technique). The rotational precision is defined by the axis shift. So as to achieve high positioning accuracy, the rotation axis shift of a flexure hinge should be as small as possible. A safety factor is also identified as regards the relationship of yield strength to maximum stress. Finally, the maximal angular deflection is presented as

$$\varphi_{\max} = S_F.\varphi, \tag{3.14}$$

where S_F denotes safety factor and φ denotes input deflection angle.

Furthermore, due to the limitations of a PEA, the safety factor as well as maximum angular deflection are both critical characteristics to guarantee material strength and to extend the working stroke of the positioning stage. Based on Table 3.2, the analysis outcomes of the elliptic joint are 9.7633e-05 mm with the rotation axis shift of 2.95 for the safety factor as well as 0.052 rad for a maximum angle deflection. The rotation axis shift of the elliptic joint is greater than that of the power function 1 with n of 2, and the right circular joint, but less than that of the corner rounded joint. Furthermore, the elliptic joint had the highest safety factor and maximum angle deflection. Hence, the elliptic joint was selected as the best appropriate hinge for incorporation into positioners in nanoindentation testing device.

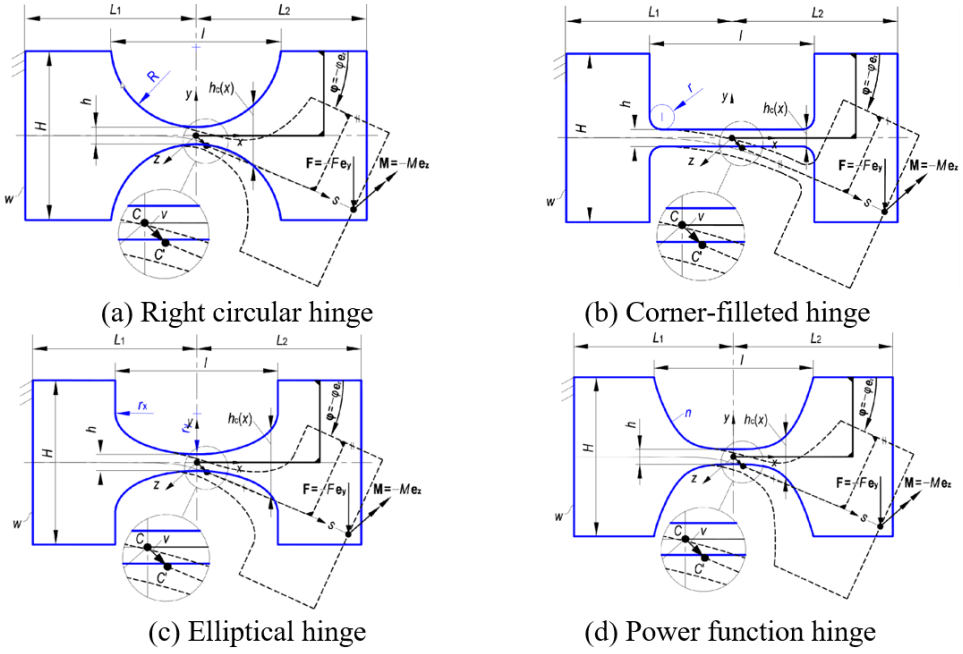

Figure 3.2. Four popular kinds of flexure-based hinges [124].

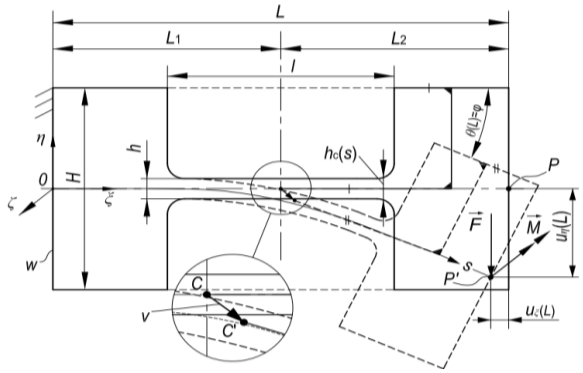

Figure 3.3. Influential factors to the theoretical categorization of a flexure-based hinge (demonstration of the primary and deflected positions) for determining the rotation axis shift [124].

Table 3.2 Specifications of four flexure hinges

Compliant joints	Geometric factors (mm)	Input deflection angle (^{o})	Rotary axis shift (v) (mm)	Safety factor (SF)	Maximum angle deflection (φ) (rad)
Right circular joint	H=10, h=0.5, L_1=10, L_2=10, l=9.987, w=5	Investigation angle (1^o)	7.211e-05	2.11	0.037
Corner rounded joint	H= 10, h= 0.5, L_1= 10, L_2= 10, l=10, w= 5	Investigation angle (1^o)	0.0002238	0.1	0.176
Elliptic joint	H=10, h= 0.5, L_1= 10, L_2=10, l=10, w= 5, r_x= 5, r_y= 2.5	Investigation angle (1^o)	9.763e-05	2.95	0.052
Power function 1 (n= 2)	H=10, h= 0.5, L_1= 10, L_2=10, l=10, w= 5	Investigation angle (1^0)	5.49e-05	1.55	0.027

Meanwhile, the rotary axis shift, the safety factor, and the maximum angle deflection are all in conflict. Hence, the hybrid optimization approach was developed in this chapter to guarantee the balance among the three quality output responses.

3.4.2. Flexure hinge design optimization

The chief geometric factors of the compliant joint have a significant impact on the output quality responses, as regards to the field of flexure-based mechanisms [125]. In this chapter, three geometric factors of the elliptic compliant joint were chosen as design variables, including the thickness of (h), x-direction radius (r_x) and y-direction radius (r_y). As a result, in order to improve the flexure hinge's output objectives, these key geometric factors must be optimized. The elliptic joint should have the following characteristics in order to be used for positioners: (i) A minor rotary axis shift to improve a linear movement accuracy; (ii) a great safety factor to ensure safety performing; and (iii) high angle deflection to improve locating space.

3.4.2.1. Design variables

The thickness (h), the x-direction radius (r_x) and y-direction radius (r_y) are the three key geometric dimensions of an elliptical hinge, as demonstrated in Fig. 3.4c. The vector of main input parameters is written as $\mathbf{X} = \left[h, r_x, r_y \right]^T$. The design variable restriction requisites were established based on specialization, machining capability, and mechanical engineering experience, as declared by:

$$\begin{cases} 0.4 \text{ mm} \le h \le 0.6 \text{ mm} \\ 4 \text{ mm} \le r_x \le 6 \text{ mm} \\ 2 \text{ mm} \le r_y \le 3 \text{ mm} \end{cases}, \tag{3.15}$$

where h, r_x, as well as r_y denote the thickness of elliptical flexure hinge, x-axis radius and y-axis radius, correspondingly. Bounds of design variables are dependent on capacity of wire electrical discharged machining (WEDM) method. A minimum thickness of 0.3 mm is required for WEDM.

3.4.2.2. Objective functions

In this chapter, the three significant responses of elliptic hinge are considered as: (i) The minor rotation axis shift, $y_1(\mathbf{X})$, is desired to guarantee the position precision. (ii) The high safety factor, $y_2(\mathbf{X})$, is required for ensuring the strength of the flexure hinge. (iii) The angular deflection, $y_3(\mathbf{X})$, is expected for being larger to broaden performing stroke proficiency. In conclusion, the optimization issue is demonstrated in the following formula:

$$\text{Seek } \mathbf{X} = \left[h, r_x, r_y \right]^T$$

$$\text{Min } y_1(\mathbf{X}), \tag{3.16}$$

$$\text{Max } y_2(\mathbf{X}), \tag{3.17}$$

$$\text{Max } y_3(\mathbf{X}). \tag{3.18}$$

Solving the problem for three objective functions to meet a range of criteria is a challenge. This study applied the method of transferring these objective functions into signal to noise for elimination of their unit differences. The results of this experiment were used as a reference in the next step of adopting the fuzzy modeling for an integration of the three objections functions into one objective function. As a result, a single-criterion

optimization problem was proposed as a replacement for the multi-criteria problem. In Taguchi analysis, a better result of signal to noise guarantees a better output objective function which indicates a positive correlation between the two aspects. Meanwhile, to reach optimized parameters, the expectation is placed on the integrated function to attain the maximum worth for attaining excessive *S/N* ratio. Accordingly, the optimal issue for combined target function, in this research, was presented as:

$$\text{Max } Z(\mathbf{X}). \tag{3.19}$$

3.4.2.3. Constraints

The elliptic hinge, which is utilized for combining into positioning stages for a nanoindentation testing device, worked under an elastic restriction of offered material, as illustrated by:

$$g(x) = \sigma \le \frac{\sigma_y}{S_F}, \tag{3.20}$$

where σ_y denotes the yield stress of the AL7075 material and S_F denotes the safety factor.

It was necessary for the rotary axis shift to be less than 0.00012.

$$y_1(\mathbf{X}) \le 0.00012, \tag{3.21}$$

The safety factor needs to be higher than 2.

$$y_2(\mathbf{X}) \ge 2, \tag{3.22}$$

It was preferred that the angle deflection be greater than 0.052 rad.

$$y_3(\mathbf{X}) \ge 0.05, \tag{3.23}$$

in which y_1, y_2, and y_3 symbolize rotation axis shift, safety factor as well as angle deflection, correspondingly.

3.4.3. Formation for calculating *S/N* ratios and experiment design

The current research adopted 3 geometric factors, namely the thickness of elliptic compliant joint (h), the x-direction radius (r_x) and the y-direction radius (r_y) as chief variables. A design of experiments (DoE) was exploited applied to figure out the connection between the input parameters and output characteristics.

The process of classifying each of 03 parameters was conducted in accordance with mechanical researchers' professional experiences, as expressed in Tab. 3.3. The L_9 (3^4) TM

was selected for the implementation of minimal experiments. The numeric experiments' outcomes are retrieved from detasFlex software, as demonstrated in Table 3.4.

Table 3.3 Design parameters and grades (unit: mm)

Symbol	Range	Grade 1	Grade 2	Grade 3
h	0.4-0.6	0.4	0.5	0.6
r_x	4-6	4	5	6
r_y	2-3	2	2.5	3

Table 3.4 Experiment outcomes and quality characteristics

Trial No.	h (mm)	r_x (mm)	r_y (mm)	y_1 (mm)	y_2	y_3 (rad)
1	0.4	4	2	7.808E-05	2.95	0.052
2	0.4	5	2.5	8.9E-05	3.319	0.058
3	0.4	6	3	9.8E-05	3.65	0.064
4	0.5	4	2.5	7.8E-05	2.36	0.041
5	0.5	5	3	9E-05	2.71	0.047
6	0.5	6	2	0.000128	3.94	0.069
7	0.6	4	3	7.9E-05	1.97	0.034
8	0.6	5	2	0.0001154	2.98	0.052
9	0.6	6	2.5	0.0001263	3.22	0.056

Then, the 03 target formulas of elliptic joint were converted into the equivalent *S/N* proportions as mentioned below.

The larger type's *S/N* was exploited for the great safety factor as well as high angle deflection, as identified by:

$$\eta = -10\log\left(\frac{1}{n}\sum_{i=1}^{n}\frac{1}{y_i^2}\right), \tag{3.24}$$

The smaller type's *S/N* was exploited for rotation axis shift, as determined by:

$$\eta = -10\log\left(\frac{1}{n}\sum_{i=1}^{n}y_i^2\right), \tag{3.25}$$

where y_i denotes the ith response and n denotes the replication of ith experiment.

The numeric outcomes of the experiments were utilized as a reference to calculate the *S/N* proportion numbers for y_1, y_2, and y_3 as presented in Eqs. (3.24) and (3.25). Details about the orthogonal array with input parameters, experiment outcomes and the *S/N* proportion numbers are demonstrated in Table 3.5.

Table 3.5 Outcome of *S/N* values

No.	h	r_x	r_y	*S/N of* y_1 (dB)	*S/N of y2* (dB)	*S/N of* y_3 (dB)
1	0.4	4	2	82.1496	9.3964	-25.6799
2	0.4	5	2.5	81.0605	10.4201	-24.7314
3	0.4	6	3	80.1868	11.2459	-23.8764
4	0.5	4	2.5	82.1139	7.4582	-27.7443
5	0.5	5	3	80.8830	8.6594	-26.5580
6	0.5	6	2	77.8368	11.9099	-23.2230
7	0.6	4	3	82.0607	5.8893	-29.3704
8	0.6	5	2	78.7529	9.4843	-25.6799
9	0.6	6	2.5	77.9678	10.1571	-25.0362

3.4.4. Establishment of fuzzy model

The proposed fuzzy procedure targets to integrate 03 inputs into 01 input. The inputs are determined by the *S/N* numbers of 03 features of the elliptic joint while the output is regarded as the combined appropriateness formula (*Z*). This *Z* formula is used for optimal process in the next step.

With reference to the datasets of input parameters and quality characteristics, the Gaussian MFs was suggested for the both inputs and output. The MFs curves were charted in Figs. 3.4(a), 3.4(b) and 3.4(c). Furthermore, based on the expertise, the input parameters and quality features are fuzzified as in the following principles: S S S (SM), S S M (M), S S L (ML), S M S (M), S M M (ML), S M L (L), S L L (VL), M S S (SM), M S M (SM), M M L (M), M M S (SM), M M M (M), M M L (ML), M L S (M), M L M (ML), M L L (L), L S S (VS), L S M (SM), L S L (SM), L M S (S), L M M (SM), L M L (M), L L S (SM), L L M (M), and L L L (ML). More specifically, S symbolizes small, M symbolizes medium, and L symbolizes large.

Illustrations for the associated MFs for input parameters and output responses are presented in Fig. 3.5, and the rules are provided in Table 3.6. The output value of fuzzy

modeling is provided in Tab. 3.7. Figures 3.6-3.8 demonstrate connections of *S/N* inputs vs. the output of this system. Figure 3.9 illustrates fuzzy rules.

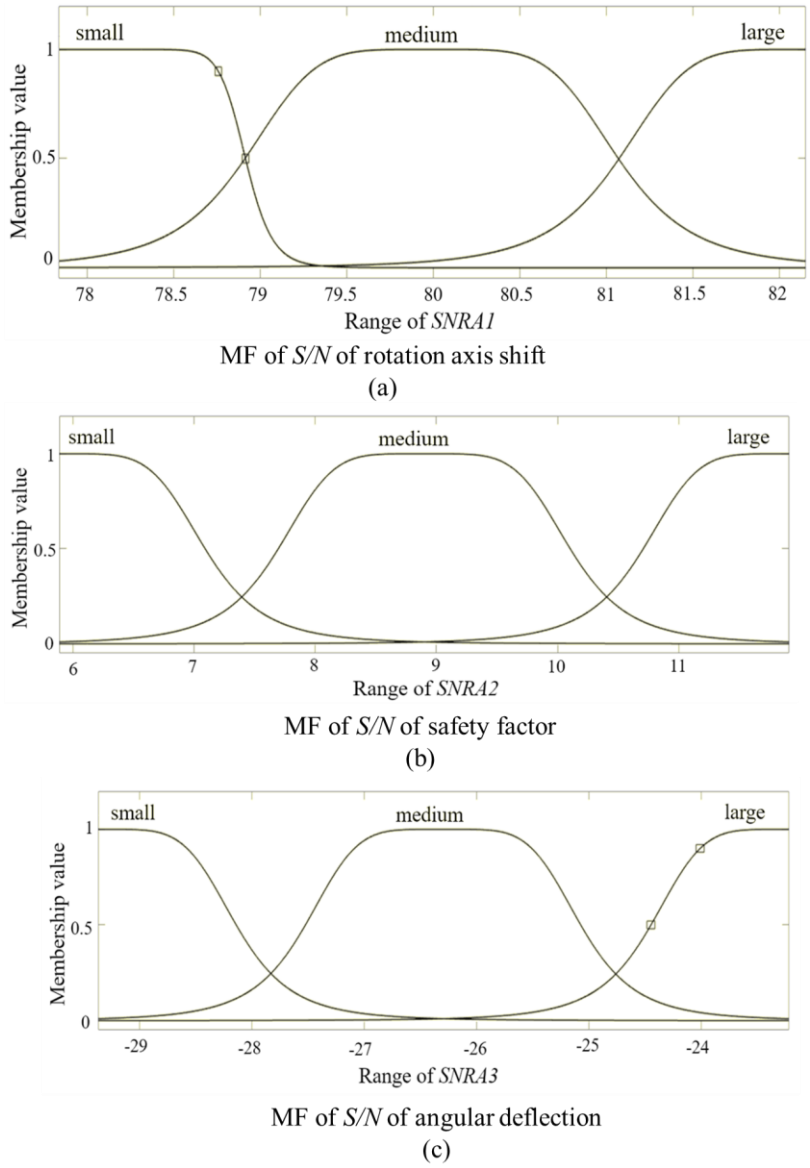

Figure 3.4. Scheme for MFs: (a) Rotary axis shift; (b) safety factor; (c) angle deflection.

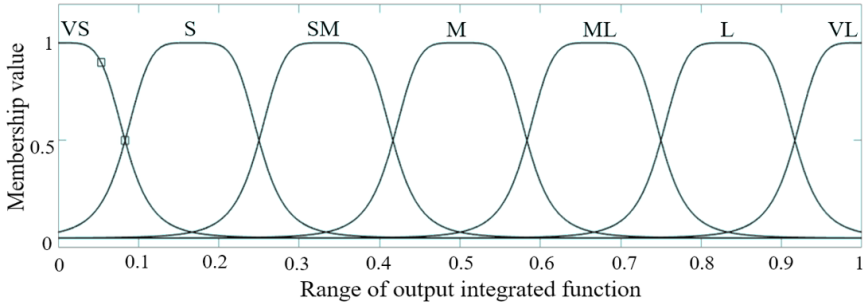

Figure 3.5. Scheme of membership function for the output combined function.

Table 3.6 Fuzzy principles for assessing elliptic compliant joint responses

Regulation	Input 1 (y_1)	Input 2 (y_2)	Input 3 (y_3)	Output
R1	S	S	S	SM
R2	S	S	M	M
R3	S	S	M	ML
R4	S	M	S	M
R5	S	M	M	ML
R6	S	M	L	L
R7	S	L	S	ML
R8	S	L	M	L
R9	S	L	L	VL
R10	M	S	S	SM
R11	M	S	M	SM
R12	M	S	L	M
R13	M	M	S	SM
R14	M	M	M	M
R15	M	M	L	ML
R16	M	L	S	M
R17	M	L	M	ML
R18	M	L	L	L
R19	L	S	S	VS
R20	L	S	M	SM
R21	L	S	L	SM
R22	L	M	S	S
R23	L	M	M	SM
R24	L	M	L	M
R25	L	L	S	SM
R26	L	L	M	M
R27	L	L	L	ML

Note: S symbolizes small, M symbolizes medium and L symbolizes large

Table 3.7 The inputs and output of fuzzy modeling

SNRA1	SNRA2	SNRA3	Output (Z)
82.1496	9.3964	-25.6799	0.363
81.0605	10.4201	-24.7314	0.59
80.1868	11.2459	-23.8764	0.79
82.1139	7.4582	-27.7443	0.27
80.8830	8.6594	-26.5580	0.446
77.8368	11.9099	-23.2230	0.886
82.0607	5.8893	-29.3704	0.0946
78.7529	9.4843	-25.6799	0.619
77.9678	10.1571	-25.0362	0.686

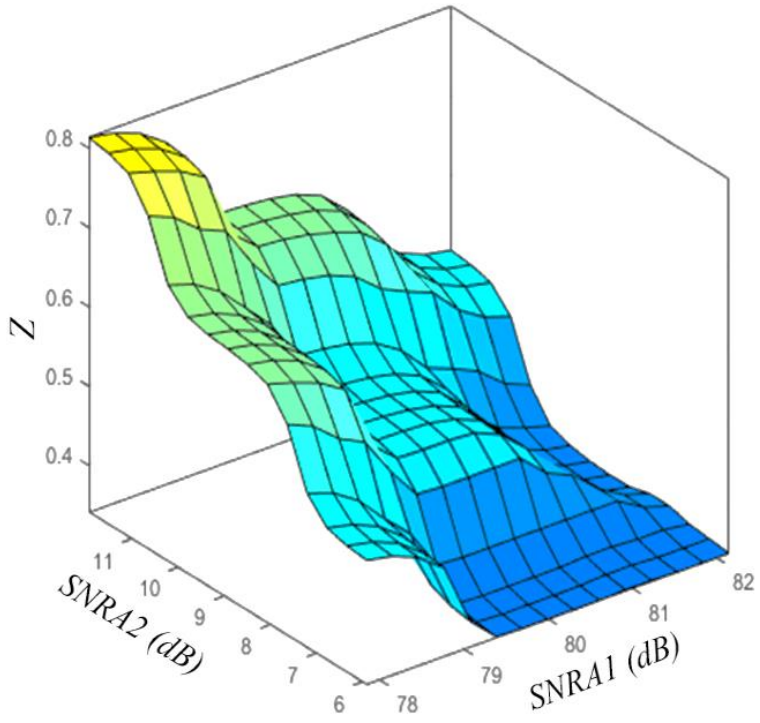

Figure 3.6. Image of *S/N* of y_1 and y_2 versus output in FIS.

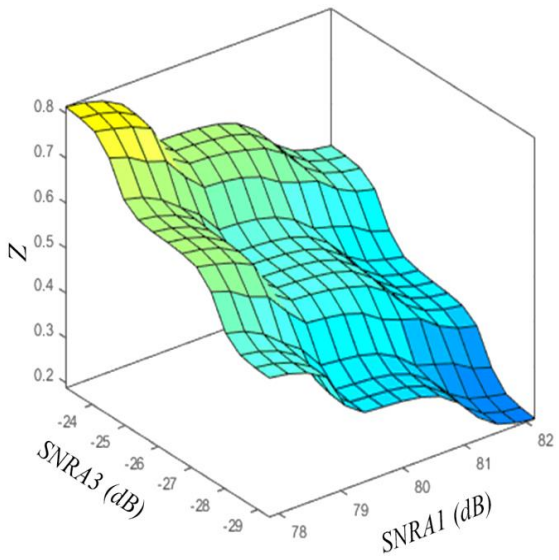

Figure 3.7. Image of *S/N* of y_1 and y_3 versus output in FIS.

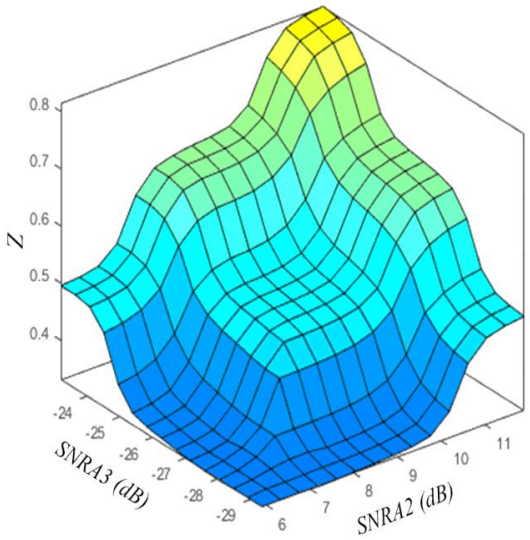

Figure 3.8. Image of *S/N* of y_2 and y_3 versus output in FIS.

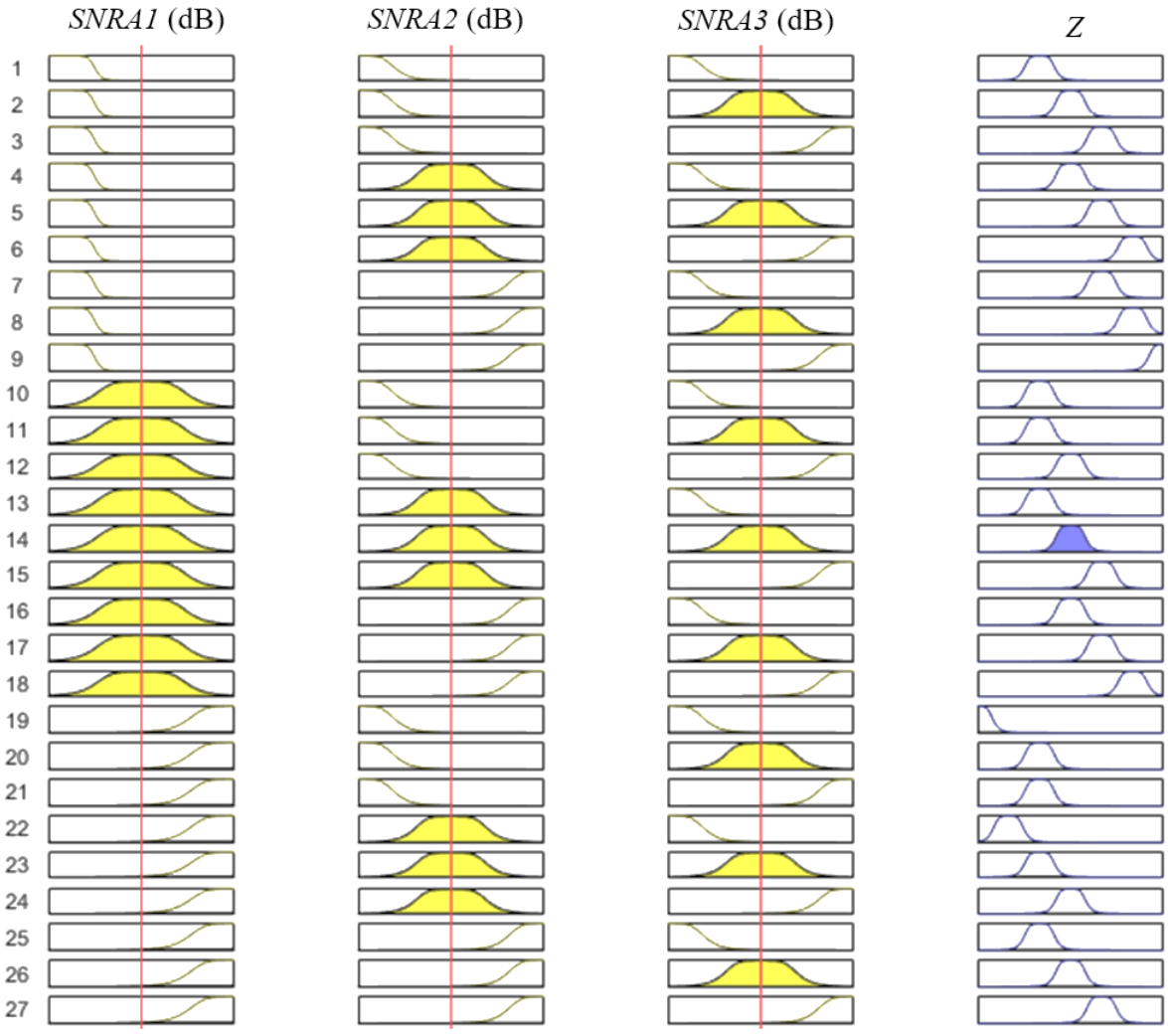

Figure 3.9. 27 fuzzy regulations.

3.4.5. Establishment for regression equation

Subsequent to the establishment of the integrated function with the adoption of fuzzy modeling, a combined regression equation was formulated for linking the input parameters and combined function, and accordingly to identify the flexure hinges' optimized parameters. The following regression equation demonstrates the connection between design variables and output fuzzy:

$$Z = -2.058 + 3.518 \times h + 0.5670 \times r_x + 0.05367 \times ry - 1.023 \times h \times h \\ -0.01867 r_x^{\,2} + 0.02067 \times r_y^{\,2} - 0.2520 \times h \times r_x - 0.7227 \times h \times r_y \tag{3.26}$$

Tables 3.8 demonstrates the ANOVA outcomes of the combined regression formula.

Table 3.8 ANOVA analysis

Source	DF	Seq SS	Contribution	Adj SS	Adj MS	P-Value
Model	8	0.522239	100.00%	0.522239	0.065280	meaningful
Linear	3	0.512998	98.23%	0.218474	0.072825	meaningful
h	1	0.019654	3.76%	0.019654	0.019654	meaningful
r_x	1	0.445211	85.25%	0.194056	0.194056	meaningful
r_y	1	0.048133	9.22%	0.031314	0.031314	meaningful
Square	3	0.003539	0.68%	0.000818	0.000273	meaningful
h*h	1	0.000209	0.04%	0.000209	0.000209	meaningful
r_x*r_x	1	0.002699	0.52%	0.000523	0.000523	meaningful
r_y*r_y	1	0.000631	0.12%	0.000040	0.000040	meaningful
2-Way Interaction	2	0.005702	1.09%	0.005702	0.002851	meaningful
h*r_x	1	0.003744	0.72%	0.000953	0.000953	meaningful
h*r_y	1	0.001958	0.38%	0.001958	0.001958	meaningful
Error	0	-	-	-	-	
Overall	8	0.522239	100.00%			

This investigation was completed at 5% importance as well as 95% assurance grades. It can be seen from Table 3.8 that the proportion on the combined regression formula of r_x

was greatest with 85.25%, and its proportion of r_y and h were extremely superior at 9.22% and 3.76%, correspondingly.

Nevertheless, the effect proportion of other effect factors was much smaller. The proportions of r_x-r_x, r_y-r_y and h-h associations were 0.52%, 0.12% and 0.04%, correspondingly. As a result, an extreme control of factors r_x as well as r_y should be established to enhance the value of Z and the error percentage for Z was 0%.

The affectability of input parameters to the combined response was measured via the exploitation of statistic method. As can be seen in Fig. 3. 10, figures for factor h ranges from 0.4 mm to 0.6 mm, and the parameter impressed the combined characteristic in decreasing slightly. Likewise, statistics for factor r_y varies from 2 mm to 3 mm, and this factor contributed to gradual decrease of the response. However, the parameter r_x was within a range [4 mm, 6 mm], and it facilitated a significant rise in the integrated quality characteristic.

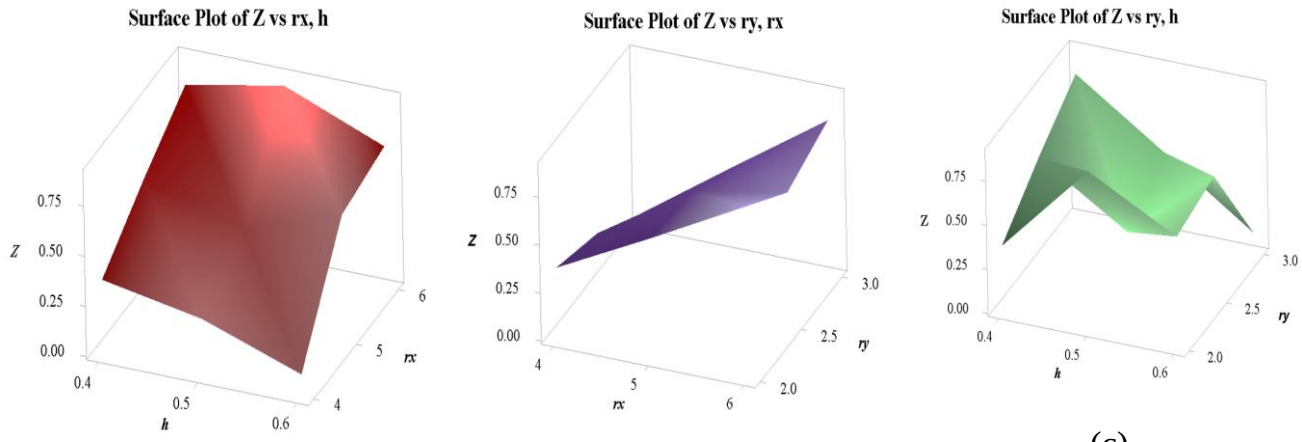

(a) (b) (c)

Figure 3.10. Impacts to Z perform of fuzzy system: (a) h and r_x, (b) r_x and r_y, (c) h and r_y.

In short, the whole impacts of chief parameters on integrated function were presented in Fig. 3.11. Simultaneously, an increase and a reduction in variety in each parameter were observed which provides evidence for mechanical researchers to modify the parameters to produce a proper design for the suggested flexure hinge.

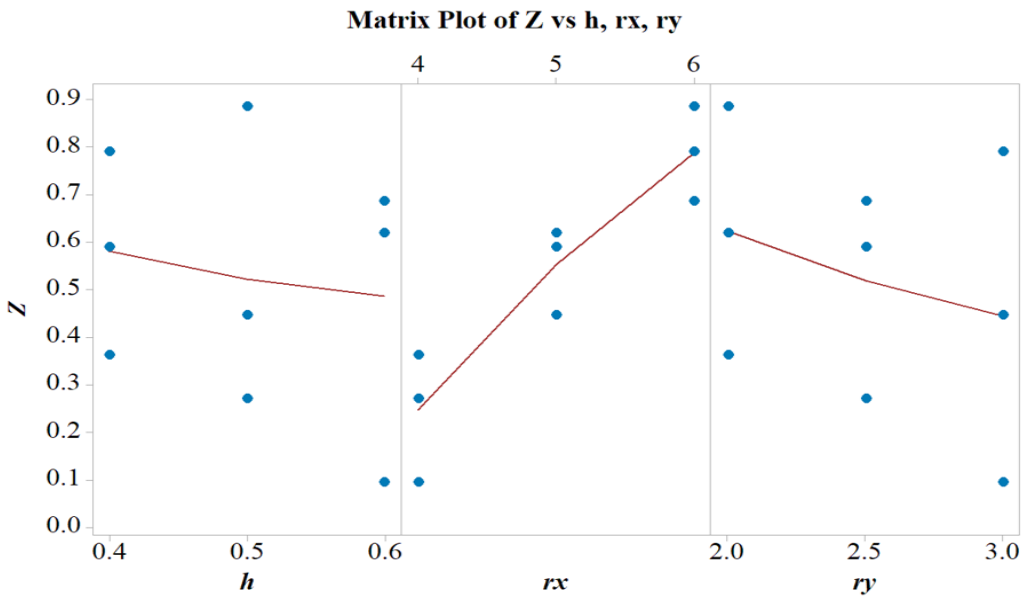

Figure 3.11. Impressionability diagram of the parameters on the combined characteristic.

3.4.6. Optimal execution

The regression equation was employed as a reference for the exploitation of the MFO algorithm to seek for suitable optimal parameters. The use of MFO algorithm aimed to identify the finest factors of elliptic joint owing to the rapid concurrence velocity to universal optimal resolutions. This algorithm is assisted to look for an optimization set for the single criterion optimization.

MATLAB 2017b was exploited for performing the MFO algorithm and maximizing the combined response. The initial factors of MFO were demonstrated in Table 3.9.

Table 3.9 Exploited initial factors for MFO

Factors	Worth
Quantity of investigating agents	50
Maximum number of reiterations	500

The optimization input parameters such as x_{val}= [0.6 6 3] as well as f_{val}= 2.76 were discovered. The optimization outcomes achieved at h= 0.6 mm, r_x = 6 mm, r_y= 3 mm, as well as Z= 2.76 equivalent to y_1= 0.000109 mm, y_2= 2.994 as well as y_3= 0.052006 rad.

3.4.7. Validation

The optimization factors (h= 0.6 mm, r_x= 6 mm, r_y=3 mm as well as Z= 2.7614 equivalent to y_1= 0.000109 mm, y_2= 2.994 as well as y_3= 0.052006 rad) were utilized to generate into

detasFlex software. After that, numeric authentications were conducted for testing the predicted outcomes. This process was executed with the similar limitations and the similar input primary angle. The confirmed outcomes were around 0.00011715 mm for the rotary axis shift, 2.95 for the safety factor, 0.052 rad for the angle deflection.

Table 3.10 represents that errors between anticipated outcomes and validations were 6.58% for the rotary axis shift, 1.47% for the safety factor, and 0.01% for the angle deflection. It can be stated that the prophesied resolutions are in an appropriate covenant with substantiated outcomes.

Table 3.11 indicates that the optimization results exceeded those of the initial design regarding the angular deflection and safety factor. Particularly, figures for the enhancement were roughly 10.46% for the safety factor, and around 10.65% for angle deflection. Conversely, a decrease for the rotary axis shift was around 21.2%. These aforementioned results confirmed the effectiveness of the novel integrated method proposed in this study in dealing with multi-criteria problems of the proposed flexure hinge.

Table 3.10 Error between the anticipated result and confirmations

Characteristics	Prediction	Confirmation	Error (%)
y_1 (mm)	0.0001094	0.0001172	6.58
y_2	2.9935	2.95	1.47
y_2 (rad)	0.052005	0.052	0.01

Table 3.11 Differences among primary response and optimal response

Characteristic	Optimal response	Primary response	Enhancement (%)
y_1 (mm)	0.0001094	9.E-05	-21.19
y_2	2.9935	2.7	10.46
y_3 (rad)	0.052006	0.05	10.65

Additionally, Table 3.12 showed that the optimal outcomes of the flexure-based joint were recompared with the outcomes of right circular joint, corner rounded joint and power function 1 (n=2). It is also revealed that the optimization joint attained the maximum worth of safety factor and maximal angle deflection, thus, this optimization joint was selected for combination into flexure-based positioning stages employed for nanoindentation testing device according to the output characteristics of offered hinge.

Table 3.12 Comparison of the optimized hinge with other hinges

Compliant joints	Factors (mm)	Investigation angle (°)	y_1 (mm)	y_2	y_3 (rad)
Right circular joint	H=10, h=0.5, L_1=10, L_2=10, l=9.987, w=5	Investigation angle (1°)	7.2113e-05	2.11	0.037
Corner rounded joint	H= 10, h= 0.5, L_1= 10, L_2= 10, l=10, w= 5	Investigation angle (1°)	0.00022379	0.1	0.176
Power function 1 (n= 2)	H=10, h= 0.5, L_1= 10, L_2=10, l=10, w= 5	Investigation angle (1^0)	5.486e-05	1.55	0.027
Optimal joint	H=10, h= 0.5, L_1= 10, L_2=10, l=10, w= 5, r_x= 5, r_y= 2.5	Investigation angle (1°)	0.00010944	2.99349	0.0520058

3.4.8. Comparison with various methods

This study employed a statistic analysis to examine the statistical aspects of the integrated method, the The Wilcoxon test to be precise. In search for the integrated objective function (Z), the calculation simulations, conducted at 5% meaningful grade and 95% warranty intervals, were repeated 30 times for every method. The Wilcoxon results were presented in Table 3.13.

The null hypothesis is that there is no chief variation between mean worth of the two algorithms. However, it is rejected as the results in Table 3.13 reveal that p-value is smaller than 0.001 (5% meaning grade) leading to the conclusion that it exists a statistic differentiation between the developed methodology and ASO algorithm [126]. In other words, the developed approach exceeds ASO algorithm concerning the capacity of resolving optimization design of offered flexure hinge.

Table 3.13 Wilcoxon's comparison of the offered method versus ASO

Count of investigations	Estimated average	p- worth	Wilcoxon statistic
30	0.0137299	<0.001	465

On the other hand, the Friedman assessment which was carried out for the integrated objective function, indicated that the divergence between the offered combined optimal methodology and the ASO algorithm at consequential degree of $\alpha = 0.05$. For each algorithm, the computational simulations were executed 30 times. The results illustrated that the p-value is slighter than 0.001, and the null hypothesis was discarded. Accordingly, there is a significant dissimilarity among developed integrated method and the ASO algorithm, as demonstrated in Table 3.14.

Table 3.14 Friedman test for the combined output response

Combined response	No.	Mean	Rankings
The offered approach	30	2.76140	60
ASO	30	2.74791	30
Total	60	2.75466	
DF	Chi-Square	P-Value	
1	30	<0.001	
Null hypothesis	H_0: Every treatment impact is 0		
Substitute hypothesis	H_1: Not all treatment impacts are 0		

Additionally, mean concurrence time for 30 runs of the offered approach and genetic algorithm (GA) [114] and ASO algorithm [126] was compared for finding a combined response. The 03 approaches were implemented with a maximal number of iteraction of 500. The outcome indicated that the concurrence velocity of the offered approach outperforms the concurrence velocity of ASO algorithm as well as GA, as demonstrated in Table 3.15.

Table 3.15 Mean concurrence time's comparison of offered approach versus ASO and GA

Combined response	Mean concurrence time (s)
The offered approach	11.446
ASO	11.867
GA	13.159

To sum up, the significant findings presented in this chapter include: (i) Elliptic joint is the best appropriate hinge for a combination into flexure-based positioner in nanoindentation testing device. (ii) An efficacious combination approach of TM, RSM, fuzzy logic, and MFO is offered for concurrently optimizing in order to boost the 03 characteristics of the compliant joint. (iii) Offered optimization hinge has superior demeanors than primary structure and other flexure-based joints. (iv) The integration optimal methodology outperforms GA as well as ASO algorithm.

Likewise, the benefits of the offered research are shortened as follows: (i) The successful application of an optimization approach for optimizing the factors of an offered hinge so as to improve three output characteristics of an offered flexure-based hinge. (ii) In the fuzzy modeling, the WFs for every target formula was cardinally allocated for a combined function. (iii) In the fuzzy modeling phase, design engineers apply specialized experience to form connections between fuzzy inputs and fuzzy outputs for improving the accurateness of optimization outcomes.

3.5. Conclusions

This chapter reports the implementation and results of a proposed combination optimal approach for the elliptic compliant joint which was expected to integrate into a flexure-based positioning stage used for locating or indenting the specimen in nanoindentation testing devices. With the use of detasFLEX software, a comparison among the four types of flexure joints including elliptic joint, power function joint 1, right circular joint and corner-rounded joint was compared in the same condition of angle displacment. The analysis outcomes revealed distinctive features of the elliptic joint and it was chosen. To concurrently achieve the targets of minor rotation axis shift, great safety factor and angular deflection, the main aspects of the elliptic compliant joint were optimized using a variety of methods, namely TM, RSM, fuzzy logic, and MFO. Initially, numeric experiments were

carried out by a combination TM and detasFlex software, followed by the conversion of three output responses into *S*/*N* values to remove the unit variations. Thereafter, fuzzy modelling was adopted for interpolating three output responses into one combined function and the response surface method was exploited to formulate an integrated regression equation. Lastly, the optimization of the flexure hinge was conducted by the Moth-flame optimization algorithm which resulted in the optimized factors at h= 0.6 mm, r_x= 6 mm, and r_y= 3 mm. The outcomes were within $10.944*10^{-5}$ mm for the rotary axis shift, 2.993 for the safety factor, $52.0058*10^{-3}$ rad for the angle deflection. Additionally, the ANOVA investigation and reactiveness investigation were used to determine major influences of the input parameters on the combined characteristic.

Moreover, the figures by Wilcoxon and Friedman tests indicated that the combined approach outperforms the ASO algorithm while the comparison among the average concurrence time for 30 operates of three algorithms including combined approach, ASO algorithm and GA showed that the convergence velocity of the offered methodology is superior than that of ASO algorithm as well as GA. These results proved the effectiveness and appropriateness of the proposed integration approach in solving multi-objective optimization problems for complicated engineering.

The current research shows some limitations. First, it is complicated to establish fuzzy rules for linking fuzzy inputs as well as fuzzy outputs. The setting of these rules is time-consuming and involves professional experiences. Thus, the suggestion for future researchers is to employ the ANFIS or various methods in the optimization procedure to simplify the computation for complex optimal troubles. However, as there exist both pros and cons for optimal calculations in each approach, the researchers should select a suitable approach for real problems.

In this thesis, the elliptic joint and other flexure joints such as leaf joint and circular joint were combined into flexure-based locating stages for positioning and indenting material sample in a nanoindentation testing device. Particularly, the optimal approach is also applicable in dealing with multi-DOF positioners and the offered combination methodology is used for resolving complicated multi-criteria optimization issues.

CHAPTER 4 DEVELOPMENT OF 01-DOF COMPLIANT STAGES FOR INDENTER

After analysis and evaluation of flexure hinges in chapter 3, this chapter presents three design alternatives for indenting the specimens to adapt various specimens from thin film to the animal bone, coating material of artificial joints in the proposed nanoindentation testing device, as illustrated in Fig 1.5.

To be more specific, the first design alternative presents the design of the 01-DOF stage inspired by the profile of the beetle leg, as well as an efficient hybrid optimization approach of RSM and advanced ANFIS for improving output responses. The second design alternative then presents the design of the 01-DOF stage according to a four-lever intensification structure, flexure-based joint shifted layout structure, zigzag-inspired flexure spring driving structure, and symmetrical six-leaf hinge-inspired parallel guiding structure, as well as an effectual approach of TM, RSM, weight factor, as well as WOA algorithm. Finally, the third design alternative presents a 01-DOF stage based on a symmetrical six-lever displacement amplification mechanism combined with elliptic flexure joints and a symmetrical six-leaf parallel guiding structure. Furthermore, analytical modeling based on the PRBM method was established to quickly evaluate the stage's initial characteristics. The Firely algorithm was then used to advance the quality response by optimizing the main factors of the third 01-DOF stage.

4.1. Motivation

A nanoindentation testing device, as shown in Fig. 1.5 (Chapter 1), consists of a raw Z-positioner, a raw XY-positioner, a refined XY-positioner, as well as a refined Z-positioner. 01-DOF stages (Z-stages) are utilized to drive the indenter for checking the mechanical properties of various specimens from soft material to harder material, as illustrated in Fig. 1.1 and Fig. 1.2. Therefore, this chapter has a motivation to develop various 01-DOF stages with a large working stroke, and small parasitic motion error. More specifically, for the harder specimens, the 01-DOF stage needs to be achieved more significant output displacement. On the other hand, for the soft specimens, the 01-DOF stage needs relatively more minor output displacement. Consequently, different 01-DOF stages with various output displacements were developed to adapt to various specimens, from soft material specimens to harder material specimens. Based on the merits of compliant mechanisms,

01-DOF stages will be designed, analyzed, simulated, and optimized for guiding the indenter.

4.2. Development and optimization of a 01-DOF stage inspired from beetle

4.2.1. Conceptual design

In order to create a new 01-DOF positioner with large output displacement and small parasitic motion for guiding the indenter to move closer to the specimens, especially bio-specimens, in nanoindentation testing device, this new design is developed according to leg profile’s beetle and four-lever amplification mechanism.

The first 01-DOF stage includes four-lever displacement amplification module and a parallel guiding mechanism module. Three main technical performances of the first 01-DOF stage are expressed as follows.

- The output displacement is more than 2.3 mm.
- Parasitic motion error is lower than 0.02.
- The safety factor is higher than 1.5.

4.2.1.1. Flexure-based positioner

Motivated by the beetle's flexible movement, a new flexure-based positioner was constructed to achieve the output displacement while decreasing parasitic motion error, as shown in Figs. 4.1. (a) and (b). Furthermore, beetles' body as well as leg movements are almost entirely in the similar surface, as is their leg flexibility. As a result, a beetle-like mechanism is appropriate for building a planate mobility structure. Figure 4.1(a) depicts a real beetle. One of the beetle's legs can be offered to be divided into five fragments in reference to the shape of each leg. This geometry can be used for creating a structure to generate linear motion. Hence, a five-segment model of the proposed positioner was created, as demonstrated in Fig. 4.1. (b). It had rigid joints as well as flexure-based hinges. Especially, the geometrical factors of flexure hinges play a significant role in CPP performance. Therefore, they were considered as the main design variables.

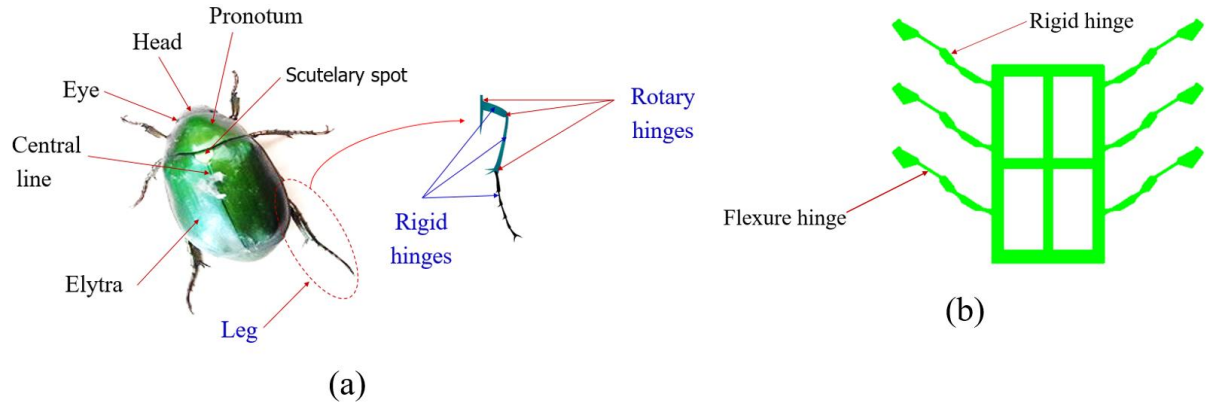

Figure 4.1. Framework of beetle-motivated stage: (a) Anatomy of beetle, (b) Flexure-based positioner.

Vertical linear motion is ensured by the beetle-like mechanism, while horizontal parasitic motion is suppressed. The overall performance of the compliant positioning platform CPP was appraised using a high displacement, a minor decoupling error, and a great safety factor. A direct design could attain a small parasitic motion, but both quality characteristics should be improved by a multi-objective optimization problem.

4.2.1.2. Displacement amplifier

A lever mechanism is traditionally exploited for increasing the magnitude of a force or displacement. As shown in Fig. 4.2, the lever structure consists of a beam supported by a affixed joint or fulcrum (a). The the lever's rotary central point is represented by spot O, the input location by point A, and the output location by point B. The following is an illustration of the lever structure's operation principle: when putting a vertical deformation Δl_1 on the input spot A, the lever will revolve the z-direction with a relative angle γ. Consequently, the point B transfers to B' and the output displacement Δl_2 can acquire in the y-direction, as demonstrated in Fig. 4.2(b). To begin with, a single lever structure is exploited to enlarge output displacement. Conversely, this structure easily generates enormous decoupling error. Based on its symmetric structure, a two-lever structure was constructed for intensifying the output displacement while ensuring a low parasitic motion error, as shown in Fig. 4.3. (b). Furthermore, a four-lever displacement amplifier was developed for amplifying larger output displacement, as shown in Fig. 4.4.

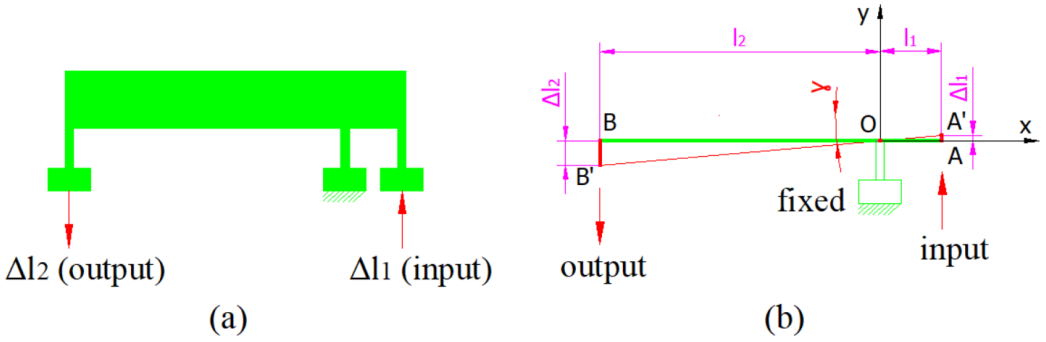

Figure 4.2. Schema: (a) Lever mechanism operation principle, (b) Amplification ratio for displacement.

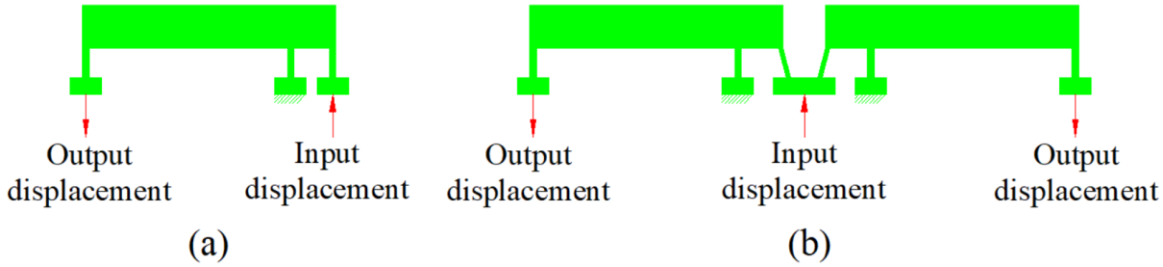

Figure 4.3. Framework of lever amplification mechanism: (a) single lever structure, (b) two-lever structure.

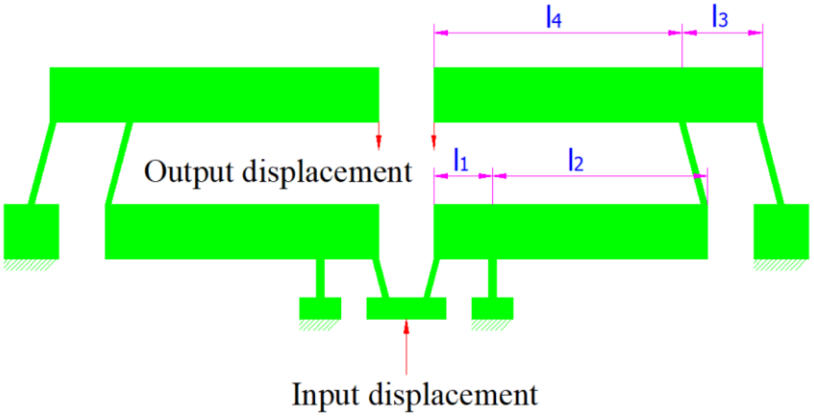

Figure 4.4. Configuration of offered four-lever intensification structure.

The intensification proportion of a lever amplifier can be approximated using a schematic diagram (see Fig. 4.2(b)) as follows:

$$r_{lever} = \Delta l_2 / \Delta l_1 = l_2 / l_1 \tag{4.1}$$

The following equation is assumed for a multi-lever displacement amplifier:

$$r_T = l_2 / l_1 \times l_4 / l_3 \tag{4.2}$$

where r_T is the four-lever amplifier's magnification proportion.

4.2.1.3. Beetle-liked platform with amplification mechanism

Operation principle of offered positioner was in accordance with the elastic deformation of the compliant hinges. The great quality feature values of offered material including yield strength, Young's modulus E as well as density are 503 MPa, 71700 MPa, and 2810 kg/m^3. The linear stage specification supposed an input displacement of 0.13 mm, as shown in Tab. 4.1.

It was made up of the following elements, as shown in Fig. 4.4: (i) 12 fixed holes were exploited for testing the positioner's characteristics on an un-vibration table, and (ii) a translational screw (positioned at the input displacement location) was employed for creating the positioner's input displacement by connecting directly with the beetle-liked mechanism. The model's overall dimensions were approximately 230mm x 222mm x 6mm.

Table 4.1 shows the platform's geometrical parameters. In order to achieve effective static performance for the locating device, the developed platform had to generate a large displacement while also maintaining a high safety factor. Furthermore, so as to successfully drive the indenter for indenting the specimen, the input displacement should be changed direction, as shown in Fig. 4.5. (c).

The structure's primary design factors were proposed according to the design domain and capability of the wire electrical discharged machining (WEDM) method and professional expertise, to guarantee a high output displacement and suitability for the fabrication via WEDM method. In this research, the key factors (length, width, and radius) of the flexure hinges affect the structure's linear motion.

In a comparison with several factors of a beetle leg simulation structure, the thickness of the flexure hinge has the greatest influence on linear motion and output displacement, in reference to the Euler-Bernoulli beam theory and the theory of flexure-based structure. Consequently, in this study, the thicknesses of the compliant hinges of a beetle-leg simulated model were used as the primary factors for determining main parameters, while the other geometrical factors were ignored.

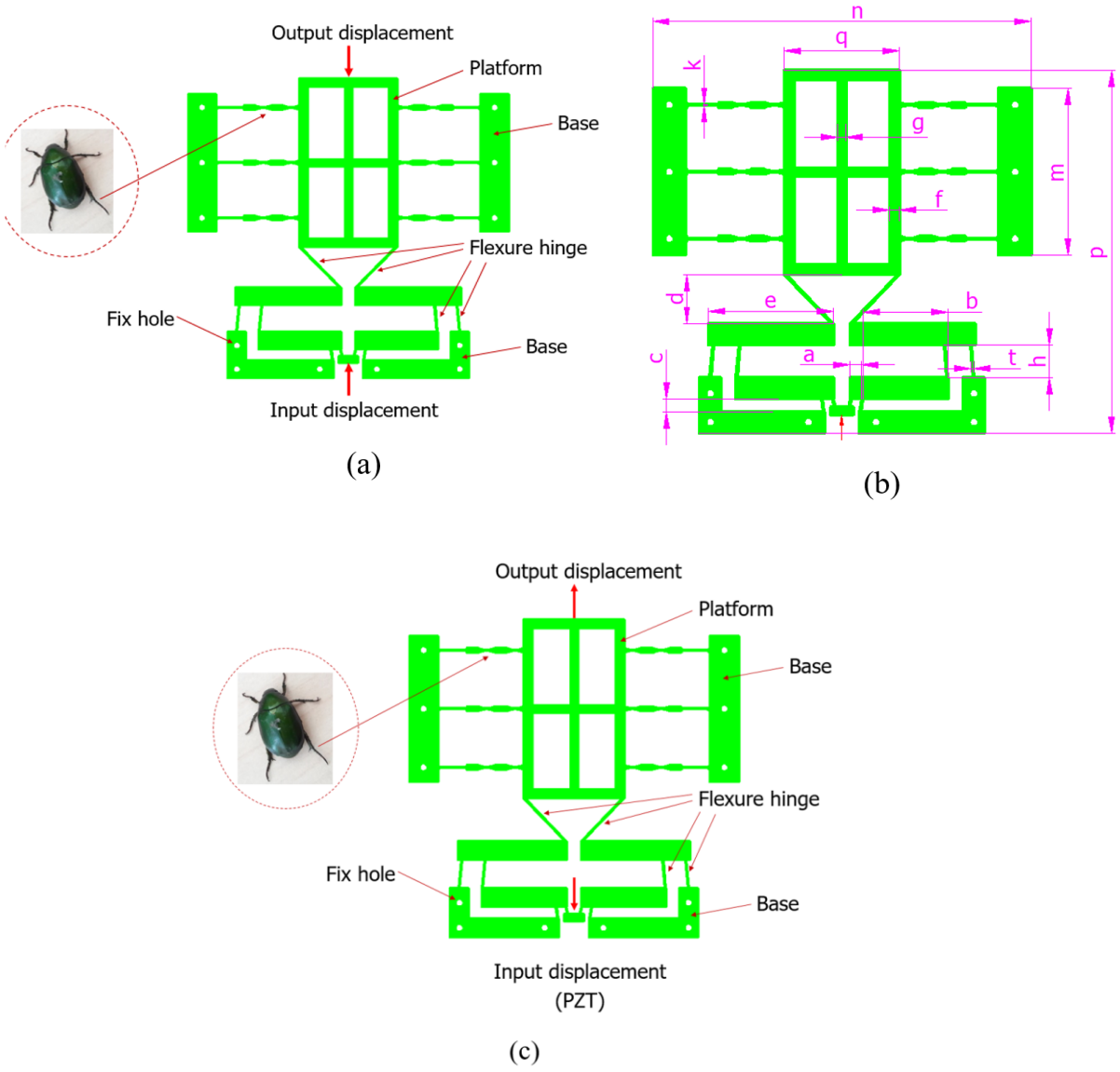

Figure 4.5. Model: (a) a platform shaped like a beetle, (b) design parameters, and (c) a stage shaped like a beetle for guiding the indenter.

Table 4.1. The beetle-like platform's structural parameters

Factors	Worth	Unit	Factors	Worth	Unit
a	6.84	mm	*h*	*18≤h≤21*	mm
b	*48≤b≤53*	mm	*t*	*0.9≤t≤1.1*	mm
c	8	mm	*m*	102	mm
d	30	mm	*n*	230	mm
e	76	mm	*p*	222	mm
f	6	mm	*q*	70	mm
g	5	mm	*k*	*0.67≤k≤0.74*	mm

4.2.2. A fundamental use for a nanoindentation testing device

The suggested stage's operating principle was according to the material's elastic deformation. It was in accordance with Hook's law. As a result, the stage was worked within the elastic constraint. It was designed to be used in a nanoindentation tester.

During the nanoindentation testing process, the offered positioner was used to position the material sample. The positioner moved in the X-direction for locating the specimen to an original accurate point before translating the indenter downward for checking the mechanical properties of the specimen.

Simultaneously, multiple microscopes were exploited to photograph the sample while monitoring its initial characteristics. The indenter would then be aimed at a depth into the checking specimen. The offered positioner would then return a reference position for preparing for future checking. Figure 1.5 depicts a fundamental use for a nanoindentation testing device.

4.2.3. Primary characteristic and parasitic motion error analysis

Inventor Professional 2018 was used in this section to create a 3D platform model, which was then simulated using FEA method in ANSYS 18.2.

The goal was to anticipate the y-direction deformation as well as the safety factor of the offered positioner. This analysis was performed using the approach of automatic meshing, and the compliant joints were refined to attain beneficial analysis exactness, as shown in Fig. 4.6.

The positioner was anchored in the holes, and the following boundary conditions were proposed. Following the design of a rough positioner, the output deformation of the stage was surveyed by increasing the translational screw's input displacement within a range [190 μm, 220 μm], correspondingly so that the static failure restriction can be tested and the maximum input displacement for the primary positioner is limited.

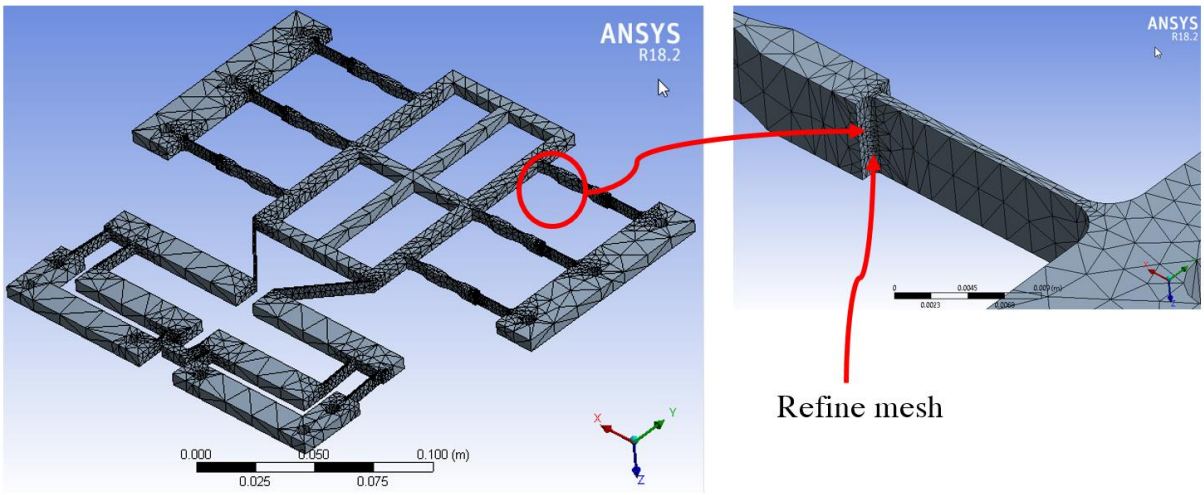

Figure 4.6. Scheme of mesh creation for the offered positioner

To identify the suitable input deformation range for ensuring strength limitation of the offered positioner, the translational screw input displacement was adjusted in the range [190 µm, 220 µm]. In addition, the output displacement was recorded as well. Based on finite element analysis by ANSYS 18.2 software, the simulated results are given in Table 4.2. The results indicated that in relation to the input displacement of 220 µm, the output deformation attains 3.8193 mm.

If the safety factor was less than one and the causing stress was superior than the crucial yield strength of the material (503 MPa), the positioner could fail due to plastic deformation. As a result, the maximum input deformation should be less than 220 µm. Conversely, when the input displacement was 190 µm, the causing stress was around 434.52 MPa, which was less than the material's yield strength. The safety factor was around 1.15.

A safety factor greater than 1.5 was preferred for ensuring the positioner's long-term viability in this research. In consequence, the input displacement was proposed to be between 10 µm to 180 µm. Using Eq. (4.3), the output deformation in the X, Y-directions, as well as by changing the input displacement from 10 µm to 180 µm, the parasitic motion error was computed. The decoupling error was minimal, as shown in Table 3.3. The attained outcomes were within 17.3608 for the intensification proportion, 1.6969 for the safety factor and 297.31 MPa for the equivalent stress. However, none of the outcomes meet the workable necessities (IP is more than 18). As a result, an optimal procedure could be performed in the next phase.

Table 4.2 The output displacement

Input displacement (mm)	Output displacement (mm)	Intensification ratio	Safety factor	Equivalent stress (MPa)
0.19	3.2985	17.36	1.1576	434.52
0.2	3.4721	17.36	1.0997	457.39
0.21	3.6457	17.36	1.0473	498.13
0.22	3.8193	17.36	0.99973	503.13

When the positioner traveled in the y-direction, a movement occurred along the x-direction, instantaneously. The unwanted transmission in the x-direction was referred to as decoupling fault. An alike investigation revealed that the decoupling fault is extremely minor, with 0.01515% (less than 1%), as shown in Table 4.3. It is possible to conclude that the parasitic motion error has little effect on the output displacement accurateness and that the offered positioner generates an appropriate linear mobility. The decoupling error was characterized as following equation:

$$e = \frac{x}{y}100\% \tag{4.3}$$

where *e* denotes the decoupling error as well as x denotes output deformation x-direction, y denotes output deformation y-direction.

Table 4.3 Output deformation and decoupling fault results

Input deformation (mm)	y-direction output deformation (mm)	x-direction output deformation (mm)	Decoupling error (%)
0.01	0.17361	2.6303e-005	0.01515
0.02	0.34721	5.2606e-005	0.01515
0.03	0.52082	7.8908e-005	0.01515
0.04	0.69442	1.0521e-004	0.01515
0.05	0.86803	1.3151e-004	0.01515
0.06	1.0416	1.5782e-004	0.01515
0.07	1.2152	1.8412e-004	0.01515
0.08	1.3888	2.1042e-004	0.01515
0.09	1.5625	2.3673e-004	0.01515
0.1	1.7361	2.6303e-004	0.01515

0.11	1.9097	2.8933e-004	0.01515
0.12	2.0833	3.1563e-004	0.01515
0.13	2.2569	3.4194e-004	0.01515
0.14	2.4305	3.6824e-004	0.01515
0.15	2.6041	3.9454e-004	0.01515
0.16	2.7777	4.2084e-004	0.01515
0.17	2.9513	4.4715e-004	0.01515
0.18	3.1249	4.7345e-004	0.01515

4.2.4. Suggested optimal methodology

4.2.4.1. Problem statement for optimization

Because the CPP was designed to work with elastic deformation of compliant joints. Consequently, the geometrical dimensions of compliant joints had a significant impact. These main features were identified as the length of the first lever, the gap among two levers, and the thicknesses of the flexure-based joints. As a result, so as to improve the output characteristics, the platform's chief geometric factors should be optimized. The offered positioner ought to satisfy the following essential responses:

(i) A minor parasitic movement error to improve linear travel accurateness;

(ii) A large output displacement to increase the platform's broad positioning capacity for testing specimen features;

(iii) A high safety factor to guarantee the positioner's longevity;

A decoupling error could be attained through beneficial structure, as portrayed in Section 4.1.4. Conversely, the displacement and safety factor were problematic for facing through the drawing procedure. As a result, it should be improved further through optimal procedure. As previously stated, the safety factor was at odds with the output deformation. Consequently, a proficient hybrid methodology was offered to trade off them both at the same time.

4.2.4.2. Design variables

The main features of flexure-based hinges substantially provided to the displacement as well as safety factor, according to the results of a few FEA simulations for checking primary responses. Four main features were considered in this study: the length of the first

lever, the gap between two levers, and the thicknesses of the flexure-based joints. $\mathbf{X} = [t, h, b, k]^T$ denoted the vector of design variables. The main features ' limit conditions were formed according to expertise and the professional expertise, as conveyed by:

$$\begin{aligned} 48 \text{ mm} \le b \le 53 \text{ mm}, \\ 19 \text{ mm} \le h \le 22.5 \text{ mm}, \\ 0.9 \text{ mm} \le t \le 1.1 \text{ mm} \\ 0.67 \text{ mm} \le k \le 0.74 \text{ mm} \end{aligned} \tag{4.4}$$

in which *t, h, b,* and *k* denote thickness of compliant joint (intensification structure), gap among two levers, the length of first lever, thickness of compliant joint (beetle's leg structure), correspondingly. The ranges of design variables are based on fabrication capacity of WEDM and design requirements.

4.2.4.3. Objective functions

The following multi-criteria functions were taken into account: (i) The 1st target function, $y_1(\mathbf{X})$, A high safety factor is necessitated for warranting the platform's strength, and it should be as high as possible. ii) The 2nd target function, $y_2(\mathbf{X})$, The output displacement along the y-axis should be as large as possible so as to increase the platform's working travel capacity for checking material sample characteristics. Finally, the optimization issue was represented as follows:

Input main parameters was considered as $\mathbf{X} = [t, h, b, k]^T$.

$$\max y_1(X) \tag{4.5}$$

$$\max y_2(X) \tag{4.6}$$

Two target characteristics are integrated into a single formula for solving the multi-objective optimal trouble. The weight factors were then assigned into two objective functions. The following is the definition of the integrated objective function:

$$y(\mathbf{X}) = -w_1 \times y_1(\mathbf{X}) - w_2 \times y_2(\mathbf{X}), \tag{4.7}$$

in which w_1 and w_2 denote the weight factors of both characteristics, correspondingly.

4.2.4.4. Constraints

Because the developed positioner was operating within the elastic limitations of the proposed material, and it was limited by:

$$g(x) = \sigma \le \frac{\sigma_y}{SF}, \tag{4.8}$$

in which σ_y denotes the yield strength of offered material; *SF* denotes the safety factor.

Greater than 1.5 of the safety factor was required as:

$$y_1(\mathbf{X}) \ge 1.5. \tag{4.9}$$

More than 2.3 mm of output displacement was required as:

$$y_2(\mathbf{X}) \ge 2.3\,\text{mm}. \tag{4.10}$$

in which y_1 and y_2 are the safety factor and displacement, correspondingly.

4.2.4.5. Offered hybrid methodology

In order to resolve the previously mentioned multi-objective optimization trouble, an efficient integration methodology of the RSM, the TM, advanced ANFIS, and TLBO was offered. Initially, the experimental data were gathered by the RSM. The enhanced ANFIS was later used to identify the connection of input parameters to output outcomes. The TM was adopted for achieving an improved ANFIS. The TM was exploited for finding the best manageable factors for the ANFIS configuration based on RSME minimization. These parameters were as follows: (1) quantity of fuzzy logic input membership functions (MFs), (2) kinds of input MFs, (3) the training technique such as combination technique or backpropagation, and (4) the type of output membership functions. Ref. [129] contains more information on ANFIS. Eventually, using the founded replacing model from the advanced ANFIS, the TLBO algorithm was used for performing multi-objective optimization at the same time. Matlab R2017 was used to carry out the programming. Fig. 4.7 depicts a flowchart for the optimal CPP process [130]. Dang et al. developed this proposed hybrid approach. The optimization procedure is divided into the following main phases:

Phase 1: Computer assisted engineering design

Step 1: Identify optimal problem

A multi-criteria optimal issue for the suggested positioner was offered to simultaneously improve both aforementioned characteristics.

Step 2: Identify key parameters and output responses

As input variables, the length of the first lever, the gap between the two levers, and the thickness of the flexure-based joints were defined. Quality characteristics such as an

enormous output y-direction displacement as well as a great safety factor were taken into account.

Step 3: Generate 3D model and simulations

A 3D model is generated exploiting the finite element method (FEM). During the analysis, the stress-strain association was computed as follows:

$$\sigma = E\varepsilon, \tag{4.11}$$

in which σ, E, ε denote stress, Young's modulus and strain, correspondingly.

Step 4: Check primary input responses

Before building the design of experiments, the primary responses were tested numerous times to limit appropriate upper and lower ranges of key parameters and both responses.

Step 5: Establish design of experiments and gather data by combining of RSM and FEA

RSM and FEA were used to collect numerical experiments. First, a 3D model was constructed as well as tested in the FEA method in steps 3 and 4. The quantities of numeric experiments were then determined applying the CCD method combined with RSM. Afterward, the projected outcomes for the output characteristics were obtained. The quantities of experiments required were calculated using the CCD method as eq. 2.8.

Phase 2: Identify the weight factor

Both output characteristics were contradictory. They also had different important weights. As a result, a WF can be established for each objective function. So far, the WF has been defined based on engineering experience and expertise. Hence, so as to quantify the WF more precisely, this study adopted the method by Dao et al. 2017 [131] to quantify the WF for every feature.

Readers can find more information about the WF computing equations in Dao et al. 2017 [131]. Each characteristic function is standardized from 0 to 1. The WF is determined below:

(1) Quantify S/N proportion

The *S/N* proportion is determined by the TM, and a higher S/N ratio value indicates greater ability. In this research, the larger-the-better is exploited for two responses, which are identified by eq. (3.24).

(2) Standardize the *S/N* proportion

The standardized S/N proportions of every target formula level are calculated as follows:

$$z_i = \frac{\eta_j - \min \eta_j}{\max \eta_j - \min \eta_j}, \tag{4.12}$$

in which η_i denotes the *S/N* worth, $\max \eta_i$ and $\min \eta_i$ denote the maximum as well as minimum worth of η_i , correspondingly, z_i denotes the standardized worth of *S/N* for the experiment ith of characteristic function (*j* = 1, 2, …, *k*), *k* denotes the quantity of characteristic formulas.

(3) Quantify the average worth of standardized *S/N* proportions

For response functions, the median worth of standardized *S/N* proportions at each grade was calculated. The *S/N* ratio values are standardized, as well as the mean of the standardized S/N proportions is expressed as:

$$a_{Li} = \frac{1}{N_{Li}} \sum_{i}^{m} z_{ij}, \tag{4.13}$$

where N_{Lji} denotes quantities of repetitions of grade ith. z_{ij} denotes the value of *S/N* ratio of grade ith of response function jth. a_{Li} is the median value of *S/N* ratio of grade ith of every design variable of every response function.

(4) Quantify the range of each input variable

The following equation was exploited for determining the variety of each grade of each input variable:

$$r_{ij} = \max\left\{z_{i,j,1}, z_{i,j,2}, ..., z_{i,j,m}\right\} - \min\left\{z_{i,j,1}, z_{i,j,2}, ..., z_{i,j,m}\right\}, \tag{4.14}$$

where r_{ij} is the variety (max-min) of the *S/N* worth for every grade of every parameter, $j = 1, 2, ...q$, q is the quantities of input variables, $m = 1, 2, ...l$, l is the number of experimental grade of every input variable.

(5) Define the weight factor

The weight factor (WF) is computed by:

$$w_i = \frac{\sum_{j=1}^{q} r_{ij}}{\sum_{i=1}^{m_{OF}} \sum_{j=1}^{q} r_{ij}}, \tag{4.15}$$

where w_i ($w_i \geq 0$) is the WF of each response function ith.

m_{OF} is the quantities of attribute functions.

Normally, the whole of weight factors for whole attribute functions equals one, and the equation is expressed as:

$$\sum_{i=1}^{m_{OF}} w_i = 1, \tag{4.16}$$

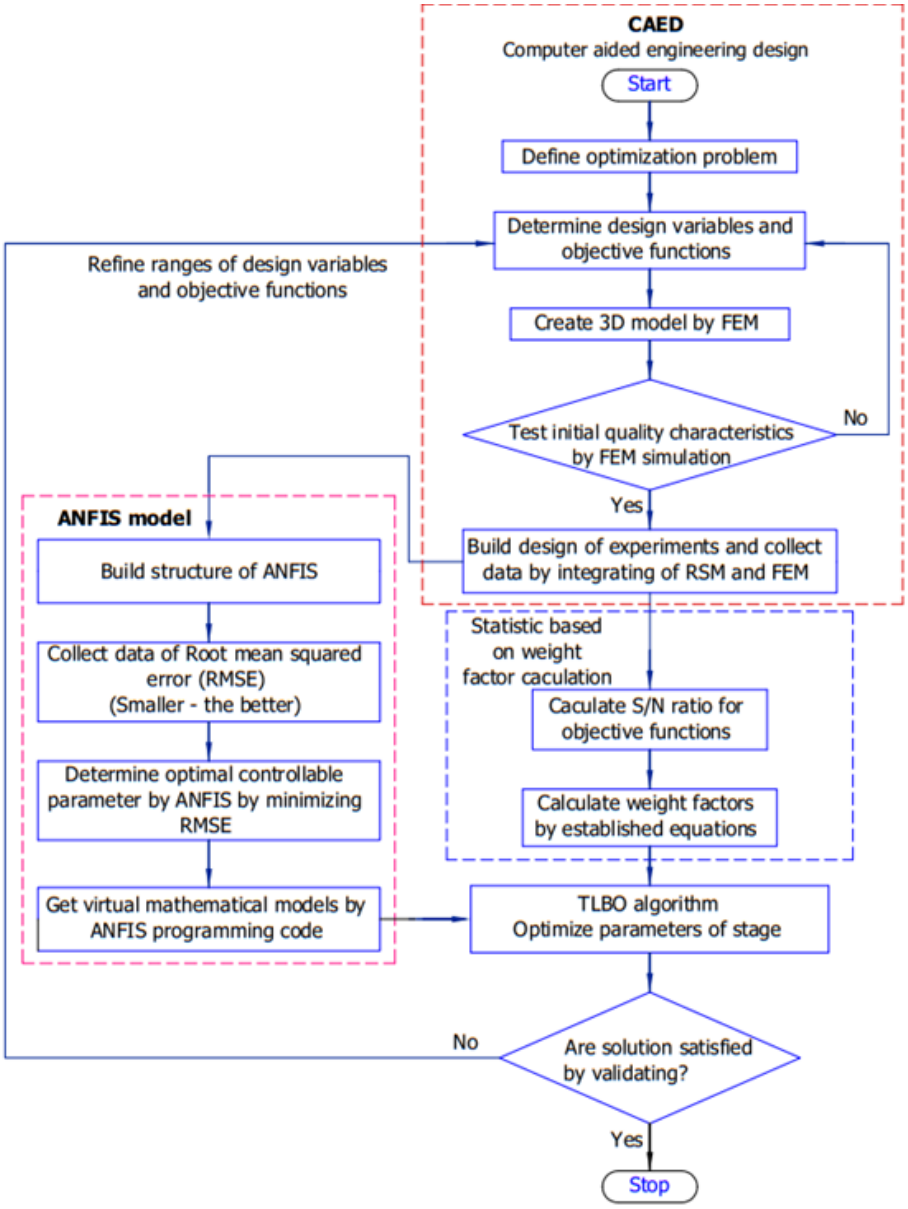

Figure 4.7 Multi-target optimization flowchart for 01 DOF flexure-based positioner.

Phase 3: Adaptive neuro-fuzzy inference system

To update the parameters, the ANFIS hybrid learning algorithm combines the gradient algorithm and the least squares method. A forward pass and a backward pass are exploited in the two-step process of studying and adjusting these adjustable parameters. In the forward pass, the preamble factors are affixed nodes, and node outputs are routed to layer 4. The least squares approach is used to define the resulting parameters. Furthermore, the four design parameters, which included the dimension of the first lever, the space between

two levers, and the thickness of the flexure-based joints, t,h,b,k had the greatest contribution to the two output features, namely the output deformation and the safety factor. As a result, the ANFIS structure for the offered positioner is expressed, as exhibited in Fig. 4.8.

ANFIS employs five network layers, as shown in Fig. 4.8, to operate the subsequent fuzzy inference stages: (1) fuzzy set database architecture, (2) fuzzy principle base architecture, (4) decision making, and (5) output defuzzification.

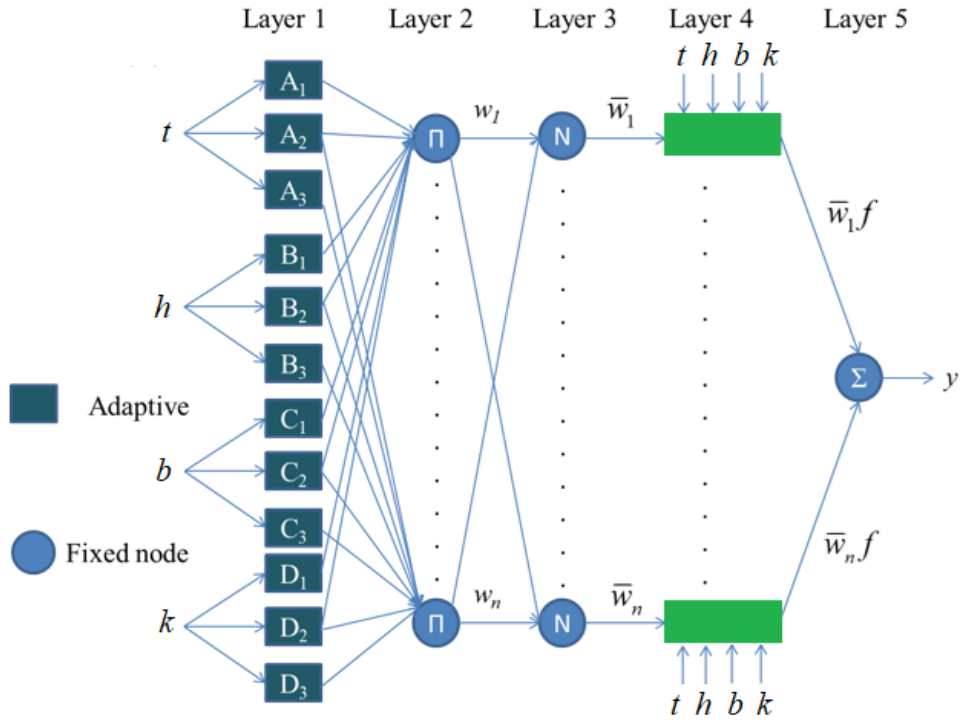

Figure 4.8. Suggested ANFIS structure for the 01-DOF flexure-based positioner.

4.2.5. Results and discussion

4.2.5.1. Gathering of numeric data

Initially, a 3D model of the offered positioner was created utilizing the FEM. Following that, a model was selected to analyze and optimize. Because there were four design variables, the CCD method created 25 experiments, which were generated by the RSM. The restrictions and inputting deformation of the suggested stage were later assigned. Finally, the values of two responses, as shown in Table 4.4, were attained by blending FEM and RSM.

Table 4.4. Counting the outcomes of experiments

No.	t (mm)	h (mm)	b (mm)	k (mm)	y_1 (mm)	y_2
1	1.0	20.75	50.5	0.705	1.8324	2.3562
2	0.9	20.75	50.5	0.705	1.8382	2.3633
3	1.1	20.75	50.5	0.705	1.8237	2.3359
4	1.0	19.0	50.5	0.705	1.5594	2.3628
5	1.0	22.5	50.5	0.705	1.7083	2.2432
6	1.0	20.75	48.0	0.705	1.949	2.3107
7	1.0	20.75	53.0	0.705	1.7089	2.3064
8	1.0	20.75	50.5	0.670	1.8473	2.4058
9	1.0	20.75	50.5	0.74	1.828	2.3224
10	0.9	19.0	48.0	0.670	1.5241	2.3751
11	1.1	19.0	48.0	0.670	1.5599	2.3374
12	0.9	22.5	48.0	0.670	1.7716	2.2326
13	1.1	22.5	48.0	0.670	1.7351	2.2422
14	0.9	19.0	53.0	0.670	1.5141	2.4065
15	1.1	19.0	53.0	0.670	1.5624	2.3441
16	0.9	22.5	53.0	0.670	1.7048	2.2387
17	1.1	22.5	53.0	0.670	1.6972	2.2104
18	0.9	19.0	48.0	0.740	1.5264	2.2961
19	1.1	19.0	48.0	0.740	1.6359	2.2674
20	0.9	22.5	48.0	0.740	1.731	2.1849
21	1.1	22.5	48.0	0.740	1.7701	2.1933
22	0.9	19.0	53.0	0.740	1.5835	2.2922
23	1.1	19.0	53.0	0.740	1.5844	2.2415
24	0.9	22.5	53.0	0.740	1.6912	2.1562
25	1.1	22.5	53.0	0.740	1.6867	2.1446

4.2.5.2. Weight factor quantification

The experimental data were later exploited for quantifying the *S/N* proportions exploiting Eq. (3.24), as demonstrated in Table 4.5. The *S/N* proportions were then standardized utilizing Eq. (4.12), as demonstrated in Table 4.6. In this Table, the standardized *S/N* proportions for safety factor (η_1) and the displacement (η_2) were Z_1, and Z_2, respectively.

Employing the Eqs. (4.14) and (4.15), the WF for the displacement and safety factor were calculated, as demonstrated in Tables 4.7 and 4.8, correspondingly. The attained values were 0.4416 for the WF of the safety factor and 0.5584 for the WF of displacement. The total value of both WFs was 1. The WF for individual feature was generally allocated a half, however, this worth was incorrect. Therefore, it is possible to result in an incorrect optimal resolution. Consequently, this chapter proposed to apply an efficient method for defining WFs.

Table 4.5 The *S/N* ratio values

No.	Safety factor (η_1)	Displacement (η_2)	No.	Safety factor (η_1)	Displacement (η_2)
1	5.26040566	7.444243	14	3.60309119	7.6277173
2	5.28785524	7.4703771	15	3.87584461	7.3995227
3	5.21906796	7.3690849	16	4.63346873	6.999918
4	3.8591506	7.4685392	17	4.59466046	6.8894174
5	4.65128282	7.0173599	18	3.67336715	7.219816
6	5.79623678	7.2748713	19	4.27513505	7.1105628
7	4.654333	7.2586926	20	4.76594136	6.7886313
8	5.3307486	7.6251904	21	4.95995604	6.8219608
9	5.23952383	7.3187405	22	3.99236135	7.2050502
10	3.66026926	7.513638	23	3.99729667	7.0107749
11	3.86193516	7.3746608	24	4.5638994	6.6737808
12	4.96731343	6.9762184	25	4.5407569	6.626926
13	4.7864902	7.013487			

Table 4.6 The standardized *S/N* proportions (z_i)

No.	Z_1 of η_1	Z_2 of η_2	No.	Z_1 of η_1	Z_2 of η_2
1	0.7557	0.8167	14	0.0000	1.0000
2	0.7682	0.8428	15	0.1244	0.7720
3	0.7368	0.7416	16	0.4698	0.3727
4	0.1168	0.8409	17	0.4521	0.2623
5	0.4779	0.3901	18	0.0320	0.5924

6	1.0000	0.6474	19	0.3064	0.4833
7	0.4793	0.6313	20	0.5302	0.1616
8	0.7878	0.9975	21	0.6187	0.1949
9	0.7462	0.6913	22	0.1775	0.5777
10	0.0261	0.8860	23	0.1797	0.3835
11	0.1180	0.7471	24	0.4381	0.0468
12	0.6220	0.3490	25	0.4275	0.0000
13	0.5396	0.3863			

Table 4.7 The safety factor's weight factor

Level	The median worth of standardized *S/N* proportions of every grade			
	A	*B*	*C*	*D*
Level 1	0.3404	0.1201	0.4215	0.3489
Level 2	0.6234	0.7534	0.6270	0.6192
Level 3	0.3893	0.5085	0.3054	0.3840
Range r_{ij}	0.2829	0.6333	0.3217	0.2704
The safety factor's weight factor: $w_1 = 0.4416$				

Table 4.8 The displacement's weight factor

Level	The median worth of each grade's standardized *S/N* proportions			
	A	*B*	*C*	*D*
Level 1	0.5366	0.6981	0.4942	0.6414
Level 2	0.7165	0.7669	0.7601	0.7015
Level 3	0.3893	0.2404	0.4496	0.3479
Range r_{ij}	0.3272	0.5265	0.3105	0.3536
The displacement's weight factor: $w_2 = 0.5584$				

4.2.5.3. Formulation of ANFIS model

ANFIS works similarly to a useful black box or alternative form in that it connects multiple inputs to the output. Key input parameters had a significant impact on both output characteristics in this chapter, and the arithmetic formulas that connected them were difficult to set up. As a result, the ANFIS technique was appropriate for the research.

In general, the ANFIS manageable features could be exploited as the default, but some were appropriate for the offered positioner and others were not. MFs include trimf, trapmf, gbellmf, gaussmf, sigmf, and pimf. This simulating process is time-consuming, but the results may not be trustworthy. To examine this influence and attain a favorable outcome, the appropriate MFs were identified to minimize the RMSE, exploited as an implementation condition of the ANFIS configuration. Furthermore, the training technique, quantity of MFs, and kinds of output MFs all have an impact on the ANFIS.

To optimize for the *RMSE*, the manageable features of the offered ANFIS were detected and classified into grades in reference to expertise and mechanical engineering skillfulness, as demonstrated in Table 4.9. The input MFs were partitioned into degrees of 3, 4, 5, and 6. Furthermore, trimf, trapmf, gbellmf, as well as gaussmf were exploited as degrees of the input MF types. The best learning strategy for the offered ANFIS configuration was divided into two categories: hybrid learning and backpropagation. Each type of output MFs separated into constant or linear worth was the final sensitive factor of ANFIS structure. It was challenging to determine the best structure for the ANFIS algorithm. Consequently, statistics and the TM were used to develop a suitable approach for defining these sensitive ANFIS parameters.

Table 4.9 The levels of controllable factors for the *RMSE*

Factors	Symbol	Level 1	Level 2	Level 3	Level 4
Quantity of input MFs	*A*	3	4	5	6
Types of input MFs	*B*	trimf	trapmf	gbellmf	gaussmf
Optimal training technique	*C*	hybrid	backpropa		
Types of output MFs	*D*	constant	linear		

To build the 16 different training experiments for the ANFIS, an orthogonal matrix design L_{16} (4^2 & 2^2) was created based on four parameters and their levels. The y-direction deformation data in Table 4.4 were used as training data, and the ANFIS

algorithm would be trained on these data. The *RMSE* values and S/N proportions were then quantified using the TM. Table 4.10 shows the outcomes of *RMSE* and S/N proportions for the safety factor, computed by the TM.

Table 4.10 L_{16} orthogonal array design for the safety factor's *RMSE*

No.	*A*	*B*	*C*	*D*	*RMSE for* y_1	*S/N* proportions for y_1 (dB)
1	3	trimf	hybrid	constant	1.6991E-06	115.3956
2	3	trapmf	hybrid	constant	1.6991E-06	115.3956
3	3	gbellmf	backproba	linear	0.97701	0.20202
4	3	gaussmf	backproba	linear	0.96576	0.302616
5	4	trimf	hybrid	linear	1.8333E-07	134.7353
6	4	trapmf	hybrid	linear	1.8128E-07	134.833
7	4	gbellmf	backproba	constant	1.6881	-4.54796
8	4	gaussmf	backproba	constant	1.6878	-4.54642
9	5	trimf	backproba	constant	1.6832	-4.52271
10	5	trapmf	backproba	constant	1.6831	-4.5222
11	5	gbellmf	hybrid	linear	7.1854E-06	102.871
12	5	gaussmf	hybrid	linear	2.4086E-06	112.3647
13	6	trimf	backproba	linear	1.097	-0.80413
14	6	trapmf	backproba	linear	1.0906	-0.75331
15	6	gbellmf	hybrid	constant	7.1147E-06	102.9569
16	6	gaussmf	hybrid	constant	6.5819E-06	103.633

To determine the optimized RMSE of the safety factor for the next ANFIS configuration, the average number of *S/N* ratios and the prime scheme of impacts of every parameter were resolved. The optimal parameters were determined using the results in Table 4.11 and Fig. 4.9 with four input MFs, trapmf, hybrid learning technique, and linear output MFs. Table 4.12 shows that the optimized *S/N* proportion of *RMSE* is 134.83, which was the highest worth in Table 4.10. It was demonstrated that a higher *S/N* proportion corresponds to a superior resolution.

Table 4.11 Average response for *S/N* proportions for the *RMSE of* the safety factor

Degreee	*A*	*B*	*C*	*D*
1	0.48569	0.66339	1.35907	0.84278
2	0.84398	0.66628	0.00000	0.51630
3	0.84158	0.69343		
4	0.54690	0.69505		
Delta	0.35828	0.03166	1.35907	0.32648
Rank	2	4	1	3

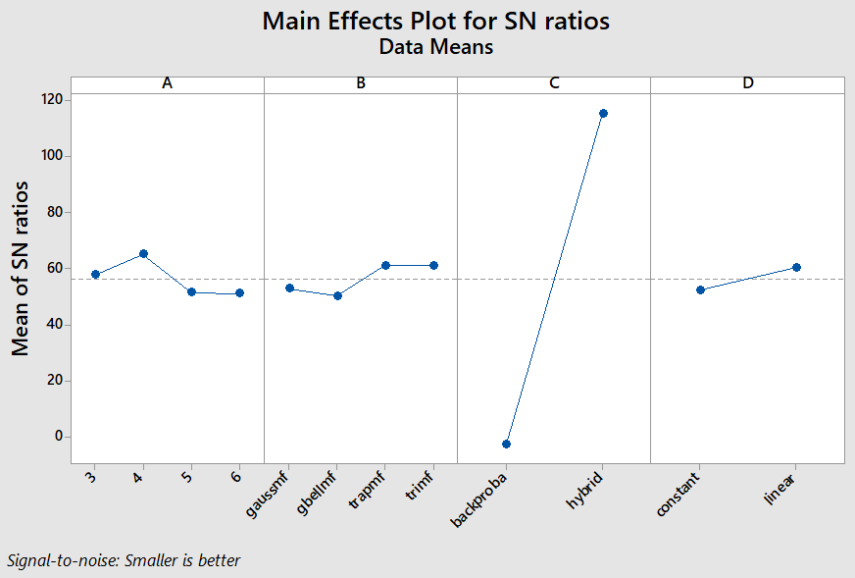

Figure 4.9. Response diagram of the *RSME* of the safety factor

Table 4.12 Prediction of optimal *RMSE of* of the safety factor

Settings				Optimized *S/N* ratio (dB) of *RMSE*
A	*B*	*C*	*D*	
4	trapmf	hybrid	linear	134.83

Correspondingly, the *RMSE* of displacement was optimized. Table 4.13 shows the *RMSE* outcomes for the displacement. The optimized manageable factors for further ANFIS configuration were detected at input MFs of 4, the trapmf, hybrid learning strategy, and linear output MFs in accordance with the average number for S/N proportions for the *RMSE* of safety factor as well as prime scheme of impacts in Table 4.14 and Fig. 4.10.

Table 4.15 also shows that the optimized *RMSE* is approximately 132.108, which is greater than the S/N ratio proportions in Table 4.13. This means that the best *RMSE* is used.

Table 4.13 L_{16} orthogonal array design for displacement *RMSE*

No.	*A*	*B*	*C*	*D*	*RMSE of* y_2	*S*/N proportions for y_2 (dB)
1	3	trimf	hybrid	constant	2.29E-06	112.8109
2	3	trapmf	hybrid	constant	2.29E-06	112.8109
3	3	gbellmf	backproba	linear	1.5641	-3.88529
4	3	gaussmf	backproba	linear	1.5527	-3.82175
5	4	trimf	hybrid	linear	2.3E-07	132.7613
6	4	trapmf	hybrid	linear	2.48E-07	132.1082
7	4	gbellmf	backproba	constant	2.2768	-7.1465
8	4	gaussmf	backproba	constant	2.2766	-7.14573
9	5	trimf	backproba	constant	2.2721	-7.12855
10	5	trapmf	backproba	constant	2.272	-7.12817
11	5	gbellmf	hybrid	linear	1.02E-05	99.82715
12	5	gaussmf	hybrid	linear	2.73E-06	111.2694
13	6	trimf	backproba	linear	1.6419	-4.30693
14	6	trapmf	backproba	linear	1.6341	-4.26557
15	6	gbellmf	hybrid	constant	9.25E-06	100.6794
16	6	gaussmf	hybrid	constant	8.63E-06	101.2775

Table 4.14 Mean response for *S/N* ratios for the displacement's *RMSE*

Level	*A*	*B*	*C*	*D*
1	0.77920	0.95733	1.93629	1.13719
2	1.13835	0.96023	0.00000	0.79910
3	1.13603	0.97653		
4	0.81900	0.97850		
Delta	0.35915	0.02117	1.93628	0.33809
Rank	2	4	1	3

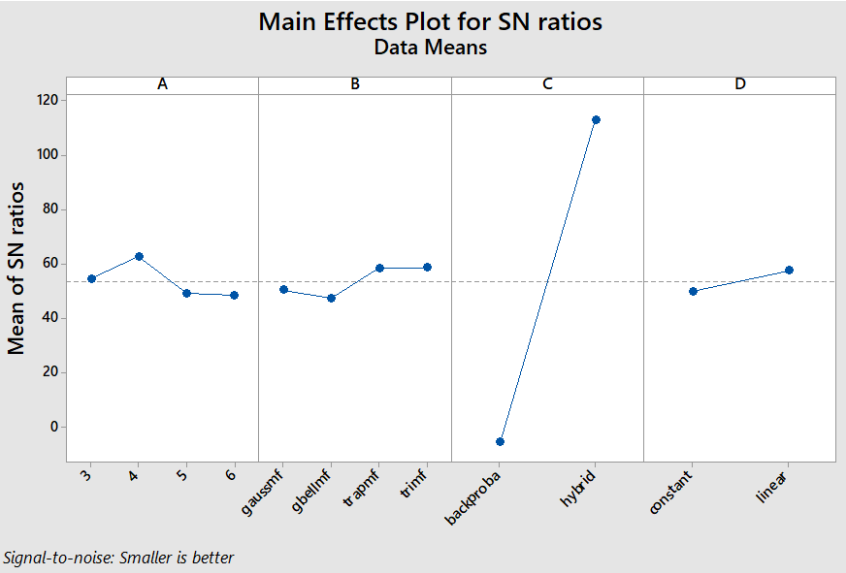

Figure 4.10. Response diagram of the *RSME* of the y-axis displacement

Table 4.15 Prediction of optimal *RMSE of* of the y-axis displacement

Settings				Optimized *S/N* proportion (dB) of *RMSE*
A	*B*	*C*	*D*	
4	trapmf	hybrid	linear	132.108

The ANFIS frequently employs standard MFs including Gaussian, sigmoidal, triangular, trapezoidal, as well as bell types. As a result, finding appropriate MFs is difficult. Based on the results on Tabs. 4.9-15, the trapezoidal was appropriate for an advanced ANFIS configuration for modeling the offered positioner in this study. The trapezoidal MF was presented as follows:

$$\mu_A(x,a,l,r,b)=\begin{cases}\dfrac{(x-a)}{(l-a)} & \mathrm{a}\le \mathrm{x}\le l\\ 1 & l<x<r\\ \dfrac{(x-b)}{(r-b)} & r\le x\le b\end{cases}, \tag{4.17}$$

in which μ_A represents the fuzzy set's MFs, a, b, l and r denote factors, while x denotes variable. The shape of trapezoidal MFs was provided in Fig. 4.11.

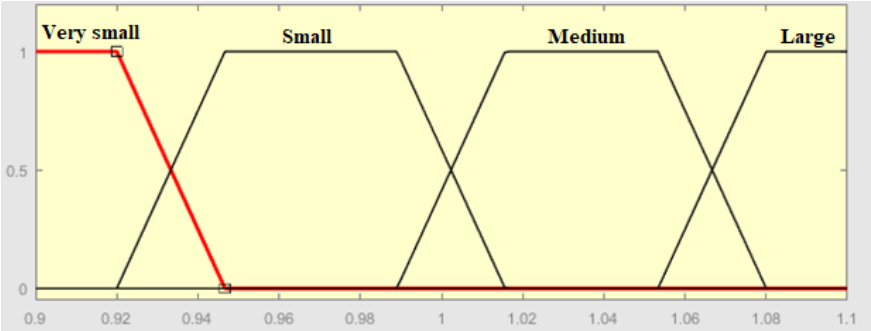

Figure 4.11. Shape of trapezoidal membership function

The improved ANFIS structure was generated subsequent to the appropriate manageable factors of ANFIS were identified by the TM, as shown in Fig. 4.12. As shown in Table 4.16, there were 1280 linear parameters. In contrast, there were 48 nonlinear parameters. Many parameters could not be determined accurately using an analytical approach. Finally, ANFIS was the best technique to use for the innovative positioner.

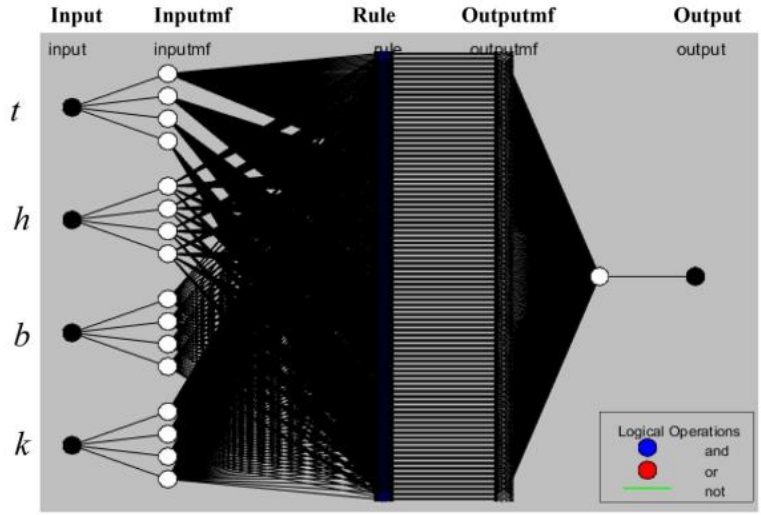

Figure 4.12. Configuration for enhanced ANFIS model

Table 4.16 ANFIS factors

Quantity of nodes	551
Quantity of linear factors	1280
Quantity of nonlinear factors	48
Totality of factors	1328
Quantity of training data pairs	25
Quantity of testing data pairs	0
Quantity of fuzzy principles	256

4.2.5.4. Optimization consequences

The developed positioner was optimized using the TLBO after obtaining the WFs and alternative models for both target formulas. Matlab 2017 was used to perform the optimization process. The TLBO's initial parameters included a population size of 30 and a tolerance of 10^{-6}. The optimized outcomes were discovered at t= 0.9 mm, h= 19 mm, b= 53 mm, k= 0.67 mm, y_1= 1.51409 and y_2= 2.4065 mm.

4.2.5.5. Sensitivity analysis

To determine the effect grade of variables on quality responses, a statistical technique was used. As shown in Figs. 4.13 and 4.14, factor t showed that in the range of 0.9 mm to 1 mm, this parameter caused y_1 and y_2 to gradually increase, but in the range of 1 mm to 1.1 m, it caused y_1 and y_2 to gradually decrease. Furthermore, factor h revealed that from 19 mm to 20.75 mm, it caused a sharp rise to y_1 and a slight rise to y_2, but from 20.75 mm to 22.5 mm, it caused a gradual decrease to y_1 and a sharp decrease to y_2.

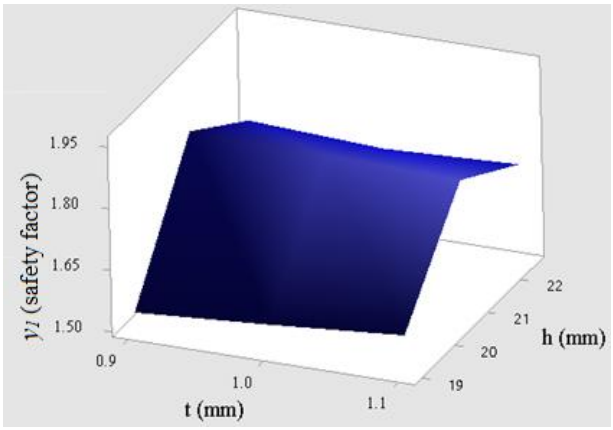

Figure 4.13. Graph for impact of t and h on y_1.

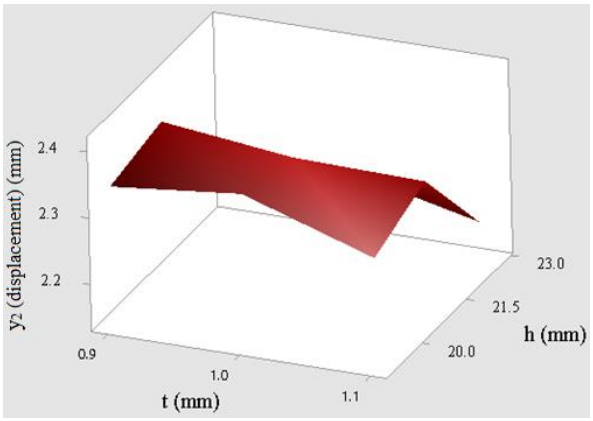

Figure 4.14. Graph for impact of t and h on y_2.

As illustrated in Figs. 4.15 and 4.16, parameter b caused a gradual increase in y_1 and y_2 from 48 mm to 50.5 mm, but a gradual decrease in y_1 and y_2 from 50.5 mm to 53 mm. Finally, factor D demonstrated that from 0.67 mm to 0.705 mm, it caused a gradual rise in y_1 and a slight rise in y_2, whereas from 0.6 mm to 0.7 mm, it caused a gradual decrease in both y_1 and y_2.

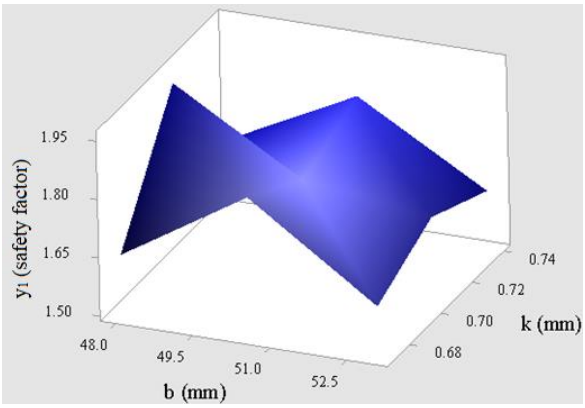

Figure 4.15. Graph for impact of *b* and *k* on y_1.

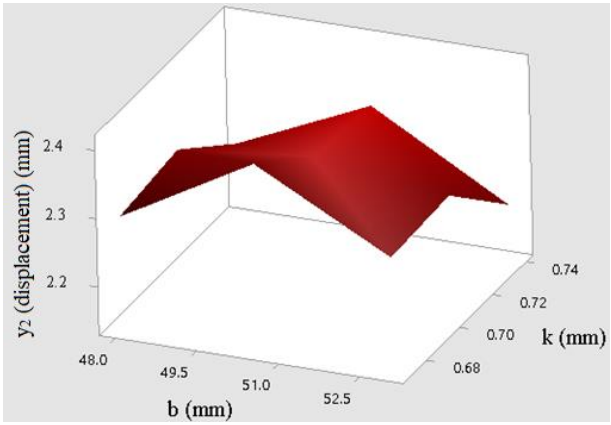

Figure 4.16. Graph for impact of *b* and *k* on y_2.

Finally, as shown in Fig. 4.17, the cumulative contribution of design variables was demonstrated. It reveals a range of rises and falls in individual parameter. As a result, the inventors could exert control over these variables in order to obtain the most suitable structure for the offered positioner.

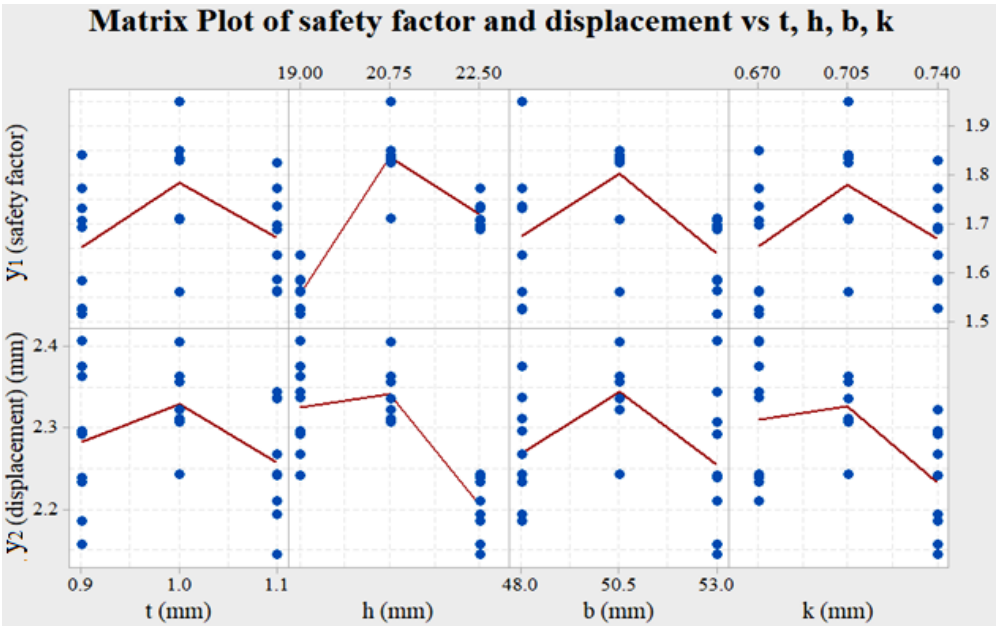

Figure 4.17. Diagram for sensitivity of each factor on the responses.

4.2.5.6. Experiment and verifications

Numerical simulations and experiments were implemented to confirm the optimized characteristics of the proposed positioner. Inventor software was used to create a 3D model with the optimized values (t = 0.9 mm, h = 19 mm, b = 53 mm, k = 0.67 mm) and then imported into ANSYS software to run simulations. Flexure hinge meshes were refined to

improve analysis quality accuracy. The prototype of the developed positioner was then manufactured using the optimal design variables via wire electrical discharged machining. The experiments were carried out as shown in Fig. 4.18: an input displacement was driven translational screw mechanism measured displacement by Digital dial indicator 1 (High precision 0.001mm, 543-390B, Mitutoyo Japan). Furthermore, the output displacement was measured using a Digital dial indicator 2 (High precision 0.001mm, 543-390B, Mitutoyo Japan) and a Digital dial indicator mounted on a Magnetic base (Mitutoyo Japan).

As shown in Tab. 4.17, the maximum y-axis deformation was 2.427 mm, and the minimum safety factor was 1.526. The FEA outcomes show that the difference between the predicted and optimized outcomes is small: the safety factor error is 0.786%. Moreover, the error for deformation between the optimized and FEA outcomes is minor at 0.824%, while the error for deformation between the experimental and FEA results is 7.581%. Therefore, the forecasted values and validations are in a good agreement. As a result, the offered combination optimization methodology was effective for optimizing the developed positioner. The experiment was repeated ten times, and the average values for the experiment outcomes were computed.

The positioning platform's strong capabilities are summed up as follows: It enabled an increase in working travel of about 2406 μm, resulting in a displacement amplification outcome of greater than 18 times. Accordingly, the working stroke of the original model outperformed that of the existing research, which emphasized the precision of the proposed theory.

Conclusions about experimental results can be highlighted below: (a) the developed system produced great displacement while maintaining a safety factor higher than 1.5 to enable the system to operate in an elastic state; and (b) the displacement outcome of the position model was 18 times higher than the input outcome.

Figure 4.19 depicts the input-output connections for FEA and experimental outcomes.

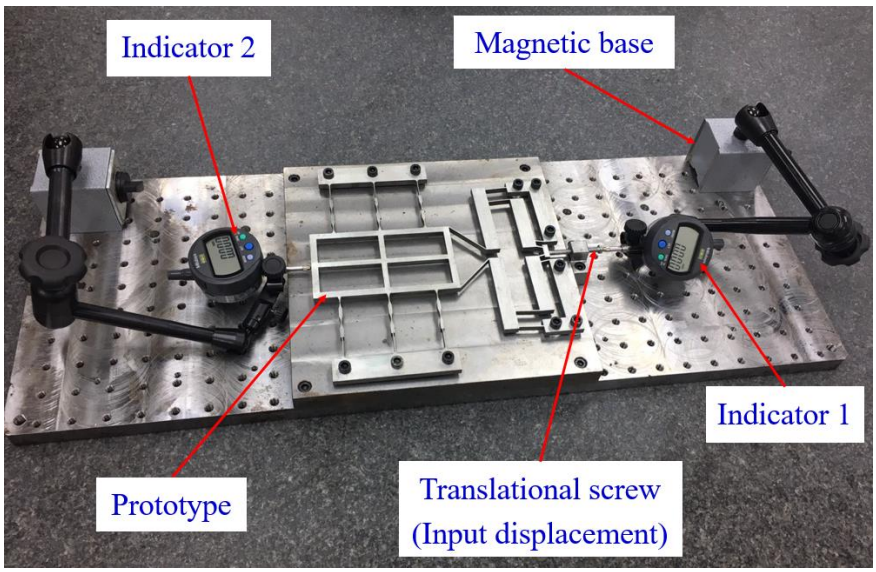

Figure 4.18. Experimental installation for the prototype.

Table 4.17 Comparison of optimization, FEA, and experimental outcomes

Responses	Optimal result	FEA result	Experimental result	Error (%) (between optimization and FEA results)	Error (%) (between FEA and experimental results)
y_1 (mm)	2.406	2.427	2.243	0.824	7.581
y_2	1.514	1.526	-	0.786	-

4.2.6. Attained consequences

For the quality characteristics of the compliant positioner, this chapter introduced an effective hybrid optimizing method. During nanoindentation testing, the developed positioner served the function of locating samples or drive the indenter. An amplifier with four-lever working operation and a beetle simulated model were incorporated into the developed positioner.

To achieve a linear displacement and reduction in parasitic motion, the positioner mimicked the biomechanical behavior of a beetle. To improve both the output displacement and the safety factor, key geometric factors of the developed positioner were put into an optimization procedure using a combination of the RSM, FEM, TM, enhanced ANFIS, and TLBO. The TM optimized the RMSE to determine controllable components for the ANFIS structure, followed by the calculation of the WFs of two responses through

several mathematical formulas. The results show that the WFs of safety factor and displacement were 0.4416 (44.16%) and 0.5584 (55.84%), correspondingly. To run the multi-target optimal trouble, the WF numbers were integrated into the TLBO algorithm. Sensitivity investigation as well as ANOVA were used to figure out the impacts as well as contributing degree of key variables to the above-mentioned excellent attributes.

The experimental outcomes also demonstrated that statistics for the optimized factors included t = 0.9 mm, h = 19 mm, b = 53 mm, and k = 0.67 mm while those of the optimized safety factor and displacement were 1.5141 and around 2.4065 mm, respectively. Furthermore, the divergence in the safety factor and output displacement between the optimal results and the FEA validations were 0.786% and 0.824%, correspondingly, as well as the percentage for divergence between the tested and predicted results was 7.581%. Therefore, it can be concluded that the developed integration method is efficient and practical to address the multi-target optimization problems for complicated designs.

4.3. Development and optimization of a new compliant Z-stage based on serial-parallel structure

4.3.1. Conceptual design

In order to develop one more a new compact 01-DOF positioner with large output displacement and small parasitic motion for indenting the specimens in nanoindentation testing device, the four-lever intensification structure, flexure-based joint shifted arrangement structure, zigzag-like compliant spring driving structure, and symmetrical six rectangular joints-based parallel driving structure were used to create this new positioner.

The second compact 01-DOF stage comprises a four-lever intensification structure module, a flexure-based joint shifted arrangement structure, a zigzag-inspired driving structure, and a parallel guiding mechanism based on symmetrical six leaves. Three main technical performances of the second compact 01-DOF stage are expressed as follows.

(i) The output displacement is more than 420 μm;

(ii) Parasitic motion error is lower than 0.04;

(iii) The safety factor is higher than 1.8.

Figure 1.5 depicts a possible application of the compliant Z-positioner provided in this study. The raw Z-positioner and XY-positioner, refined XY-positioner and Z-positioner make up this system. The raw XY-positioner is exploited for primary rough locating, the refined XY-positioner is exploited for fine locating the specimen, and the raw Z-positioner

is used to get the specimen close to the indenter. Eventually, the refined flexure-based Z-positioner is used for locating the indenter to attain the position of the specimen.

4.3.1.1 Combined structure to intensify the displacement

A lever configuration is advantageous for intensifying force and displacement numbers. Figure 4.19 illustrates the operation of a single lever structure for extending displacement in the Z-direction. Point O, in particular, demonstrates an affixed point that represents the lever's revolving point. Furthermore, M as well as N represent the input as well as output points, correspondingly.

The lever structure's operation is expressed below: when placing a deformation Δd_1 in the input point M, the lever will revolve the Z-direction with an angle. As a result, point N proceeds to N' which produces the output deformation Δd_2 in the y-direction. This structure, on the other hand, easily produces a high decoupling error. As a result, a structure to intensify the deformation with symmetrical multi-levers was developed to attain high output deformation and low parasitic motion. Later, to further reduce the decoupling error, a zigzag-inspired parallel driving structure was embedded into the intensification structure, as shown in Fig. 4.20 [132]. To reduce the decoupling error even further, a parallel driving structure relied on symmetrical six leaves was also embedded into the aforementioned structure. The intensification rate can be relatively attained according to the physical features of the lever mechanism:

$$r_{lever} = \Delta d_2 / \Delta d_1 = d_2 / d_1 \tag{4.18}$$

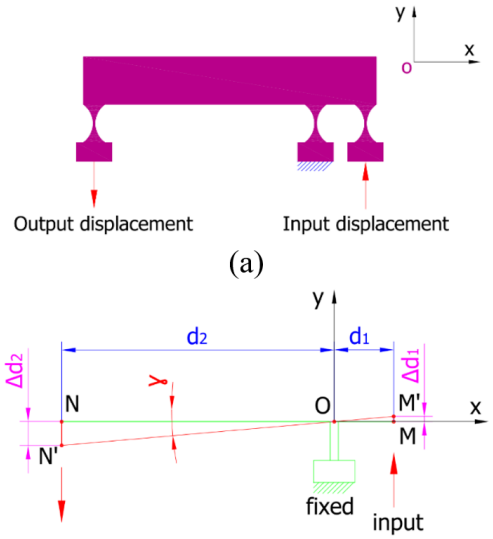

Figure 4.19. Plot for: (a) a lever structure, (b) operating principle of intensification rate.

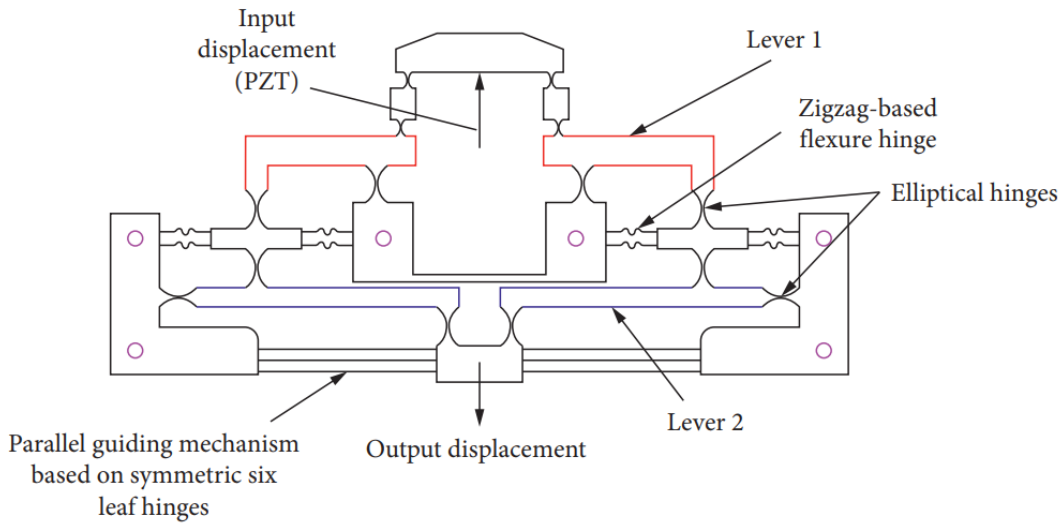

Figure 4.20. Offered integration intensification structure.

The multi-lever displacement intensification proportion equation is as follows:

$$r_{lever} = k \times d_2 / d_1 \tag{4.19}$$

k is supposed to be used to select 4 for a four-lever amplifier. Because of flexure hinge influences including thickness, rotary features of various joints, stroke deficiency, and the space between successive levers, Eq. (4.19) is improper to quantify intensification proportion. It is necessary to exploit FEM method to ensure accurate results. Similarly, to improve high stiffness and reduce decoupling error, a force-transmitting guiding structure inspired by zigzag springs and a parallel driving structure relied on symmetrical six leaves were combined to a Z-stage magnification mechanism.

4.3.1.2 Compliant Z-stage

Excellent properties of material Al-7075 include 503 MPa for great yield strength, 71700 MPa for Young's modulus, 2810 kg/m^3 for light density, 0.33 for Poisson's proportion. Therefore, this material was offered in this study to build the suggested Z-positioner. Furthermore, to exceed the performing movement of 40 μm, the Physik-instrument PEA actuator (P-225.x0) or translational crew was exploited to produce input deformation as well as linked to the offered integration intensification structure.

In particular, Fig. 4.21 [132] depicts the chief geometrical features of the offered compliant Z-positioner. The Z-positioner consists of the subsequent components: (i) The Z-positioner is located using fifteen affixed holes; (ii) the input displacement for the Z-

positioner can be generated using a PZT actuator or translational screw. In addition, to reduce decoupling error, the Z-positioner incorporates a force-transmitting driving structure inspired zigzag springs and a parallel driving structure.

The total dimension of the Z-positioner is approximately 301 mmx162 mmx16 mm. An elliptical joint is offered for exploiting in order to attain rotary center's precision and extreme output movement at the same time, especially when compared to common flexure hinges. Furthermore, to reduce decoupling error and reach flexibility, a parallel driving structure is integrated into the Z-positioner. Furthermore, by testing primary characteristics, an input displacement of 65 μm is offered in order to ensure the offered positioner working in proper strength conditions.

The proposed Z-positioner would be advanced in order to generate linear deformation for use in in-situ nano-indentation testing device. The geometric dimensions of the Z-positioner are shown in Table 4.18. As a result, some key stage factors must be considered in the optimization progression to improve the Z-output positioner's responses.

Table 4.18 Geometric factors of the compliant Z-stage

Factor	Worth	Factor	Worth	Factor	Worth	Unit
a	114.5	*j*	6.5	*i*	15	mm
b	301	*k*	3.5	*t*	15	mm
c	60	*m*	32.5	*u*	73	mm
d	20	*n*	16	*M*	$0.55 \leq M \leq 0.65$	mm
e	17	*o*	1	*N*	$0.6 \leq N \leq 0.9$	mm
f	21	*q*	8	*P*	$0.9 \leq P \leq 1.2$	mm
g	5	*r*	8	*K*	$49 \leq K \leq 53$	mm
h	22	*s*	35			

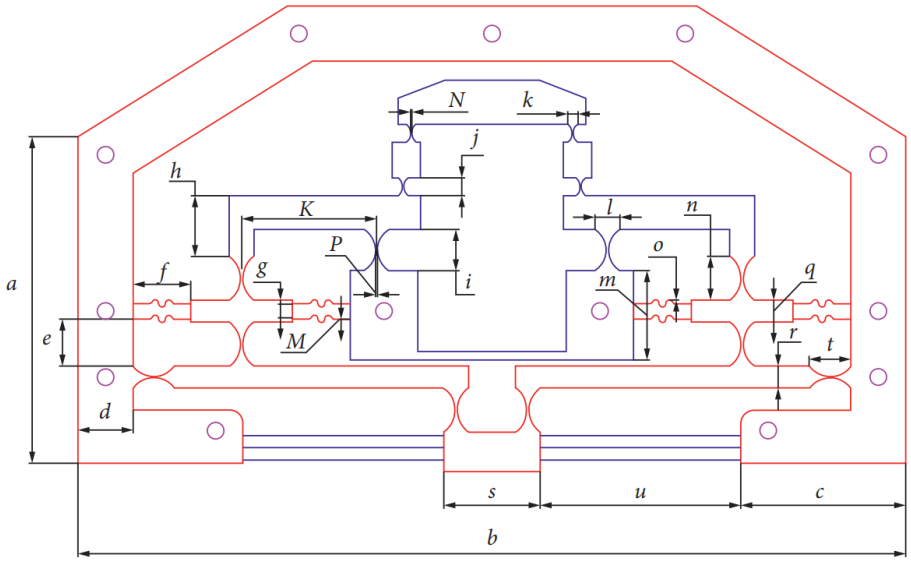

Figure 4.21. Z-positioner's key geometrical parameters.

4.3.2. Methodology

4.3.2.1. Formulation of optimal problem

The flexure-based Z-positioner should meet the following requirements: (i) a high safety factor (F_1) is required to ensure working in elastic limitation of the Z-positioner; (ii) a high Z-direction deformation (F_2) is required for expanding working stroke to locate and indent a specimen.

In reference to the WOA's global convergence quality characteristics, an incorporation methodology of the TM, RSM, weight factor quantifying technique in reference to signal to noise, and the WOA is offered for stabilizing between its responses and advancing the output characteristics of the Z-positioner. MATLAB 2017 would be used to implement a WOA algorithm. This combination methodology diagram, as demonstrated in Fig. 4.22, is offered. The Z-positioner's optimal issue is simplified as below.

Look for the chief variables: $\boldsymbol{X}$=[M,N,P,K]

Maximize $F_1(X)$:

$$F_1\left(M,\ N,\ P,\ K\right), \tag{4.20}$$

Maximize $F_2(X)$:

$$F_2\left(M,\ N,\ P,\ K\right), \tag{4.21}$$

Subject to constraints:

$$\sigma_{\max} \le \frac{\sigma_y}{n}, \tag{4.22}$$

$$\begin{cases} 0.55\text{mm} \le M \le 0.65\text{ mm}; 0.6\text{ mm} \le N \le 0.9\text{ mm} \\ 0.9\text{ mm} \le P \le 1.1\text{ mm}; 49\text{ mm} \le K \le 53\text{ mm} \end{cases}, \tag{4.23}$$

where F_1 as well as F_2 symbolize the safety factor as well as deformation, correspondingly. The four major parameters influential to the output features are *M, N, P* and *K*, which were then adopted as input design variables. *M, N, P, K* represent the thickness of the zigzag-inspired flexure springs, the thickness of the first elliptic hinge (first lever intensification structure), the thickness of the second elliptic joint (second lever intensification structure), and the space between the second elliptic joint center and the driving elliptic joint center, respectively. The bounds of design variables are determined based on WEDM fabrication technique and design targets.

Moreover, σ_y denotes offered material's yield strength, $\sigma_{\max}$ denotes the flexure positioner's maximum stress and *n* symbolizes the safety factor.

It is suggested that the safety factor should be higher than 1.8 to prevent plastic breakdowns in designing the Z-positioner.

The setting of restriction range for input variables with a selection of their smaller and higher bounds to guarantee a compact flexure mechanism is demonstrated in Eq. (4.23).

4.3.2.2. Hybrid approach

This study introduced a combination method [132] used for the optimization of the key geometric factors to enhance the offered positioner's output characteristics. Dang et al. [132] suggested hybrid approach for this study.

Firstly, the TM was adopted to set up beginning numerical experiments, followed by an employment of the RSM to generate regression functions for examining relations between input variables and two quality characteristics. The whole quadratic formula is proper for the developed Z-positioner, as shown in the equation below:

$$F_j = \beta_0 + \sum_{i=1}^{n} \beta_i \mathrm{x}_i + \sum_{i=1}^{n} \beta_{ij} \mathrm{x}^2{}_i + \sum_{i=1}^{n-1} \sum_{j=i+1}^{n} \beta_{ij} \mathrm{x}_i \mathrm{x}_j + \varepsilon_i \tag{4.24}$$

where the β_i *(i=0, 1, 2, …, n)* symbolizes unidentified regression cofficients, β_{ij} *(i<j)* represents association cofficients and $x_1, x_2, \ldots, x_n$ illustrate chains of *n* predictors connected with a feature variable F_j, and ε is a haphazard error.

In addition, ANOVA was used for identifying the percentage of significant contributions of each factor to the quality attributes.

Then, based on the signal to noise, weight factors were figured out for each response to enhance optimal calculation outcomes. Driven by the weight factor quantifying technique in Ref. [131], the WFs for every feature were precisely quantified. Each target was standardized within the range of 0 to 1 before the WFs were allocated to quality features.

In accordance with computed WFs, the total weighted target function was defined by:

$$f = w_1 f_1 + w_2 f_2, \tag{4.25}$$

where f_1, f_2 and f represent the safety factor, output displacement and the combined function, respectively while w_1 and w_2 symbolize the weight factor numbers of f_1 as well as f_2. The weight factor was calculated by equations shown in Eqs. (3.24, 4.12-4.16).

Derived from the regression functions associated with the weight factors, the WOA was conducted to identify the optimized parameters for solving the multi-target optimization with good convergence quality and low cost.

Whale optimization algorithm

Lastly, the WOA simulated the catching demeanors of humpback whales in searching for and attacking preys, given the bubble-net feeding manner was developed by Mirjalili and Lewis [133]. There are two major phases in the WOA: (i) Exploitation phase: encompassing quarry and helix acquainting whereabouts are conducted, (ii) Exploration phase: researching for a prey is extraordinarily performed. Further information is provided in Ref. [133]. The numerical formula for each phase is presented as follows.

(i) **Exploitation phase (**Bubble Net Attacking Method)

Two steps should be completed to build up arithmetic formulas for the bubble net manners of humpback whales. Descriptions of these both steps are provided below.

(a) **Surrounding quarry**

When finding out the quarry's whereabouts, humpback whales encircle the target. As it is impossible to define the circumstance of the optimal model in the inspection region, the WOA assumes that the existing best potential solution is the target quarry or is the approaching target. Then, the biggest inspection agent is identified and other inspection

agents may attempt to adjust their conditions close to the greatest investigation agent. The formulations of statistical equations are presented below.

$$\vec{D} = \left| \vec{C} . \vec{X}^{*}(t) - \vec{X}(t) \right| \tag{4.26}$$

$$\vec{X}(t+1) = \vec{X}^{*}(t) - \vec{A} . \vec{D} \tag{4.27}$$

where *t* symbolizes the present repetition, X^{*} represents the whereabout vector of the greatest gained resolution, X denotes the location vector, | | is the absolute worth. X^{*} must be acquainted in every repetition if it has a superior outcome. The A and C are coefficient vectors calculated in the following formula:

$$\vec{A} = 2\vec{a} \cdot \vec{r} - \vec{a} \tag{4.28}$$

$$\vec{C} = 2 . \vec{r} \tag{4.29}$$

where $\vec{a}$ drops in a variety [2,0] through reiterations and $\vec{r}$ denotes a haphazard vector in a variety [0,1].

For an employment of shrinking, the value of $\vec{a}$ is reduced in the Eq. (4.28) and the alternation variability of $\vec{A}$ can be declined by $\vec{a}$. Moreover, $\vec{A}$ represents an indiscriminate value in the interval from –a to a where a is reduced in [2,0] over the course of reiterations.

Setting indiscriminate values for $\vec{A}$ varies in range [-1, 1], the updated position of an inquiry agent is determined anywhere from the primary spot of the agent to the locality of the existing giant agent.

(b) ***Helix apprising whereabout***

When the computation of the width between the whale and prey at their matching whereabouts (X,Y) and (X^{*}, Y^{*}), a coiled model for locations of whales and preys to mimic the coiled curve describing humpback whales' movement is expressed by:

$$\vec{X}(t+1) = \vec{D'} \cdot e^{bm} \cdot \cos(2\pi l) + \vec{X}^{*}(t) \tag{4.30}$$

in which $\vec{D}' = \left| \vec{X}^*(t) - \vec{X}(t) \right|$ displays the space between the i[th] whale and the objective, b denotes an unchangeable value for defining the model of the logarithmic coil, m represents a haphazard digit in a variety [-1, 1]. This behavior in WOA demonstrates changes in whereabouts of whales in optimization procedure. For a simultaneous formulation of this behavior, there is a 50% probability for desiring among the shrinking encompassing process and the coiled form. A statistical formula to update the location of whales is presented below.

$$\vec{X}(t+1) = \begin{cases} \vec{X}^*(t) - \vec{A}.\vec{D} & if \quad p < 0.5 \\ \vec{D}' \cdot e^{bl} \cdot \cos(2\pi l) + \vec{X}^*(t) & if \quad p < 0.5 \end{cases} \tag{4.31}$$

in which *p* symbolizes the contingent worth in a variety [0, 1].

(ii) **Exploration phase (Investigation for quarry)**

It is possible to exploit a similar approach in reference to the difference of $\vec{A}$ vector to investigate the victim (exploration). In reality, humpback whales do the searching arbitrarily based on the position of each other. Accordingly, $\vec{A}$ can be used as the indiscriminate values greater than 1 or less than -1 to remotely track the investigation agent's route through a reference whale. Herein, compared to the exploitation phase, the location of an inquiry agent in the exploration phase is monitored by the use of an indiscriminately selected inquiry agent in relation to the greatest realized agent. This mechanism and $|\vec{A}| > 1$ emphasize exploration and allow the WOA algorithm to carry out a global investigation. The arithmetical formula is formed as follows.

$$\vec{D} = \left| \vec{C} \cdot \overrightarrow{X_{rand}} - \vec{X} \right| \tag{4.32}$$

$$\vec{X}(t+1) = \overrightarrow{X_{rand}} - \vec{A} \cdot \vec{D} \tag{4.33}$$

where $\overrightarrow{X_{rand}}$ denotes an indiscriminate whereabout vector (an arbitrary whale) preferred based on current population.

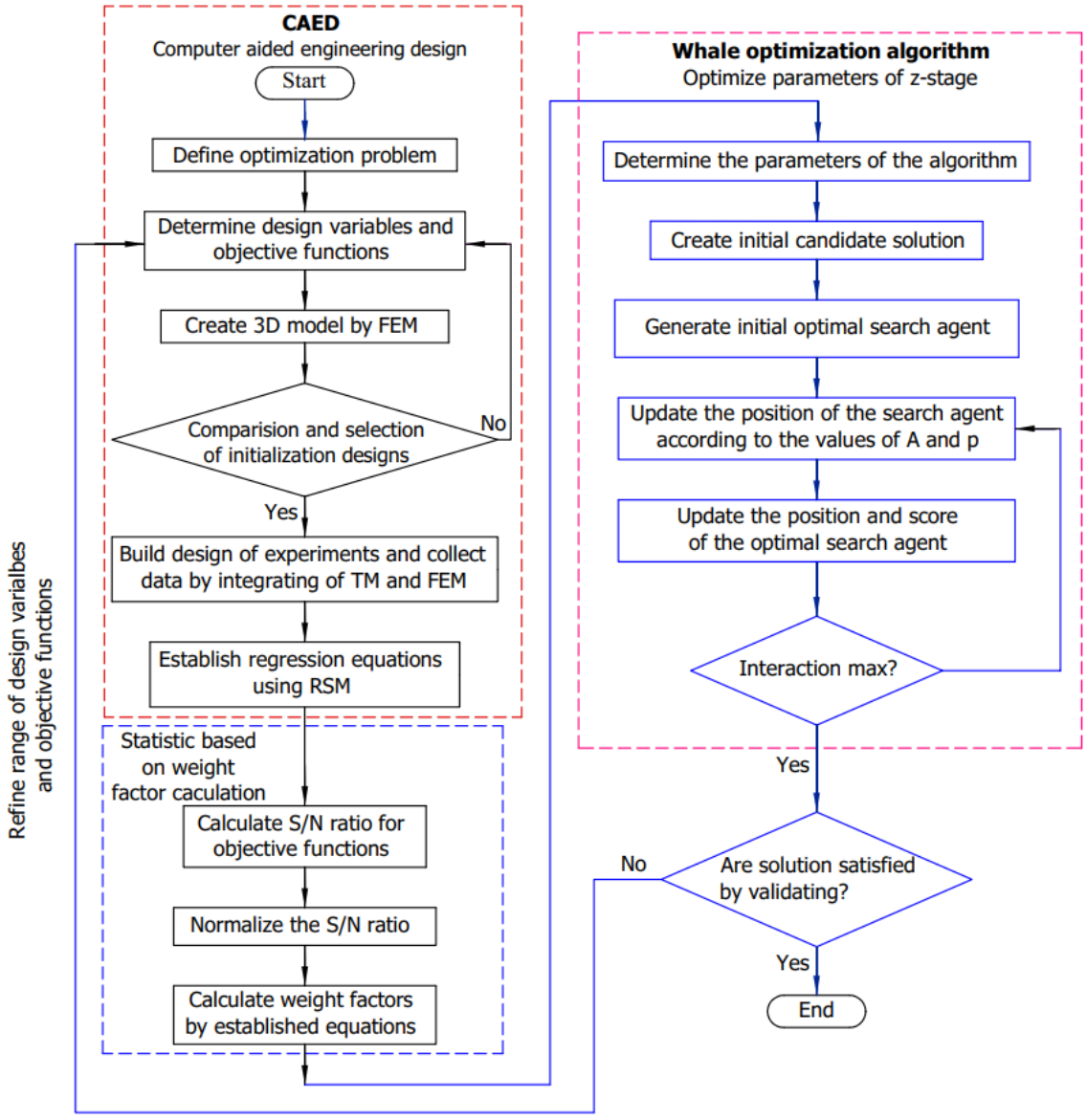

Figure 4.22. Flowchart to illustrate the suggested optimal method.

The whale optimization algorithm procedure

The first step in developing the WOA algorithm is establishing indiscriminate solutions. In practice, inquiry agents inform their whereabouts by using an indiscriminately selected inquiry agent or the best solution attained for each reiteration. The A parameter is decreased in range [2,0] in order to support both the exploration and exploitation. An indiscriminate inquiry agent is favored when $|\vec{A}| > 1$, while the best solution is preferred when $|\vec{A}| < 1$ for announcing the place of the inquiry agents. Based on the p worth, there is a probability of 50% to choose one of the two processes.

As a result, if the worth is greater than 0.5, the examination individuals change their places utilizing Eq. (4.30), or otherwise adopting Eq. (4.27). The WOA can exchange

between a helix and rounded stroke. Finally, the WOA algorithm stops by the carrying out of a stopping criterion. From a theoretical perspective, it is reasonable to regard the global WOA algorithm thanks to its advantages of exploration and exploitation abilities. Furthermore, the suggested hyper-cube configuration identifies an investigation region within the best resolution area and allows other inquiry agents to make use of the best present indicator. Informed variation of the hunt vector A enables the WOA algorithm to examine the travel of exploration and exploitation with ease: by reducing A, many reiterations are assigned to exploration ($|A| \geq 1$) while the rest is for exploitation ($|A| < 1$). Especially, the novel algorithm includes only major internal modified factors (A and C). More information is provided in Ref. [133].

4.3.3. Results and discussion

4.3.3.1. Evaluation of initial features and parasitic motion error

Initially, a flexure Z-positioner was created in the Inventor software, followed by exporting the Z-direction output deformation and safety factor of offered Z-positioner through the ANSYS software. To be specific, an automatic meshing method for the flexure hinges were applied to attain precise analysis outcomes, as illustrated in Fig. 4.23.

To examine the safety factor, the parasitic motion error and intensification proportionality presented in Table 4.20, the output displacement of Z-positioner was investigated by varying the input displacement within the range of 5 μm to 60 μm.

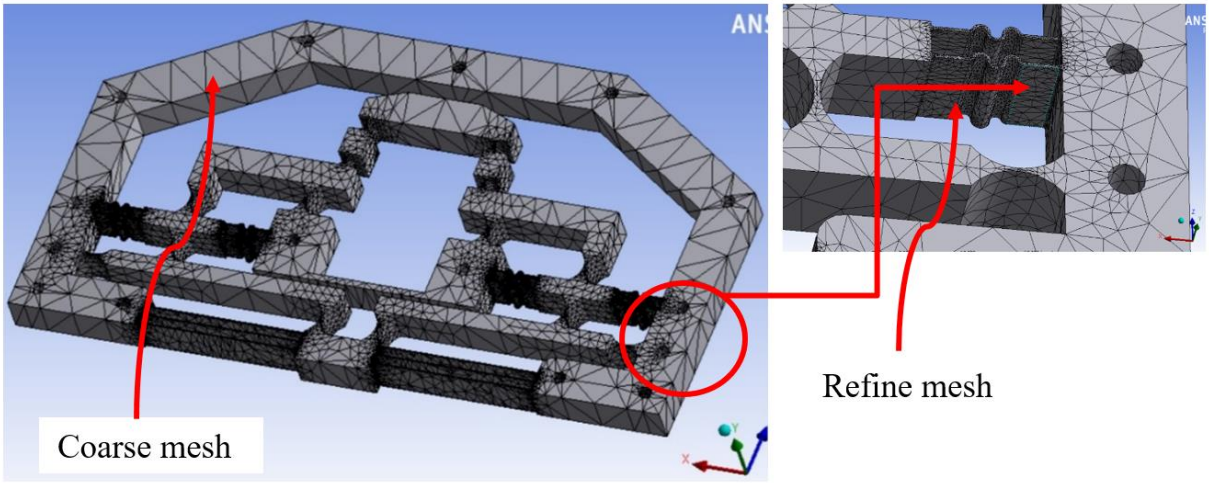

Figure 4.23. Mesh formulation of offered Z-positioner.

So as to assess the suggested Z-stage's strength conditions, the input movement was altered in a range [65 μm, 120 μm] with a varying step of 5 μm. Additionally, the FEA can

perform an exporting activity of the matching output deformation. The results in Table 4. 19 indicated that the output displacement has a value of 714.5 μm when the input displacement is 120 μm. In this case, the safety factor is under 1 which can cause a damage to the stage. To ensure the safety operation, the maximum input should be lower than 120 μm. Another case, the input displacement was equal to 115 μm, the resulted stress was about 491.89 MPa while safety factor was 1.023. Particularly, to maintain a proper operation of the positioner, a safety factor of greater than 1.8 would be required. Moreover, the input deformation would be offered from 5 μm to 65 μm to evaluate the output displacement and the parasitic motion error was calculated by using Eq. (4.36). The outcomes revealed that the parasitic motion error was quite small with 0.039 %, as given in Table 4.20. These statistics proved the precision of the suggested Z-positioner. Additionally, it was found that the safety factor was 1.8092, exaggeration fraction was 5.95. However, as no results could satisfy the exaggeration ration requirements (ER of more than 6), it is necessary to conduct an optimal procedure to enhance the quality attributes.

Table 4.19 Output deformation, exaggeration ratio, safety factor, and stress

Input displacement (μm)	Output deformation (μm)	Exaggeration ratio	Safety factor	Equivalent stress (MPa)
65	387	5.95	1.8092	278.02
70	416.77	5.95	1.68	299.41
75	446.54	5.95	1.568	320.8
80	476.31	5.95	1.47	342.18
85	506.07	5.95	1.3835	363.57
90	535.84	5.95	1.3066	384.96
95	565.61	5.95	1.2379	406.34
100	595.38	5.95	1.176	427.73
105	625.15	5.95	1.12	449.12
110	654.92	5.95	1.0691	470.5
115	684.69	5.95	1.0226	491.89
120	714.46	5.95	0.97998	513.28

It can be seen that when the Z-positioner moved along the Z-axis, the movement of X-axis also happened. This unanticipated movement caused the parasitic motion error. Figures in Table 4.20 indicate that the parasitic motion error was extremely small with 0.0389 % (< 1 %); thus, did not significantly affect the output displacement accuracy. The parasitic motion error is computed as follows.

$$e_d = \frac{x_o}{z_o} 100\% \tag{4.34}$$

where e_d denotes the parasitic motion error, while x_o as well as z_o symbolize the x-axis output displacement and the z-axis output displacement, respectively.

Table 4.20 Outcomes of output displacement and parasitic motion error

Input deformation (μm)	Output z-direction displacement (μm)	Output x-direction displacement (μm)	Parasitic motion error (%)	Enlargement ratio
5	29.77	0.0116	0.0389	5.95
10	59.54	0.0232	0.0389	5.95
15	89.31	0.0348	0.0389	5.95
20	119.08	0.0464	0.0389	5.95
25	148.85	0.0579	0.0389	5.95
30	178.61	0.0695	0.0389	5.95
35	208.38	0.0811	0.0389	5.95
40	238.15	0.0927	0.0389	5.95
45	267.92	0.1043	0.0389	5.95
50	297.69	0.1159	0.0389	5.95
55	327.46	0.1275	0.0389	5.95
60	357.23	0.1391	0.0389	5.95

4.3.3.2. Orthogonal array experiment and mathematical model

Derived from the expertise and manufacturing capability, each factor was divided into three degrees in Table 4.21. The L_9 (3^4) orthogonal array was employed to set up starting numbers of experiments. This study applied the FEM in ANSYS software to compute the safety

factor (F_1) as well as Z-axis displacement (F_2). Details about numerical investigating outcomes are presented in Table 4.22.

Table 4.21 Input dimensions and their levels (unit: mm)

Factors	Variation	Level 1	Level 2	Level 3
M	0.55-0.65	0.55	0.6	0.65
N	0.6-0.9	0.6	0.75	0.9
P	0.9-1.2	0.9	1.05	1.2
K	49-53	49	51	53

Table 4.22 Numeric outcomes

No.	*M*	*N*	*P*	*K*	F_1	F_2 (μm)
1	0.55	0.6	0.9	49	2.1846	423.89
2	0.55	0.75	1.05	51	1.8968	392.88
3	0.55	0.9	1.2	53	1.8956	253.77
4	0.6	0.6	1.05	53	1.615	221.14
5	0.6	0.75	1.2	49	2.1052	401.83
6	0.6	0.9	0.9	51	1.944	370.74
7	0.65	0.6	1.2	51	1.6641	309.1
8	0.65	0.75	0.9	53	1.7837	211.66
9	0.65	0.9	1.05	49	2.2807	381.09

The establishment of regression equations was displayed below:

$$F_1 = 109.2 - 31.00*M + 0.5896*N - 0.1536*P - 3.740*K + 25.14*M*M + 0.09333*N*N - 0.05778*P*P + 0.03562*K*K \quad (4.35)$$

$$F_2 = -25134 + 640.1*M + 646.2*N + 252.9*P + 1028*K - 1002*M*M - 392.7*N*N - 142.4*P*P - 10.50*K*K \quad (4.36)$$

Tables 4.36 and 4.37 present ANOVA outcomes of the safety factor and output deformation. The computation was performed at 5% significance degree as well as 95% assurance degree.

Table 4.23 revealed that the percentage for the contribution of *K* to the safety factor F_1 was greatest, at 84.34%, and the impact rates for *N* and *K* - *K* relation were relatively high,

at 17.43% and 9.85% correspondingly. However, the percentages for *M*, *P* and *M* - *M* relation were quite small, at 2.50%, 2.47% and 1.92%, correspondingly. Therefore, it is essential to strictly control parameters *K* and *N* to improve the value of F_1.

Table 4.24 indicated that the percentage for the contribution of *K* to the safety factor F_2 was highest, at 83.07%, and the impact rates for *M* and *K* - *K* relation were relatively high, 8.73% and 6.50% correspondingly. However, the percentages for *N*, *P* as well as the interactions between *N* and *N*, *P* and *P*, *M* and *M* were quite small, at 0.81%, 0.53%, 0.29%, 0.04% and 0.02%, correspondingly. As a result, it is important to effectively monitor factors *K* and *M* to enhance the value of F_1. Moreover, the impact of error for F_1 and F_2 was at 0%.

Table 4.23 ANOVA outcomes for F_1

Source	DF	Seq SS	Influence	Adj SS	Adj MS	P-Worth
Pattern	8	0.412320	100.00%	0.412320	0.051540	Considerable
Linear	4	0.363795	88.23%	0.363795	0.090949	Considerable
M	1	0.010292	2.50%	0.010292	0.010292	Considerable
N	1	0.071854	17.43%	0.071854	0.071854	Considerable
P	1	0.010201	2.47%	0.010201	0.010201	Considerable
K	1	0.271448	65.83%	0.271448	0.271448	Considerable
Square	4	0.048525	11.77%	0.048525	0.012131	Considerable
*M***M*	1	0.007900	1.92%	0.007900	0.007900	Considerable
*N***N*	1	0.000009	0.00%	0.000009	0.000009	Considerable
*P***P*	1	0.000003	0.00%	0.000003	0.000003	Considerable
*K***K*	1	0.040613	9.85%	0.040613	0.040613	Considerable
Error	0	-	-	-	-	
Total	8	0.412320	100.00%			

Table 4.24 ANOVA outcomes for F_2

Source	DF	Seq SS	Influence	Adj SS	Adj MS	P-Worth
Pattern	8	54299.7	100.00%	54299.7	6787.5	Considerable
Linear	4	50580.8	93.15%	50580.8	12645.2	Considerable
M	1	4742.7	8.73%	4742.7	4742.7	Considerable
N	1	441.5	0.81%	441.5	441.5	Considerable
P	1	288.3	0.53%	288.3	288.3	Considerable
K	1	45108.3	83.07%	45108.3	45108.3	Considerable
Square	4	3718.9	6.85%	3718.9	929.7	Considerable
*M*M*	1	12.6	0.02%	12.6	12.6	Considerable
*N*N*	1	156.1	0.29%	156.1	156.1	Considerable
*P*P*	1	20.5	0.04%	20.5	20.5	Considerable
*K*K*	1	3529.7	6.50%	3529.7	3529.7	Considerable
Error	0	-	-	-	-	
Total	8	54299.7	100.00%			

4.3.3.3. Sensitivity analysis

Statistic method was applied to determine the contribution grade of chief input parameters to the quality responses. Within the range [0.55, 0.65], parameter *M* produced a minor decrease of F_1 as well as F_2, as illustrated in Fig. 4.24. Meanwhile, within the range [0.65, 0.75], factor *N* contributed to a stable rise of F_1 as well as a steady instability of F_2.

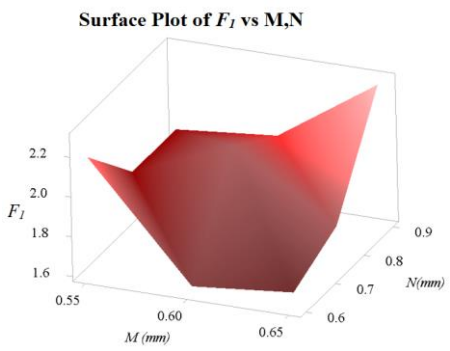

(a)

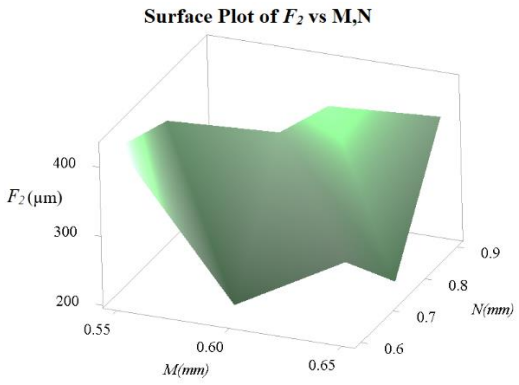

(b)

Figure 4.24. Plot for impacts of *M* and *N* vs. (a) safety factor; (b) the output displacement.

Besides, from 0.9 mm to 1.2 mm, parameter *P* produced a gradual fall of F_1 and F_2, as exhibited in Fig. 4.25. Additionally, from 50 mm to 51.5 mm, parameter *K* contributed to a dramatic decrease of F_1 and a slow drop of F_2, while in the range [51.5, 53], it produced a gentle drop of F_1 and a significant decrease of F_2.

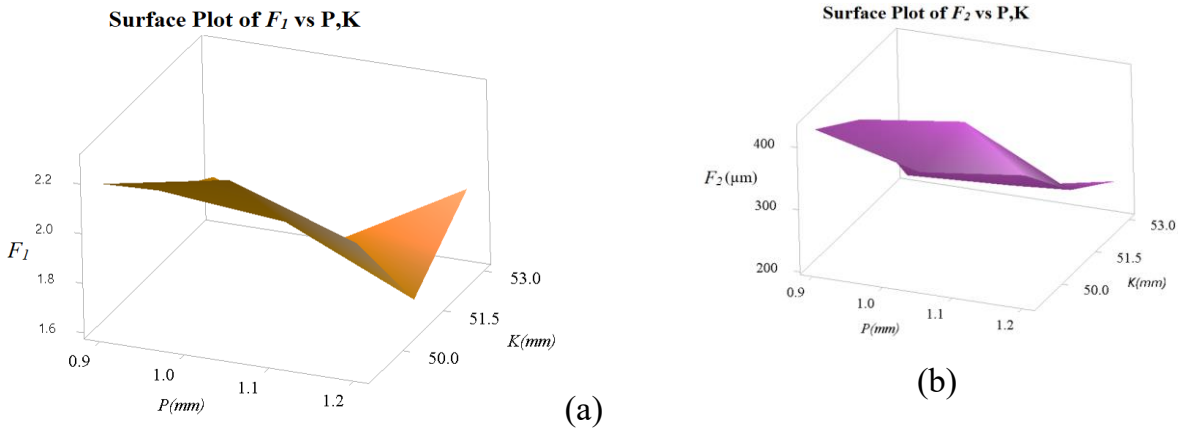

(a) (b)

Figure 4.25. Plot for impacts of *P* and *K* vs. (a) safety factor; (b) the output displacement.

To conclude, Fig. 4.26 illustrated all types of input variables' impacts on the output responses, with descriptions of the increase and decrease in each factor. These outcomes can serve as a reference for adjusting the main parameters to attain the most successful structure of the Z-positioner.

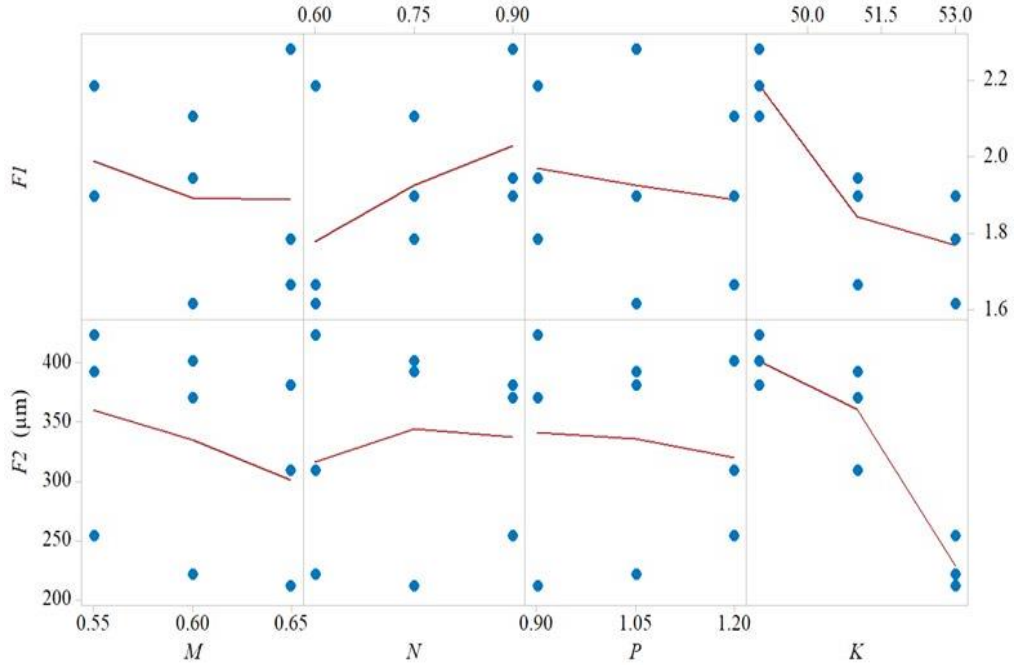

Figure 4.26. Responsiveness of key variables on both output features.

4.3.3.4. Calculation of weight factor

Generally, the totality of the two WFs equals 01. An allocation of 0.5 is normally given to the weight factor of each characteristic; but this value may not be accurate which would lead to the imprecision in the optimal process. Therefore, this section aims to develop a proper approach for the specification of the weight factors.

After the collected statistics were converted into signal to noise scales using Eq. (3.24), as shown in Table 4.25, these ratios were standardized applying Eq. (4.12), as presented in Table 4.26. Particularly, the standardized signal to noise scales for safety factor (η_1) and the deformation (η_2) signified z_1, as well as z_2, respectively. Exploiting the Eqs. (4.29) and 4.30, the computation of the WFs for safety factor and deformation was carried out, as demonstrated in Tables 4.27 and 4.28. Next, the computed WFs for every characteristic were assigned to optimization processes in the WOA.

Table 4.25 The inquiry outcomes and *S/N* scales

No.	F_1	F_2 *(mm)*	η_1 of F_1 (dB)	η_2 of F_2 (dB)
1	2.185	423.9	6.78743859	52.5450634
2	1.897	392.9	5.56043082	51.8851984
3	1.896	253.8	5.55493400	48.0888056
4	1.62	221.1	4.16345053	46.8933461
5	2.105	401.8	6.46586723	52.0808472
6	1.94	370.7	5.77392521	51.3813889
7	1.664	309.1	4.42358841	49.801980
8	1.784	211.7	5.02643625	46.5127758
9	2.281	381.1	7.16136325	51.6205511

Table 4.26 Values of standardized *S/N* scales (z_i)

S/N scales		Standardized *S/N* scales (z_i)	
η_1 (dB)	η_2 (dB)	z_1 of η_1	z_2 of η_2
6.78743859	52.5450634	0.875	1.000
5.56043082	51.8851984	0.466	0.891
5.55493400	48.0888056	0.464	0.261

4.16345053	46.8933461	0.000	0.063
6.46586723	52.0808472	0.768	0.923
5.77392521	51.3813889	0.537	0.807
4.42358841	49.801980	0.087	0.545
5.02643624	46.5127758	0.288	0.000
7.16136325	51.6205510	1.000	0.847

Table 4.27 Weight factor of F_1

Degree	Median worth of **s**tandardized *S/N* scales at every degree			
	M	*N*	*P*	*K*
Degree 1	0.6018	0.3207	0.5668	0.8811
Degree 2	0.4351	0.5073	0.4887	0.3633
Degree 3	0.4582	0.6671	0.4396	0.2507
Variation r_{ij}	0.1667	0.3464	0.1271	0.6304
WF of F_1: w_1 = 0.5150				

Table 4.28 Weight factor for F_2

Degree	The median value of standardized *S/N* scales at each level			
	M	*N*	*P*	*K*
Degree 1	0.7173	0.5361	0.6024	0.9233
Degree 2	0.5977	0.6046	0.6001	0.7477
Degree 3	0.4640	0.6384	0.5765	0.1081
Variation r_{ij}	0.2533	0.1022	0.0258	0.8151
WF of F_2: w_2 = 0.485				

4.3.3.5. Optimal results and verifcations

Initially, mathematical experiments were conducted by employing the TM which resulted in the construction of Z-positioner design and a set of calculated figures. With the experimental result, the RSM was utilized to build up regression formulas for the safety factor and output deformation, followed by the step of defining the WFs via Eqs. (3.24,

4.12-4.16). Assigning the WFs to the formula in Eq. (4.25), the multi-target optimal problem was addressed with the use of the WOA algorithm. MATLAB 2017 software was selected for executing the optimization processes which produced the following outcomes: M = 0.55 mm, N = 0.8238 mm, P = 0.9 mm, K = 49 mm, F_1 = 2.3824568 and F_2 = 454.551127 µm. These results indicated that the optimization numbers of two responses were suitable for either micro/nano-indentation devices, high precision positioning systems and maintaining strength limitations of offered materials.

4.3.3.6. Dynamic analysis

These outcomes of the optimized Z-positioner were then exploited for the building of 3D model to evaluate dynamic qualities of the first 06 modes, as demonstrated in Fig. 4.28. Resonant frequency results were 336.11 Hz for 1st mode, 589.53 Hz for 2nd mode, 594.75 Hz for 3rd mode, 596.36 Hz for 4th mode, 601.63 Hz for 5th mode as well as 605.49 Hz for 6th mode. So as to prevent damages for the optimized Z-positioner, these resonant frequency values should be avoided.

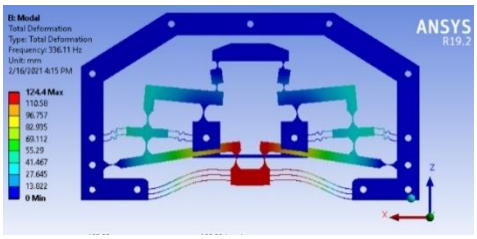

336.11 Hz for 1st resonant frequency mode

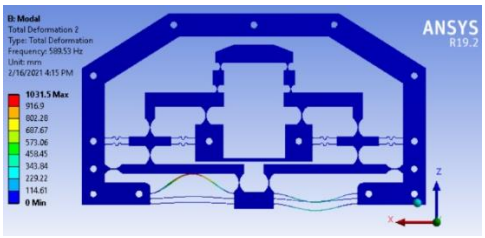

589.53 Hz for 2nd resonant frequency mode

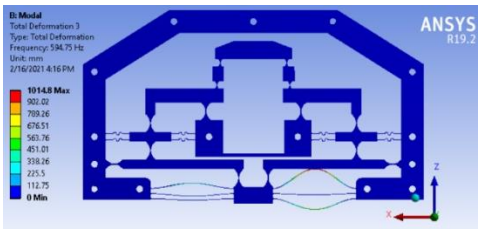

594.75 Hz for 3rd resonant frequency mode

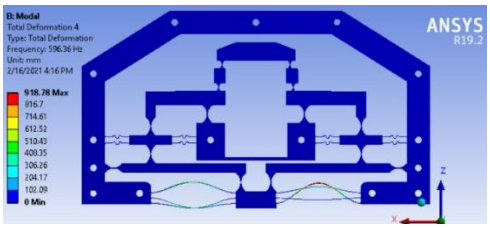

596.36 Hz for 4th resonant frequency mode

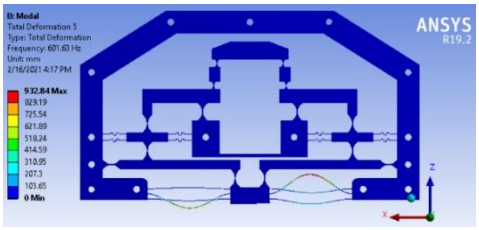

601.63 Hz for 5th resonant frequency mode

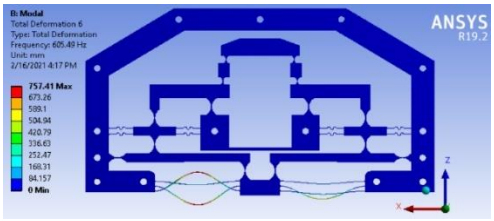

605.49 Hz for 6th resonant frequency mode

Figure 4.27. Six first modes of the optimized Z-positioner.

4.3.3.7. Statistic analysis

The efficiency of the integration method was evaluated via Cuckoo search algorithm [134]. This section reports a comparison in terms of behavior evaluation between the combination approach and CSA, with statistical analysis conducted by the Wilcoxon at 5% significance degree and 95% warranty degree.

Computation processes were repeated 35 times for each algorithm to be retrieved and obtain optimal outcomes with identical constraint settings. Computed results of the Wilcoxon technique were displayed in Tables 4.29 and 4.30. The null hypothesis assumed that there was no statistically noteworthy alteration among the average values of the abovementioned algorithms. However, as the test outcomes indicated a p-worth of lower than 0.05, the null assumption was discarded. Accordingly, the conclusion is that behaviors of the offered algorithm differ from that of CSA. More details are given in Tables 4.31 and 4.32.

Table 4.29 Wilcoxon's comparability of offered approach versus CSA for the F_1

Totality for appraisals	Forecasted median	p-worth	Wilcoxon statistic
35	0.2376	≤0.001	630

Table 4.30 Wilcoxon's comparability of offered approach versus CSA for the F_2

Totality for appraisals	Forecasted median	p-worth	Wilcoxon result
35	17.538	≤0.001	630

Moreover, the Friedman, a non-parametric test technique, was applied to determine the differences between the offered integration algorithm and the CSA at consequential level of α= 0.05. Again, computation processes were repeated 35 times for each algorithm to be retrieved and attain optimization outcomes with identical constraint settings. As the test outcomes revealed a p-worth of lower than 0.05, the null hypothesis was rejected. It confirms the conclusion that behaviors of the novel algorithm differ from that of CSA. More information can be found in Tables 4.31 and 4.32.

Table 4.31 Friedman investigations for the F_1

Response	Totality for appraisals	Mean	Totality of Ranks
F_1 by offered algorithm	35	2.1743	70
F_1 by CSA	35	2.3825	35
Totality	70	2.2784	
DF	Chi-Square	P-value	
1	35	≤0.001	
Null hypothesis	H_0: All treatment effects are 0		
Substitute hypothesis	H_1: Not all treatment effects are 0		

Table 4.32 Friedman investigations for the F_2

Response	Totality for appraisals	Mean	Totality of Ranks
F_1 by offered algorithm	35	437.58	70
F_1 by CSA	35	454.55	35
Totality	70	446.07	
DF	Chi-Square	P-value	
1	35	≤0.001	
Null hypothesis	H_0: All treatment effects are zero		
Substitute hypothesis	H_1: Not all treatment effects are zero		

4.3.3.8. Verification

The optimal outcomes including M= 0.55 mm, N= 0.82377 mm, P= 0.9 mm and K= 49 mm were utilized to develop another simulated model of the Z-positioner to confirm and assess the error between FEA and the integration methodology. The experiment was implemented with similar conditions and input deformation to validate the outcomes through 3D model establishment, based on the projected results of the integration method. The computed results indicated the Z-displacement of approximately 436.04 μm as well as

the safety factor of about 2.224. Besides, the divergences between the predicted and verified outcomes for the deformation as well as safety factor were at 4.24528% and 7.12486% correspondingly, as reported in Table 4.33. As a result, the foreseen outcomes were in a great agreement with the certified outcomes.

In addition, statistics in Table 4.34 confirmed that the optimal outcomes outperformed those of the initial design. To be specific, there was an improvement of approximately 3.708% for the safety factor and roughly 18.498% for the deformation. Therefore, it can be concluded that the offered integration method is effective enough to address multi-target optimization issues of the Z-positioner.

Table 4.33 Error between projected outcomes and confirmations

Responses	Predicting	Affirmation	Error (%)
F_1	2.38245	2.22	7.1
F_2 (mm)	454.551	436	4.2

Table 4.34 Enhancement of optimized structure to beginning structure

Characteristics	Foremost structure	Optimization structure	Enhancement (%)
F_1	2.22	2.29	3.7
F_2 (mm)	436	468.08	18.5

Furthermore, Tab. 4.35 demonstrates a comparison between the offered Z-positioner and other existing nanoindentation devices in current research. The outcomes pointed out several advances of the novel Z-positioner such as having greater output displacement and smaller parasitic motion error which enhance the indentation precision.

Table 4.35 Difference of the offered Z-positioner with previous researches

Researches	Dimensional specifications	Output deformation
Hu Huang et al. [9]	103mm×74mm×60mm	11.44 μm
Hu Huang et al. [11]	200mm×135mm×200mm	40 μm
The offered positioner	30mm×162 mm×16mm	454 μm

4.3.4. Achieved results

This chapter reports a procedure of proposing an original design of the flexure Z-positioner via a combination of the four-lever intensification structure, flexure joint athwart layout structure, a compliant spring driving structure inspired by zigzag shape and a parallel driving structure based on symmetrical 06 rectangular joints utilized for nano/micro-indentation testing devices. The construction of the Z-stage was also resulted from a proficient combination approach of the TM, FEM, RSM, weight factor quantifying technique in reference to signal to noise and WOA. The purpose of using this integration method was to optimize main geometrical factors in order to improve important features of the Z-positioner including the output deformation and safety factor. To be specific, the two responses' WFs were calculated through equation chains in order to improve computation accuracy of the optimal outcomes.

First, an initial design was evaluated and developed by FEA to obtain excellent qualities facilitated by several advantages of the offered integration flexure structure of the four-lever amplifier, zigzag driving structure and parallel guiding structure. Next, sets of statistical experimental data were generated by TM, followed by the determination of the output displacement and safety factor via FEA. Subsequently, regression functions among four chief variables and output characteristics were set by employing the response surface method. The next step was defining the signal to noise ratios and WFs for each attribute. Lastly, based on the established regression formulas, the WOA algorithm was applied to identify the optimization factors.

The calculation outcomes indicated that the WFs were 0.515 for F_1 and 0.485 for F_2 which were then assigned to the WOA so as to address the multi-criteria optimization problems. Moreover, a responsiveness assessment as well as ANOVA were figured out the impacts of the input variables to the output features. The optimized results were at M = 0.55 mm, N = 0.82377 mm, P = 0.9 mm and K = 49 mm. In addition, the optimized safety factor and displacement were about 2.3824568 and approximately 454.551127 μm, respectively.

Statistical outcomes of the Wilcoxon and Friedman non-parametric tests suggested that the offered algorithm outperformed the Cuckoo search method. In addition, the errors between optimization outcomes and FEA validation results for the safety factor and Z-direction displacement were 7.1% and 4.2%, respectively, which indicated a close

connection between the FEA verifications and the predicted outcomes for the hybrid approach. Moreover, the optimized outcomes exceeded the outcomes of the primary structure, with an improvement of approximately 3.708% and 18.498% for the safety factor and the displacement, respectively.

In the carrying out of this study, there were some difficulties including a great amount of time spent on building up a good primary structure with excellent responses and formulating an appropriate approach for multi-objective optimal issues. Accordingly, it is necessary to apply the topology optimization in developing a beginning design of structure, in order to shorten the time and advance output responses of the design.

4.4. Structural dynamic modelling of a new compliant 01-DOF stage utilizing symmetric six levers based on the PRBM method and Lagrange principle

4.4.1. Conceptual design

In order to develop one more a new compact 01-DOF positioner with high first natural frequency, large output displacement and small parasitic motion for indenting the specimens in a nanoindentation testing device, this new positioner was developed according to a six-lever displacement amplifier and parallel six-leaf hinge guiding mechanism.

The third compact 01-DOF stage includes six-lever displacement amplification mechanism module and six-leaf hinge guiding mechanism module. Three main technical performances of the third compact 01-DOF stage are expressed as follows.

(ii) The output displacement is more than 420 μm;

(iii) Parasitic motion error is lower than 0.04;

(iv) The safety factor is higher than 1.8;

(v) The first natural frequency is more than 200.

A new compliant 01-DOF positioner is derived from symmetrical six-lever deformation magnifier with elliptic compliant joints and a parallel guiding mechanism with symmetrical six-leaf, as illustrated in Fig. 4.28. Moreover, the initial dimensions and design variables are shown in Tab. 4.36.

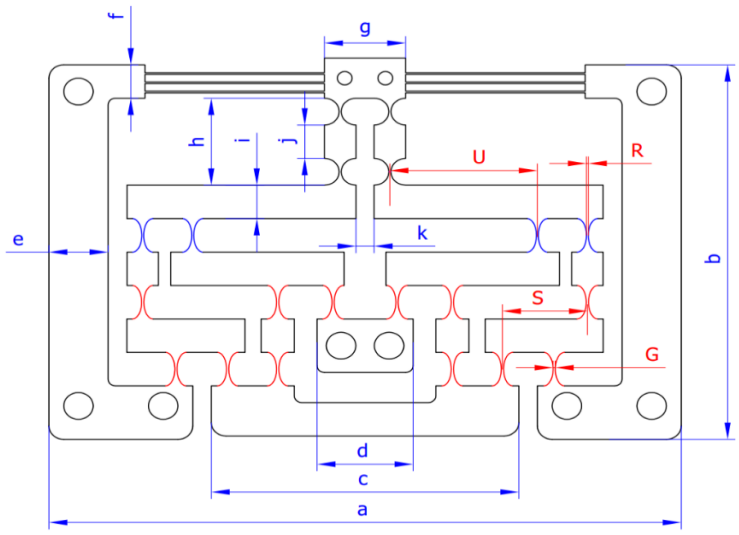

Figure 4.28. Main geometrical parameters of the compliant 01-DOF stage.

In Fig. 4.29, the displacement amplifier includes three floors with six levers which are employed to enlarge the working displacement of the stage. Specifically, the number of odd floors will ensure that the input displacement has the same direction with the output displacement. For this purpose, controlling the the number of floors will ensure the amplification ratio and the direction of the output displacement in order to monitor effectively the indentation process. Meanwhile, the parallel guiding mechanism is consisted of six leaf hinges, which is aimed to generate the translation motion, ie., eliminated parasitic motion errors from the remain (x and y) axes. It consists of lever amplification mechanism of 1st floor (LAM #1), 2nd floor (LAM #2), and of 3rd floor (LAM #3). The input is acted via piezoelectric actuator (PZT).

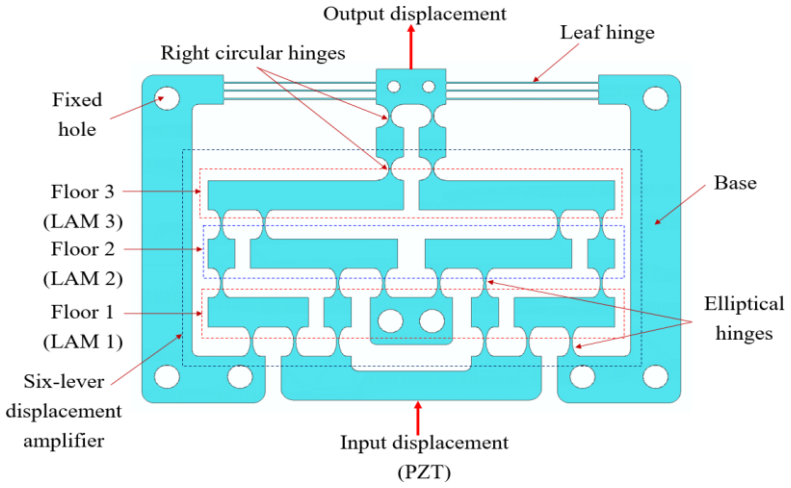

Figure 4.29. Proposed compliant 1-DOF stage.

The material of the proposed 01-DOF stage was manufactured by material Al-7075 because of the outstanding properties of this material. The 01-DOF positioner comprises:

(i) fixed holes, (ii) a PZT actuator, (iii) parallel guiding mechanism, and (iv) six-lever displacement amplifier. The sum dimension of stage is around 171mm x 108mm x 10mm. The elliptical hinge is chosen for the stage due to its excellent benefits [123]. Table 1 provides the key dimensions of the stage. Specifically, *G* is the thickness of elliptic joint of the LAM #1 and LAM #2, *R* is the thickness of elliptic joint of the LAM #3, *S* and *U* are the thickness values of right circular joint and leaf joint of the output end.

Table 4.36 Dimensional factors of the proposed stage

Symbol	Value	Symbol	Value	Unit
a	171	*i*	6	mm
b	108	*j*	10	mm
c	82	*k*	5	mm
d	26	*m*	12	mm
e	16	*G*	$0.65 \leq G \leq 0.75$	mm
f	10	*R*	$0.5 \leq R \leq 0.7$	mm
g	22	*S*	$0.5 \leq S \leq 0.65$	mm
h	26	*U*	$0.5 \leq U \leq 0.6$	

4.4.2. Proposed method

The stage is designed according to the multi-lever amplifier and the parallelogram mechanism. Then, an analytical modelling is performed via the combination of PRBM and Lagrange to establish the dynamic equation of the stage. The flowchart of offered optimization approach [135] for stage is illustrated in Fig. 4.30. It is briefly summarized as follows.

- A conceptual structure of the 1-DOF positioner is predetermined, i.e., constructed kinematic scheme.
- Predetermine the technical specifications for the 1-DOF stage.
- Establish the dynamic equation for the 1-DOF stage by developing the PRBM and Lagrange's method.
- Verify the theoretical results by using ANSYS software.
- If the mathematical models are corrected, the process moves to next step. Otherwise, the process turns back the step 1.
- Determine the design variables, objective function and constraint function.

- Firely algorithm is adopted to dynamic responses of the offered positioner.
- The optimized results are verified via simulations in ANSYS software.
- The first frequency of the offered positioner is benchmarked with that of prior studies.

4.4.2.1 Firefly algorithm

Firefly algorithm [120] is selected for maximizing the frequency due to its intelligent behaviors. Firefly algorithm (FA) was proposed by Yang [120]. This optimizer was motivated by the flashing nature of fireflies. The firefly's flash is exploited as a signal to fascinate other fireflies. The algorithm had three regulations: (i) Total of fireflies are unisexual, and one firefly are fascinated by all other fireflies. (ii) Fascination is proportionate to the brightness. Hence, the less bright one goes to the brighter one. The fascination is proportionate to the brightness. (iii) If there are not any fireflies brighter than a specified firefly, it goes to travel arbitrarily. The brilliance should be related with the objective function. According to above-mentioned regulations, the flowchart of this algorithm is exhibited in Fig. 4.31. The details of FA can be found in Ref. [120].

4.4.2.2. Analytical structure modelling based on PRBM method and Lagrange's principle

To rapidly assess initial quality characteristics of the developed compliant 01-DOF positioner such as the first natural frequency and displacement amplification ratio, structure modelling of the compliant stage is built via a series of equations (eqs. 4.37-4.62) chain based on the PRBM method. The analytical calculation results will be verified by the FEM calculation results. There are three main flexure hinges integrated into developed compliant 01-DOF positioner. The main parameters of right circular joint, elliptic joint and leaf hinge were illustrated in Figs. 4.34-36, respectively. In Fig. 4.34, some main parameters include the thickness of the right circular joint t_c, radius of the right circular joint (r) and the width of the right circular hinge (b_c). Figure 4.35 shows the thickness of the elliptic joint (h), the width of the elliptic joint (w), the two semi-axes of the elliptic joint (a and b). In Fig. 4.36, a_r is the thickness of the leaf hinge and b_r is the width of the rectangular joint.

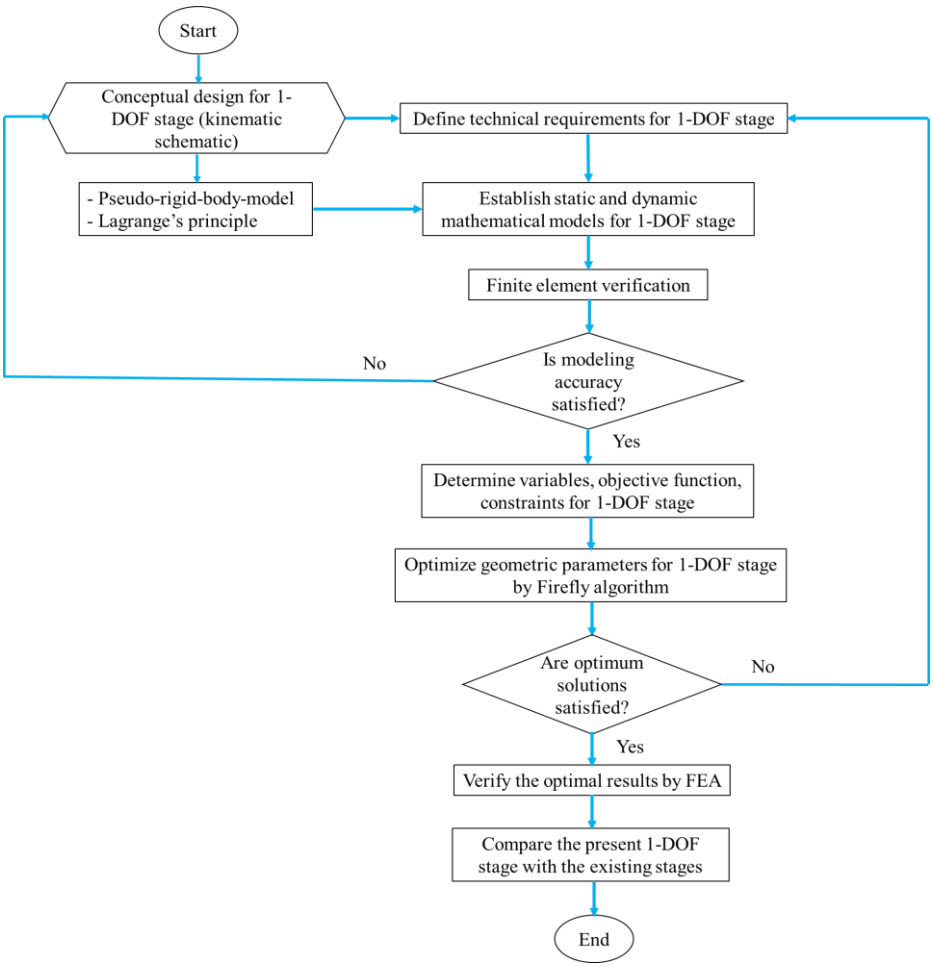

Figure 4.30. Flowchart of proposed optimization method for 1-DOF stage.

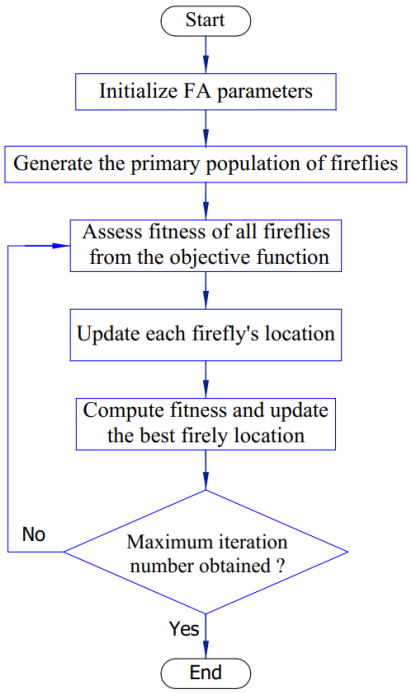

Figure 4.31. The flowchart of Firefly algorithm.

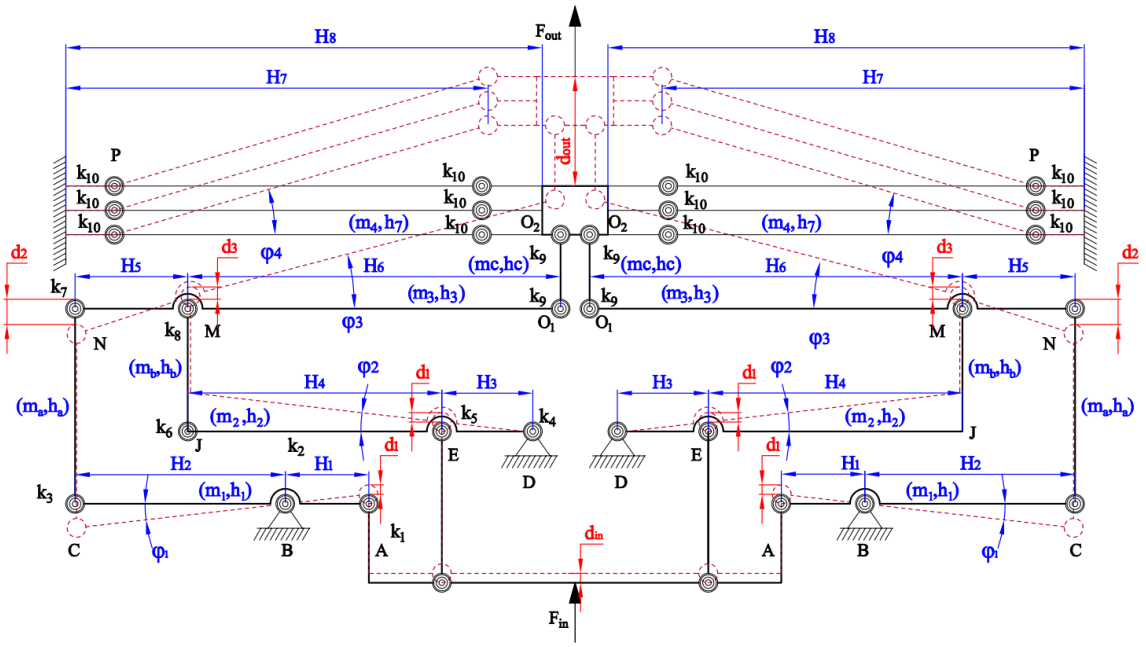

Figure 4.32. Pseudo-rigid-body diagram of 01-DOF stage.

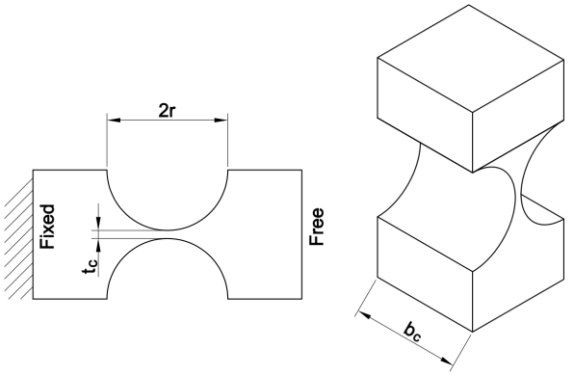

Figure 4.33. Main parameters of right circular hinge.

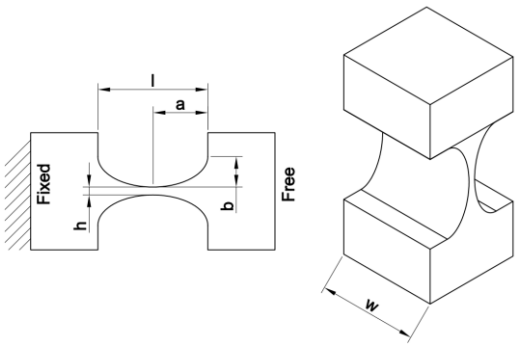

Figure 4.34. The main parameter of flexure elliptical hinge.

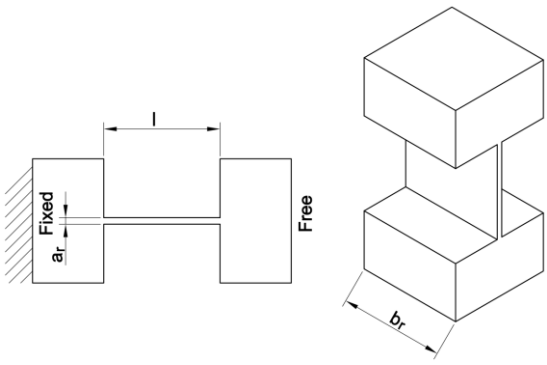

Figure 4.35. The main parameter of flexure leaf hinge.

In Figs. 4.29 and 4.32, the input displacements of LAM #1, LAM #2 and the output end consit of d_{in}, d_{outC} and d_{outJ}, and d_{out}, respectively. The output displacement of LAM #1 and LAM #2 is the input displacement of the LAM #3. The dynamic formulas of the developed positioner are formed according to a chain of equations as.

$$d_{in}\frac{H_2}{H_1} = d_{outC} = d_2 \tag{4.37}$$

$$d_{in}\left(\frac{H_3 + H_4}{H_3}\right) = d_{outJ} = d_3 \tag{4.38}$$

$$d_{out} = d_2\left(\frac{H_6}{H_5}\right) + d_3\left(\frac{H_5 + H_6}{H_5}\right) \tag{4.39}$$

$$d_{out} = d_{in}\left(\frac{H_2H_3H_6 + H_1(H_3 + H_4)(H_5 + H_6)}{H_1H_3H_5}\right) \tag{4.40}$$

$$\mathrm{AR} = \frac{d_{out}}{d_{in}} = \frac{H_2H_3H_6 + H_1(H_3 + H_4)(H_5 + H_6)}{H_1H_3H_5} \tag{4.41}$$

where m_i denotes the mass, H_i denotes the length and and φ_j (i = 1, 2...6, 7), (j = 1, 2, 3, 4) represents the rotary angular of the rigid links.

The torsional stiffness of the right circular hinge (K_C) is described in Eq. (4.42). The torsional stiffness of elliptical hinge (K_E) is depicted in Eq. (4.44). The torsional stiffness of leaf hinge (K_L) is formed in Eq. (4.45). The moment of inertia of the rigid links (I_j) are described in Eq. (4.46).

$$K_C = \frac{2Eb_c{t_c}^{2,5}}{9\pi r^{0,5}} \tag{4.42}$$

$$N_E = \frac{2\left[\sqrt{4\left(\frac{b}{h}\right)+1}\left(6\left(\frac{b}{h}\right)^2 + 4\left(\frac{b}{h}\right)+1\right)\right] + 6\left(\frac{b}{h}\right)\left(2\left(\frac{b}{h}\right)+1\right)^2 \arctan\left(\sqrt{4\left(\frac{b}{h}\right)+1}\right)}{\left(2\left(\frac{b}{h}\right)+1\right)\left(4\left(\frac{b}{h}\right)+1\right)^{5/2}} \tag{4.43}$$

$$K_E = \frac{Ewh^3}{6N_El_e} \tag{4.44}$$

$$K_L = \frac{Ea^3b}{12l} \tag{4.45}$$

$$I_j = \frac{mxH_j^2}{12} \tag{4.46}$$

In Fig. 4.32, the kinetic energy of the proposed stage is defined by.

$$E_k = \sum_{1}^{7}\left(E_t + E_r\right) = \sum_{1}^{7}\left(\frac{1}{2}m_i v_i^2 + \frac{1}{2}I_i\dot{\varphi}_j^2\right) \tag{4.47}$$

Using Eq. (11), the kinetic energy of each rigid link/part is calculated as.

$$\begin{aligned} E_k = {} & \frac{1}{2}m_1\left(\frac{H_1+H_2}{2}\dot{\varphi}_1\right)^2 + \frac{1}{2}I_1\dot{\varphi}_1{}^2 + \frac{1}{2}m_2\left(\frac{H_3+H_4}{2}\dot{\varphi}_2\right)^2 + \frac{1}{2}I_2\dot{\varphi}_2{}^2 + \frac{1}{2}m_a\left(\frac{H_1+H_2}{2}\dot{\varphi}_1\right)^2 \\ & + \frac{1}{2}m_b\left((H_3+H_4)\dot{\varphi}_2\right)^2 + \frac{1}{2}m_3\left(\frac{H_5+H_6}{2}\dot{\varphi}_3\right)^2 + \frac{1}{2}I_3\dot{\varphi}_3{}^2 + \frac{1}{2}3m_4\left(\frac{H_7}{2}\dot{\varphi}_4\right)^2 \\ & + \frac{1}{2}I_4\dot{\varphi}_4{}^2 + \frac{1}{2}m_c\left((H_5+H_6)\dot{\varphi}_3\right)^2 \end{aligned} \tag{4.48}$$

In Fig. 4.32, the elastic energy of the proposed stage is defined as.

$$E_V = \sum_{j=1}^{4}\frac{1}{2}K_j\varphi_j^2 \tag{4.49}$$

The elastic energy is attained by the deformation of elliptic joint, right circular joint and leaf joint.

$$E_V = \frac{1}{2}(k_1+k_2+k_3)\varphi_1^2 + \frac{1}{2}(k_4+k_5+k_6)\varphi_2^2 + \frac{1}{2}(k_7+k_8+2k_9)\varphi_3^2 + (6k_{10})\varphi_4^2 \tag{4.50}$$

The rotation angular and angular velocity of every link are symbolled $(\varphi_j, \dot{\varphi}_j)$. Relationships between the rotary angulars is determined by.

$$\varphi_1 = \frac{d_{in}}{H_1} \tag{4.51}$$

$$\varphi_2 = \left(\frac{H_1}{H_3+H_4}\right)^2\varphi_1 \tag{4.52}$$

$$\varphi_3 = \left(\frac{\left(H_2H_3H_6 + H_1\left(H_3+H_4\right)\left(H_5+H_6\right)\right)}{H_3H_5\left(H_5+H_6\right)}\right)\varphi_1 \tag{4.53}$$

$$\varphi_4 = \left(\frac{\left(H_2H_3H_6 + H_1\left(H_3+H_4\right)\left(H_5+H_6\right)\right)}{H_3H_5H_7}\right)\varphi_1 \tag{4.54}$$

By applying an input force F_{in}, the work is defined as.

$$W = \frac{1}{2}F_{in}d_{in} \tag{4.55}$$

Considering $W = E_V$, the input force and the input displacement have formed a relation as follows.

$$\frac{1}{2}F_{in}d_{in}=\frac{1}{2}\left[\begin{array}{l}\left(k_1+k_2+k_3\right)\dfrac{1}{H_1^{\,2}}+\left(k_4+k_5+k_6\right)\dfrac{1}{\left(H_3+H_4\right)^2}\\+\left(k_7+k_8+2k_9\right)\left(\dfrac{\left(H_2H_3H_6+H_1\left(H_3+H_4\right)\left(H_5+H_6\right)\right)}{H_1H_3H_5\left(H_5+H_6\right)}\right)\\+6k_{10}\left(\dfrac{\left(H_2H_3H_6+H_1\left(H_3+H_4\right)\left(H_5+H_6\right)\right)}{H_1H_3H_5H_7}\right)^2\end{array}\right]d_{in}^2 \tag{4.56}$$

If the input stiffness of the stage ($K_{in} = F_{in}/d_{in}$) divides both sides by d_{in}^2, the stiffness is determined as.

$$K_{in}=\left(k_1+k_2+k_3\right)\frac{1}{H_1^{\,2}}+\left(k_4+k_5+k_6\right)\frac{1}{\left(H_3+H_4\right)^2}$$
$$+\left(k_7+k_8+2k_9\right)\left(\frac{\left(H_2H_3H_6+H_1\left(H_3+H_4\right)\left(H_5+H_6\right)\right)}{H_1H_3H_5\left(H_5+H_6\right)}\right)+6k_{10}\left(\frac{\left(H_2H_3H_6+H_1\left(H_3+H_4\right)\left(H_5+H_6\right)\right)}{H_1H_3H_5H_7}\right)^2 \tag{4.57}$$

In the structure, the kinetic energy (E_k) and elastic energy (E_v) may be conveyed. These two energies are assembled into Lagrange function as $\mathbf{L} = E_k - E_v$.

$$\sum_{j=1}^{4}\left\{\frac{d}{dt}\left(\frac{\partial L}{\partial\dot{\varphi}_j}\right)-\frac{\partial L}{\partial\varphi_j}=Q_j\right\} \tag{4.58}$$

The equation of motion can be defined as follows.

$$\bar{M}\ddot{\varphi}_1+\bar{K}\varphi_1=0 \tag{4.59}$$

$$\overline{M}=m_1\left(\frac{H_1+H_2}{2}\right)^2+I_1+m_2\left(\frac{H_1}{2}\right)^2+I_2\left(\frac{H_1}{H_3+H_4}\right)^2+m_a\left(\frac{H_1+H_2}{2}\right)^2+m_b\left(H_1\right)^2+$$
$$m_3\left(\frac{\left(H_2H_3H_6+H_1\left(H_3+H_4\right)\left(H_5+H_6\right)\right)}{2H_3H_5}\right)^2+I_3\left(\frac{\left(H_2H_3H_6+H_1\left(H_3+H_4\right)\left(H_5+H_6\right)\right)}{H_3H_5\left(H_5+H_6\right)}\right)^2+$$
$$3m_4\left(\frac{\left(H_2H_3H_6+H_1\left(H_3+H_4\right)\left(H_5+H_6\right)\right)}{2H_3H_5}\right)^2+I_4\left(\frac{\left(H_2H_3H_6+H_1\left(H_3+H_4\right)\left(H_5+H_6\right)\right)}{H_3H_5H_7}\right)^2+$$
$$m_c\left(\frac{\left(H_2H_3H_6+H_1\left(H_3+H_4\right)\left(H_5+H_6\right)\right)}{H_3H_5}\right)^2 \tag{4.60}$$

$$\overline{K}=\left(k_1+k_2+k_3\right)+\left(k_4+k_5+k_6\right)\left(\frac{H_1}{H_3+H_4}\right)^2+\left(k_7+k_8+2k_9\right)\left(\frac{\left(H_2H_3H_6+H_1\left(H_3+H_4\right)\left(H_5+H_6\right)\right)}{H_3H_5\left(H_5+H_6\right)}\right)^2$$
$$+6k_{10}\left(\frac{\left(H_2H_3H_6+H_1\left(H_3+H_4\right)\left(H_5+H_6\right)\right)}{H_3H_5H_7}\right)^2 \tag{4.61}$$

The first natural frequency of the proposed positioner is defined as the following equation:

$$f = \frac{1}{2\pi}\left(\frac{\overline{K}}{\overline{\overline{M}}}\right)^{0.5} \tag{4.62}$$

which has the unit of Hertz.

4.4.3. Verification of established analytical models

Analytical results are validated by using Finite element analysis (FEA). From the theory, the natural frequency was 176.96 Hz, and the first natural frequency was 195.07 Hz from the FEA results. As given in Table 4.37, the deviation error of the theory to the FEA test is roughly 9.28%. Therefore, the formulated modelling method is a good enough and reliable approach to evaluate the initial characteristic of the developed stage.

Table 4.37 Validation for the analytical result through FEA result

Response	Theory	FEA	Error (%)
f (Hz)	176.96	195.07	9.28

4.4.4. Parameter optimization of 1-DOF positioner

The 1st natural frequency values are as minimal or maximal as feasible to elude the resonance among motors or PZT actuators, and flexure 1-DOF positioner. The 1st natural frequency should be preferred as large as feasible to boost the positioners' quick reaction. Additionally, the angular frequency is proportionate to the flexure positioner's natural frequency. To boost response time and prevent the positioner's resonance phenomena, it is therefore suggested to maximize the initial natural frequency. The goal of the optimization issue in this research is to increase the resonance frequency, which is identified as follows.

Seek variable vector: $\mathbf{x} = [x_1, x_2, x_3, x_4]$

$$\text{Maximize } f(\mathbf{x}) \tag{4.63}$$

Constraint

$$f(\mathbf{x}) > 200 \text{ Hz} \tag{4.64}$$

Limits of design variables (unit: mm):

$$\begin{cases} 0.65 \le x_1 \le 0.75 \\ 0.5 \le x_2 \le 0.7 \\ 0.5 \le x_3 \le 0.65 \\ 0.5 \le x_4 \le 0.6 \end{cases} \tag{4.65}$$

in which $f(\mathbf{x})$ symbolizes the resonant frequency. Meanwhile, x_1, x_2, x_3, and x_4 are the dimensions R, G, S, and U, respectively. Especially, the range of design variables depends on the design experiences and the characteristics of different floors. Specifically, the thickness of 1st floor should be more than that of 2nd floor. In addition, the thickness of 2nd floor should be more than that of 3rd floor. This is a need to permit the strength of proposed stage as well as reduce the lost of displacement energy. Meanwhile, suitable thickness of various positions of different floors should be defined by optimization process in order to find the most appropriate values for proposed structure.

Based on the Eqs. (4.37-4.65), MATLAB 2017 was employed to develop the integration approach of PRBM method and Lagrange's principle, and Firefly algorithm. Consequently, the optimization factors of the offered positioner were detected at G = 0.75 mm, R = 0.7 mm, S = 0.65 mm, U = 0.6 mm. The results found that the 1st natural frequency is approximately 226.8458 Hz. The convergence of the proposed algorithm is provided in Fig. 4.36.

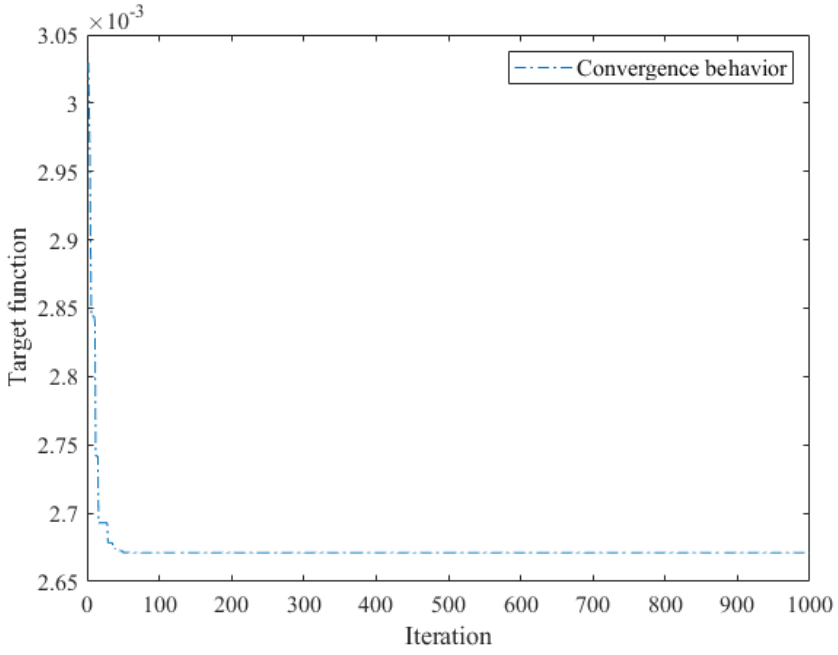

Figure 4.36. Convergence plot of the proposed algorithm

Besides, a parametric/sensitive study is performed to demonstrate the influences of design variables on the 1st natural frequency, the output displacement, and the safety factor. This work is performed according to response surface method and FEA. The effects of the variable parameters on the first natural frequency, the output deformation, and the safety factor are provided in Fig. 4.37 (a-e), Fig. 4.38 (a-e) and Fig. 4.39 (a-e), respectively.

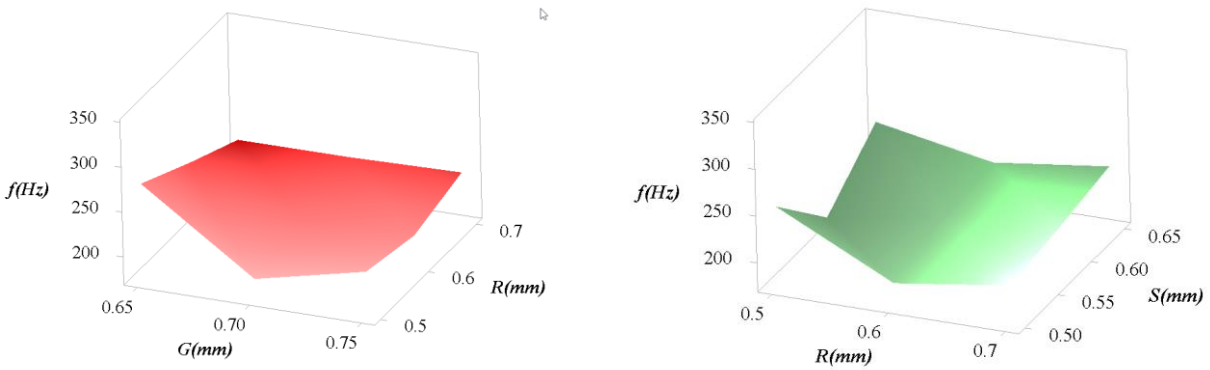

(a)

(b)

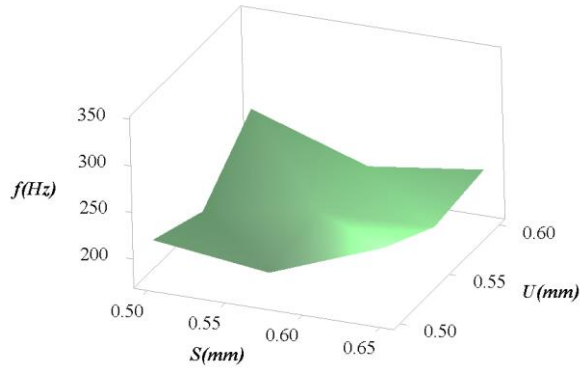

(c)

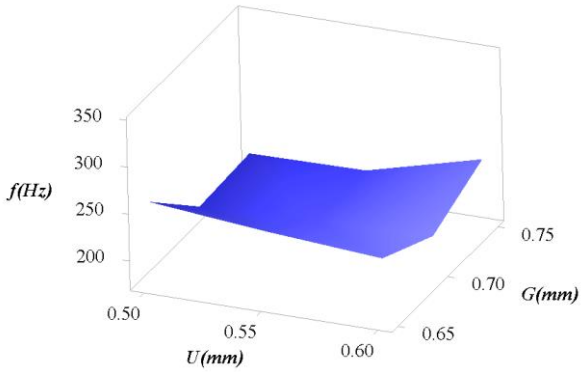

(d)

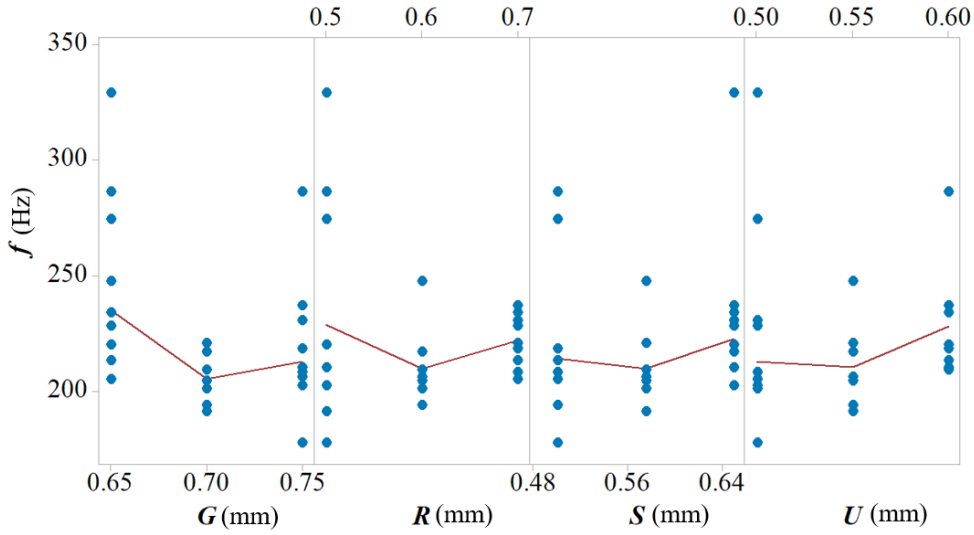

(e)

Figure 4.37. Trends of the frequency based on the alteration of the key stage dimensions: (a) 1st natural frequency with factors *G* and *R*, (b) 1st natural frequency with factors *R* and *S*, (c) 1st natural frequency with factors *S* and *U*, (d) 1st natural frequency with factors *U* and *R*, (e) 1st natural frequency with factors *G*, *R*, *S* and *U*.

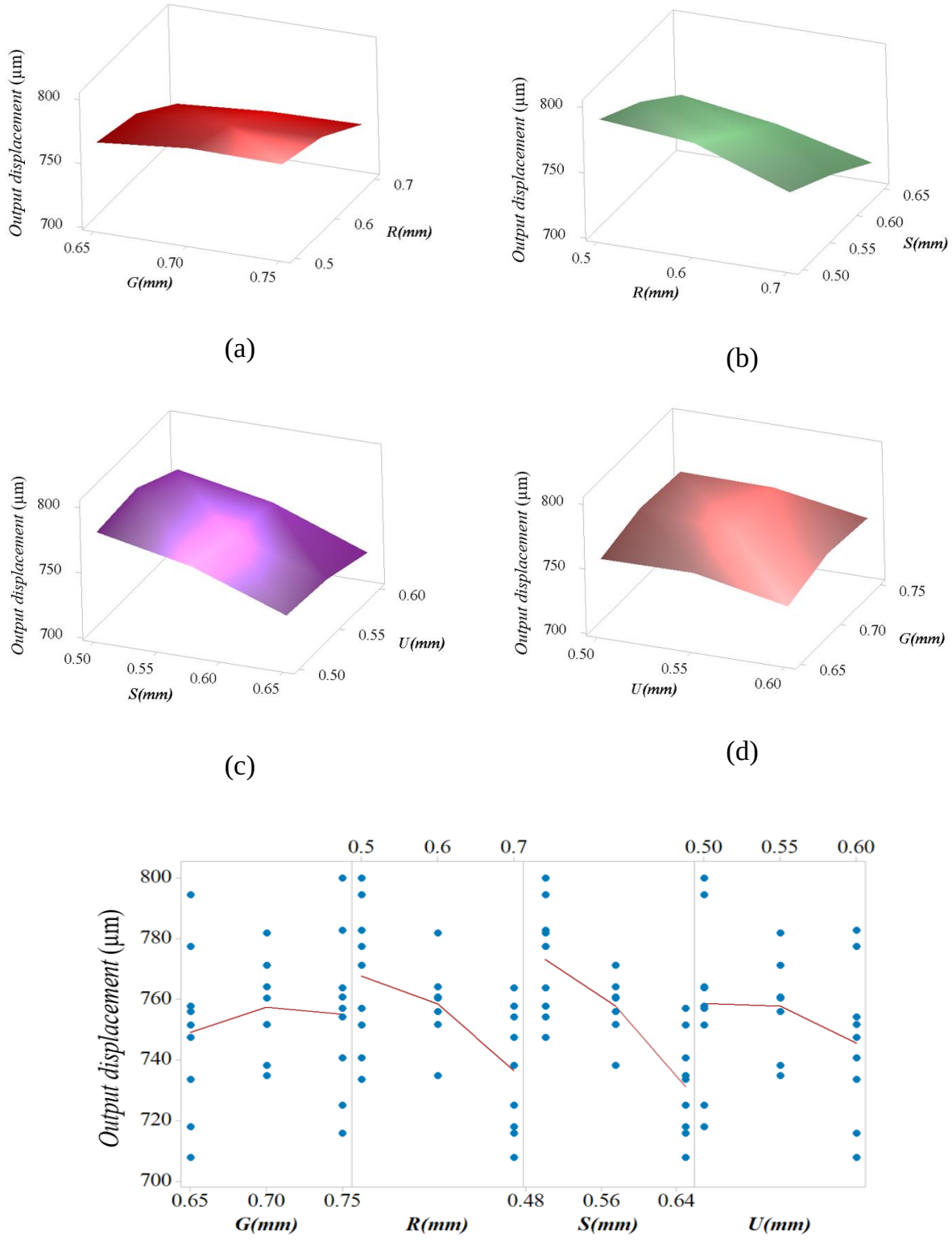

Figure 4.38. Trends of the output displacement (input displacement of 52 µm) based on the alteration of the key stage dimensions: (a) output displacement versus *G* and *R*, (b) output displacement versus *R* and *S*, (c) output displacement versus *S* and *U*, (d) output displacement versus *U* and *R*, (e) output displacement versus *G*, *R*, *S* and *U*.

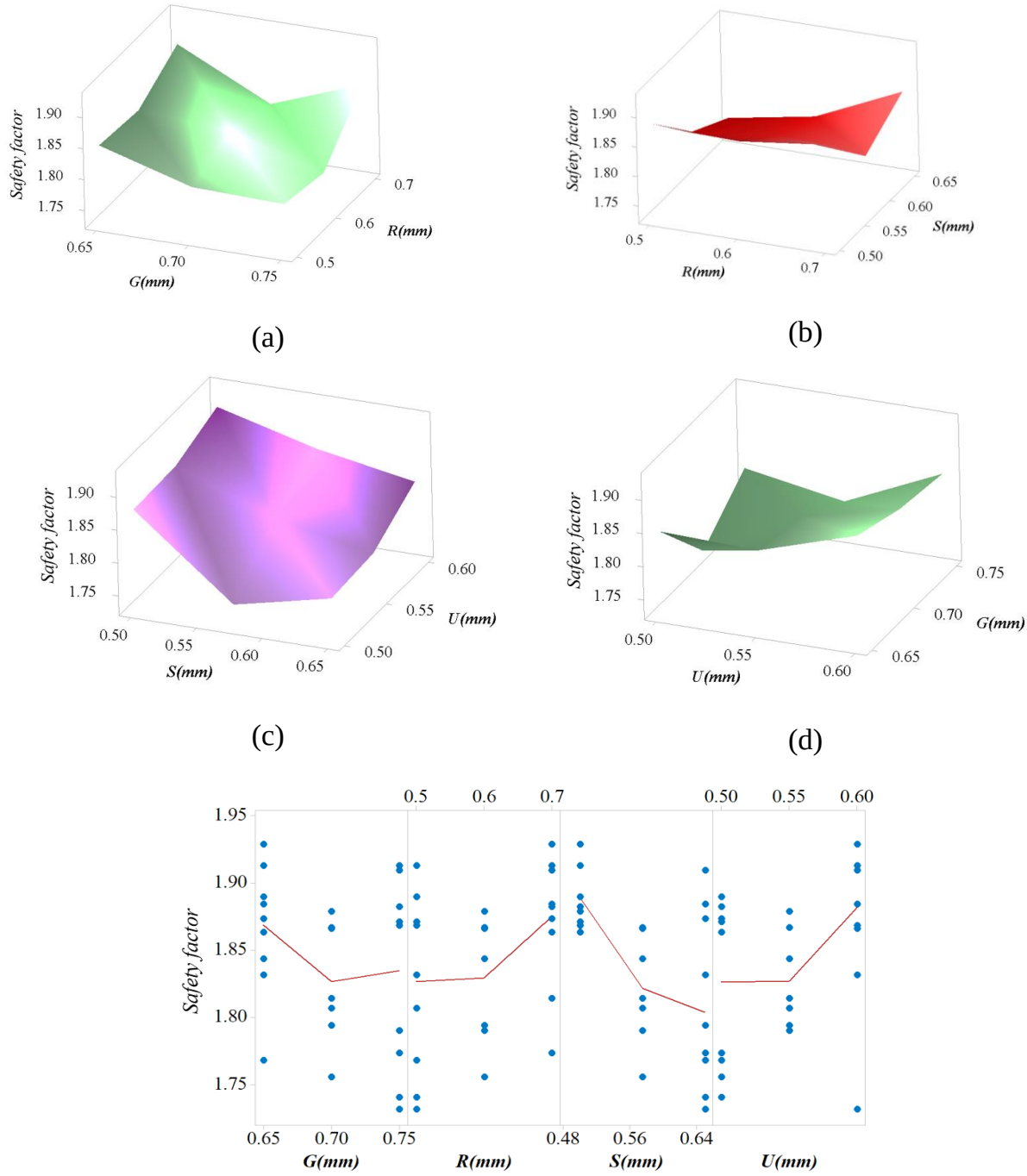

Figure 4.39. Trends of the safety factor (input displacement of 52 μm) based on the alteration of the key stage dimensions: (a) safety factor with factors *G* and *R*, (b) safety factor with factors *R* and *S*, (c) safety factor with factors *S* and *U*, (d) safety factor with factors *U* and *R*, (e) safety factor with factors *G*, *R*, *S* and *U*.

4.4.5. FEA Validation and comparison

The optimized parameters were used to draw a 3D model. The FEA result showed 1st natural frequency has a value of 250.01 Hz. In comparison with the result of draft model, the

frequency of the developed positioner was advanced up to 28.19%, as provided in Tab. 4.38. Furthermore, the error of optimization with FEA result for the first natural frequency is 9.27 %, as illustrated in Table 4.39.

This means that the presented method framework is a reliable tool for modeling the stage. Furthermore, the resonant frequency numbers of six modes (1-6) are 250.01 Hz, 846.6 Hz, 897.53 Hz, 1146.6 Hz, 1305 Hz and 1392.3 Hz, correspondingly. Figure 4.40 demonstrates the 1st natural frequency of the 01-DOF positioner. Consequently, the above-mentioned resonant frequency values should be considered in order to evade the damage of the proposed 1st.

Table 4.38 Comparison of the optimized design with the draft design

Characteristic	Optimization outcome	Primary outcome	Advancement (%)
f (Hz)	**226.8458**	176.96	**28.19**

Table 4.39 Verification of the optimized result by FEA

Response	Optimal design	Simulation	Error (%)
f (Hz)	**226.8458**	250.01	9.27

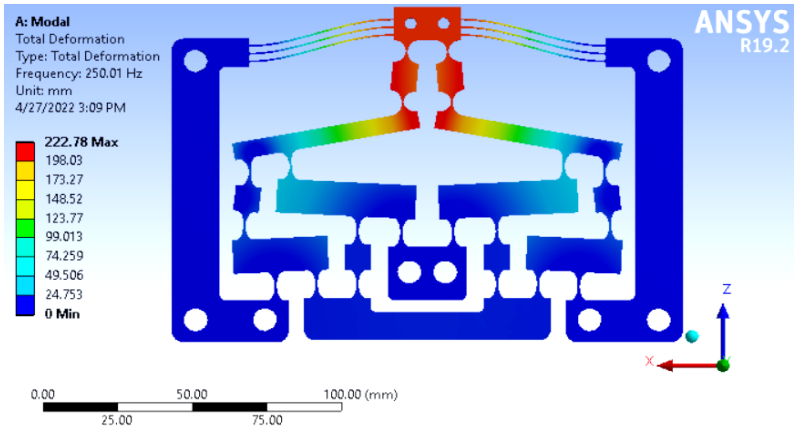

Figure 4.40. The frequency result of the optimized positioner.

In this work, the Skewness criterion is employed to define the mesh quality. The outcomes found that the average value of this criterion is about 0.66, as given in Fig. 4.41. This value ensures a good mesh for the stage during the simulation.

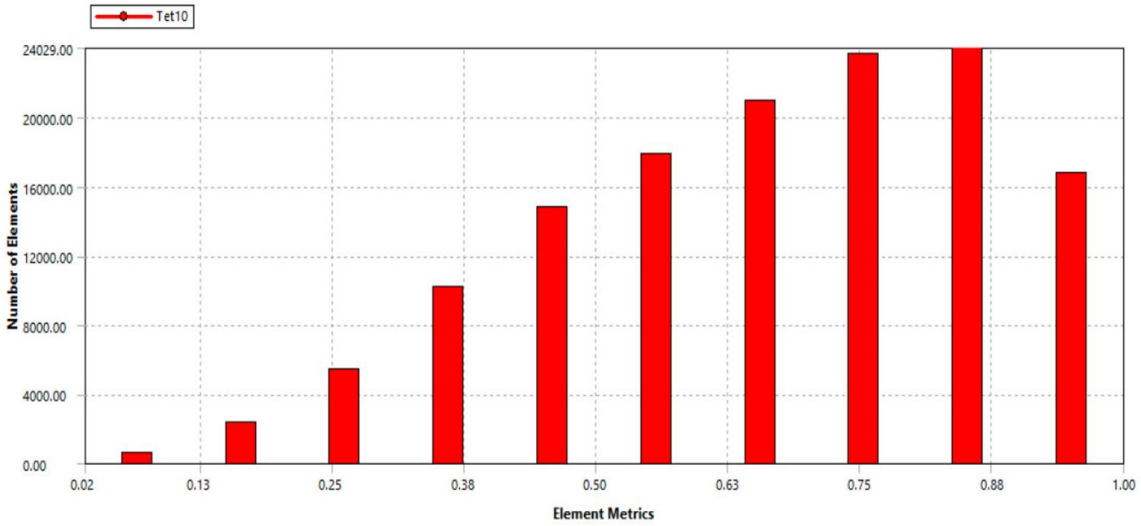

Figure 4.41. Skewness criteria for meshing quality

In comparison with other optimization methods, the offered method was compared with the differential evolutionary algorithm (DE) [136] and Neural network algorithm (NNA) [137]. The achieved frequency from the present method and two DE and NNA were almost similar, as given in Table 4.40.

Table 4.40 Comparison between the presented method and other methods

Response	Presented method	DE	NNA
f (Hz)	**226.8458**	**226.8456**	**226.8448**

Table 4.41 provides a comparison of the present design with the several existing designs. The results found that the frequency of the present stage is superior to others.

Table 4.41 Comparison of the present design with previous designs

Studies	Dimensions	First-order resonant frequency (Hz)
Xu [138]	100 mm × 100 mm x 10 mm	91.97
Li and Tian [139]	NA	192.00
Chau et al. [140]	120 mm x 50 mm x 10 mm	79.517
The proposed design	**171 mm x 108 mm x 10 mm**	**250.01**

4.4.6. Achieved results

The third design alternative of 01-DOF stage was developed according to symmetrical six-lever displacement amplifier combined elliptic compliant joints as well as symmetrical six-

leaf parallel driving structure for checking mechanical properties of various specimens. Specifically, analytical model was established based on the PRBM method and Lagrange method to quickly assess the initial performance of the developed positioner. The achieved outcomes illustrated that the 1st resonant frequency of the offered positioner is superior than several previous studies [138–140].

4.5. Conclusions

This chapter presents three design alternatives as well as optimal methods for boosting the output features of the offered positioners for indenting the specimens in nanoindentation testing device. Each design has its own merits and demerits. Based on the different specimens, each compliant 01-DOF stage and optimization methods should be considered to choose for indenting the specimen in the nanoindentation testing device.

CHAPTER 5 DEVELOPMENT OF COMPLIANT STAGES FOR LOCATING A MATERIAL SPECIMEN

After the development of the proposed compliant 01-DOF stages for indenting the specimens, this chapter will present 02-DOF stages and rotary stage for locating the specimens in the proposed nanoindentation testing device, as illustrated in Fig. 1.5. Firstly, the initial design alternative of an XY stage is developed for locating the specimens based on a four-lever amplification mechanism and a parallel guiding mechanism with a zigzag-based flexure hinge. Secondly, the second XY stage design alternative is developed for locating the specimens according to an eight-lever amplification mechanism combined with elliptic joints as well as a parallel guiding mechanism. Finally, to reduce the number of actuators, the design alternative of rotary stage is built based on a four-lever displacement amplifier, a parallel guiding mechanism inspired by the profile's beetle leg, a compliant cartwheel hinge, and a rotary platform.

5.1. Motivation

As illustrated in Fig. 1.5 (Chapter 1), a nanoindentation testing device requires indenter driver, a raw Z-positioner, a raw XY-positioner, a refined XY-positioner or a refined rotary-positioner, and a fine Z-positioner. In previous chapter, a positioner for inderter was developed. In this chapter, a XY-fine positioner or a fine rotary-positioner are utilized to locate the specimens for checking the mechanical properties of the various specimens. Therefore, this chapter has a motivation to develop XY stages and a rotary stage with large output displacement to expand output working stroke for locating the precise positions of the specimens. Based on the merits of compliant mechanisms, proposed compliant XY stages are utilized for locating the precise positions of specimens and moving the specimens closer to the indenter, as well as controlling specimens for indenting many points on the specimens. Specifically, the proposed rotary stage is utilized to reduce the number of actuators and locate the specimens' positions for testing the mechanical properties of many points on the specimens.

5.2. Development and optimization of a compliant XY positioner

5.2.1. Conceptual design

The specimens were located on the positioning stage, as illustrated in Fig. 1.5. In order to guide the specimens closer to the indenter for indenting many points on the specimens, a

new 02-DOF positioner was developed to achieve a large displacement amplification ratio for expanding working stroke of the stage in locating the specimens in nanoindentation testing device.

The first 02-DOF stage includes four-lever displacement amplification module and a parallel guiding mechanism module. Three main technical performances of the first 02-DOF stage are expressed as follows.

- The displacement amplification is more than 18.
- The safety factor is higher than 1.5.
- The first natural frequency is more than 45 (Hz).

5.2.1.1. Hybrid displacement amplifier

The application of the lever mechanism can be found in magnifying the worth of force or displacement. Fig. 5.1 depicts the use of one lever mechanism to amplify output displacement despite the possibility of easily creating decoupling error. To satisfy the requirements of amplifying larger output displacement, reducing decoupling error and generating linear motion according to symmetrical configuration, a four-lever displacement intensification structure is developed, as demonstrated in Fig. 5.2. With the advancement of this amplifier's structural attributes, the intensification proportion can be roughly attained:

$$r_{lever} = \Delta l_2 / \Delta l_1 = l_2 / l_1 \tag{5.1}$$

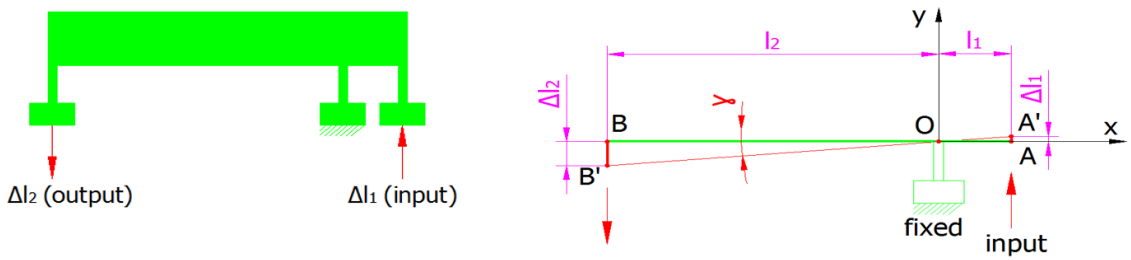

(a) (b)

Figure 5.1. Scheme of: (a) The lever structure's performing rule, (b) Investigation of intensification proportion.

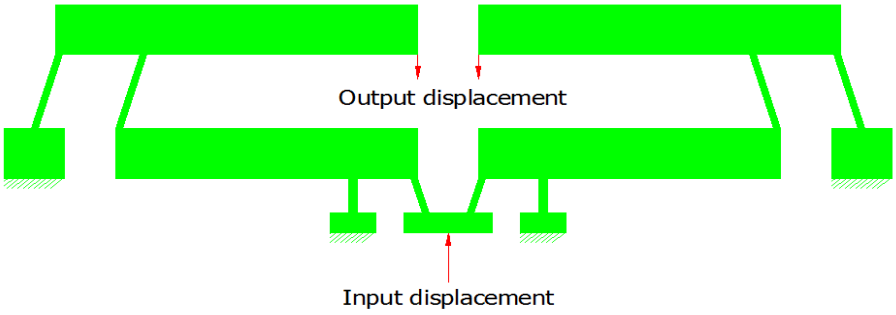

Figure 5.2. Model of four-lever structure.

The equation for multi-lever displacement intensification mechanism is presented as follows:

$$r_{lever} = N \times l_2 / l_1 \tag{5.2}$$

Regarding the four-lever displacement intensification mechanism case in this research, N is supposed to be 4. However, eq. (5.2) fails to meet the demand of being exact for multi-levers due to the lever's length, the flexure hinge and the angle between lever and flexure hinge. Therefore, to achieve higher accurateness, it is necessary to adjust the intensification proportion by FEA.

5.2.1.2. Compliant XY micro-positioning stage

The operation of compliant XY micro-positioning stage (CMS) depends on the material's elastic deformation. The positioner can be exploited to position the specimen in nanoindentation analyzing process to examine the material's properties. The material Al 7075 was offered for the offered positioner owing to its impressive yield strength of 503 MPa, Young's modulus of 71700 MPa, low density of 2810 kg/m^3 and Poisson's coefficient of 0.33. An input displacement of 0.19 mm was suggested for XY positioner [141] in order to maintain strength conditions. Fig. 5. 3 illustrates the proposed XY stage which comprises of (i) 18 fixed holes were exploited for locating the stage on an un-vibration table to check its features, (ii) a piezoelectric actuator (PEA) was exploited to produce the positioner's input deformation through direct connection with the symmetric four-lever structure. The whole dimensional specifications of offered positioner was around 339 mm×339 mm×6 mm. After a comparison with rectangular flexure hinge, right circular hinge was selected to achieve higher precision of rotary center motion. Additionally, zigzag-based flexure hinge was developed and integrated in the stage to better flexibility and gain larger displacement. Table 5.1 demonstrates geometrical parameters of the proposed XY stage which was

developed to generate linear displacement used in indentation testing micro-positioning system. Hence, to facilitate the performance of offered XY positioner, some chief factors of the stage should be optimized.

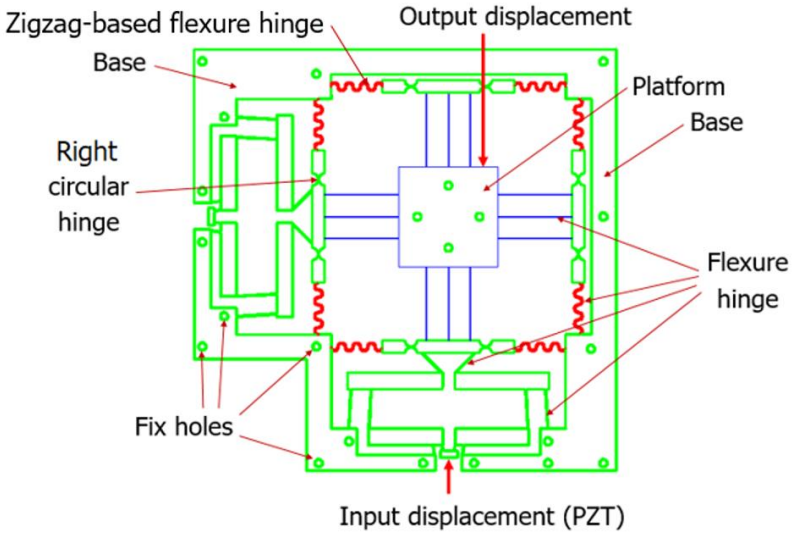

(a)

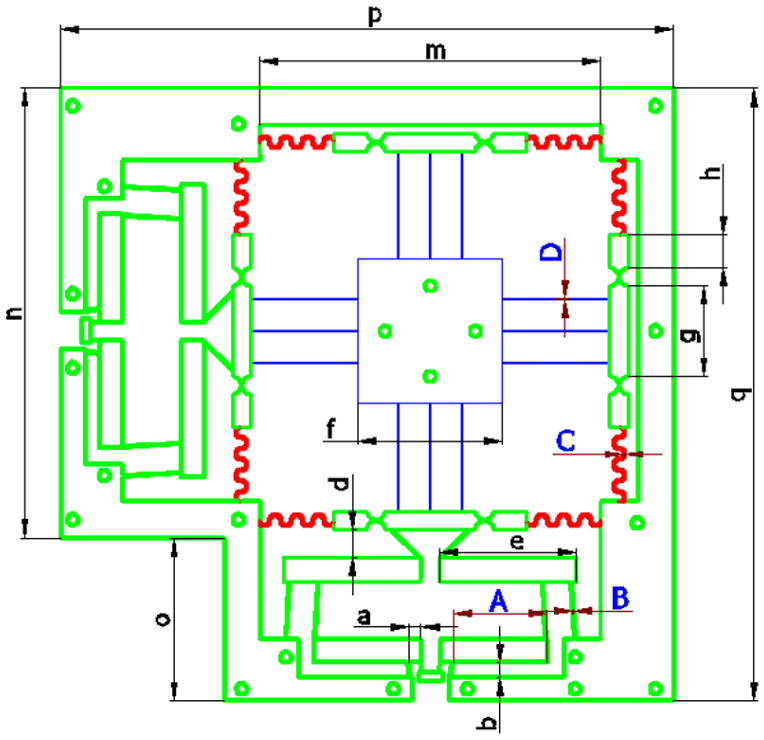

(b)

Figure 5.3. Model: (a) XY stage, (b) design parameters.

Table 5.1 Geometrical parameters of the XY stage

Par.	Value	Par.	Value	Par.	Value	Unit
a	6.84	*m*	189	*x*	30	mm
b	8	*n*	249	*y*	280	mm
c	32	*h*	18	*A*	*51≤A≤54*	mm
d	16	*o*	90	*B*	*0.9≤B≤1.1*	mm
e	76	*p*	339	*C*	*0.5≤C≤0.7*	mm
f	80	*q*	339	*D*	*0.5≤D≤0.7*	mm
g	50					

5.2.2. Formulation of optimal problem

It is important for the positioner in this research to meet these requests: (i) the 1st natural frequency (F_1) is as high as possible to advance rapid response of the positioner, (ii) high y-direction deformation (F_2) to enlarge broad positioning capacity for checking characteristics of material sample. A hybrid approach developed from the combination of the TM, the RSM and the NSGA-II [142] is proposed to provide a balance. The formulation of the optimal issue for the XY-positioner is presented as.

Find the design variables: $\mathbf{X}=[A,B,C,D]$

Maximize the output displacement (F_1):

$$F_1(A,\ B,\ C,\ D), \tag{5.3}$$

Maximize the 1st natural frequency (F_2):

$$F_2(A,\ B,\ C,\ D), \tag{5.4}$$

Subject to constraints:

$$\sigma_{\max} \le \frac{\sigma_y}{SF}, \tag{5.5}$$

$$\begin{cases} 51\text{ mm} \le A \le 54\text{ mm};\ 0.9\text{ mm} \le B \le 1.1\text{ mm} \\ 0.5\text{ mm} \le C \le 0.7\text{ mm};\ 0.5\text{ mm} \le D \le 0.7\text{ mm} \end{cases}, \tag{5.6}$$

in which F_1 as well as F_2 denote the quality attributes. A, B, C, D denote the length of 1st lever, thickness of compliant joint (lever intensification structure), thickness of compliant

joint (platform structure), thickness of zigzag-based compliant spring, correspondingly. Bouds of design variables are determined by capacity of WEDM and designer requirements.

In addition, $\sigma_{\max}$ denotes the maximum stress of the flexure hinges; *SF* denotes the safety factor; and σ_y denotes the limit stress of the offered material Al 7075.

To guarantee plastic success, it is compulsory for the safety factor to be as as high as possible. In this study, a safety factor of 1.5 was chosen for the offered positioner.

The design variables were limited in the range of Eq. (5.6). The lower bounds for the design parameters were chosen to ensure compliance, and the upper bounds of the geometric dimensions were proposed to gain a compact structure.

5.2.3. Methodology

The developed integrated method aims to examine the influences of the parameters on a developed positioner with multi-target responses and search for optimized parameters of the offered positioner. First, the TM was employed to identify an orthogonal array for the shaping of numerical experiments' number and ANOVA was run to measure the meaningful influence percentage of every factor to the output response. Next, the RSM is used for establishment of linear and nonlinear multivariate connections among chief variables and the quality characteristics. The following equation presents a full quadratic model which is a right form for the offered positioner:

$$F_j = \beta_0 + \sum_{i=1}^{n} \beta_i \mathrm{x}_i + \sum_{i=1}^{n} \beta_{ij} \mathrm{x}^2{}_i + \sum_{i=1}^{n-1} \sum_{j=i+1}^{n} \beta_{ij} \mathrm{x}_i \mathrm{x}_j + \varepsilon_i \qquad (5.7)$$

where the β_i *(i=0, 1, 2, …, n)* symbolize unidentified regression coefficients, β_{ij} *(i<j)* are interaction coefficients $x_1, x_2, \ldots, x_n$ of *n* predictors related to a feature variable F_j, ε is a haphazard error.

Lastly, in reference to the mathematical models, the NGSA-II was utilized to figure out the optimized parameters. The use of NGSA-II in multi-target optimization problems is appropriate owing to its ability to align with the global Pareto solutions. This algorithm can produce a Pareto optimal set for multi-target optimization. Basically, the NSGA-II algorithm possess these characteristics: Nondomination is the core of NSGA-II; crowding distance ensures the diversity among the resolutions of a population; and crowding selection operator: Selection of suitable candidates to form child population. It can be pseudo code as follows: (i) generate initial population P randomly; (ii) quantify the value of each

objective function; (iii) define ranks of each candidate solution using dominance criteria; (iv) compute crowding distance for each candidate solution; (v) carry out a selection by crowding selection operator; (vi) generate child population using crossover and mutation; (vii) generate a new population; repeat until convergence. MATLAB 2017 was used to perform the NSGA-II algorithm. Table 5.2 presented the initial parameters of NGSA-II and Fig. 5.4 depicted the diagram of the developed integrated approach [141].

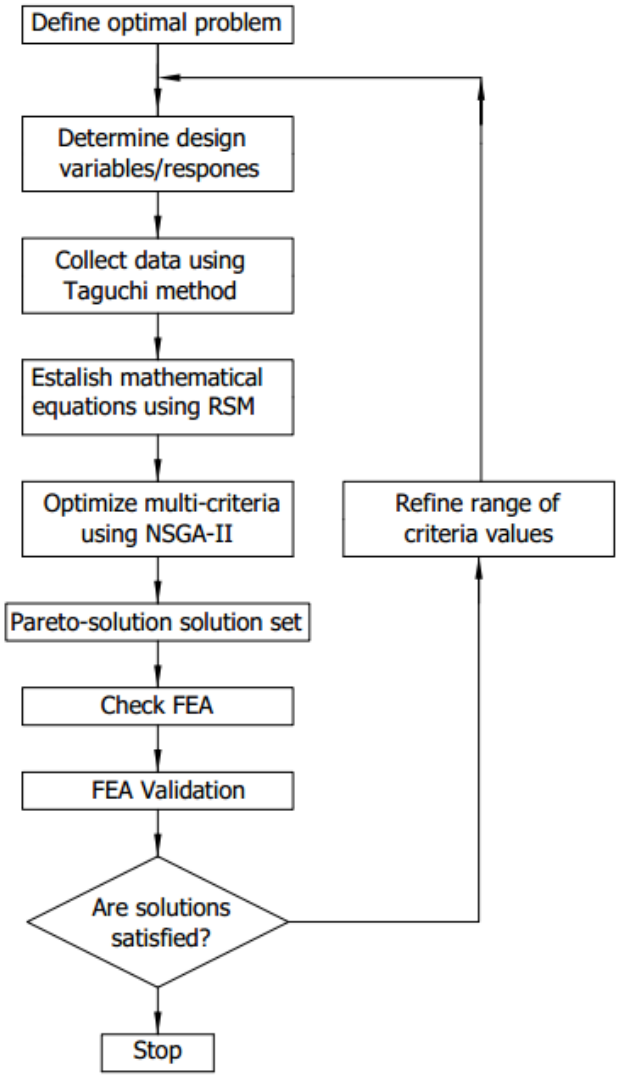

Figure 5.4. Flow chart for the developed optimization method.

Table 5.2 Initial parameters for NGSA-II

Parameters	Value
Quantity of initial samples	100
Quantity of samples per iteration	500
Mutation probability	0.8
Crossover probability	0.01

5.2.4. Results and discussion

5.2.4.1. Orthogonal array experiment and mathematical model

Every factor was classified into three grades on the basis of professional expertise, as demonstrated in Tab. 5.3. The L_9 (3^4) orthogonal array of TM was adopted for forming the quantity of experiments. The 1st natural frequency (F_1) and output y-axis deformation (F_2) were gathered from FEA in ANSYS 18.2 and outcomes of the numeric experiments were shown in Tab. 5.4.

Table 5.3 Design factors and their degrees (unit: mm)

Parameters	Variation	Degree 1	Degree 2	Degree 3
A	51-54	51	52.5	54
B	0.9-1.1	0.9	1	1.1
C	0.5-0.7	0.5	0.6	0.7
D	0.5-0.7	0.5	0.6	0.7

Table 5.4 Numerical results

Trial No.	*A*	*B*	*C*	*D*	Displacement	1st natural frequency
1	51	0.9	0.5	0.5	4.0386	44.3
2	51	1	0.6	0.6	3.6812	49.002
3	51	1.1	0.7	0.7	3.327	56.357
4	52.5	0.9	0.6	0.7	3.6108	48.743
5	52.5	1	0.7	0.5	3.8077	47.21

6	52.5	1.1	0.5	0.6	3.765	52.54
7	54	0.9	0.7	0.6	3.7797	47.323
8	54	1	0.5	0.7	3.6214	48.862
9	54	1.1	0.6	0.5	3.8284	47.515

Statistics in Table 5.4 suggested the formulation of the Eq. (5.7) to specify the connections among the design variables and y-axis displacement and the 1st natural frequency of the offered positioner. The outcomes demonstrated that the determination coefficients of the mathematical mode of F_1 as well as F_2 were 99.9% and 98.11%, respectively. Therefore, the regression formula of F_1 is almost precise and the regression formula of F_2 is relatively accurate, as demonstrated in Tables 5.5 and 5.6.

Table 5.5 Estimated regression coefficients for the displacement

Term	Coef	SE Coef	T-worth	P-worth
Cons.	3.2788	9.4341	0.348	0.787
A	0.0393	0.1864	0.211	0.868
B	8.3641	7.3739	1.134	0.460
C	-11.6206	8.6463	-1.344	0.407
D	-1.8087	0.1838	-9.841	0.064
*A***B*	-0.1585	0.1485	-1.067	0.479
*A***C*	0.2258	0.1485	1.520	0.370
*B***C*	-1.2043	1.5753	-0.764	0.584

Table 5.6 Estimated regression coefficients for 1st natural frequency

Term	Coef	SE Coef	T-worth	P-worth
Cons.	-99.786	751.42	-0.133	0.916
A	2.139	14.85	0.144	0.909
B	474.630	587.33	0.808	0.567
C	-541.787	688.67	-0.787	0.576
D	25.825	14.64	1.764	0.328
*A***B*	-8.664	-0.732	0.598	0.598
*A***C*	9.904	11.83	0.837	0.556
*B***C*	23.986	125.47	0.191	0.880

The regression formulas were attained below:

$$F_1 = 3.2788 + 0.0393A + 8.3641B - 11.6206C - 1.8087D - 0.1585AB + 0.2258AC - 1.2043BC \quad (5.8)$$

$$F_2 = -99.786 + 2.139A + 474.630B - 541.787C + 25.825D - 8.664AB + 9.904AC + 23.986BC \quad (5.9)$$

Afterward, ANOVA was employed to identify the contribution of the meaningful parameters on the output features of the developed positioner. Information in Table 5.4 was a reliable source for the use of MINITAB 16.0 software in data analysis according to the RSM.

Table 5.7 ANOVA for the displacement

Source	DF	Inf. (%)	Adj SS	Adj MS	F-ratio	P-worth
A	1	1.83	0.000013	0.000013	0.04	0.868
B	1	14.18	0.000373	0.000373	1.29	0.46
C	1	14.29	0.000523	0.000523	1.81	0.407
D	1	68.2	0.02804	0.02804	96.84	0.064
*A*B*	1	0.92	0.00033	0.00033	1.14	0.479
*A*C*	1	0.43	0.000669	0.000669	2.31	0.37
*B*C*	1	0.06	0.000169	0.000169	0.58	0.584
Error	1	0.1	0.00029	0.00029		
Sum	8	100				

Table 5.8 ANOVA for the 1st natural frequency

Source	DF	Inf. (%)	Adj SS	Adj MS	F-ratio	P-worth
A	1	6.1	0.0381	0.0381	0.02	0.909
B	1	44.25	1.1995	1.1995	0.65	0.567
C	1	4.63	1.1368	1.1368	0.62	0.576
D	1	38.35	5.7165	5.7165	3.11	0.328
*A*B*	1	3.35	0.9852	0.9852	0.54	0.598
*A*C*	1	1.36	1.2874	1.2874	0.54	0.556

*B*C*	1	0.07	0.0671	0.0671	0.04	0.88
Error	1	1.89	1.8368	1.8368		
Sum	8	100				

Tables 5.7 and 5.8 indicate the ANOVA outcomes of the y-axis displacement and the 1st natural frequency, implemented at 5% meaning degree and 95% assurance degree. Figures in Tab. 6.7 suggest that the contribution proportionality on the y-axis deformation F_1 of *D* was best with 68.2%, and its proportion of *C* and *B* were significantly higher at 14.29% and 14.18%, respectively. Meanwhile, the contribution proportionality of other influence factors was much lower. Its proportion of *A*, *A*-*B* association, *A*-*C* association and *B*-*C* association were 1.83%, 0.92%, 0.43% and 0.06%, correspondingly. Accordingly, it is necessary to strictly control *D* for an improvement of F_2. Moreover, details in Table 8 illustrated a higher contribution proportion of *B* and *D*, compared to other design's parameters, on the 1st natural frequency F_2, with 44.25% and 38.35%, respectively. Conversely, its influence ratio on F_2 of *A* and *C*, association between *A* and *B*, association between *A* and C as well as association *B* and *C* were small with 6.1%, 4.63%, 3.35%, 1.36% and 0.07%, respectively. As a result, it is of necessity to strictly control *B* and *D* to guarantee a better 1st natural frequency. Furthermore, the contribution percentage of error was 0.1% and 1.89% for F_1 as well as F_2, correspondingly.

5.2.4.2. Parameter optimization using an integrated approach of TM, RSM and NSGA-II

According to Eqs. (5.8) and (5.9), MATLAB 2017 software was utilized to propose the integrated approach of RSM and NSGA-II. The result listed three potential options for the best resolution, as demonstrated in Tab. 5.9. 1st potential was selected as the greatest optimized design because it it completely convinces the above design targets such as the y-axis displacement was 3.862 mm, the 1st natural frequency was 45.983 and the smallest safety factor was higher than 1.5. Additionally, the optimized factors were also detected at *A* = 54 mm, *B* = 0.962 mm, *C* = 0.574 mm as well as *D* = 0.562 mm.

Table 5.9 Comparison among potential optimization candidates

Key variables	1st potential	2nd potential	3rd potential
A	54	52.957	53.087
B	0.962	0.933	0.934
C	0.574	0.517	0.59
D	0.562	0.598	0.56
F_1 (mm)	3.862	3.845	3.858
F_2 (Hz)	45.983	46.29	45.7

5.2.5. Validation

A simulation validation was implemented through the use of a 3D model based on the optimized parameters of 1st potential in Tablele 5.9, with the similar limitations and the similar input deformation. The hybrid approach's predicted outcomes were utilized to esTablelish the results of FEA model. The maximum y-axis deformation was 3.862 mm and the 1st natural frequency was 45.983. Figures in Tablele indicated that the divergence between optimized result and FEA test was not significant, with 2.1932% for the y-axis deformation error and 0.05% for the 1st natural frequency error. The conclusion of the comparison illustrated the advances of the proposed hybrid algorithm as an appropriate method to examine input – output response connections in optimization of multi-target problem of the developed XY positioner. Accordingly, the suggested method is reliable and efficient enough to be used in finding optimal solutions for the XY positioner.

Tablele 5.10 Error between predicted outcome and FEA outcome

Features	Predicted outcome	FEA outcome	Error (%)
F_1 (mm)	3.862	3.9486	2.1932
F_2 (Hz)	45.983	46.006	0.05

5.2.6. Comparison with previous study

Statistics for intensification proportion in this research was put in a comparison with those in the existing studies, as presented in Tablele 5.11. The outcome was positive with a higher intensification proportion in the current study, at 20.78 to be precise.

Tablele 5.11 Comparison result with previous study

Studies	Intensification proportion
[143]	15.51
[144]	16.4
This study	20.78

5.2.7. Achieved results

This chapter presented the procedure of proposing a new XY positioner utilized for locating the specimens in nanoindentation testing device, by combining the four-lever mechanism and zigzag springs to generate a better output displacement intensification. For an enhancement of the working stroke, the geometrical factors of a XY-positioner were optimized using the TM, RSM, and NSGA-II. The optimization outcomes were detected at A= 54 mm, B= 0.962 mm, C= 0.574 mm, D= 0.562 mm, F_1= 3.862 mm and F_2= 45.983 mm. Additionally, it is demonstrated that errors between the optimization outcomes and the FEA validations for the 1st natural frequency and y-axis displacement were 2.1932% and 0.05%, respectively. The validation result of FEA was seen approaching to the forecasted one in the hybrid approach. Future studies will fabricate a prototype and examine its behaviors to check the FEA results. The displacement intensification proportion of developed positioner was higher than that of several previous studies [143,144].

5.3. Development and optimization of a compliant 02-DOF positioner

5.3.1. Conceptual design

In order to contribute the new design of other XY positioner for locating the specimens with large output displacement and high 1st natural frequency to enhance the reaction velocity and the working stroke of the offered positioner, the second design alternative of a XY-positioner is developed based on the eight-lever displacement intensification combined elliptic joints and parallel guiding mechanism.

The second 02-DOF positioner includes four-lever displacement magnifier combined elliptic joints module and a parallel guiding mechanism module. Two main technical performances of the first 02-DOF positioner are expressed as follows.

- The safety factor is higher than 1.5.
- The first natural frequency is more than 100 (Hz).

5.3.1.1. Design scheme of 1-DOF mechanism

The operation principles of a 1-DOF positioner with an eight-lever displacement intensification structure and a parallel structure were described in Figure 5.5. The amplifier is employed to magnitude the stage's displacement while the parallelogram is for producing a proper transition in expected motions and reducing unexpected ones. Precisely, this scheme aims to propose an innovative design with a large intensification proportion and small decoupling error.

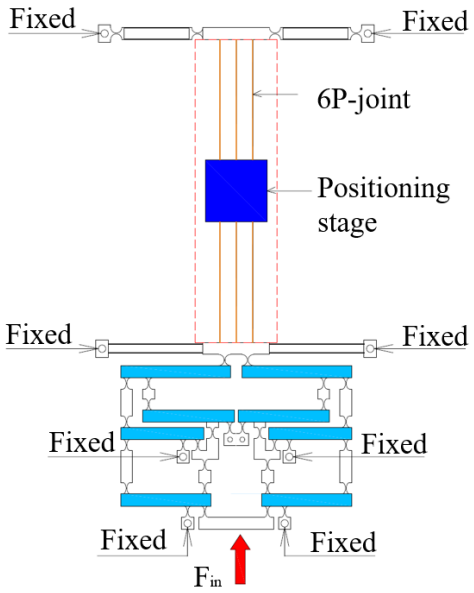

Figure 5.5. Schematic for 1-DOF symmetrical configuration.

5.3.1.2. Operation scheme of 2-DOF stage

The action principles and design diagram of a offered XY-positioner are demonstrated in Fig. 5.6(a) [145], with reference to those of the the 1-DOF stage in Fig. 5.5. Basically, the 2-DOF positioner's design is a module-based schematic with the module being symmetrically arranged in both horizontal and vertical directions. As a result, the 2-DOF stage comprises of 4 modules of the 1-DOF platform and the offered positioner is where to position the specimens in nanoindentation testing device. Fig. 5.6(a) illustrates the P-joint, or the so-called prismatic joint, with a leaf joint to produce a large deformation while the remaining positions were made from the elliptic joints for a guarantee of good qualities. The 2-DOF stage's working mechanism originally in reference to the deformations of the elliptic hinges, right circular joints and P-joints as well as regulates by PZA actuator. The chief dimensional factors of the suggested positioner is presented in Fig. 5.6(b) [145] while their values are demonstrated in Tablele 5.12.

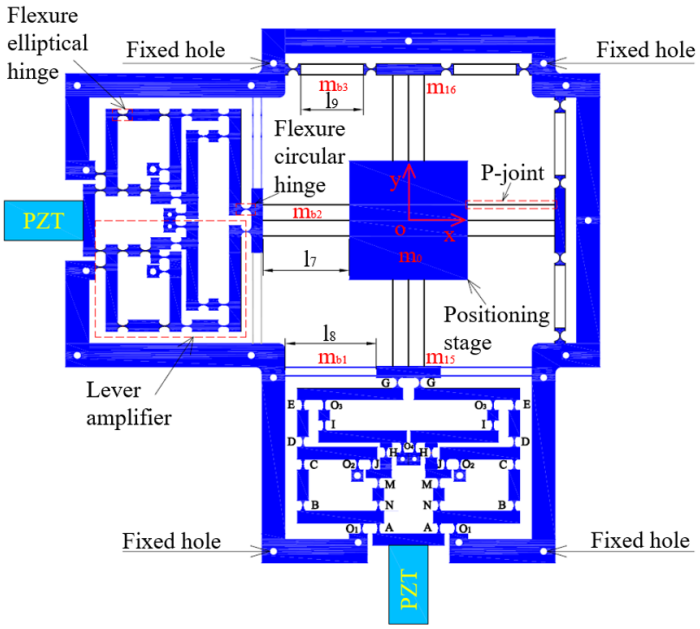

(a)

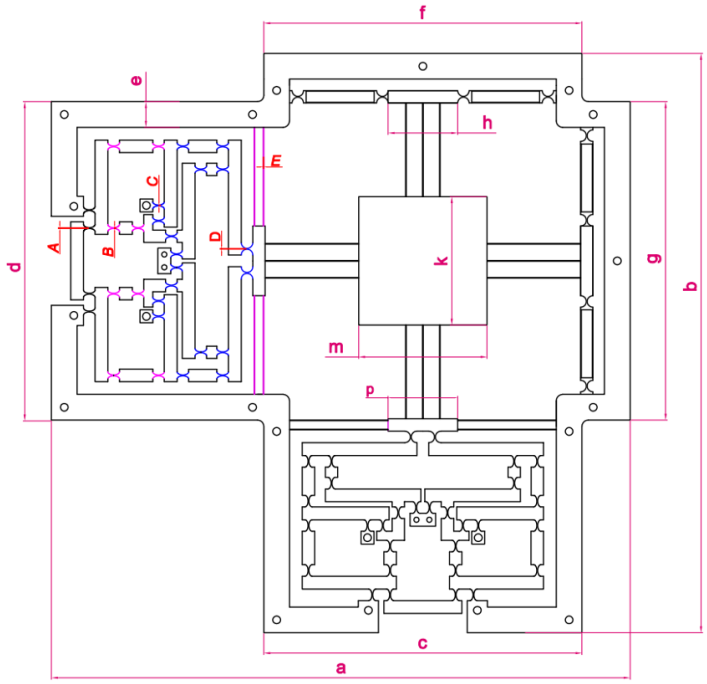

(b)

Figure 5.6. Offered XY-positioner: (a) Design diagram, (b) chief dimensional parameters.

Tablele 5.12 Chief geometrical factors of the offered XY-positioner

Parameter	Worth	Factor	Worth	Unit
a	451	*k*	100	mm
b	451	*m*	100	mm
c	248	*p*	54	mm

d	248	*A*	*0.9≤A≤1.1*	mm
e	20	*B*	*0.7≤B≤0.9*	mm
f	248	*C*	*0.6≤C≤0.8*	mm
g	248	*D*	*0.6≤D≤0.8*	mm
h	54	*E*	*0.6≤E≤0.7*	mm

Fig. 5.6(b) and Tablele 1 indicate that the factors *A*, *B* and *C* in various colours present the thickness of elliptic joints at first lever floor, second lever floor as well as third and fourth lever floors, correspondingly. Furthermore, *D* is the thickness of right circular joint at end of fourth lever floor, and *E* is the thickness of rectangular joint of the parallel driving structure. Figures for the expected technology requirements of the suggested positioner are given in Table 5.13.

Table 5.13 The expected technical specifications of XY-positioner

Technical specifications	Expected outcomes
Working dimension	451x451 (mm)
Desired operating travel	770x770 (μm)
Expected resonant frequency	100 (Hz)
Expected displacement magnification proportion	7
Decoupling error	0.04 (%)

5.3.2. Proposed methodology

The modeling as well as dimensional optimization synthesis approach for the compliant XY-positioner that was offered in this part was an outcome of combining analytical methods and metaheuristic algorithms. The kineostatic and dynamic formulas for the XY-positioner were established in the current study by combining the deformable mechanics theory, the elastic beam theory, and the Lagrange technique.

5.3.2.1. Modeling and dimensional optimization synthesis

A flowchart to illustrate the proficient method [145] for modeling and dimensional optimization synthesis for the offered positioner is presented in Fig. 5.7. This proposed hybrid approach was developed by Dang et al. Its procedure includes the following stages:

- Stage 1: A theoretical design of the XY-positioner is constructed by kinematic serial scheme.
- Stage 2: Propose the technical requirements of the offered XY-positioner.
- Stage 3: Set up the kineostatic and dynamic arithmetical formulas for the XY-positioner by applying the deformable mechanics theory, the elastic beam theory, and Lagrange technique.
- Stage 4: Validate the precisions of arithmetical formulas by FEA method.
- Stage 5: If the kinematic and dynamic formulas are accurate, the calculational procedure continues with next stage. Otherwise, the procedure goes back the stage 1.
- Stage 6: Define the chief variables, targets and constraint functions for the XY-positioner.
- Stage 7: The NNA algorithm is exploited to optimize the factors of the XY-positioner for advancing the dynamic performance of the developed positioner.
- Stage 8: Optimized outcomes are confirmed by FEM method. If it fulfilled, the offered positioner will be constructed.
- Stage 9: The dynamic characteristic of the XY-positioner is compared with the prior various positioners.

5.3.2.2. Neural network algorithm

Motivated by the Artificial neural network (ANN), a novel optimizer called Neural network algorithm (NNA) was proposed [121]. It is viewed as a metaheuristic optimizer which builds on populations DE algorithm [146], PSO algorithm [147], NSGA-III [148], and so on. In order to achieve the best overall ideal results, this method seeks to minimize errors between the outcome and estimated values. A flowchart to describe the NNA [145] is shown in Fig. 5.8.

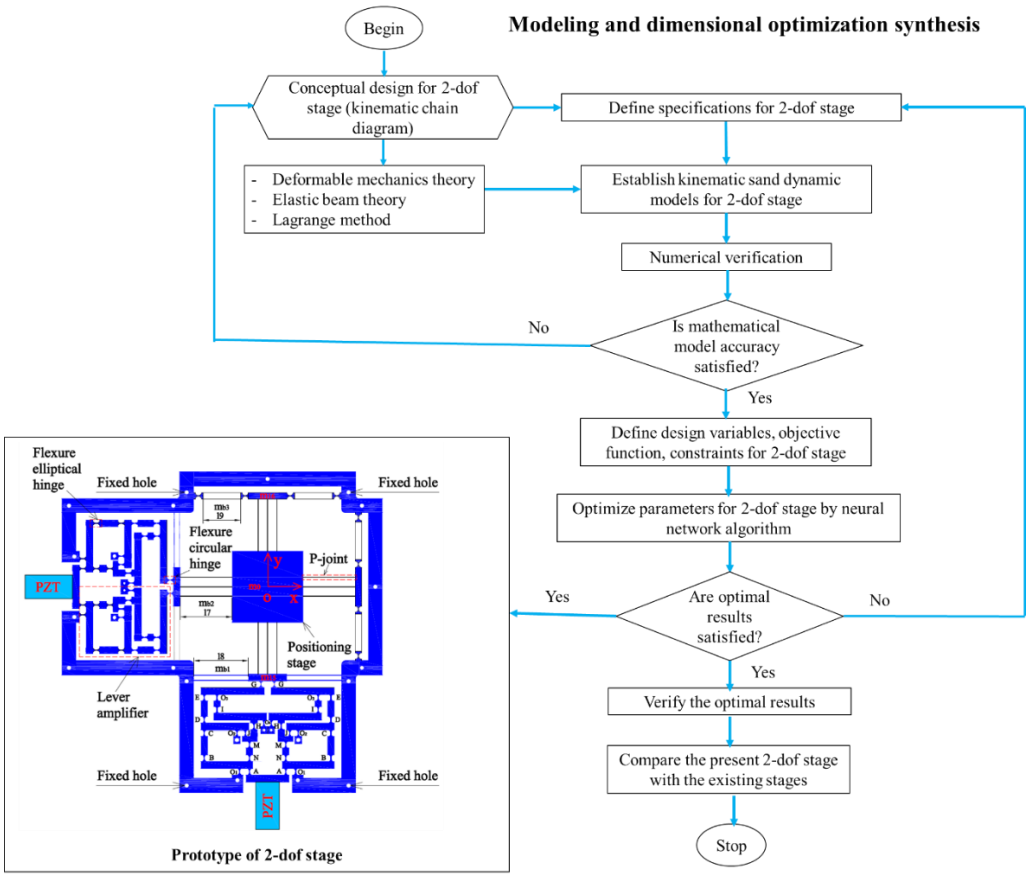

Figure 5.7. Offered XY-positioner modeling and optimization synthesis flowchart.

A pattern solution (P_s) is identified as.

$$P_s = [x_1, x_2, ..., x_d], \ d\text{: problem size.} \tag{5.10}$$

A matrix of pattern resolution (X) is determined by.

$$X = \begin{bmatrix} x_1^1 & x_2^1 & \cdots & x_D^1 \\ \vdots & & \ddots & \vdots \\ x_1^{npop} & x_2^{npop} & \cdots & x_D^{npop} \end{bmatrix}, \ npop \text{ is the population number.} \tag{5.11}$$

The i^{th} cost of function is established as follows.

$$C_i = f\left(x_1^i, x_2^i, ..., x_D^i\right). \tag{5.12}$$

A weight matrix is defined by.

$$W(t) = \begin{bmatrix} W_1^1 & W_2^i & \cdots & W_D^{npop} \\ \vdots & & \ddots & \vdots \\ W_{npop}^1 & W_{npop}^i & \cdots & W_{npop}^{npop} \end{bmatrix} = \begin{bmatrix} W_{11} & \cdots & W_{i1} & \cdots & W_{npop1} \\ \vdots & & & \ddots & \vdots \\ W_{1\ npop} & & W_{i\ npop} & \cdots & W_{npop\ npop} \end{bmatrix}. \tag{5.13}$$

The weight value is defined by.

$$\sum_{j=1}^{npop} w_{ij}(t) = 1, \qquad i \in npop \tag{5.14}$$

$$w_{ij} \in U(0,1), \quad i, j \in npop \tag{5.15}$$

A new matrix (X) is formulated as.

$$X_j^{new}(t+1) = \sum_{t=1}^{npop} w_{ij}(t) \times X_t(t), \quad j \in npop. \tag{5.16}$$

$$X_i(t+1) = X_i(t) + X_i^{new}(t+1), \quad i \in npop. \tag{5.17}$$

The following formula is exploited to update the weight matrix.

$$W_t^{update}(t+1) = W_i(t) + 2 \times rand \times \left(W^{target}(t) - W_i(t)\right), \quad i \in nppop \tag{5.18}$$

An exploration bias occurs when the weighting and new solution are affected. The function operator is quantified by taking into account that $rand > \psi$ (ψ is the resolutions proportion).

$$X_t^*(t+1) = X_i(t+1) + 2 \times rand \times \left(X^{target}(t) - X_i(t+1)\right), \quad i \in nppop \tag{5.19}$$

The NNA is exploited in this study with a primary population of 20, a maximum repetition limit of 500, and a ψ of 1.

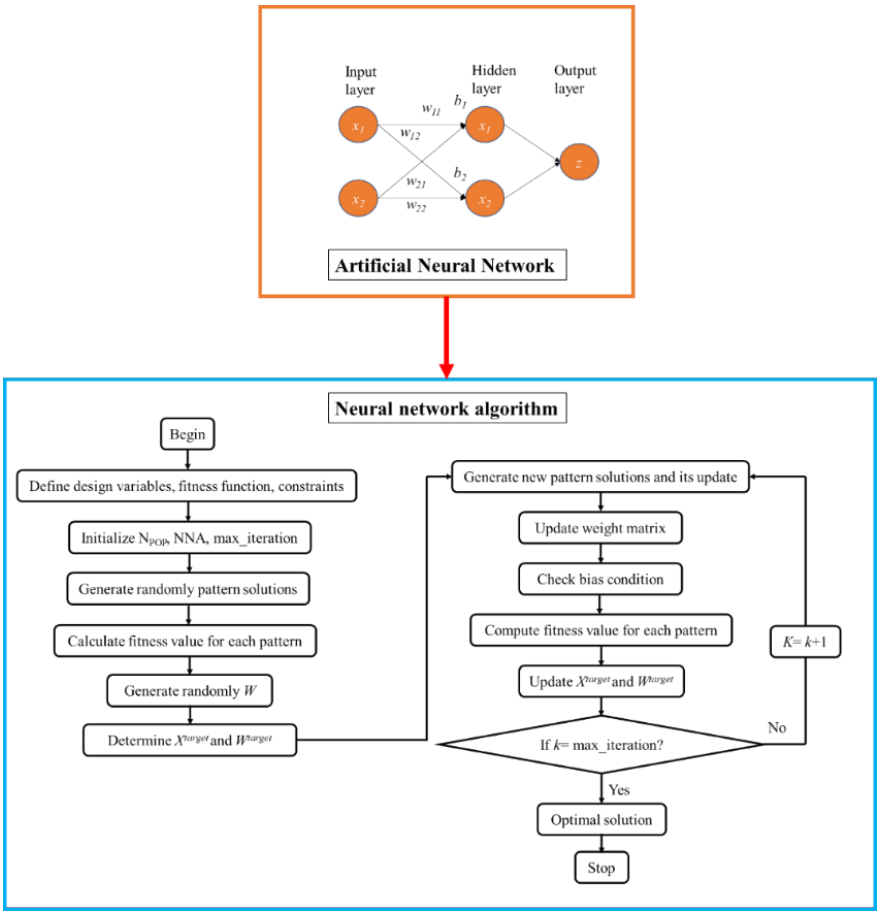

Figure 5.8. Schematic diagram of neural network algorithm.

5.3.3. Results and discussion

5.3.3.1. Kinetostatics and dynamics modeling

The behaviors of the 2-DOF positioner were assessed by performing the kinetostatics and dynamics, with the analysis being conducted through the application of the elastic beam theory, Lagrange method and deformable mechanics theory. This study also analyzed the specifications of the 2-DOF positioner such as displacement intensification proportion, stiffness, working travel, and resonant frequency.

Step 1: Modeling of magnification proportion and input stiffness

Figure 5.9 depicts a modified displacement lever magnifier (MDLD), also known as a version of the lever magnifier. It comprises of major factors of the different amplification floors' s lever lengths. As the structure is symmetrical, a half of displacement magnifier is selected for an analysis of quality characteristics of the developed XY-positioner.

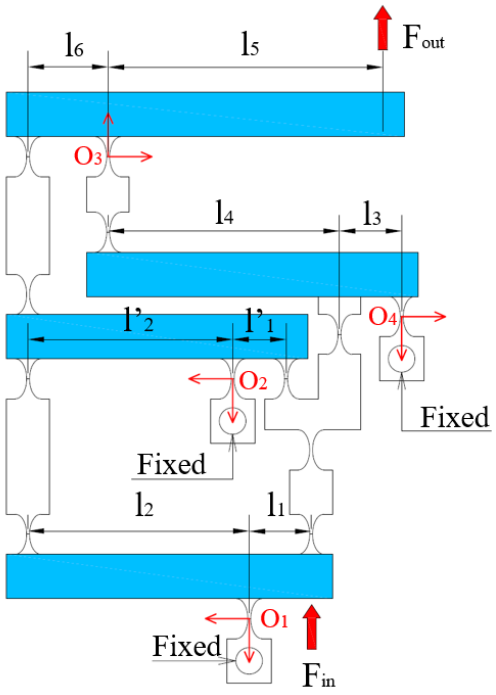

Figure 5.9. A hybrid magnification structure.

Fig. 5.10 illustrates a schematic diagram of the MDLD with three major levers, namely the lever amplification mechanism #1,2 and 3 (LAM1, LAM2 and LAM3). Besides, the parameters of lengths of levers (l_1, l_2, l_1', l_2', l_3, l_4, l_5, and l_6) are also in Fig. 5.10 in which O_1, O_2, O_3, and O_4 are the rotation centers of the levers.

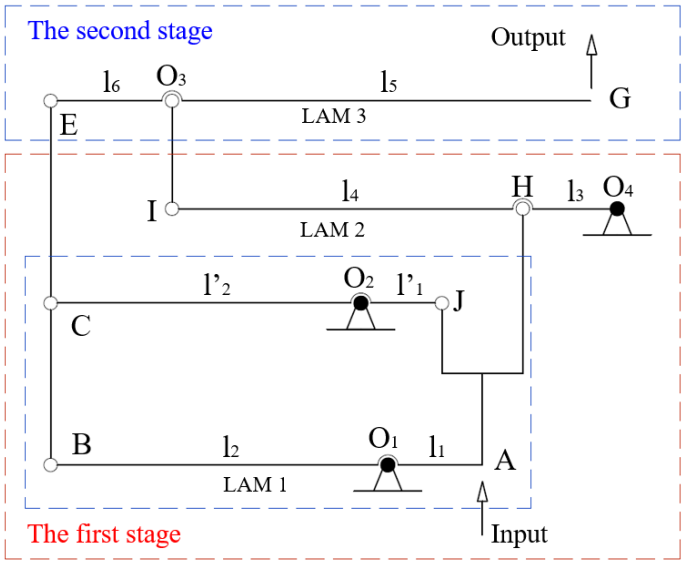

Figure 5.10. The adjusted displacement lever magnification structure's diagram.

The operation of MDLD depends on three levers LAM1, LAM2, and LAM3, as indicated in Fig. 5.10, and the amplifier's output displacement is determined in the following formula [149].

$$\delta_{out}=\left[\frac{l_5}{l_6}\left(\frac{l_2}{l_1}+\frac{l_4}{l_3}+1\right)+\frac{l_4}{l_3}+1\right]\delta_{in}, \tag{5.20}$$

in which δ_{in} and δ_{out} denote the input and output displacement, respectively. Then, the intensification proportion is quantified as:

$$A=\frac{l_5}{l_6}\left(\frac{l_2}{l_1}+\frac{l_4}{l_3}+1\right)+\frac{l_4}{l_3}+1, \tag{5.21}$$

where *A* denotes the displacement intensification proportion.

The goal of creating a significant deformation and minimizing the stage's unexpected motions is achieved as triplet types of compliant joints are strategically positioned in the initial design. Right flexure circular joint dimensions are illustrated in Fig. 5.11, which also explains how force and torque recovery while the structure is in use.

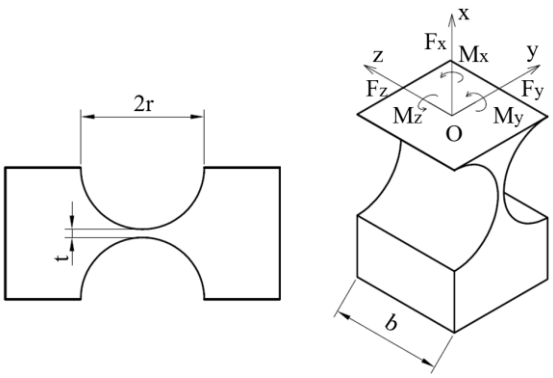

Figure 5.11. A right circular joint schematic.

In the investigation of the structure's input rigidity, the lateral force and the torque are exploited to generate the general spring with bending rigidity ($K^{c}_{\delta xFx}$) and the torsion rigidity ($K^{c}_{\theta zMz}$), respectively. The linear rigidity ($K^{c}_{\theta yMy}$) is formulated by the axial force for the right circular joint.

Moreover, the leaf beam's torsion and linear rigidity are symbolized by $K^{l}_{\theta zMz}$ and $K^{l}_{\theta yMy}$.

Correspondingly, the compliant elliptic joint is aligned with bending rigidity ($K^{e}_{\delta_X F_X}$) generated by lateral force, torsion rigidity ($K^{e}{}_{\theta zMz}$) generated by the torque, and linear rigidity ($K^{e}_{\theta yMy}$) produced by the axial force [150].

$$K^{c}_{\theta zMz} = \frac{2Ebt^{2.5}}{9\pi r^{0.5}}, \tag{5.22}$$

$$K^{c}_{\theta yMy} = \frac{Ebt^{0.5}}{\pi\left(r^{0.5} - 0.5t^{0.5}\right)}, \tag{5.23}$$

$$K^{c}_{\delta xFx} = \frac{2Ebt^{2.5}}{3\pi r^{1.5}\left(3r + t\right)}, \tag{5.24}$$

Major components including length, width, and thickness, as well as the direction of force and torque operating on the compliant rectangular joint, are shown in a simplified configuration scheme of the compliant rectangular joint in Figure 5.12.

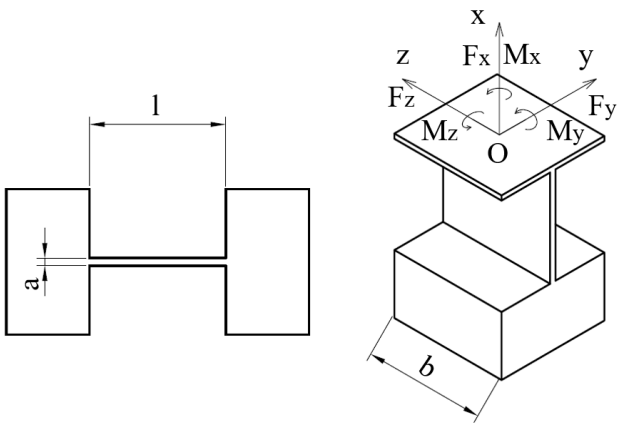

Figure 5.12. A rectangular joint schematic.

Next, the under formulas demonstrate a detailed calculation of the compliant elliptic joint's rigidity that bends in various axes.

$$K^{e}_{\theta zMz} = \frac{2Eba_X^2}{3 \in f\left(\beta_y\right)}, \tag{5.25}$$

$$K^{e}_{\theta yMy} = \frac{Eb^3}{12 \in g\left(\beta_y\right)}, \tag{5.26}$$

$$K^{e}_{\delta_X F_X} = \frac{Eb}{\in g\left(\beta_y\right)}, \tag{5.27}$$

$$\beta_X = \frac{t}{2a_X}, \tag{5.28}$$

$$\beta_y = \frac{t}{2a_y}, \tag{5.29}$$

$$\in = \frac{a_X}{a_y} = \frac{\beta_y}{\beta_x}, \tag{5.30}$$

$$f\left(\beta_y\right) = f\left(\in \beta_x\right) = \frac{1}{2\beta_y + \beta_y^2}\left(\frac{3+4\beta_y+2\beta_y^2}{\left(1+\beta_y\right)\left(2\beta_y+\beta_y^2\right)} + \frac{6\left(1+\beta_y\right)}{\left(\sqrt{2\beta_y+\beta_y^2}\right)^3}\tan^{-1}\sqrt{\frac{2+\beta_y}{\beta_y}}\right), \tag{5.31}$$

$$g\left(\beta_y\right) = g\left(\in \beta_x\right) = \frac{2\left(1+\beta_y\right)}{\sqrt{2\beta_y+\beta_y^2}}\tan^{-1}\sqrt{\frac{2+\beta_y}{\beta_y}} - \frac{\pi}{2}, \tag{5.32}$$

in which *b* represents the compliant joint's thickness, *E* for the fabricating material's elastic modulus, *r* for a compliant circular notched joint's radius and *t* for the circular/elliptic joint's smallest width. Additionally, *a* and *l* denote the width and length of

the leaf beam, correspondingly. The dimensionless factor for the elliptic joint geometry a_x is symbolized by (β_x) and (a_y) by (β_y). The multiplication factor of proportion for major to minor axes is denoted by sign ($\in$) while sign ($f(\beta_x)$) and ($f(\beta_y)$) is the dimensionless compliance factor for (β_x) and (β_y), correspondingly.

The equivalent input force (F_{in}) is determined by applying an input displacement (δ_{in}) to the positioner's input end and using the equation below to compute it.

$$F_{in} = K_{in}\delta_{in}, \tag{5.33}$$

where K_{in} denotes the micromanipulator's input stiffness.

Figure 5.13 explains the primary and operating statuses of MDLD. The deformation angles created by location alteration of multi-lever structure in present various grades of the structure's deformation while in operation.

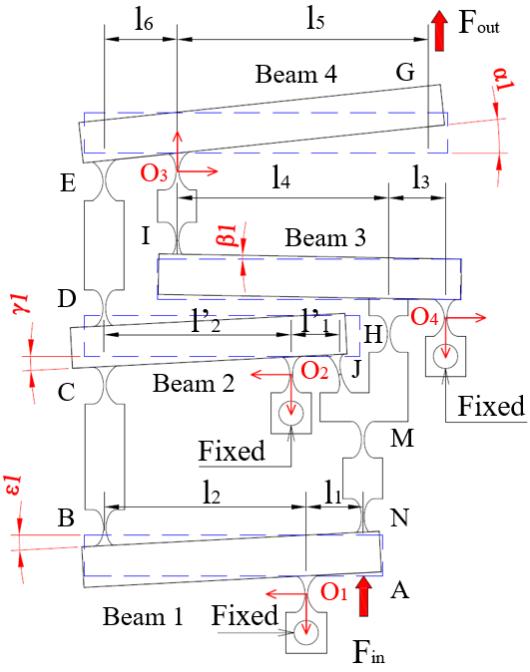

Figure 5.13. Scheme of the half hybrid intensification structure's force and deformation.

A diagram to illustrate the force analysis of 4th beam, 3rd beam, 2nd beam and 1st beam in a lever intensification structure is presented in Figs. (5.14-17), providing information of the applied force, moment, rotary angle and the elastic joint's deformation. Only half of the intensification structure is examined because of the symmetrical structure. Fig. 5.13

depicts the major force analysis for the intensification structure while Fig. 5.14 explains the formation of formulas by the mechanic balance status of 4th beam.

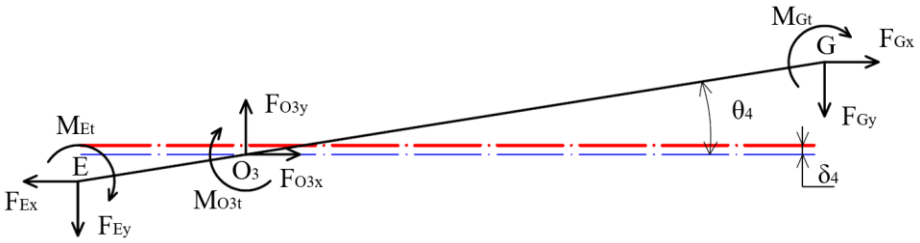

Figure 5.14. Forced diagram of 4th beam.

The subsequent force balance formulas can be formulated below

$$F_{O3y} = F_{Ey} + F_{Gy}, \tag{5.34}$$

$$F_{Ey} l_6 = F_{Gy} l_5 + M_{O3t} + M_{Gt} + M_{Et}, \tag{5.35}$$

Particularly, the bending moments of the points O_3, G, and E are denoted as M_{O3t}, M_{Gt}, and M_{Et}. Three numbers F_{O3y}, F_{Ey} and F_{Gy} forces are operating at points O_3, E, and G in the y- direction while the system is in operation, correspondingly. The displacement worth at point G is created by combining the displacement because of joints at O_3 rotating around its axis ($l_5\theta_4$) and displacement because of drift (δ_4). Moreover, by multiplying rigidity by deformation, the forces F_{O3y} as well as F_{Gy} can be identified, as presented in the below formulas.

$$F_{O3y} = K_{O3x}\delta_4, \tag{5.36}$$

$$F_{Gy} = K_{Gy}\left(l_5\theta_4 - \delta_4\right), \tag{5.37}$$

$$M_{O3t} = K_{O3t}\theta_4, \tag{5.38}$$

$$M_{Gt} = K_{Gt}\theta_4, \tag{5.39}$$

$$M_{Et} = K_{Et}\theta_4, \tag{5.40}$$

where K_{O3x} denotes the lateral bending rigidity by the force F_{O3y}, and K_{Gl} denotes the G point's output rigidity of the MDLM. Furthermore, the rotary rigidities K_{O3t}, K_{Gt}, and K_{Et} are the rigidities of the compliant joints at points O_3, G, and E, correspondingly.

The outcomes are attained by replacing Eqs. (5.36) to (5.37) into Eq. (5.34).

$$K_{O3x}\delta_4 = F_{Ey} + K_{Gy}\left(l_5\theta_4 - \delta_4\right), \tag{5.41}$$

$$\delta_4 = \frac{F_{Ey} + K_{Gy} l_5\theta_4}{K_{O3x} + K_{Gy}}, \tag{5.42}$$

The outcomes are attained by replacing Eqs. (5.37) to (5.40) into Eq. (5.35).

$$F_{Ey}l_6 = K_{Gy}l_5\left(l_5\theta_4 - \delta_4\right) + K_{O3t}\theta_4 + K_{Gt}\theta_4 + K_{Et}\theta_4, \tag{5.43a}$$

$$F_{Ey}l_6 + K_{Gy}l_5\delta_4 = \left(K_{Gy}l_5^2 + K_{O3t} + K_{Gt} + K_{Et}\right)\theta_4, \tag{5.43b}$$

where F_{Ey}, F_{O3y} as well as F_{Gy} denote the forces generated when the structure operates at points E, O_3, and G, correspondingly.

By replacing Eq. (5.42) into the preceding Eq. (5.43b), the θ_4 and δ_4 can be attained.

$$F_{Ey}l_6 + K_{Gy}l_5\frac{F_{Ey} + K_{Gy}l_5\theta_4}{K_{O3x} + K_{Gy}} = \left(K_{Gy}l_5^2 + K_{O3t} + K_{Gt} + K_{Et}\right)\theta_4, \tag{5.44}$$

$$F_{Ey}l_6\left(K_{O3x} + K_{Gy}\right) + K_{Gy}l_5\left(F_{Ey} + K_{Gy}l_5\theta_4\right) = \left(K_{O3x} + K_{Gy}\right)\left(K_{Gy}l_5^2 + K_{O3t} + K_{Gt} + K_{Et}\right)\theta_4, \tag{5.45}$$

$$\theta_4 = \frac{l_6\left(K_{O3x} + K_{Gy}\right) + K_{Gy}l_5}{\left(K_{O3x} + K_{Gy}\right)\left(K_{Gy}l_5^2 + K_{O3t} + K_{Gt} + K_{Et}\right) - K_{Gy}^2l_5^2}F_{Ey}, \tag{5.46}$$

$$\delta_4 = \frac{F_{Ey} + K_{Gy}l_5\dfrac{l_6\left(K_{O3x} + K_{Gy}\right) + K_{Gy}l_5}{\left(K_{O3x} + K_{Gy}\right)\left(K_{Gy}l_5^2 + K_{O3t} + K_{Gt} + K_{Et}\right) - K_{Gy}^2l_5^2}F_{Ey}}{K_{O3x} + K_{Gy}}, \tag{5.47a}$$

$$\delta_4 = \frac{\left(K_{O3x} + K_{Gy}\right)\left(K_{Gy}l_5^2 + K_{O3t} + K_{Gt} + K_{Et}\right) - K_{Gy}^2l_5^2 + K_{Gy}l_5\left(l_6\left(K_{O3x} + K_{Gy}\right) + K_{Gy}l_5\right)}{\left(K_{O3x} + K_{Gy}\right)\left[\left(K_{O3x} + K_{Gy}\right)\left(K_{Gy}l_5^2 + K_{O3t} + K_{Gt} + K_{Et}\right) - K_{Gy}^2l_5^2\right]}F_{Ey}, \tag{5.47b}$$

$$\delta_4 = \frac{K_{Gy}l_5^2 + K_{O3t} + K_{Gt} + K_{Et} + K_{Gy}l_5l_6}{\left(K_{O3x} + K_{Gy}\right)\left(K_{Gy}l_5^2 + K_{O3t} + K_{Gt} + K_{Et}\right) - K_{Gy}^2l_5^2}F_{Ey}, \tag{5.47c}$$

The intensification proportion and input stiffness of 4th beam are calculated by.

$$\lambda_4 = \frac{l_5\theta_4 - \delta_4}{l_6\theta_4 + \delta_4}, \tag{5.48}$$

$$K_{in4} = \frac{F_{Ey}}{l_6\theta_4 + \delta_4}, \tag{5.49}$$

The subsequent formulas can be attained by replacing Eqs. (5.46) and (5.47c) into Eqs. (5.48) and (5.49).

$$\lambda_4 = \frac{l_5\left[l_6\left(K_{O3x} + K_{Gy}\right) + K_{Gy}l_5\right] - \left(K_{Gy}l_5^2 + K_{O3t} + K_{Gt} + K_{Et} + K_{Gy}l_5l_6\right)}{l_6\left[l_6\left(K_{O3x} + K_{Gy}\right) + K_{Gy}l_5\right] + \left(K_{Gy}l_5^2 + K_{O3t} + K_{Gt} + K_{Et} + K_{Gy}l_5l_6\right)}, \tag{5.50a}$$

$$\lambda_4 = \frac{l_5l_6\left(K_{O3x} + K_{Gy}\right) - \left(K_{O3t} + K_{Gt} + K_{Et} + K_{Gy}l_5l_6\right)}{l_6\left(K_{O3x} + K_{Gy}\right) + 2K_{Gy}l_5l_6 + K_{Gy}l_5^2 + K_{O3t} + K_{Gt} + K_{Et}}, \tag{5.50b}$$

$$\lambda_4 = \frac{l_5 l_6 K_{O3x} - K_{O3t} - K_{Gt} - K_{Et}}{K_{Gy}\left(l_5 + l_6\right)^2 + K_{O3x} l_6^2 + K_{O3t} + K_{Gt} + K_{Et}}, \tag{5.50c}$$

$$K_{in4} = \frac{\left(K_{O3x} + K_{Gy}\right)\left(K_{Gy} l_5^2 + K_{O3t} + K_{Gt} + K_{Et}\right) - K_{Gy}^2 l_5^2}{K_{Gy}\left(l_5 + l_6\right)^2 + K_{O3x} l_6^2 + K_{O3t} + K_{Gt} + K_{Et}}, \tag{5.51}$$

Figure 5.25 is a diagram to illustrate the force analysis of 3rd beam.

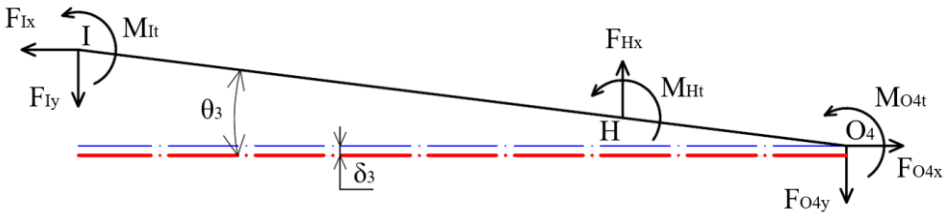

Figure 5.15. Third beam forced scheme.

The force and moment are determined by considering the balance status of 3rd beam.

$$F_{Hy} = F_{Iy} + F_{O4y}, \tag{5.52}$$

$$F_{Hy} l_3 = F_{Iy}\left(l_3 + l_4\right) + M_{It} + M_{Ht} + M_{O4t}, \tag{5.53}$$

where M_{O4t}, M_{It}, as well as M_{Ht} denote moments of bending of the points O_4, I, and H. Furthermore, F_{O4y}, F_{Hy} as well as F_{Iy} are forces operating at point O_4, H and I along the y-axis, correspondingly.

The displacement worth at point I is a integration of both deformations comprising deformation based on joints at O_4 revolving surrounding its axis ($(l_3 + l_4)\theta_3$) and deformation based on drift (δ_3).

Additionally, the forces F_{O4y} as well as F_{Iy} are identified as follows.

$$F_{O4y} = K_{O4x}\delta_3, \tag{5.54}$$

$$F_{Iy} = K_3\left[\left(l_3 + l_4\right)\theta_3 + \delta_3\right], \tag{5.55}$$

$$M_{O4t} = K_{O4t}\theta_3, \tag{5.56}$$

$$M_{It} = K_{It}\theta_3, \tag{5.57}$$

$$M_{Ht} = K_{Ht}\theta_3, \tag{5.58}$$

in which K_{O4x} denotes the lateral bending rigidity via force F_{O4y}, and K_3 denotes the I point's output rigidity. K_{O4t} is the O_4 point's rotary rigidity, K_{It}, and K_{Ht} are the rotary rigidity I, and H, correspondingly.

The outcomes are attained by replacing Eqs. (5.54) and (5.55) into Eqs. (5.52).

$$F_{Hy} = K_3\left(\left(l_3 + l_4\right)\theta_3 + \delta_3\right) + K_{O4x}\delta_3, \tag{5.59}$$

$$\delta_3 = \frac{F_{Hy} - K_3\left(l_3 + l_4\right)\theta_3}{K_{O4x} + K_3}, \tag{5.60}$$

The outcomes are attained by replacing Eqs. (5.55) to (5.58) into Eq. (5.53).

$$F_{Hy}l_3 = K_3\left(l_3 + l_4\right)\left(\left(l_3 + l_4\right)\theta_3 + \delta_3\right) + K_{O4t}\theta_3 + K_{It}\theta_3 + K_{Ht}\theta_3, \tag{5.61a}$$

$$F_{Hy}l_3 = K_3\left(l_3 + l_4\right)\delta_3 + \left(K_3\left(l_3 + l_4\right)^2 + K_{O4t} + K_{It} + K_{Ht}\right)\theta_3, \tag{5.61b}$$

The θ_3 as well as δ_3 are attained by replacing Eq. (5.60) into Eq. (5.61b).

$$F_{Hy}l_3 = K_3\left(l_3 + l_4\right)\frac{F_{Hy} - K_3\left(l_3 + l_4\right)\theta_3}{K_{O4x} + K_3} + \left[K_3\left(l_3 + l_4\right)^2 + K_{O4t} + K_{It} + K_{Ht}\right]\theta_3, \tag{5.62a}$$

$$F_{Hy}l_3\left(K_{O4x} + K_3\right) - K_3\left(l_3 + l_4\right)F_{Hy} = \left[\left(K_{O4x} + K_3\right)\left[K_3\left(l_3 + l_4\right)^2 + K_{O4t} + K_{It} + K_{Ht}\right] - K_3^2\left(l_3 + l_4\right)^2\right]\theta_3, \tag{5.62b}$$

$$\theta_3 = \frac{l_3\left(K_{O4x} + K_3\right) - K_3\left(l_3 + l_4\right)}{\left(K_{O4x} + K_3\right)\left[K_3\left(l_3 + l_4\right)^2 + K_{O4t} + K_{It} + K_{Ht}\right] - K_3{}^2\left(l_3 + l_4\right)^2}F_{Hy}, \tag{5.63}$$

$$\delta_3 = \frac{F_{Hy} - K_3\left(l_3 + l_4\right)\dfrac{l_3\left(K_{O4x} + K_3\right) - K_3\left(l_3 + l_4\right)}{\left(K_{O4x} + K_3\right)\left[K_3\left(l_3 + l_4\right)^2 + K_{O4t} + K_{It} + K_{Ht}\right] - K_3^2\left(l_3 + l_4\right)^2}F_{Hy}}{K_{O4x} + K_3}, \tag{5.64a}$$

$$\delta_3 = \frac{K_3\left(l_3 + l_4\right)^2 - K_3l_3 + K_{O4t} + K_{It} + K_{Ht}}{\left(K_{O4x} + K_3\right)\left[K_3\left(l_3 + l_4\right)^2 + K_{O4t} + K_{It} + K_{Ht}\right] - K_3^2\left(l_3 + l_4\right)^2}F_{Hy}, \tag{5.64b}$$

In the case of 3rd beam, the intensification proportion and input stiffness are conveyed as.

$$\lambda_3 = \frac{\left(l_3 + l_4\right)\theta_3 + \delta_3}{l_3\theta_3 + \delta_3}, \tag{5.65}$$

$$K_{in3} = \frac{F_{Hy}}{l_3\theta_3 + \delta_3}, \tag{5.66}$$

The subsequent formulas are attained by replacing Eqs. (5.63) and (5.64b) into Eqs. (5.65) and (5.66).

$$\lambda_3 = \frac{\left(l_3 + l_4\right)\left[l_3\left(K_{O4x} + K_3\right) - K_3\left(l_3 + l_4\right)\right] + K_3\left(l_3 + l_4\right)^2 - K_3l_3 + K_{O4t} + K_{It} + K_{Ht}}{l_3\left[l_3\left(K_{O4x} + K_3\right) - K_3\left(l_3 + l_4\right)\right] + K_3\left(l_3 + l_4\right)^2 - K_3l_3 + K_{O4t} + K_{It} + K_{Ht}}, \tag{5.67a}$$

$$\lambda_3 = \frac{l_3\left(K_{O4x} + K_3\right)\left(l_3 + l_4\right) - K_3\left(l_3 + l_4\right)^2 + K_3\left(l_3 + l_4\right)^2 - K_3l_3 + K_{O4t} + K_{It} + K_{Ht}}{l_3^2\left(K_{O4x} + K_3\right) - K_3l_3\left(l_3 + l_4\right) + K_3\left(l_3 + l_4\right)^2 - K_3l_3 + K_{O4t} + K_{It} + K_{Ht}}, \tag{5.67b}$$

$$\lambda_3 = \frac{l_3\left(K_{O4x}+K_3\right)\left(l_3+l_4\right)-K_3 l_3+K_{O4t}+K_{It}+K_{Ht}}{l_3^2\left(K_{O4x}+K_3\right)-K_3 l_3\left(l_3+l_4\right)+K_3\left(l_3+l_4\right)^2-K_3 l_3+K_{O4t}+K_{It}+K_{Ht}}, \quad (5.67c)$$

$$K_{in3} = \frac{\left(K_{O4x}+K_3\right)\left(K_3\left(l_3+l_4\right)^2+K_{O4t}+K_{It}+K_{Ht}\right)-K_3^2\left(l_3+l_4\right)^2}{l_3^2\left(K_{O4x}+K_3\right)-K_3 l_3\left(l_3+l_4\right)+K_3\left(l_3+l_4\right)^2-K_3 l_3+K_{O4t}+K_{It}+K_{Ht}}, \quad (5.68)$$

$$K_3 = \frac{K_{O3y}K_{in4}}{K_{O3y}+K_{in4}}, \quad (5.69)$$

The force analysis scheme of 2nd beam is demonstrated in Fig. 5.16.

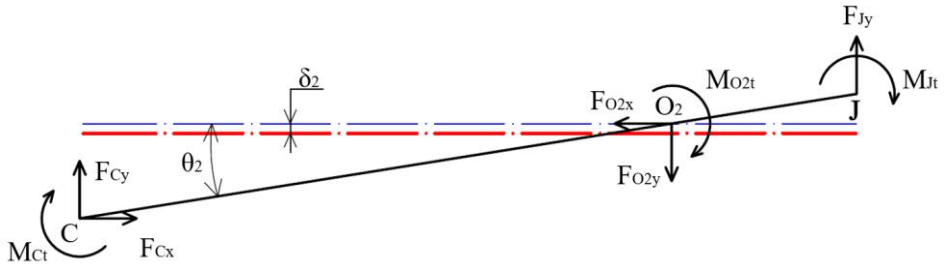

Figure 5.16. 2nd beam force scheme.

The forces and moments are expressed using a similar calculation for 2nd beam.

$$F_{O2y} = F_{Cy} + F_{Jy}, \quad (5.70)$$

$$F_{Jy} l_1^{'} = F_{Cy} l_2^{'} + M_{O2t} + M_{Jt} + M_{Ct}, \quad (5.71)$$

in which M_{O2t}, M_{Jt}, and M_{Ct} denote bending moments at the O_2, J, and C points, correspondingly. The forces operating at points O_2, C, and J along y-axis are F_{O2y}, F_{Cy} and F_{Jy}, correspondingly.

The deformation worth at point C results from combining the deformation because of hinges at O_2 revolving surrounding its axis ($l'_2\theta_2$) and deformation because of drift (δ_2).

Additionally, F_{O2y} and F_{Cy} are computed by.

$$F_{O2y} = K_{O2x}\delta_2, \quad (5.72)$$

$$F_{Cy} = K_2\left(l_2^{'}\theta_2 - \delta_2\right), \quad (5.73)$$

$$M_{O2t} = K_{O2t}\theta_2, \quad (5.74)$$

$$M_{Ct} = K_{Ct}\theta_2, \quad (5.75)$$

$$M_{Jt} = K_{Jt}\theta_2, \quad (5.76)$$

where K_{O2x} denotes the lateral bending rigidity by force F_{O2y} and K_2 is the output rigidity of the E point. K_{O2t} is the rotary rigidity of the O_2 point. K_{Jt}, and K_{Ct} are the rotary rigidity of J, and C points, correspondingly.

The following formulas are attained by replacing Eqs. (5.72) and (5.73) into Eq. (70),

$$K_{O2x}\delta_2 = F_{Jy} + K_2\left(l_2^{'}\theta_2 - \delta_2\right), \tag{5.77}$$

$$\delta_2 = \frac{F_{Jy} + K_2 l_2^{'}\theta_2}{K_{O2x} + K_2}, \tag{5.78}$$

The following formulas are attained by replacing Eqs. (5.73) to (5.76) into Eq. (5.71).

$$F_{Jy}l_1^{'} = K_2 l_2^{'}\left(l_2^{'}\theta_2 - \delta_2\right) + K_{O2t}\theta_2 + K_{Ct}\theta_2 + K_{Jt}\theta_2, \tag{5.79a}$$

$$F_{Jy}l_1^{'} + K_2 l_2^{'}\delta_2 = \left(K_2 l_2^{'2} + K_{O2t} + K_{Ct} + K_{Jt}\right)\theta_2, \tag{5.79b}$$

The θ_2 and δ_2 are attained by replacing Eq. (5.78) into above Eq. (5.79b).

$$F_{Jy}l_1^{'} + K_2 l_2^{'}\frac{F_{Jy} + K_2 l_2^{'}\theta_2}{K_{O2x} + K_2} = \left(K_2 l_2^{'2} + K_{O2t} + K_{Ct} + K_{Jt}\right)\theta_2, \tag{5.80a}$$

$$F_{Jy}l_1^{'}\left(K_{O2x} + K_2\right) + K_2 l_2^{'}\left(F_{Jy} + K_2 l_2^{'}\theta_2\right) = \left(K_{O2x} + K_2\right)\left(K_2 l_2^{'2} + K_{O2t} + K_{Ct} + K_{Jt}\right)\theta_2, \tag{5.80b}$$

$$\theta_2 = \frac{l_1^{'}\left(K_{O2x} + K_2\right) + K_2 l_2^{'}}{\left(K_{O2x} + K_2\right)\left(K_2 l_2^{'2} + K_{O2t} + K_{Ct} + K_{Jt}\right) - K_2^2 l_2^{'2}}F_{Jy}, \tag{5.81}$$

$$\delta_2 = \frac{F_{Jy} + K_2 l_2^{'}\dfrac{l_1^{'}\left(K_{O2x} + K_2\right) + K_2 l_2^{'}}{\left(K_{O2x} + K_2\right)\left(K_2 l_2^{'2} + K_{O2t} + K_{Ct} + K_{Jt}\right) - K_2^2 l_2^{'2}}F_{Jy}}{K_{O2x} + K_2}, \tag{5.82a}$$

$$\delta_2 = \frac{\left(K_{O2x} + K_2\right)\left(K_2 l_2^{'2} + K_{O2t} + K_{Ct} + K_{Jt}\right) - K_2^2 l_2^{'2} + K_2 l_2^{'}\left[l_1^{'}\left(K_{O2x} + K_2\right) + K_2 l_2^{'}\right]}{\left(K_{O2x} + K_2\right)\left[\left(K_{O2x} + K_2\right)\left(K_2 l_2^{'2} + K_{O2t} + K_{Ct} + K_{Jt}\right) - K_2^2 l_2^{'2}\right]}F_{Jy}, \tag{5.82b}$$

$$\delta_2 = \frac{\left(K_{O2x} + K_2\right)\left(K_2 l_2^{'2} + K_{O2t} + K_{Ct} + K_{Jt}\right) - K_2^2 l_2^{'2} + K_2^2 l_2^{'2} + K_2 l_2^{'} l_1^{'}\left(K_{O2x} + K_2\right)}{\left(K_{O2x} + K_2\right)\left[\left(K_{O2x} + K_2\right)\left(K_2 l_2^{'2} + K_{O2t} + K_{Ct} + K_{Jt}\right) - K_2^2 l_2^{'2}\right]}F_{Jy}, \tag{5.82c}$$

$$\delta_2 = \frac{K_2 l_2^{'2} + K_{O2t} + K_{Ct} + K_{Jt} + K_2 l_2^{'} l_1^{'}}{\left(K_{O2x} + K_2\right)\left(K_2 l_2^{'2} + K_{O2t} + K_{Ct} + K_{Jt}\right) - K_2^2 l_2^{'2}}F_{Jy}, \tag{5.82d}$$

Likewise, the intensification proportion as well as the input rigidity of 2nd beam are identified as.

$$\lambda_2 = \frac{l_2^{'}\theta_2 - \delta_2}{l_1^{'}\theta_2 + \delta_2}, \tag{5.83}$$

$$K_{in2} = \frac{F_{Jy}}{l_1^{'}\theta_2 + \delta_2}, \tag{5.84}$$

The subsequent formulas are attained by replacing Eqs. (5.81) and (5.82d) into Eqs. (5.83) and (5.84).

$$\lambda_2 = \frac{l_2^{'}\left[l_1^{'}\left(K_{O2x}+K_2\right)+K_2 l_2^{'}\right]-\left(K_2 l_2^{'2}+K_{O2t}+K_{Ct}+K_{Jt}+K_2 l_2^{'} l_1^{'}\right)}{l_1^{'}\left[l_1^{'}\left(K_{O2x}+K_2\right)+K_2 l_2^{'}\right]+K_2 l_2^{'2}+K_{O2t}+K_{Ct}+K_{Jt}+K_2 l_2^{'} l_1^{'}}, \tag{5.85a}$$

$$\lambda_2 = \frac{l_1^{'} l_2^{'}\left(K_{O2x}+K_2\right)-\left(K_{O2t}+K_{Ct}+K_{Jt}+K_2 l_2^{'} l_1^{'}\right)}{l_1^{'2}\left(K_{O2x}+K_2\right)+2K_2 l_2^{'} l_1^{'}+K_2 l_2^{'2}+K_{O2t}+K_{Ct}+K_{Jt}}, \tag{5.85b}$$

$$\lambda_2 = \frac{l_1^{'} l_2^{'} K_{O2x}-\left(K_{O2t}+K_{Ct}+K_{Jt}\right)}{l_1^{'2}\left(K_{O2x}+K_2\right)+2K_2 l_2^{'} l_1^{'}+K_2 l_2^{'2}+K_{O2t}+K_{Ct}+K_{Jt}}, \tag{5.85c}$$

$$K_{in2} = \frac{\left(K_{O2x}+K_2\right)\left(K_2 l_2^{'2}+K_{O2t}+K_{Ct}+K_{Jt}\right)-K_2^2 l_2^{'2}}{l_1^{'2}\left(K_{O2x}+K_2\right)+2K_2 l_2^{'} l_1^{'}+K_2 l_2^{'2}+K_{O2t}+K_{Ct}+K_{Jt}}, \tag{5.86}$$

$$K_2 = \frac{K_{Ey} K_{in4}}{K_{Ey}+K_{in4}}, \tag{5.87}$$

The force diagram of 1st beam is demonstrated in Fig. 5.17.

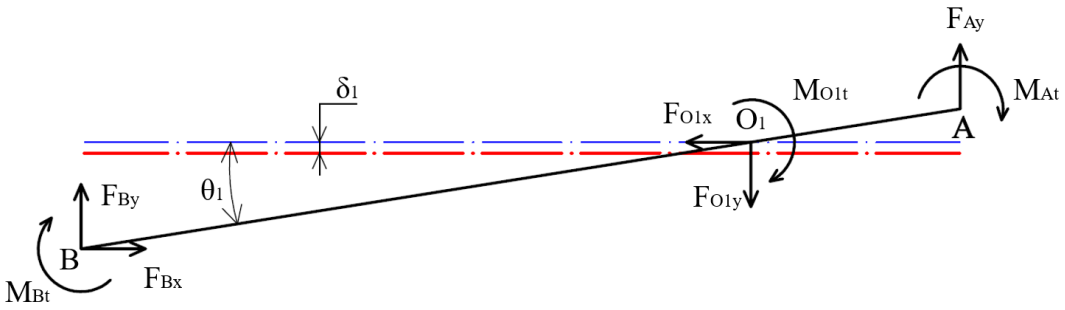

Figure 5.17. First beam forced scheme.

The below formulas result from a similar considering of the first beam's balance status.

$$F_{O1y} = F_{Ay} + F_{By}, \tag{5.88}$$

$$F_{Ay} l_1 = F_{By} l_2 + M_{O1t} + M_{Bt} + M_{At} \tag{5.89}$$

where M_{O1t} denotes the bending moments of the O_1 point while M_{At}, and M_{Bt} denote the bending moments of the A, and B points, correspondingly. The force is operating at points O_1, A, and B along y-axis are F_{O1y}, F_{Ay} and F_{By}, correspondingly.

The deformation worth at point B originates from a mixture of the displacement because of joints at O_1 revolving surrounding its axis ($l_2\theta_1$) and deformation because of drift (δ_1).

Moreover, the forces F_{O1y} as well as F_{By} are determined as.

$$F_{By} = K_1\left(l_2\theta_1 - \delta_1\right) \tag{5.90}$$

$$F_{O1y} = K_{O1x}\delta_1, \tag{5.91}$$

$$M_{O1t} = K_{O1t}\theta_1, \tag{5.92}$$

$$M_{Bt} = K_{Bt}\theta_1, \tag{5.93}$$

$$M_{At} = K_{At}\theta_1, \tag{5.94}$$

in which K_{O1x} denotes the lateral bending rigidity by force F_{O1y} and K_1 denotes the output rigidity of the B and A points, correspondingly. K_{O1t} denotes the rotary rigidity of the O_1 point, while K_{At}, and K_{Bt} are the rotary rigidity A, and B points, correspondingly.

The similar 2nd beam, the θ_1 as well as δ_1 are calculated by:

$$\theta_1 = \frac{l_1\left(K_{O1x}+K_1\right)+K_1l_2}{\left(K_{O1x}+K_1\right)\left(K_1l_2^2+K_{O1t}+K_{Bt}+K_{At}\right)-K_1^2l_2^2}F_{Ay}, \tag{5.95}$$

$$\delta_1 = \frac{K_1l_1l_2+K_1l_2^2+K_{O1t}+K_{Bt}+K_{At}}{\left(K_{O1x}+K_1\right)\left(K_1l_2^2+K_{O1t}+K_{Bt}+K_{At}\right)-K_1^2l_2^2}F_{Ay}, \tag{5.96}$$

The intensification proportion and input stiffness of the first beam are determined by.

$$\lambda_1 = \frac{l_2\theta_1-\delta_1}{l_1\theta_1+\delta_1}, \tag{5.97}$$

$$k_{in1} = \frac{F_{Ay}}{l_1\theta_1+\delta_1}, \tag{5.98}$$

The outcomes are attained by replacing Eqs. (5.95) and (5.96) into Eqs. (5.97) and (5.98).

$$\lambda_1 = \frac{l_1l_2K_{O1x}-\left(K_{O1t}+K_{Bt}+K_{At}\right)}{l_1^2\left(K_{O1x}+K_1\right)+2K_1l_1l_2+K_1l_2^2+K_{O1t}+K_{Bt}+K_{At}}, \tag{5.99}$$

$$K_{in1} = \frac{\left(K_{O1x}+K_1\right)\left(K_1l_2^2+K_{O1t}+K_{Bt}+K_{At}\right)-K_1^2l_2^2}{l_1^2\left(K_{O1x}+K_1\right)+2K_1l_1l_2+K_1l_2^2+K_{O1t}+K_{Bt}+K_{At}}, \tag{5.100}$$

$$K_1 = K_{12}+K_{13}, \tag{5.101}$$

$$K_{12} = \frac{K_{y12}K_{in2}}{K_{y12}+K_{in2}}, \tag{5.102}$$

$$K_{y12} = \frac{K^e_{\theta yMy}}{2}+\frac{2K^e_{\theta yMy}}{5} = \frac{9K^e_{\theta yMy}}{10}, \tag{5.103}$$

$$K_{13}=\frac{K_{y13}K_{in3}}{K_{y13}+K_{in3}}, \tag{5.104}$$

$$K_{y13}=\frac{2K^{e}_{\theta yMy}}{5}, \tag{5.105}$$

in which K_1 denotes the output rigidity that integrates A and B points, K_{12} denotes the output rigidity that integrates 1st beam and second beam, and K_{13} denotes the output rigidity that integrates 1st beam and 3rd beam. Additionally, the intermediary rigidity between 1st beam and 2nd beam, and the intermediary rigidity between 1st beam and 3rd beam denote K_{y12} and K_{y13}, correspondingly.

$$K_{O1t}=K_{O2t}=K_{O4t}=K_{At}=K^{e}_{\theta zMz}, \tag{5.106}$$

$$K_{Bt}=K_{Ct}=K_{Dt}=K_{It}=K_{O3t}=K_{Et}=\frac{K^{e}_{\theta zMz}}{2}, \tag{5.107}$$

$$K_{Ht}=K_{Jt}=K_{Mt}=K_{Nt}=\frac{2K^{e}_{\theta zMz}}{5}, \tag{5.108}$$

$$K_{Gt}=K^{c}_{\theta zMz}, \tag{5.109}$$

$$K_{O3y}=K_{Ey}=K_{Cy}=\frac{K^{e}_{\theta yMy}}{2}, \tag{5.110}$$

$$K_{O1x}=K_{O2x}=K_{O4x}=K^{e}_{\delta xFx}, \tag{5.111}$$

$$K_{O3x}=\frac{K^{e}_{\delta xFx}}{2}, \tag{5.112}$$

$$K_{b2}=K^{l7}_{\theta zMz}=\frac{Eba^{3}}{12l_{7}}, \tag{5.113}$$

$$K^{l7}_{\theta yMy}=\frac{Eba}{l_{7}}, \tag{5.114}$$

$$K_{b1}=K^{l8}_{\theta zMz}=\frac{Eba^{3}}{12l_{8}}, \tag{5.115}$$

$$K^{l9}_{\theta zMz}=\frac{Eba^{3}}{12l_{9}}, \tag{5.116}$$

$$K_{b3}=\frac{2K^{l9}_{\theta zMz}K^{c}_{\theta zMz}}{K^{c}_{\theta zMz}+4K^{l9}_{\theta zMz}}, \tag{5.117}$$

where $K^{l7}_{\theta zMz}$, $K^{l8}_{\theta zMz}$ as well as $K^{l9}_{\theta zMz}$ are the rigidities produced by the torque of rectangular joints l_7, $l_{8,}$ and l_9, correspondingly. Additionally, K_{b1}, K_{b2} as well as K_{b3}

denote rigidity conversion of $K_{\theta zMz}^{l7}$, $K_{\theta zMz}^{l8}$ and $K_{\theta zMz}^{l9}$, which aims to simplify the formulas. Lastly, the linear rigidity formed by the axial force of rectangular joint l_7 is displayed by worth $K_{\theta yMy}^{l7}$. Finally, the total two-stage lever intensification proportion is defined as.

$$A=\lambda_4\left(\lambda_1+\lambda_3+1\right)+\lambda_3+1, \tag{5.118}$$

$F_{in} = 2F_{Ay}$ is discovered, and the input rigidity of the symmetrical intensification structure is computed as.

$$K_{in}=\frac{F_{in}}{l_1\theta_1+\delta_1}=\frac{2F_{Ay}}{l_1\theta_1+\delta_1}=2K_{in1}, \tag{5.119}$$

Fig. 5.18 is a scheme to present a stage's simplified rigidity with the positioner being driven along y-axes and Figure 5.19 shows a shortened principle scheme of the offered positioner.

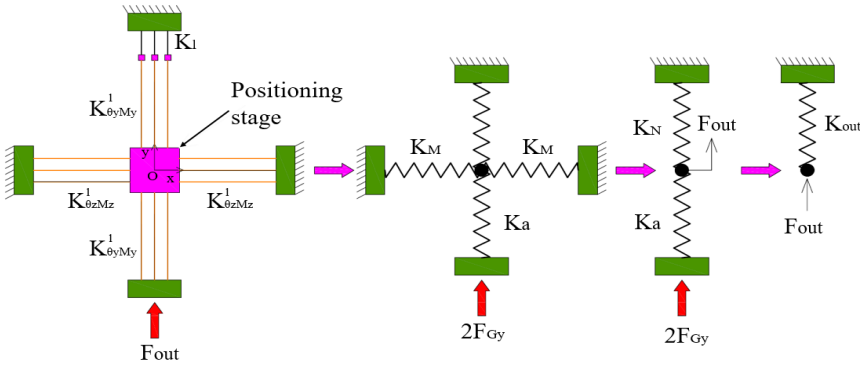

Figure 5.18. The output structure's rigidity.

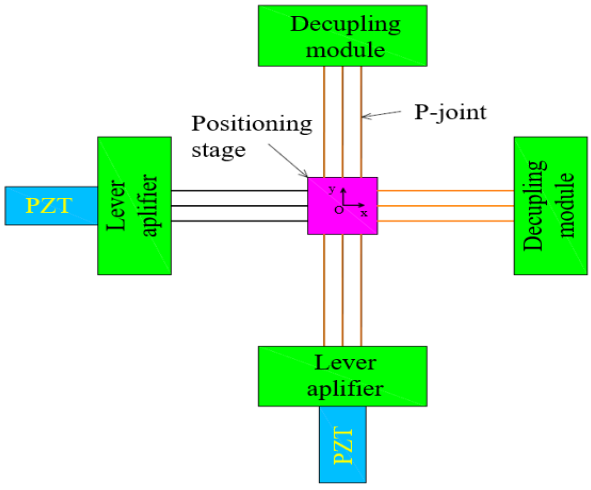

Figure 5.19. Shortened principle scheme of the offered positioner.

Letting d_{out} denotes the positioner's output deformation and d_{in} denotes the input deformation in the vertical axis. Furthermore, the rotary angles of the prismatic beams are symbolized as ω_{b1}, ω_{b2}, ω_{b3}, α_1, β_1, γ_1, and ε_1, which are determined as.

$$\omega_{b1} = \frac{d_{out}}{l_8}, \tag{5.120}$$

$$\omega_{b2} = \frac{d_{out}}{l_7}, \tag{5.121}$$

$$\omega_{b3} = \frac{d_{out}}{l_9}, \tag{5.122}$$

$$\alpha_1 = \frac{d_{out}}{l_5}, \tag{5.123}$$

$$\beta_1 = \frac{d_{out}}{(l_3 + l_4)} \frac{l_6}{l_5}, \tag{5.124}$$

$$\gamma_1 = \frac{d_{out}}{l_2'} \frac{l_6}{l_5}, \tag{5.125}$$

$$\varepsilon_1 = \frac{d_{out}}{l_2} \frac{l_6}{l_5}, \tag{5.126}$$

The potential energy contained within the compliant joints is defined as.

$$E_p = \frac{1}{2}\left[\sum_{i=A}^{B} K_i {\varepsilon^2}_1 + \sum_{i=J}^{D} K_i {\gamma^2}_1 + \sum_{i=O4}^{I} K_i {\beta^2}_1 + K_G {\alpha^2}_1\right] + \frac{1}{2}\sum_{j=b1}^{b3} K_j {\omega^2}_j \tag{5.127a}$$

$$\begin{aligned} E_p = \frac{1}{2}[\ & K_{At}\varepsilon_1^2 + K_{O1t}\varepsilon_1^2 + K_{Bt}\varepsilon_1^2 + K_{Jt}\gamma_1^2 + K_{O2t}\gamma_1^2 + K_{Dt}\gamma_1^2 + \\ & K_{O4t}\beta_1^2 + K_{Ht}\beta_1^2 + K_{It}\beta_1^2 + K_{Gt}\alpha_1^2\ ]2 + \left[4K_{b1}{\omega_{b1}}^2 + 6K_{b2}{\omega_{b2}}^2 + 2K_{b3}{\omega_{b3}}^2\right] \end{aligned} \tag{5.127b}$$

The rigidity K_N are attained by replacing Eqs. (5.120) to (5.126) into Eq. (127b).

$$\begin{aligned} K_N = 2 & \left[\begin{array}{l} \left(\frac{l_6}{l_2 l_5}\right)^2 \left(K_{At} + K_{O1t} + K_{Bt}\right) + \left(\frac{l_6}{l'_2 l_5}\right)^2 \left(K_{Jt} + K_{O2t} + K_{Dt}\right) \\ + \left(\frac{l_6}{(l_4 + l_3) l_5}\right)^2 \left(K_{O4t} + K_{Ht} + K_{It}\right) + \left(\frac{1}{l_5}\right)^2 K_{Gt} \end{array}\right] \\ & + \left[4\left(\frac{1}{l_8}\right)^2 K_{b1} + 6\left(\frac{1}{l_7}\right)^2 K_{b2} + 2\left(\frac{1}{l_9}\right)^2 K_{b3}\right], \end{aligned} \tag{5.128}$$

The positioner's output rigidity K_{out} and K_{Gl} are then determined.

$$K_{out} = \frac{K_N K_a}{K_N + K_a}, \tag{5.129}$$

in which K_a is depicted in Fig. 5.18 and identified as.

$$K_a = \frac{3K_{\theta yMy}^{l7}}{2}, \tag{5.130}$$

$$K_{Gl} = 0.5K_{out}, \tag{5.131}$$

where K_N denotes the positioner's integrated rigidity in one direction, K_a denotes the beam's rigidity $K_{\theta yMy}^{l7}$, and K_{out} denotes the positioner's output rigidity.

To provide a basic calculation, the geometrical features and the offered material properties of the positioner are given in Table 5.14.

Table 5.14 Geometrical factors and the properties of AL7075-T6 for the developed positioner

l_1	l_2	l'_1	l'_2	l_3	l_4	l_5	l_6	l_7	l_8	l_9
13.9	49.7	12	46	14	52	61.8	18	73	76.9	65.9
r	t (circular)	a (l_8, l_9)	a (l_7)	ax	ay	t (elliptic)	b	l	E (GPa)	σ_r (MPa)
4.5	0.6	0.6	0.8	4.5	2.5	0.65	16	9	71.7	503

Step 2: Modeling of dynamics

Lagrange method is exploited to calculate the natural frequencies by quantifying the kinetic kinetic energy (T) and potential energy (V). Figure. 5.20 shows the mass scheme.

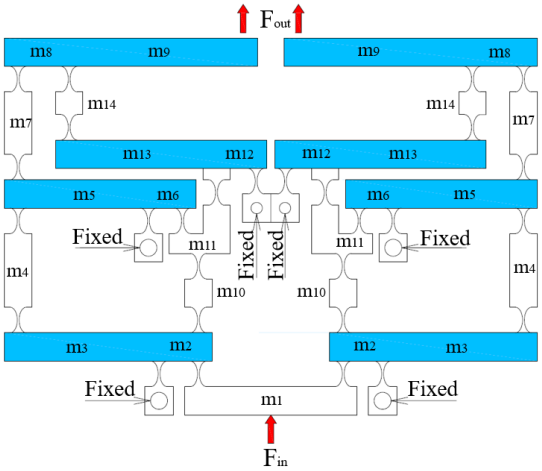

Figure 5.20. Symmetrical structure with two 2-stage magnification mechanism.

Figs. 5.6 and Fig. 5.20 show where the masses are located in the offered model. The next step of motion classification will be performed using the components' position and motion trajectory to support the computation of the developed model's natural frequency.

The joints m_2, m_3, m_5, m_6, m_8, m_9, m_{12}, m_{13}, m_{b1}, m_{b2}, m_{b3} illustrate the rotary and translational movements. The joints m_0, m_1, m_4, m_7, m_{10}, m_{11}, m_{14}, m_{15}, m_{16} notice the translations. The entire positioner's kinetic energy is determined as follows.

$$T = T_{\eta_1} + T_{\eta_2}, \tag{5.132}$$

$$T_{\eta_1} = T_{\eta_2} = \sum_{i=m_2}^{m_{16}} T_i + \sum_{j=m_{b1}}^{m_{b3}} T_j, \tag{5.133}$$

$$T_{m_0} = \frac{1}{2} m_0 \left(vA\right)^2 = \frac{1}{2} m_0 \left(\dot{\eta}_1 A\right)^2 = \frac{m_0 A^2}{2} \eta_1^{\cdot 2}, \tag{5.134}$$

$$T_{m_1} = \frac{m_1}{2} \eta_1^{\cdot 2}, \tag{5.135}$$

$$T_{m_4} = \frac{1}{2} m_4 \left(\frac{v\lambda_1}{2}\right)^2 2 = \frac{m_4 \lambda_1^2}{4} \eta_1^{\cdot 2}, \tag{5.136}$$

$$T_{m_7} = \frac{m_7 \lambda_2^2}{4} \eta_1^{\cdot 2}, \tag{5.137}$$

$$T_{m_{10}} = \frac{m_{10}}{4} \eta_1^{\cdot 2}, \tag{5.138}$$

$$T_{m_{11}} = \frac{m_{11}}{4} \eta_1^{\cdot 2}, \tag{5.139}$$

$$T_{m_{15}} = \frac{m_{15} A^2}{2} \eta_1^{\cdot 2}, \tag{5.140}$$

$$T_{m_{16}} = \frac{m_{16} A^2}{2} \eta_1^{\cdot 2} \tag{5.141}$$

$$T_{m_2} = \frac{1}{2} m_2 \left(\frac{v}{2}\right)^2 2 + \frac{1}{2} \frac{m_2 l_1^2}{3} \left(\frac{v}{l_1}\right)^2 2 = \frac{7m_2}{12} v^2 = \frac{7m_2}{12} \eta_1^{\cdot 2} \tag{5.142}$$

$$T_{m_3} = \frac{7m_3 \lambda_1^2}{12} \eta_1^{\cdot 2}, \tag{5.143}$$

$$T_{m_5} = \frac{7m_5 \lambda_2^2}{12} \eta_1^{\cdot 2}, \tag{5.144}$$

$$T_{m_6} = \frac{7m_6}{12} \eta_1^{\cdot 2}, \tag{5.145}$$

$$T_{m_8} = \frac{7m_8 A^2}{12} \eta_1^{\cdot 2}, \tag{5.146}$$

$$T_{m_9} = \frac{7m_9A^2}{12}\eta_1^{\cdot 2}, \tag{5.147}$$

$$T_{m_{12}} = \frac{7m_{12}}{12}\eta_1^{\cdot 2}, \tag{5.148}$$

$$T_{m_{13}} = \frac{7m_{13}\lambda_3^2}{12}\eta_1^{\cdot 2} \tag{5.149}$$

$$T_{m_{b1}} = \frac{1}{2}m_{b1}\left(vA\right)^2 4 + \frac{1}{2}\frac{m_{b1}l_8^2}{3}\left(\frac{vA}{l_8}\right)^2 4 = \frac{8m_{b1}A^2}{3}v^2 = \frac{8m_{b1}A^2}{3}\eta_1^{\cdot 2}, \tag{5.150}$$

$$T_{m_{b2}} = \frac{1}{2}m_{b2}\left(vA\right)^2 6 + \frac{1}{2}\frac{m_{b2}l_7^2}{3}\left(\frac{vA}{l_7}\right)^2 6 = 4A^2m_{b2}\eta_1^{\cdot 2}, \tag{5.151}$$

$$T_{m_{b3}} = \frac{1}{2}m_{b3}\left(vA\right)^2 2 + \frac{1}{2}\frac{m_{b3}l_9^2}{3}\left(\frac{vA}{l_9}\right)^2 2 = \frac{4A^2m_{b3}}{3}\eta_1^{\cdot 2}, \tag{5.152}$$

Potential energy:

$$V = \frac{1}{2}k_1\eta_1^2 + \frac{1}{2}k_2\eta_2^2, \tag{5.153}$$

The following Lagrange's equation: Lagrangian mechanics identifies a mechanical system to be a pair (*M*, *L*) of a construction area *M* and a smooth function *L*=*L*(*q*,*v*,*t*) called Lagrangian.

$$L = T - V,$$

$$Md^{**}{}_i + Kd_i = F_i, \tag{5.154}$$

$$\frac{d}{d_t}\frac{\partial T}{\partial \mu^*{}_i} - \frac{\partial T}{\partial \mu_i} + \frac{\partial V}{\partial \mu_i} = F_i,$$

in which i = 1; 2 denotes the free vibration of horizontal-and vertical-directions of the positioner. F_i denotes a nonconservative generalized force matching to coordinate. Considering the equivalent mass $M = diag\{M\}$ as well as the stiffness $K = diag\{k\}$, a conservative system is computed as.

$$M_{\eta^{**}} + K_\eta = 0, \tag{5.155}$$

$$\frac{d}{d_t}\frac{\partial T}{\partial \mu^*{}_i} - \frac{\partial T}{\partial \mu_i} + \frac{\partial V}{\partial \mu_i} = 0, \tag{5.156}$$

The results are attained by replacing Eqs. (5.133) to (5.152) into Eq. (5.132)

$$T=\left[\frac{m_0A^2}{2}+\frac{m_1}{2}+\frac{7m_2}{12}+\frac{7m_3\lambda_1^2}{12}+\frac{m_4\lambda_1^2}{4}+\frac{7m_5\lambda_2^2}{12}+\frac{7m_6}{12}+\frac{m_7\lambda_2^2}{4}+\frac{7m_8A^2}{12}\right.$$
$$+\frac{7m_9A^2}{12}+\frac{m_{10}}{4}+\frac{m_{11}}{4}+\frac{7m_{12}}{12}+\frac{7m_{13}\lambda_3^2}{12}+\frac{m_{14}\lambda_3^2}{4}+\frac{m_{15}A^2}{2}+\frac{m_{16}A^2}{2}+\frac{8m_{b1}A^2}{3} \quad (5.157)$$
$$\left.+4A^2m_{b2}+\frac{4A^2m_{b3}}{3}\right]\left[\eta^{*2}{}_1\eta^{*2}{}_2\right],$$

$$\frac{\partial T}{\partial\mu^*_i}=\left[m_0A^2+m_1+\frac{7m_2}{6}+\frac{7m_3\lambda_1^2}{6}+\frac{m_4\lambda_1^2}{2}+\frac{7m_5\lambda_2^2}{6}+\frac{7m_6}{6}+\frac{m_7\lambda_2^2}{2}+\frac{7m_8A^2}{6}\right.$$
$$+\frac{7m_9A^2}{6}+\frac{m_{10}}{2}+\frac{m_{11}}{2}+\frac{7m_{12}}{6}+\frac{7m_{13}\lambda_3^2}{6}+\frac{m_{14}\lambda_3^2}{2}+m_{15}A^2+m_{16}A^2+\frac{16m_{b1}A^2}{3} \quad (5.158)$$
$$\left.+8A^2m_{b2}+\frac{8A^2m_{b3}}{3}\right]\left[\eta^*{}_1\eta^*{}_2\right],$$

$$\frac{d}{d_t}\frac{\partial T}{\partial\mu^*_i}=\left[m_0A^2+m_1+\frac{7m_2}{6}+\frac{7m_3\lambda_1^2}{6}+\frac{m_4\lambda_1^2}{2}+\frac{7m_5\lambda_2^2}{6}+\frac{7m_6}{6}+\frac{m_7\lambda_2^2}{2}+\frac{7m_8A^2}{6}\right.$$
$$+\frac{7m_9A^2}{6}+\frac{m_{10}}{2}+\frac{m_{11}}{2}+\frac{7m_{12}}{6}+\frac{7m_{13}\lambda_3^2}{6}+\frac{m_{14}\lambda_3^2}{2}+m_{15}A^2+m_{16}A^2+\frac{16m_{b1}A^2}{3} \quad (5.159)$$
$$\left.+8A^2m_{b2}+\frac{8A^2m_{b3}}{3}\right]\left[\eta^{**}{}_1\eta^{**}{}_2\right],$$

$$\frac{\partial T}{\partial\mu_i}=0, \quad (5.160)$$

$$\frac{\partial V}{\partial\mu_i}=\left[k_1+k_2\right]\left[\eta_1\eta_2\right], \quad (5.161)$$

Numbers *M* as well as *K* are attained by replacing Eqs. (5.159) to (5.161) into Eq. (5.156)

$$M=m_0A^2+m_1+\frac{7m_2}{6}+\frac{7m_3\lambda_1^2}{6}+\frac{m_4\lambda_1^2}{2}+\frac{7m_5\lambda_2^2}{6}+\frac{7m_6}{6}+\frac{m_7\lambda_2^2}{2}$$
$$+\frac{7m_8A^2}{6}+\frac{7m_9A^2}{6}+\frac{m_{10}}{2}+\frac{m_{11}}{2}+\frac{7m_{12}}{6}+\frac{7m_{13}\lambda_3^2}{6}+\frac{m_{14}\lambda_3^2}{2}+m_{15}A^2 \quad (5.162)$$
$$+m_{16}A^2+\frac{16m_{b1}A^2}{3}+8A^2m_{b2}+\frac{8A^2m_{b3}}{3},$$

$$K=K_{in}=2K_{in1}, \quad (5.163)$$

The natural frequency (*f*) of the positioner is attained by resolving Eq. (5.155).

$$f=\frac{1}{2\pi}\left(\frac{K}{M}\right)^{0.5}. \quad (5.164)$$

5.3.3.2. Evaluation and verifications of mathematical models

The discrepancy between the theoretical and FEA values is roughly 5.426%, as shown in Table 5.15. This indicates that the suggested kineostastic-based approach, which uses the

Lagrange technique, elastic beam theory, and deformable mechanic theory, is capable of modeling both the statics and dynamics of the positioner that is being supplied.

Table 5.15 Theoretical and simulation errors

Response	Theoretical outcome	FEA outcome	Error (%)
f (Hz)	92.1219	87.381	5.426

5.3.4. Structural optimization

5.3.4.1. Optimal issue description

In avoidance of resonance among the motors, PZT actuators and flexure-based positioner, the 1st natural frequency modes should be at the maximum or minimum point. Particularly, to raise the degree of rapid responsiveness of the offered positioner and produce no resonance phenomena in the offered positioner, it is essential for the 1st natural frequency to be as high as possible. Additionally, as the angular frequency is proportionate to the compliant stage's natural frequency, the 1st natural frequency is introduced to obtain the two targets mentioned above. The optimization method in this study aims to maximize the resonant frequency, as presented in the following formulas.

Seek design variable vector: $\mathbf{X} = [x_1, x_2, x_3, x_4, x_5]$

$$\text{Maximize } f(\mathbf{x}) \tag{5.165}$$

Constraint:

$$f(\mathbf{x}) > 100 \text{ Hz} \tag{5.166}$$

Design variables (unit: mm):

$$\begin{cases} 0.7 \le x_1 \le 0.9 \\ 0.6 \le x_2 \le 0.8 \\ 0.6 \le x_3 \le 0.75 \\ 0.6 \le x_4 \le 0.7 \\ 0.6 \le x_5 \le 0.7 \end{cases} \tag{5.167}$$

where $f(\mathbf{x})$ denotes the resonant frequency. Moreover, x_1, x_2, x_3, x_4 and x_5 are the dimensions of *A*, *B*, *C*, *D*, and *E*, correspondingly.

5.3.4.2. Optimized consequences

Referring to Eqs. (5.10-5.167), MATLAB R2017b was used to develop an integration strategy of kinetostatic analysis-based method and NNA algorithm. Consequently, the

positioner's optimization factors at A = 0.9 mm, B = 0.8 mm, C = 0.7 mm, D = 0.7 mm, and E = 0.7 mm were discovered, as well as the 1st natural frequency was 112.0995 Hz.

5.3.4.3. Verification and comparisons

The optimized parameters were utilized for the creation of a 3D positioner. The FEA outcome by the ANSYS software, as provided in Table 5.16, revealed that the first natural frequency of the 2-DOF stage was 106.98 Hz, which was higher than that of the initial design, at 21.69% to be precise. Additionally, as shown in Table 5.17, the error between the optimization outcome and FEA outcome was 4.785 %. Additionally, the 06 modes (1-6) have resonance frequencies of 106.9 Hz, 121.8 Hz, 328.7 Hz, 335.5 Hz, 602.4 Hz, and 603.9 Hz, correspondingly. Figure 5.21 reports the outcomes of the initial form examination of the 1st natural frequency. To avoid causing destruction to the optimized positioner, evade the resonant frequency worth listed above.

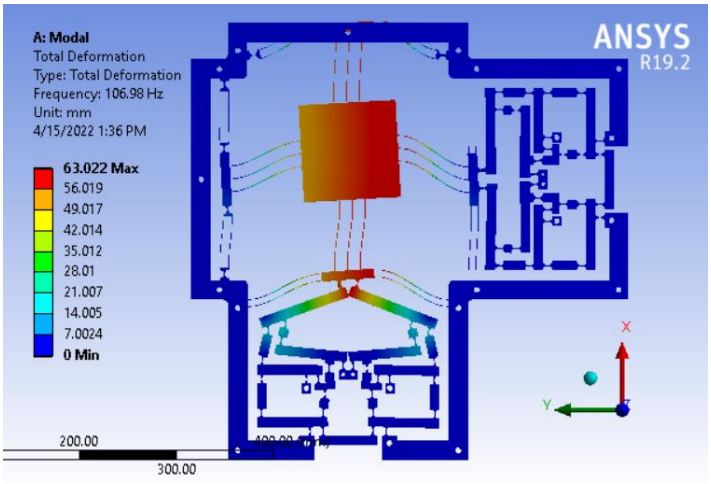

Figure 5.21. The optimal XY-positioner's the first mode shape investigation of resonant natural frequency.

Table 5.16 Advancement among optimization outcome and primary outcome

Characteristic	Optimization outcome	Primary outcome	Enhancement (%)
f (Hz)	112.0995	92.1219	**21.69**

Table 5.17 Error between optimization outcome and FEA outcome

Characteristic	Optimization outcome	FEA outcome	Error (%)
f (Hz)	**112.099**	**106.9**	**4.79**

According to the FEA outcomes in the ANSYS software, the equivalent stress of the optimization positioner's material was 270.8 MPa, as shown in Fig. 5.22, the total output displacement was 877.4 µm, as shown in Fig. 5.23. Moreover, the results indicated a proportion of 7.8 for displacement intensification, output force of 3480.4 N, as well as a decoupling error of roughly 0.02%. To be more specific, the obtained operating travel of XY positioner was 787.63 µm x 794.5 µm. These consequences lead to the conclusion that the attained optimization outcomes met the expected technological requirements of the XY positioner.

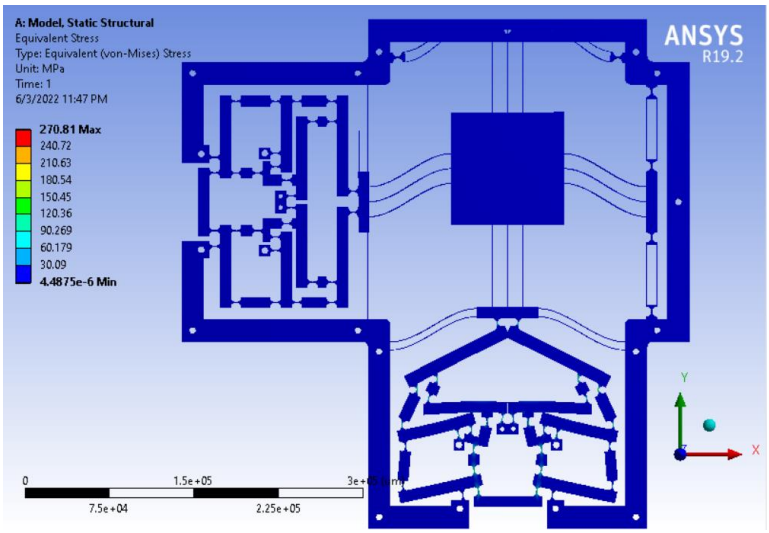

Figure 5.22. Equivalent stress of the optimized XY-positioner.

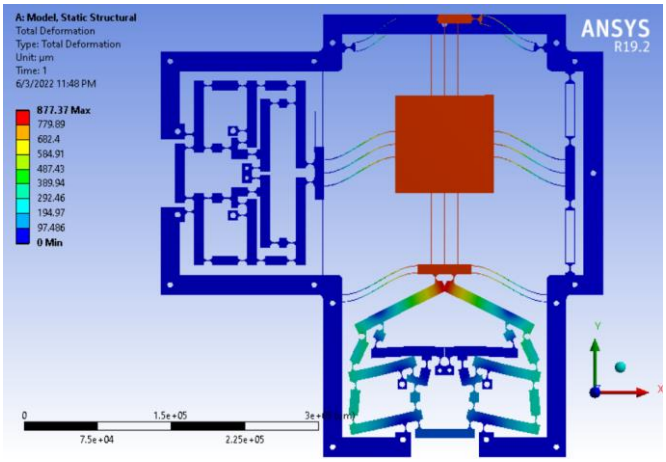

Figure 5.23. Whole deformation of the optimized XY-positioner.

5.3.5. Achieved results

The research introduced a developed modeling and dimension optimization synthesis of the XY-positioner which can be employed to position a specimen in a in-situ nanoindentation. The formulation of this advanced approach originates from the

combination of kinetostatic analysis-based quantifying technique, Lagrange approach and the neural network algorithm. Initially, a XY-positioner was developed through a combination of an eight-lever displacement intensification structure with elliptic joints and a symmetrical parallelogram. Next, a series of XY-positioner's mathematical formulas was created with the use of kinetostatic analysis-based approach, concerning the displacement intensification proportion and the input stiffness. The Lagrange technique is then exploited to build the dynamic equation for the XY-positioner. Finally, the suggested positioner's 1st natural frequency was maximized by using the NNA algorithm.

The optimized outcomes reported a good value of the positioner frequency, at 112.1 Hz to be precise. Moreover, the mathematical formulas were in a tight connection with the simulation validations. The responsiveness level of the new positioner was also higher than that of the existing models.

Compared with the previous designs of XY-positioner, the offered structure generated a better frequency, as shown in Table 5. 18.

Table 5.18 Difference of the offered XY-positioner with the prior structures

2-DOF structure	Dimensional specifications	Frequency (Hz)
Zhu et al. [151]	NA	59.3
Wu and Xu [152]	NA	80
Current structure	451mm x 451mm x 16mm	**112.1**

5.4. Development and optimization of a compliant rotary stage

5.4.1. Conceptual design

In the second design alternative, the stage is designed according to a four-lever displacement intensification structure, a parallel guiding mechanism inspired by the profile's beetle leg, a compliant cartwheel joint, and a rotary platform to reduce the number of actuators.

The rotary positioner includes four-lever displacement amplification module, a parallel guiding mechanism inspired by the profile's beetle leg module, a compliant cartwheel joint module, and a rotary platform module. Three main technical performances of the rotary positioner are expressed as follows.

- The output displacement is more than 1.9 mm
- The safety factor is higher than 1.5

5.4.1.1. Kinetic structure

Examples of compliant micro-positioners including 01-DOF [56], 02-DOFs [153], and 03-DOFs [154] are demonstrated in Figs. 5.24 a–c. Nevertheless, little attention has been paid to a compliant rotation positioner for indentation device. In the current research, a rotation would be used as a replacement for a linear motion to position specimens which are tested by indenter and monitored via microscope before as well as after indentation process. That only pure rotation was utilized for a direct design of a rotation stage would lead to a complex further controller. However, with both translation and rotation, it is much easier to control the suggested positioner by resolving the linear end. In summary, the working principle of the offered positioner relied on a movement from a linear to rotation movement, as shown in Fig. 5.24(d).

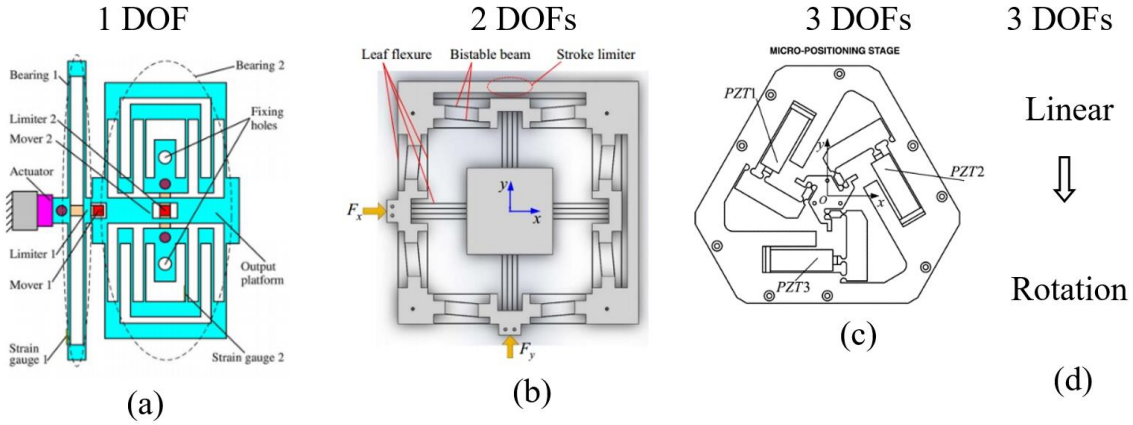

Figure 5.24. Different micro-positioners: (a) a DOF micro-positioner [56], (b) a 2-DOF micro-positioner [153], (c) a 3-DOF micro-positioner [154].

5.4.1.2. Hybrid displacement amplifier

The lever mechanism has been of great significant in amplifying the load or displacement. Its structure is presented in Fig. 5.25, including a beam stationed on an affixed joint. Point O is for the lever rotary center, A for the input end and B for the output end. A brief description of the lever structure's working principles illustrates that when putting a vertical deformation Δl_1 on the input point A, the lever will revolve the Z-direction with a relative γ angle. Hence, the point B transfers to B' and the output deformation Δl_2 can attain in the y-axis. Although one lever mechanism is useful for output deformation magnification, it easily produces a large parasitic motion. Accordingly, to satisfy the

requirements of amplifying larger output displacement and generating linear movement on the basis of symmetrical configuration, a four-lever displacement intensification structure is introduced, as illustrated in Fig. 5.26 b (2nd case). With this intensification structure's features, the intensification proportion can be roughly computed as:

$$r_{lever} = \Delta l_2 / \Delta l_1 = l_2 / l_1 . \tag{5.168}$$

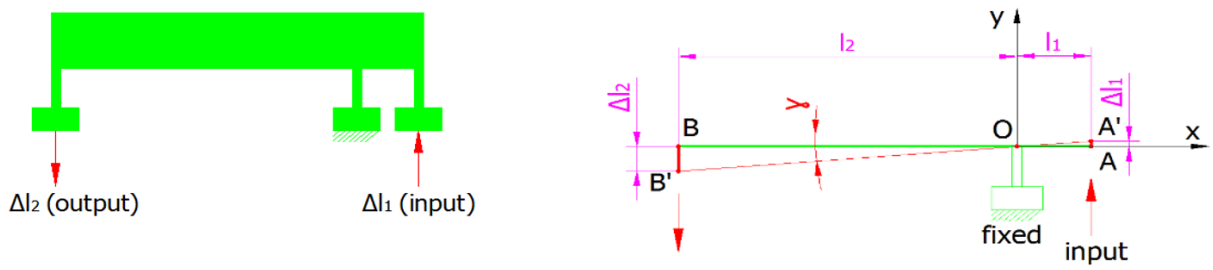

(a) (b)

Figure 5.25. Operating rule diagram of: (a) Lever structure, (b) Intensification proportion analysis.

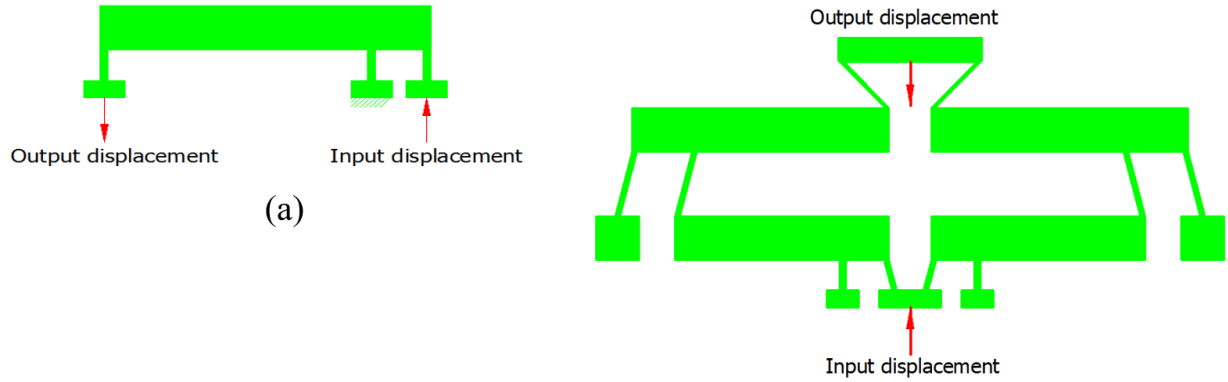

(a) (b)

Figure 5.26. Configuration of lever intensification mechanism: (a) one-lever structure, (b) four-lever structure.

The formula of multi-lever displacement intensification proportion is assumed as follows:

$$r_{lever} = N \times l_2 / l_1 . \tag{5.169}$$

A FEA in the ANSYS software could be adopted for generating design structure as well as comparing the intensification proportion for the first case and the second case. Initial investigation limits for the two models were shown in Figs. 5.26 a, b. The worth of input displacement was set within a variation [0.1 mm, 0.24 mm]. D_{old} as well as D_{new} symbolize

for the achieved output displacement of 1st case and 2nd case in the Y-direction while A_{old} and A_{new} represent intensification proportions for first circumstance and second circumstance, as demonstrated in Tables 5.19 – 20. An increase of roughly 221.6% was seen in the intensification proportion, as shown in Table 5.21 and Fig. 5.27.

Table 5.19 First case's intensification proportion

Input (mm)	D_{old} (mm)	A_{old}
0.1	0.443	4.43
0.12	0.532	4.43
0.14	0.620	4.43
0.16	0.709	4.43
0.18	0.797	4.43
0.2	0.886	4.43
0.22	0.975	4.43
0.24	1.063	4.43

Table 5.20 Second case's intensification proportion

Input (mm)	D_{new} (mm)	A_{new}
0.1	1.425	14.25
0.12	1.710	14.25
0.14	1.995	14.25
0.16	2.280	14.25
0.18	2.564	14.25
0.2	2.849	14.25
0.22	3.134	14.25
0.24	3.419	14.25

Table 5.21 Comparison of the first and second cases' intensification proportions

Input (mm)	A_{old}	A_{new}	Advancement (%)
0.1	4.43	14.25	221.6
0.12	4.43	14.25	221.6
0.14	4.43	14.25	221.6
0.16	4.43	14.25	221.6
0.18	4.43	14.25	221.6
0.2	4.43	14.25	221.6
0.22	4.43	14.25	221.6
0.24	4.43	14.25	221.6

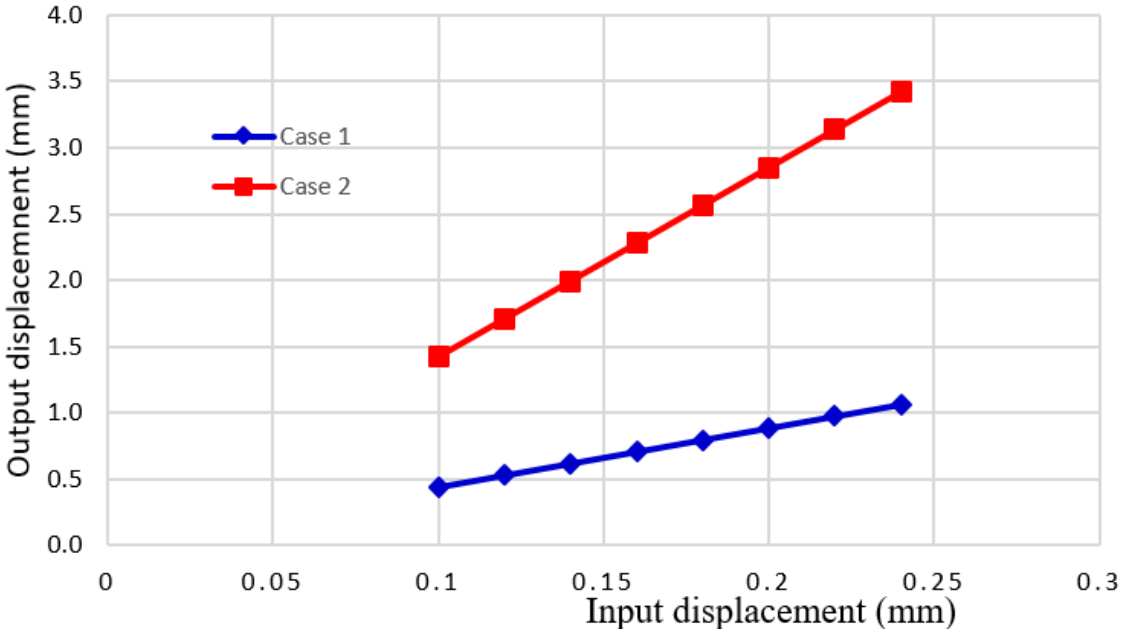

Figure 5.27. Input displacement and output displacement for the first and second cases.

5.4.1.3. Compliant rotary positioner

The working rule of the offered positioner relied on the suggested materials' strength limitation. The offered positioner was employed to locate specimens in nanoindentation testing and Fig. 1.5 illustrates a fundamental application for nanoindentation tester.

The material Al 7075 was chosen for the suggested positioner owing to its high yield strength of 503 MPa, Young's modulus of E = 71700 MPa, a light density of 2810 kg/m^3

and Poisson's ratio of 0.33. Specifications of rotation positioner supposed the input displacement to be at 0.19 mm.

Fig. 5.28 displays the proposed positioner which was developed in connection with the beetle's profile to achieve a proper compliance. Components of the offered positioner includes: (i) sixteen affixed holes to position the stage on an un-vibration table, (ii) a piezoelectric actuator (PEA) (positioned at the input deformation location) to produce the input deformation for the positioner by a direct connection with the beetle-liked configuration and rotation structure.

The dimensional specifications of the suggested positioner were roughly 280 mm× 376 mm ×6 mm. The offered rotation positioner was proposed to build a linear deformation which would result in an increase in high rotation angle for indentation checking devices. Geometric factors of the offered rotation positioner were presented in Fig. 5.29 and Table 5.22.

Of all geometric parameters, factors *A*, *B*, *C*, and *D* were chosen as the chief variables owing to its significant influences on the responses while the others were selected as constants.

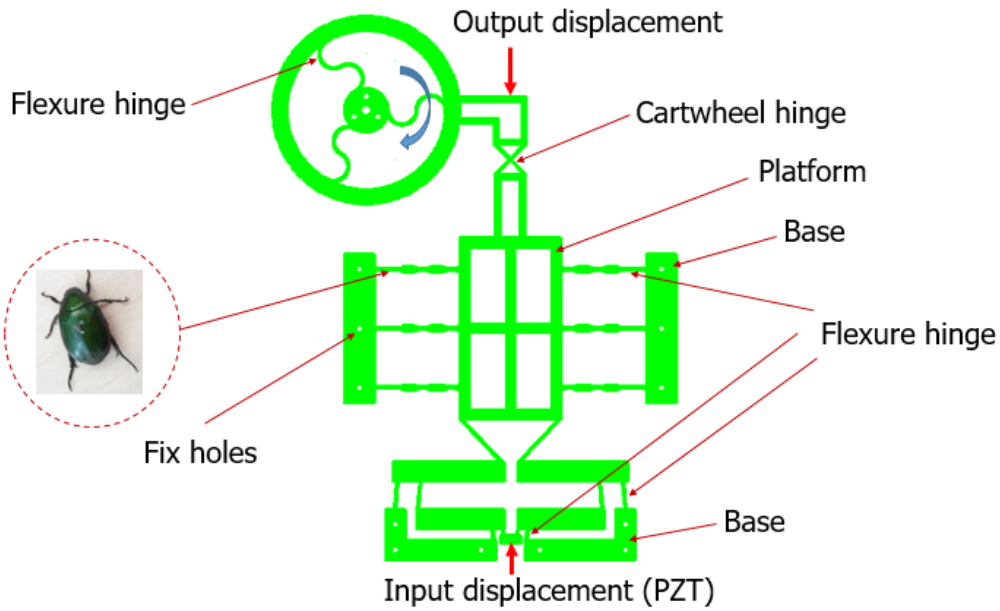

Figure 5.28. Configuration of Beetle-motivated positioner.

Table 5.22 The flexure rotation positioner's geometric factors (unit: mm)

Factors	Worth	Factors	Worth	Factors	Worth
a	6.84	*m*	222	*x*	30
b	20	*n*	230	*y*	280
c	8	*o*	70	*z*	376
d	30	*p*	30	*A*	*51≤A≤53*
e	76	*q*	70	*B*	*1≤B≤1.2*
f	6	*r*	65	*C*	*0.5≤C≤0.7*
g	5	*t*	10	*D*	*0.5≤D≤0.7*
h	102				

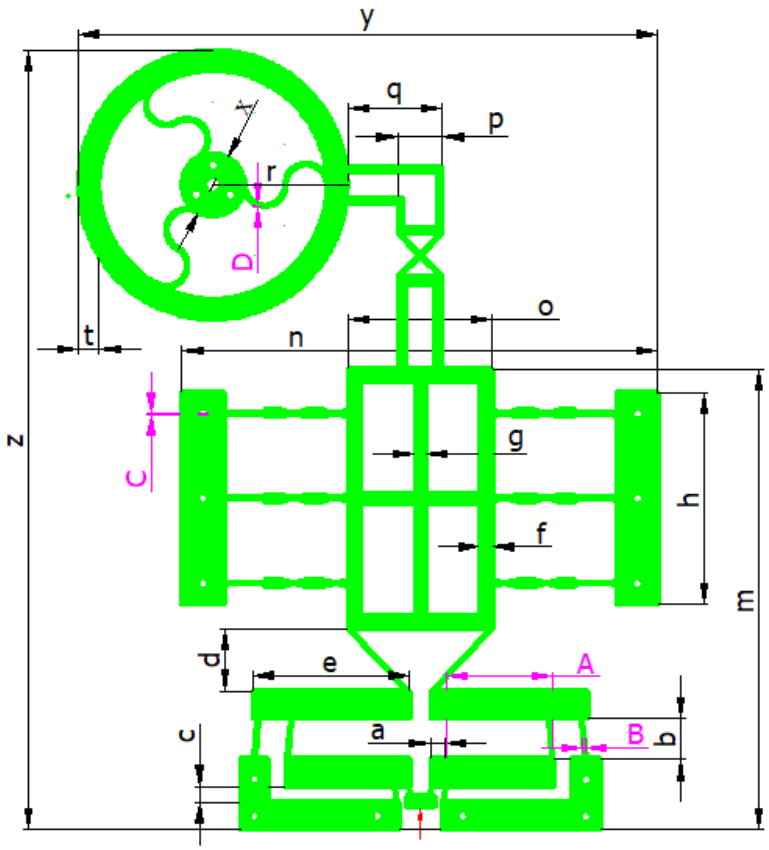

Figure 5.29. The flexure rotation positioner's design factors.

5.4.2. Methodology

So as to optimize quality responses of the suggested positioner, the combination methodology of TM, FEM, RSM and TLBO [155] could be built up for concurrent multi-target optimal problem, as displayed in a flow chart in Fig. 5.30. This combination method was offered by Dang et al. The optimal procedure was expressed as:

Phase 1: Computer-assisted engineering design

With the aid of advances of computer software and applications, a great number of computational analyses can be well performed per second. In this study, a CAED was carried out for the offered positioner optimization, adopting the below procedure.

Step 1: Define an optimization problem

In an indentation device, the offered positioner is utilized as a positioning platform and its input motion is controlled by a PZT although the travel of the PZT is restricted. Accordingly, this research aims to optimize geometrical factors of the offered positioner, for a maximization of both safety factor and displacement. Multi-target optimization issue for the positioner was implemented to attain better the output responses.

Step 2: Develop a suitable mechanical structure

Some draft models which simulated the structure of beetles, were suggested for a proper compliant design and a description of the positioner's primary actions. Next, the most appropriate design was chosen.

Step 3: Determine chief variables and output features

To obtain the best quality features, parameters such as the length of 1st lever A, the thicknesses of compliant joint B, C and D were considered as chief variables owing to their significant contributions to the positioner's action. Details of the parameters can be found in Fig. 5.29. To satisfy practical customer demands, it is necessary to fulfill a great operating travel and an extreme safety factor through the simultaneous optimization.

Step 4: Design 3D-FEA structure

A 3D-FEA structure was formed for the purpose of quantifying analysis, with an exporting of quality features.

Step 5: Assess primary output attributes

In the analysis of the 3D design, in case the positioner's specifications were met, phase 2 would be implemented. However, if it fails to satisfy the specifications, step 2 would be conducted again.

Phase 2: RSM and regression modelling

In the carrying out of optimal procedure, several experiments were established as well as numerical data were gathered, followed by an action of generating regression formulas to match the design variables and output characteristics.

Step 6: **Set up experiment design**

Initially, the TM was employed for identifying an orthogonal array for an establishment of several numerical experiments as it could perform a few experiments. Then, ANOVA was exploited to figure out the major influence of key parameters.

Step 7: Collect numerical data

Numeric experiments could be conducted with the use of a combination approach of FEA and RSM and the offered 3D design in Step 4. This contributed to the successful exporting of both output characteristics' outcomes.

Step 8: Form regression formulas

Next, the RSM was adopted to examine the linear and nonlinear multivariate association among the chief parameters and the quality characteristics. As the relations were mainly nonlinear, it is appropriate to select a complete quadratic type as a proper pattern for the offered positioner, as shown in Eq. 4.26. The TLBO algorithm made use of these target functions.

Phase 3: Optimization using TLBO

With the target formulas defined in Step 8, the optimal procedure continued with the employment of TLBO algorithm. The TLBO has been employed widely [156] and it was also selected for the offered positioner. The working rules of this algorithm are similar to the teaching-learning capacity of teachers and students in a classroom. The projected outcomes of TLBO are students' grades which depend on teachers' teaching. It is predicted that great achievements of students' outcomes from great training of great teachers. Additionally, students can also learn from each other in classes to broaden their knowledge, sharpen their skills and better their grades. Courses are viewed as design variables and students' results are similar to the fitness worth of the optimal procedure. There were two phases in the algorithm: (i) teacher phase where the potentials were erratically allocated over the investigation area and the best resolution was specified and (ii) leaner phase where participants expanded their new knowledge through interactions with other students. More information about the TLBO was presented in Reference [156].

The multi-target design optimization for a 1-DOF positioner exploiting the TLBO was described with sub-stage procedure as follows.

Stage 1: Identify the optimization problem and optimize the parameters

Set up the population size *np*, the quantity of design variables *nd*, and limitations of lower and upper of design variables, ending conditions/ maximal quantity of repetition.

In this study, 03 target formulas were regarded for the 1-DOF positioner as: (i) The 1st target formula, $f_1(\mathbf{X})$ indicating the safety factor as large as possible, (ii) the 2nd target formula, $f_2(\mathbf{X})$ symbolizing the output deformation for ensuring strength of material and desired as high as possible.

The optimal issue is established below:

Min $f(\mathbf{x}) = -w_1 f_1(\mathbf{x}) - w_2 f_2(\mathbf{x})$

Subject to $\mathbf{X} \in x_i = 1, 2, ..., nd$

in which $f_1(\mathbf{X}), f_2(\mathbf{X})$ denote the single target, $f(\mathbf{X})$ denotes the integrated target function. $\mathbf{x}$ symbolizes the vector of design variables in order to $L_{L,i} \le x_i \le U_{L,i}$. $L_{L,i}$ and $U_{L,i}$ are the lower limitation and upper limitation of design variables.

Stage 2: Set up a population

An arbitrary population was created based on the population number (quantity of learners) and quantity of design variables (quantity of courses), as illustrated below.

$$pop = \begin{bmatrix} x_1^1 & \cdots & x_2^1 & x_{nd-1}^1 & x_{1-nd}^1 \\ x_1^2 & \cdots & x_2^2 & x_{nd-1}^2 & x_{nd}^2 \\ \vdots & \cdots & \vdots & \vdots & \vdots \\ x_1^{np-1} & \cdots & x_2^{np-1} & x_{nd-1}^{np-1} & x_{nd}^{np-1} \\ x_1^{np} & \cdots & x_2^{np} & x_{nd-1}^{np} & x_{nd}^{np} \end{bmatrix} \begin{matrix} \rightarrow f(\mathbf{X}^1) \\ \rightarrow f(\mathbf{X}^2) \\ \rightarrow \cdots \\ \rightarrow f(\mathbf{X}^{np-1}) \\ \rightarrow f(\mathbf{X}^{np}) \end{matrix}, \quad (5.170)$$

in which one row illustrates a potential item of a 1-DOF positioner (a leaner) in the population (class). $f(\mathbf{X}^{1,2,...,np-1,np})$ was the equivalent target function worth. $f(\mathbf{X})$ was the integrated target function of two target functions. *Pop* is the population.

Stage 3: Teacher phase

The integrated target function of a 1-DOF positioner was expected to attain the lowest worth, and the greatest resolution would operate as a teacher $\mathbf{X}_{teacher} = \mathbf{X}_{\min f(\mathbf{X})}$. In this algorithm, the teacher often attempted to push the population's mean $\mathbf{X}_{mean}$ into $\mathbf{X}_{teacher}$. Accordingly, solution $\mathbf{x}^i$ was calculated as:

$$\mathbf{X}^{new,i} = \mathbf{X}^i + r(\mathbf{X}_{teacher} - T_F \mathbf{X}_{mean}), \quad (5.171)$$

in which $\mathbf{x}^{new,i}$ and $\mathbf{x}^{i}$ symbolize the updated and current resolutions of *i*, *r* denotes the arbitrary quantity varying from 0 to 1, T_F denotes a teaching parameter, selected as 1 or 2. $\mathbf{X}_{mean}$ is the average of resolution that is defined by the subsequent formula:

$$\mathbf{X}_{mean} = \left[m\left(pop\left(\sum_{j=1}^{np} x_1^j \right) \right) m\left(pop\left(\sum_{j=1}^{np} x_2^j \right) \right) \cdots \left(pop\left(\sum_{j=1}^{np} x_{nd-1}^j \right) \right) \times \left(pop\left(\sum_{j=1}^{np} x_{nd}^j \right) \right) \right] \quad (5.172)$$

in which $m(.)$ is the average of data set.

If the outcomes show that the updated resolution, $\mathbf{x}^{new,i}$ outperforms the existing resolution, $\mathbf{x}^{i}$, the updated resolution is selected and otherwise $\mathbf{x}^{i}$ is chosen. In contrast, if $f\left(\mathbf{x}^{new,i}\right) < f\left(\mathbf{x}^{i}\right),\ \mathbf{x}^{i} = \mathbf{x}^{new,i}$, if $f\left(\mathbf{x}^{new,i}\right) \geq f\left(\mathbf{x}^{i}\right),\ \mathbf{x}^{i} = \mathbf{x}^{i}.$

Stage 4: Student phase

As mentioned earlier, students can expand their knowledge by interacting with each other in a class; thus, the solution is that random interaction would provide more chances to learn new things. The modified formula for the learner phase below was suggested to define updated details between resolution *i* and *j*:

$$\begin{cases} \mathbf{X}^{new,i} = \mathbf{X}^{i} + r\left(\mathbf{X}^{i} - \mathbf{X}^{j}\right) \text{ if } f\left(\mathbf{X}^{i}\right) < f\left(\mathbf{X}^{j}\right) \\ \mathbf{X}^{new,i} = \mathbf{X}^{i} + r\left(\mathbf{X}^{j} - \mathbf{X}^{i}\right) \text{ if } f\left(\mathbf{X}^{i}\right) > f\left(\mathbf{X}^{j}\right) \end{cases}, \quad (5.173)$$

in which $\mathbf{x}^{j}$ is a resolution different from $\mathbf{x}^{i}$.

If the outcome of target function is greater, the $\mathbf{x}^{new}$ is selected, i.e. $\mathbf{x}^{i}$ transforms to $\mathbf{X}^{new}$, otherwise $\mathbf{X}^{i}$.

Step 5: Ending standard

When a cycle/repetition is attained, the procedure ends. Otherwise, activities in 3rd and 4th steps are repeated until attaining a preestablished ending standard.

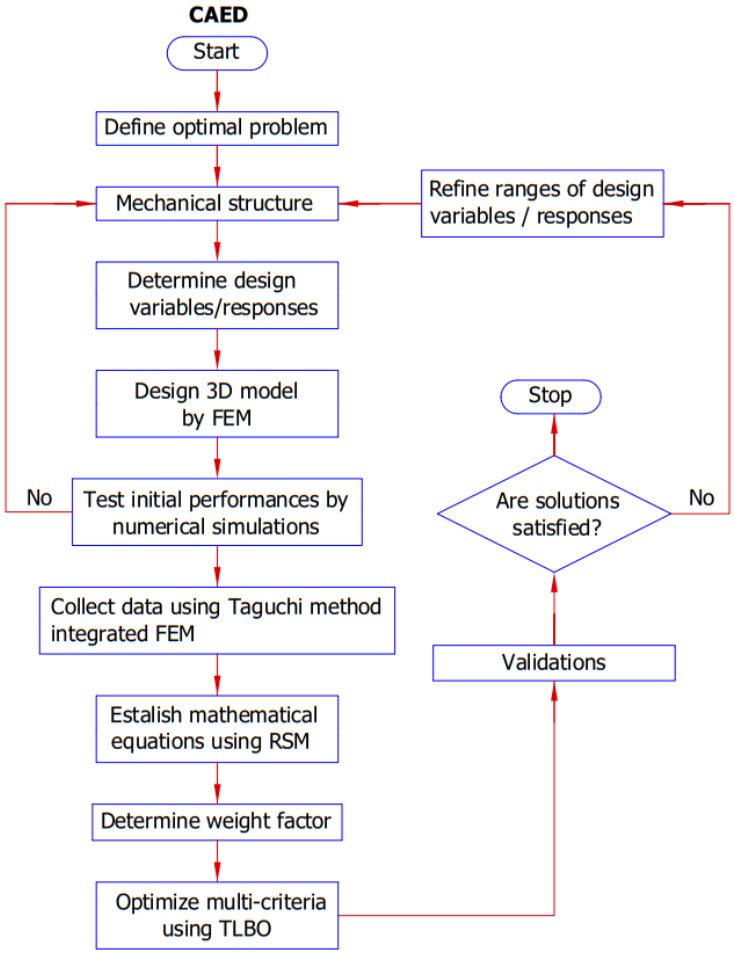

Figure 5.30. Flowchart of multi-objective optimization approach.

Phase 4: Determine weight factor

As the offered positioner expected a great safety factor as well as a great deformation value, the signal to noise (*S/ N)* proportion for both attributes was explained in the equation 3.24. Practically, it is difficult to attain a large displacement and high safety factor simultaneously as they are in conflict with each other. To strike a balance, the trial-error method would be exploited but it is expensive. Another possibility is to integrate multiple targets into a single target by multiplying each target with a matching weight factor. Conventionally, the WF is identified with reference to the priority of each response and customer's requirements. Changes in the weight worth would lead to dissimilar optimized results while the response is very sensitive to design parameters. Accordingly, the WF is expected to be precisely computed to guarantee an accurate exporting of the optimized safety factor as well as output deformation. In the current research, thanks to the well-

formed arithmetical formulas, the WF was allocated for the safety factor and output displacement. As a result, it is easy to control the WF in case the customer requirements change.

This work suggests the totality of the weighted target function to be calculated as:

$$f = w_1 f_1 + w_2 f_2, \tag{5.174}$$

in which, f_1, f_2 and f denote safety factor, displacement, and totality of the weighted target function, correspondingly. w_1, and w_2 represent the weight factor numbers of f_1 and f_2, correspondingly. Herein, $0 \le w_i \le 1$ and $\sum_{i=1}^{2} w_i = 1$. The total of weight is supposed to be a convex integration of the targets. Each individual target for the optimization can be defined by a single optimization resolution on the Pareto front.

Some examples of methods to measure the numbers of w_1 and w_2 are the expertise, the direct assignment methodology, an eigenvector methodology, an empty methodology, a minimal information methodology, as well as an arbitrarily defined methodology. Nevertheless, these approaches produce low level of accuracy and require a complicated procedure. Consequently, I applied techniques introduced by Dao et al. [131] to quantify the WF for every characteristic in reference to arithmetic formulas prior to an optimization process in order to attain more precise outcome in reference to the Eqs. (3.24, 4.12-4.16).

Phase 5: Statistics analysis for developed integrated approach

To perform an evaluation of the offered combination approach's performance, a non-parametric statistical analysis, the Wilcoxon's rank signed assessment, was exploited to compare the other algorithms in order to point out major differences between these algorithms and the offered approach.

5.4.3. Results and discussion

5.4.3.1. Collection of data

Classification of every parameter into three levels depends on professional expertise, as demonstrated in Table 5.23. The L_9 (3^4) orthogonal array of TM was employed to set up the experiment quantity. The safety factor (F_1) and deformation (F_2) were gathered, as illustrated in Table 5.24.

Table 5.23 Design factors and their degrees (unit: mm)

Variables	Variation	Degree 1	Degree 2	Degree 3
A	51-53	51	52	53
B	1-1.2	1	1.1	1.2
C	0.5-0.7	0.5	0.6	0.7
D	0.5-0.7	0.5	0.6	0.7

Then, the ANOVA was exploited to figure out major influences of every factor to the characteristics and the MINITAB 18 software was exploited for an analysis of the experimental data, as shown in Table 5.42.

Table 5.24 Experimental results and responses

No.	*A*	*B*	*C*	*D*	F_1	F_2 (mm)
1	51	1	0.5	0.5	1.5800	2.1726
2	51	1.1	0.6	0.6	1.5645	1.8280
3	51	1.2	0.7	0.7	1.5348	1.6166
4	52	1	0.6	0.7	1.5587	1.7421
5	52	1.1	0.7	0.5	1.4766	1.6637
6	52	1.2	0.5	0.6	1.5866	2.0411
7	53	1	0.7	0.6	1.4634	1.5807
8	53	1.1	0.5	0.7	1.4821	1.9220
9	53	1.2	0.6	0.5	1.5091	1.9174

The regression equations were attained as follows:

$$F_1 = -43.54 + 1.867A - 6.780B + 2.532C + 1.770D - 0.01832A*A + 3.103B*B - 2.352C*C - 1.462D*D \quad (5.175)$$

$$F_2 = 29.39 - 0.437A - 2.03B - 47.92C - 0.419D - 0.019A*B + 0.757AC + 5.856B*C \quad (5.176)$$

Tables 5.25 as well as 5.26 presents the ANOVA outcomes of the safety factor and deformation, conducted at 5% meaning degree and 95% guarantee degree. As can be seen in Table 5.18, the contribution ratios to the safety factor F_1 of *A* and *C* as well as the *B*-*B* collaboration between were more meaningful than the others, at 47.44%, 28.42% and

10.86%, correspondingly. However, the percentage for the influence on the F_1 of *B* and *D*, *C*-*C* association, *A*-*A* association as well as *D*-*D* association were extremely low, at 0.76%, 0.09%, 6.24%, 3.78% and 2.41%, correspondingly. As a result, it is essential to strictly control *A* and *C* for an increase of the safety factor. Additionally, Table 5.19 reveals that the percentage of the displacement F_2 of *C* was highest with 84.34%, and that of *D* was also high, at 11.61% while the remaining factors made unsignificant contributions with a much lower percentage. To be more specific, the percentage of *A* and *B*, *A*-*B* association, *A*-*C* association as well as *B*-*C* collaboration were 2.02%, 0.33%, 0.11%, 0.31% and 1.25%, correspondingly. Accordingly, it is vital to strictly control parameters *C* and *D* to improve the worth of F_2. Moreover, the influence percentage of error was 0% and 0.03% for F_1 and F_2, correspondingly.

Table 5.25 ANOVA for the safety factor

Source	DF	Seq SS	Influence	Adj SS	Adj MS	P-Worth
Model	8	0.017736	100.00%	0.017736	0.002217	Significant
Linear	4	0.013606	76.71%	0.013606	0.003401	Significant
A	1	0.008415	47.44%	0.008415	0.008415	Significant
B	1	0.000134	0.76%	0.000134	0.000134	Significant
C	1	0.005040	28.42%	0.005040	0.005040	Significant
D	1	0.000016	0.09%	0.000016	0.000016	Significant
Square	4	0.004130	23.29%	0.004130	0.001033	Significant
*A***A*	1	0.000671	3.78%	0.000671	0.000671	Significant
*B***B*	1	0.001926	10.86%	0.001926	0.001926	Significant
*C***C*	1	0.001106	6.24%	0.001106	0.001106	Significant
*D***D*	1	0.000427	2.41%	0.000427	0.000427	Significant
Error	0					
Total	8	0.017736	100.00%			

Table 5.26 ANOVA for the displacement

Source	DF	Seq SS	Influence	Adj SS	Adj MS	P- Worth
Model	7	0.320994	99.97%	0.320994	0.045856	0.036
Linear	4	0.315632	98.30%	0.120716	0.030179	0.043

A	1	0.006475	2.02%	0.000033	0.000033	0.667
B	1	0.001059	0.33%	0.004390	0.004390	0.096
C	1	0.270810	84.34%	0.076496	0.076496	0.023
D	1	0.037288	11.61%	0.001507	0.001507	0.161
2-Way Interaction	3	0.005362	1.67%	0.005362	0.001787	0.172
*A*B*	1	0.000355	0.11%	0.000002	0.000002	0.910
*A*C*	1	0.001007	0.31%	0.003340	0.003340	0.109
*B*C*	1	0.004000	1.25%	0.004000	0.004000	0.100
Error	1	0.000101	0.03%	0.000101	0.000101	
Total	8	0.321094	100.00%			

5.4.3.2. Sensitivity analysis

Statistic method was exploited to measure the impact degree of chief variables on the quality attribute. As presented in Fig. 5.31, within a variation [51 mm, 52 mm], factor *A* contributed to an insignificant drop of F_1 and F_2; however, within a variation [52 mm, 53 m], it led to a remarkable decrease of F_1 and an insignificant rise of F_2. For factor *B*, it led to a significant fall of F_1 and an insignificant rise of F_2 within the a variation [1 mm, 1.1 mm]; but, a variation [1.1 mm, 1.2 mm], there were a dramatical rise of F_1 and a slight increase of F_2.

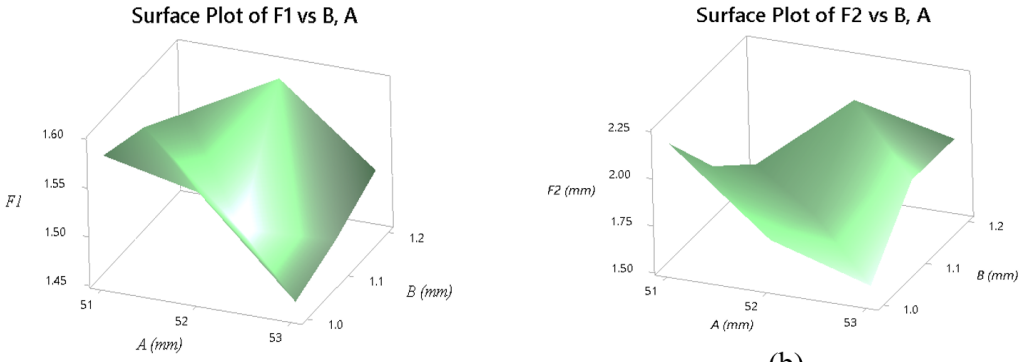

(a) (b)

Figure 5.31. Impacts of *A* and *B* on: (a) safety factor; (b) the output deformation.

As displayed in Fig. 5.32, parameter *C*, within a variety [0.5 mm, 0.6 mm], contributed an unsignificant fall of F_1 but a great fall of F_2; however, within a variety [0.6 mm, 0.7 mm], a dramatic rise of both F_1 and F_2 was observed while a variety [0.6 mm, 0.7 mm], there was a stable reduction of both F_1 and F_2.

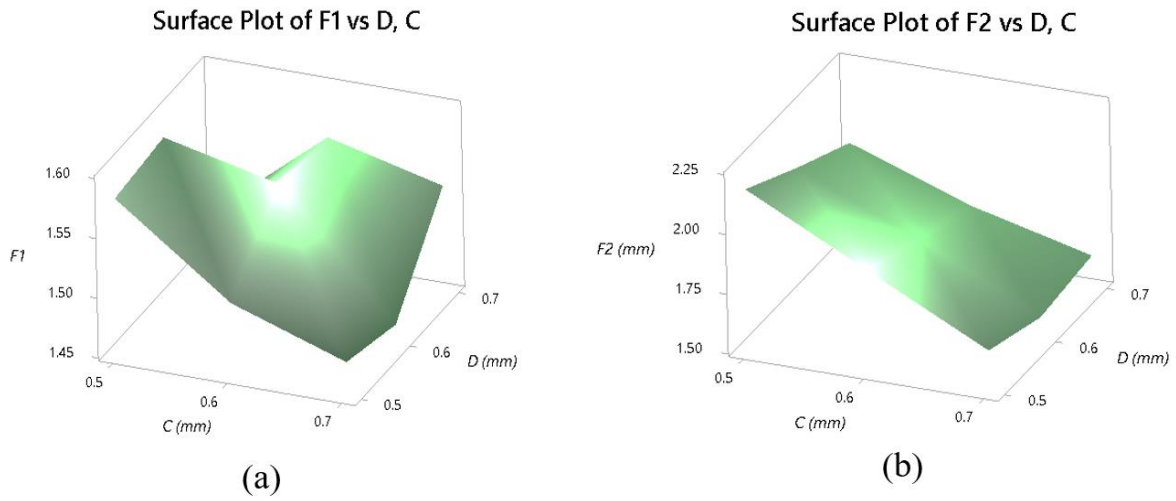

Figure 5.32. Effect diagram of *C* and *D* on: (a) safety factor and (b) the output displacement.

To sum up, overall influences of the chief variables were depicted in Fig. 5.33. The outcomes showed a variety of rises and drops in each factor which can serve as a reference for the mechanical engineers to manage these factors to attain a best design for the offered positioner.

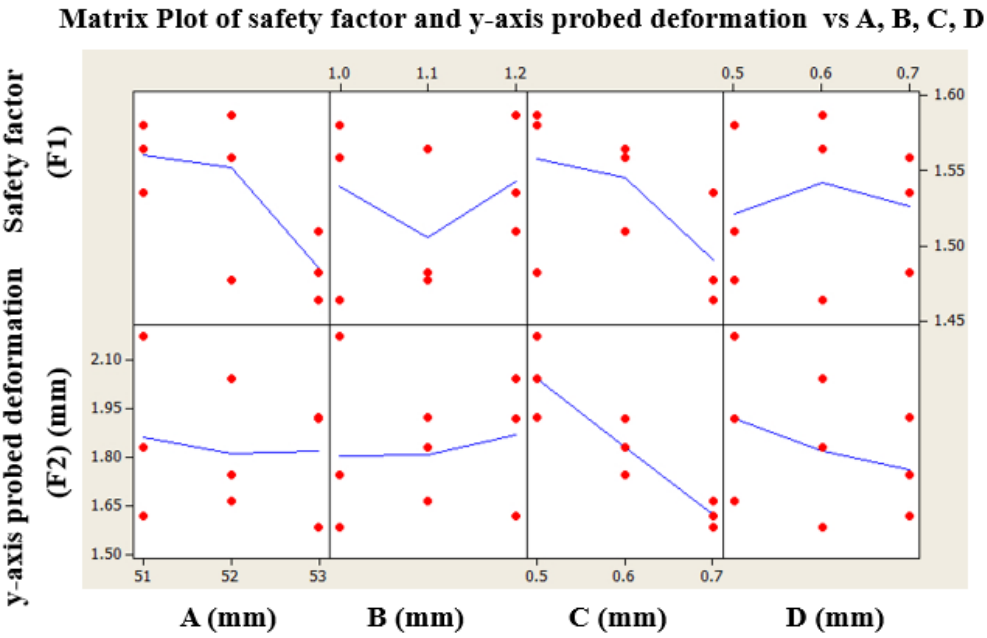

Figure 5.33. Sensitivity of the manageable factors on the attributes.

Derived from computational outcomes shown in Table 5.24, the *S/N* proportion worth (η_1 and η_2) were quantified by Eq. 3.34, as presented in Table 5.27. Next, the median worth and median variety for the standardized *S/N* proportions were identified for every degree of every factor by exploiting the Eq. (4.12), as given in Table 5.28. The Eq. (4.15) was

utilized to measure the WF of features and the outcomes revealed that the weight factor for safety factor as well as deformation were 0.6 and 0.4, correspondingly. With the use of a set of pre-established formulas, these values were precisely measured and applied for further optimization processes in the TLBO. Accordingly, it can be concluded that the percentage for the displacement was significantly greater than that of the safety factor for the rotation positioner. This conclusion is in line with the author's professional expertise in the field of flexure-based structure.

Table 5.27 Experiment outcomes and *S/N* proportions

Trial No.	f_1	f_2 *(mm)*	η_1 of f_1 (dB)	η_2 of f_2 (dB)
1	1.580	2.173	3.973	6.740
2	1.565	1.828	3.888	5.240
3	1.535	1.617	3.721	4.172
4	1.559	1.742	3.855	4.822
5	1.477	1.664	3.385	4.422
6	1.587	2.041	4.009	6.197
7	1.463	1.581	3.307	3.977
8	1.482	1.922	3.418	5.675
9	1.509	1.917	3.574	5.654

Table 5.28 Values of standardized *S/N* proportions (z_i)

S/N proportions		Standardized *S/N* proportions (z_i)	
η_1 (dB)	η_2 (dB)	z_1 of η_1	z_2 of η_2
3.9731	6.7396	0.9484	1.0000
3.8875	5.2395	0.8265	0.4570
3.7210	4.1721	0.5893	0.0706
3.8553	4.8215	0.7805	0.3057
3.3853	4.4215	0.1111	0.1609
4.0093	6.1973	1.0000	0.8037

3.3073	3.9770	0.0000	0.0000
3.4176	5.6751	0.1571	0.6147
3.5744	5.6543	0.3804	0.6071

Table 5.29 The weight factor for the safety factor

Degree	The median worth of standardized *S/N* proportions at each level			
	A	B	C	D
Degree 1	0.7881	0.5764	0.7019	0.4800
Degree 2	0.6306	0.3649	0.6625	0.6088
Degree 3	0.1792	0.6566	0.2858	0.5090
Variety r_{ij}	0.6089	0.2917	0.4160	0.1288
The F_1's weight factor: w_1 = 0.6				

Table 5.30 The weight factor for the displacement

Level	The median worth of standardized *S/N* proportions at each level			
	A	B	C	D
Level 1	0.5092	0.4352	0.8036	0.5893
Level 2	0.4234	0.4109	0.4202	0.4202
Level 3	0.4073	0.4938	0.2821	0.3303
Range r_{ij}	0.1019	0.0830	0.5215	0.2590
The F_2's weight factor: w_2 = 0.4				

5.4.3.3. Optimal results and statistical analysis

The MATLAB 2017 software was exploited to carry out the optimization procedure, with the optimized results including A = 51 mm, B = 1 mm, C = 0.5 mm, D = 0.667 mm, F_1 = 1.56 and F_2 = 2.1 mm.

The efficiency of the suggested algorithm was put into a comparison with another evolutionary algorithm, the AEDE algorithm [157].

For the purpose of assessing statistic manners of the combination optimization approach, the Wilcoxon's rank signed assessment which has been commonly used for a statistical analysis, was employed at 5% meaningful degree and 95% guarantee intervals. The calculational simulations were performed with 40 runs for every algorithm. The outcomes of Wilcoxon's rank signed assessment were displayed in Tables 5.24 and 5.25.

In this work, the null hypothesis supposed that there was no significant differentiation among median numbers of both algorithms. However, the outcomes in Tables 5.31 and 5.32 indicated that the p-worth was lower than 0.05 which led to a rejection of the null hypothesis. In other words, there was a statistically significant dissimilarity among the developed and AEDE algorithms which supports the conclusion that the suggested combination approach is superior than the AEDE algorithm in dealing with the multi-criteria optimization problem.

Table 5.31 Wilcoxon's comparison of offered algorithm versus AEDE for F_1

Number for tests	Anticipated mean	p- worth	Wilcoxon statistic
40	0.0020	0.000	820

Table 5.32 Wilcoxon's comparison of offered algorithm versus AEDE for F_2

Sample for tests	Anticipated mean	p-worth	Wilcoxon statistic
40	0.00175	0.000	820

In contrast, the Friedman Test [158] is a non-parametric technique which can be considered as a substitution to the one-way ANOVA with recurrent measures. This test would identify the dissimilarity among the designed approach and the AEDE algorithm at noteworthy degree of $\alpha = 0.05$. Two separate Friedman tests for the safety factor as well as deformation were performed. The calculational simulations were carried out with 40 runs for every algorithm. The outcome indicated that the p-worth was less than 0.05 which rejected the null hypothesis. It means that there was a differentiation among the offered combination optimization approach and the AEDE, as presented in Tables 5.33-34.

Table 5.33 Friedman test for the F_1

Attribute	Quantity of assessments	Mean	Totality of Ranks
F_1 by offered approach	40	1.5586	80.0
F_1 by AEDE	40	1.5566	40.0
Total	80	1.5576	
DF	Chi-Square	P-Worth	
1	40.00	0.000	
Null hypothesis	H_0: All treatment influences are 0		
Alternative hypothesis	H_1: Not all treatment influences are 0		

Table 5.34 Friedman test for the F_2

Attribute	Quantity of assessments	Mean	Totality of Ranks
F_2 by offered approach	40	2.096	80.0
F_2 by AEDE	40	2.094	40.0
Total	80	2.095	
DF	Chi-Square	P-Worth	
1	40.00	0.000	
Null hypothesis	H_0: All treatment influences are 0		
Alternative hypothesis	H_1: Not all treatment influences are 0		

5.4.4. Validation

The optimization factors (A = 51 mm, B = 1 mm, C = 0.5 mm, D = 0.6674 mm, F_1 = 1.558 and F_2 = 2.096 mm) were exploited to build the 3D design. Afterward, experiment confirmations were carried out for a validation of the projected outcomes. The experiment was conducted with the similar initial conditions and input displacement, the highest displacement has a value of 2.096 mm and the smallest safety factor was equal to 1.558. As illustrated in Table 5.35, the errors among the anticipated outcomes and confirmations

are under 7% for both responses. It suggests that the anticipated resolutions are aligned with the verified outcomes.

The comparison showed that the optimized outcomes outperformed the results in the initial design. After the optimization, an increase of roughly 3.708% and 18.498% for the safety factor as well as the displacement, respectively, was witnessed. Details are provided in Table 5.36. These conclusions proved the efficiency of the combination approach in solving multi-target optimization design of the offered positioner.

Table 5.35 Error between foreseen outcomes and confirmation outcomes

Responses	Prediction	Validation	Error (%)
Safety factor	1.558	1.5533	0.30
Displacement (mm)	2.096	1.9621	6.82

Table 5.36 Advancement between primary outcome and optimization outcome

Attributes	Primary outcome	Optimization outcome	Advancement (%)
Safety factor	1.5023	1.558	3.708
Displacement (mm)	1.7688	2.096	18.498

5.4.5. Achieved results

This chapter reports a proficient combination approach for the flexure rotation positioner which can be exploited for nanoindentation tester. The design mimicked the bio-mechanical behaviors of beetles to attain a good translation motion and extreme degree of flexibility. To improve the operating travel, the optimization of the geometric parameters of the offered positioner was conducted through an integrated approach of the TM, RSM-based FEM and TLBO. The safety factor and displacement were regarded as two target functions. Next, the weight factor of two features were computed via the establishment of several sets of formulas. The outcome indicated that the safety factor has a WF value of 0.5995 (59.95%) and displacement has a WF of 0.4005 (40.05%), correspondingly. The computed WF values were embedded into the TLBO to resolve the multi-target optimization. The ANOVA was used to measure the influences of chief variables on the output features. The attained outcomes showed that the optimization factors were detected

at A = 51 mm, B = 1 mm, C = 0.5 mm, D = 0.6674 mm as well as the optimized safety factor was 1.558 and the optimized displacement was about 2.096 mm. These findings suggested the close alignment between the projected and validated results. Moreover, computations by the Wilcoxon's rank signed test and Friedman test revealed remarkable advances of the developed hybrid optimization algorithm in comparison with the AEDE algorithm. Therefore, it is a practical approach in solving the multi-target optimization issue for complicated engineering issue.

5.5. Conclusions

This chapter presents three mechanical design alternatives including compliant two XY stages, rotary stage as well as optimal methods so as to enhance the output attributes of the proposed stages for positioning the specimens in the nanoindentation tester system. Each design has its own merits and demerits. Based on the different working conditions of the nanoindentation tester or precision positioning system, each compliant stage and optimization methods should be considered to choose for suitable working conditions.

The XY-positioner prototype will be created for the study's future work, and experiments will be conducted to verify the analytical findings. The analytical outcomes will also be confirmed, and a closed loop system will be employed to improve the offered positioner's accurateness in terms of location.

CHAPTER 6 CONCLUSIONS AND RECOMMENDATIONS

6.1. Conclusions

In this thesis, a flexure hinge, three designs of 1-DOF positioner, two designs of 2-DOF positioner, and a rotary stage have been developed for nanoindentation device.

Firstly, a new optimization design approach was developed for optimizing the output attributes of flexure hinge. The four types of compliant joints including corner-rounded joint, right circular joint, power function joint 1 and elliptic joint were compared via the detasFLEX software for the rotation axis shift, maximal angle deflection and safety factor with the same worth of primary investigation angle. Then, the investigation outcomes revealed unique features of the elliptic hinge which was selected with the desire to achieve excellent performances of rotary axis shift, safety factor and maximal angle deflection, consequently, in this research, hybrid methodology of the TM, fuzzy logic reasoning, RSM and MFO algorithm was developed to enhance simultaneously above-mentioned three quality features. Moreover, the attained results were of $10.94*10^{-5}$ mm for the rotation axis shift, 2.99 for the safety factor and $52.006*10^{-3}$ rad for the angle deflection. The Wilcoxon and Friedman results illustrated the advances of the integrated method compared to the ASO algorithm. In addition, a comparison among the mean convergence time for 30 runs of algorithms including the developed methodology, ASO algorithm as well as GA was carried out. The outcomes showed that the proposed method performed a better convergence speed compared to that of ASO algorithm and GA. Accordingly, with reference to the above-mentioned results, the proposed integration method proved to be beneficial and effectual in solving multi-target optimization issues in complex engineering. In this study, the elliptic joint and other compliant joints such as leaf joint and circular joint were blended into flexure-based positioners for locating and indenting the specimen in nanoindentation testing device.

Secondly, three new design alternatives of 01-DOF positioning stages were proposed for driving the indenter. Moving to more detailed analysis, the first 01-DOF stage was integrated the four-lever mechanism amplifier and beetle-liked structure. The first 01-DOF stage replicated the biomechanical behavior of beetle with the aim of achieving a linear displacement and decreasing parasitic motion. To attain a better result of both output displacement and safety factor, a combination of the improved ANFIS, TLBO, the RSM,

FEM, TM is employed for optimizing the chief geometrical factors of developed platform. The procedure started with the first step of optimizing the root mean squared error (*RMSE*) by the TM to identify proper controllable parameters for the ANFIS structure and continued with the next step of calculating the weight factor of both responses via formulating several sets of statistic-based formulas. The results revealed that the WFs of safety factor and displacement were 0.4416 (44.16%) and 0.5584 (55.84%), respectively. The values of these WFs were integrated into the TLBO algorithm which could offer solutions to multi-target optimization troubles. The sensitivity analysis as well as ANOVA were conducted to define the effects and significant contributions of design variables on the two quality characteristics. The results illustrated that the optimal safety factor was 1.5141 and the optimal displacement was approximately 2.4065 mm. Additionally, the results depicted that the errors between the optimal results and the FEA validations for the safety factor and output displacement were 0.786% and 0.824%, respectively. The error between experimental result and the predicted result was about 7.581%. These outcomes illustrated the usefulness and effectiveness of the offered combination approach for the first 01-DOF positioner in solving multi-target optimization issues for complicated designs. In addition, the second design was based on two-lever displacement amplifier, flexure shift mechanism and parallel guiding mechanism. The new hybrid optimization approach of the TM, RSM, and weight factor quantification technique in accordance with signal to noise and WOA algorithm was proposed for optimizing the quality features of the second design alternative of a 01-DOF stage. The results show that the output Z-displacement was about 436.04 μm and the safety factor was around 2.224 and the error between predicted consequences and verifications for the displacement and safety factor was 4.245282% and 7.124857%, respectively. Accordingly, the projected outcomes were in a great agreement with the verified outcomes. The third 01-DOF design was based on six-lever amplifier and parallel guiding mechanism. Analytical model of the proposed third compliant 01-DOF stage was built based on the PRBM method and Lagrange method. The results illustrates that the 1st natural frequency of analytical result was 176.957 Hz and the first natural frequency of FEA result was 191.5 Hz and an error between analytical result and FEA test is rather small with an error of the first natural frequency with 7.59%. The comparison result pointed out that the analytical modelling approach based on the PRBM method is appropriate for examining the relation between the input and output

characteristics for initial characteristics of the compliant 01-DOF positioner. Consequently, the suggested analytical method is reliable and effective enough to evaluate the initial quality characteristic for the proposed compliant 01-DOF positioner.

Finally, three new design alternatives were proposed for locating specimens in nanoindentation testing device as well as precise positioning system. The first compliant XY-positioner was based on four-lever displacement amplifier and guiding parallel guiding according to zigzag-based flexure spring. A new hybrid optimization approach of the TM, RSM, and NSGA-II algorithm was proposed for optimizing the quality characteristics of the compliant XY-positioner. The optimized results were found at the output displacement of 3.862 mm and the first natural of 45.983 Hz. Additionally, the results indicated that the errors between the optimization outcomes and the FEA validations for the first natural frequency and y-axis displacement were 2.1932% and 0.05%, correspondingly. Statistics for the FEA validations were in line with the estimated outcomes for the combination approach. Further experiments in the future will fabricate a prototype and assess its behaviors for the purpose of result verifications. The second design of rotary stage was based on the profile's beetle leg, cartwheel hinge and rotation platform based on three leaf flexure hinges. A new hybrid optimization approach of TM, RSM, weight factor quantification technique according to signal to noise and TLBO algorithm was developed for optimizing the quality features of the compliant rotary stage. The result found that the WFs of safety factor and displacement are 0.5995 (59.95%) and 0.4005 (40.05%), respectively. Then, these WF's values were integrated into the TLBO algorithm to solve the multi-objective optimization problem. Moreover, the optimized safety factor was 1.558 and the optimized displacement was about 2.096 mm which illustrates a great alignment of the projected outcomes to the validated results. Statistics of the Wilcoxon's rank signed assessment and Friedman assessment suggested that the developed hybrid optimization algorithm was greater than the AEDE algorithm. Consequently, it is a proficient methodology to solve the multi-target optimization issue for complex design. The second 02-DOF positioner design was based on an eight-lever displacement intensification structure with elliptic joints and parallel guiding structure. Analytical model of the proposed 2nd 02-DOF positioner was established based on the kinetostatic analysis-based method and Lagrange method. Later on, the neural network algorithm is utilized for optimizing the main parameters in order to improve the quality characteristic of the offered

positioner. The results showed that an error between analytical result and FEA test was 4.785 %. The optimized result illustrated that the frequency of stage was 112.0995 Hz.

In addition, the sensitivity analysis as well as ANOVA were performed for determining the influences and major contributions of design variables to the output features. Based on the optimized outcomes and the FEA validations, the proposed hybrid approaches are reliable and efficient enough to address multi-target optimization issues for complex designs.

The achieved results and proposed methods from this thesis can be utilized for desiging and optimizing in mechanical engineering and related engineering.

6.2. Recommendations

In this thesis, the author developed compliant 01-DOF stages, 02-DOF stages and rotary stage. Meanwhile, a fully complete nanoindentation testing device was not developed. Therefore, in the future research, the new directions will recommend as follows:

- Develop more compliant positioning stages intended to apply for in situ nanoindentation testing device and precise positioning system.

- Develop more compliant positioning stages inspired from advantageous features of animals for precise positioning system.

- Develop new optimal approaches for enhancing compliant positioning stages.

- Fabricate and test the characteristics of the new compliant positioning stages.

- Further study may help mechanical designers develop principles and guidelines in order to support in the development of new and improved positioning stages intended application for in situ nanoindentation testing device as well as wafer alignment systems.

REFERENCES

[1] Ebenstein, D. M., & Pruitt, L. A. (2006). Nanoindentation of biological materials. Nano today, 1(3), 26-33.

[2] Hu, Z., Lynne, K. J., Markondapatnaikuni, S. P., & Delfanian, F. (2013). Material elastic–plastic property characterization by nanoindentation testing coupled with computer modeling. Materials Science and Engineering: A, 587, 268-282.

[3] Nohava, J., Randall, N. X., & Conté, N. (2009). Novel ultra nanoindentation method with extremely low thermal drift: Principle and experimental results. Journal of Materials Research, 24(3), 873-882.

[4] O'Brien, W. (2005). Long-range motion with nanometer precision. Photonics Spectra, 39(6), 80-81.

[5] Lecocq, M., Linares, J. M., Chaves-Jacob, J., Coyle, T., Roffino, S., Eyraud, M., Gigmes, D., Decherchi, P. & Dousset, E. (2020). Total knee arthroplasty with a Ti6Al4V/PEEK prosthesis on an osteoarthritis rat model: behavioral and neurophysiological analysis. Scientific Reports, 10(1), 1-15.

[6] Safaei, M., & Anton, S. R. (2016, September). Sensing and energy harvesting performance, and fatigue life of embedded piezoelectric transducer in total knee arthroplasty. In Smart Materials, Adaptive Structures and Intelligent Systems (Vol. 50497, p. V002T07A010). American Society of Mechanical Engineers.

[7] Hu, Z. (2017). Characterization of materials, nanomaterials, and thin films by nanoindentation. Microscopy Methods in Nanomaterials Characterization, 165-239.

[8] Zhang, W., Li, J., Xing, Y., Nie, X., Lang, F., Yang, S., ... & Zhao, C. (2020). Experimental study on the thickness-dependent hardness of SiO2 thin films using nanoindentation. Coatings, 11(1), 23.

[9] Huang, H., Zhao, H., Mi, J., Yang, J., Wan, S., Xu, L., & Ma, Z. (2012). A novel and compact nanoindentation device for in situ nanoindentation tests inside the scanning electron microscope. AIP Advances, 2(1), 012104.

[10] Huang, H., Shi, C., Zhao, H., & Zhang, L. (2013). Influence of friction on the residual morphology, the penetration load and the residual stress distribution of a Zr-based bulk metallic glass. AIP Advances, 3(4), 042116.

[11] Huang, H., Zhao, H., Mi, J., Yang, J., Wan, S., Yang, Z., ... & Geng, C. (2011).

Experimental research on a modular miniaturization nanoindentation device. Review of Scientific Instruments, 82(9), 095101.

[12] Alderete, N., Zaheri, A., & Espinosa, H. D. (2019). A novel in situ experiment to investigate wear mechanisms in biomaterials. Experimental Mechanics, 59(5), 659-667.

[13] Jiang, C., Lu, H., Zhang, H., Shen, Y., & Lu, Y. (2017). Recent advances on in situ SEM mechanical and electrical characterization of low-dimensional nanomaterials. Scanning, 2017.

[14] Gianola, D. S., Sedlmayr, A., Mönig, R., Volkert, C. A., Major, R. C., Cyrankowski, E., Asif, S. A. S. , Warren, O. L. & Kraft, O. (2011). In situ nanomechanical testing in focused ion beam and scanning electron microscopes. Review of Scientific Instruments, 82(6), 063901.

[15] Rabe, R., Breguet, J. M., Schwaller, P., Stauss, S., Haug, F. J., Patscheider, J., & Michler, J. (2004). Observation of fracture and plastic deformation during indentation and scratching inside the scanning electron microscope. Thin Solid Films, 469, 206-213.

[16] Larry L.Howell, Compliant Mechanisms, John Wiley & Sons, 2001.

[17] Premanand, S., & Arunkumar, G., Review on design of compliant mechanism for automotive application–a toplogy optimization approach, (2018).

[18] Sung, E., Slocum, A. H., Ma, R., Bean, J. F., & Culpepper, M. L. (2011). Design of an ankle rehabilitation device using compliant mechanisms. Journal of Medical Devices, 5(1).

[19] Lotti, F., Tiezzi, P., Vassura, G., & Zucchelli, A. (2002, November). Mechanical structures for robotic hands based on the compliant mechanism concept. In 7th ESA Workshop on Advanced Space Technologies for Robotics and Automation (pp. 1-8).

[20] Rodríguez-Cianca, D., Weckx, M., Torricelli, D., Gonzalez, J., Lefeber, D., & Pons, J. L. (2015, November). A compliant 2-dof ankle-foot system for a biologically inspired humanoid robot. In 2015 IEEE-RAS 15th International Conference on Humanoid Robots (Humanoids) (pp. 264-269). IEEE.

[21] Wei, J., Ye, H., Van Zeijl, H. W., Sarro, P. M., & Zhang, G. Q. (2012). Single-Mask Fabrication of Temperature Triggered MEMS Switch for Cooling Control in SSL

System. Procedia Engineering, 47, 849-852.

[22] Lobontiu, N., Paine, J. S., Garcia, E., & Goldfarb, M. (2001). Corner-filleted flexure hinges. J. Mech. Des., 123(3), 346-352.

[23] Lobontiu, N., Garcia, E., Hardau, M., & Bal, N. (2004). Stiffness characterization of corner-filleted flexure hinges. Review of scientific instruments, 75(11), 4896-4905.

[24] Xu, P., Jingjun, Y., Guanghua, Z., & Shusheng, B. (2008). The stiffness model of leaf-type isosceles-trapezoidal flexural pivots.

[25] P. Xu, P., Jingjun, Y., Guanghua, Z., Shusheng, B., & Zhiwei, Y. (2008). Analysis of rotational precision for an isosceles-trapezoidal flexural pivot. Journal of mechanical design, 130(5).

[26] Yong, Y. K., Lu, T. F., & Handley, D. C. (2008). Review of circular flexure hinge design equations and derivation of empirical formulations. Precision engineering, 32(2), 63-70.

[27] Lobontiu, N., & Paine, J. S. (2002). Design of circular cross-section corner-filleted flexure hinges for three-dimensional compliant mechanisms. J. Mech. Des., 124(3), 479-484.

[28] Tian, Y., Shirinzadeh, B., & Zhang, D. (2010). Closed-form compliance equations of filleted V-shaped flexure hinges for compliant mechanism design. Precision Engineering, 34(3), 408-418.

[29] Tseytlin, Y. M. (2002). Notch flexure hinges: an effective theory. Review of Scientific Instruments, 73(9), 3363-3368.

[30] Lobontiu, N., Paine, J. S., Garcia, E., & Goldfarb, M. (2002). Design of symmetric conic-section flexure hinges based on closed-form compliance equations. Mechanism and machine theory, 37(5), 477-498.

[31] Zhang, X., & Zhu, B. (2018). Topology optimization of compliant mechanisms. Singapore: Springer.

[32] Pei, X., Yu, J., Zong, G., Bi, S., & Su, H. (2009). The modeling of cartwheel flexural hinges. Mechanism and Machine Theory, 44(10), 1900-1909.

[33] Verotti, M., Dochshanov, A., & Belfiore, N. P. (2017). A comprehensive survey on microgrippers design: Mechanical structure. Journal of Mechanical Design, 139(6), 060801.

[34] Hubbard, N. B., Culpepper, M. L., & Howell, L. L. (2006). Actuators for

micropositioners and nanopositioners.

[35] Wu, Z., & Xu, Q. (2018, February). Survey on recent designs of compliant micro-/nano-positioning stages. In Actuators (Vol. 7, No. 1, p. 5). MDPI.

[36] Gu, G. Y., Li, C. X., Zhu, L. M., & Su, C. Y. (2015). Modeling and identification of piezoelectric-actuated stages cascading hysteresis nonlinearity with linear dynamics. IEEE/ASME Transactions on Mechatronics, 21(3), 1792-1797.

[37] Ling, M., Howell, L. L., Cao, J., & Chen, G. (2020). Kinetostatic and dynamic modeling of flexure-based compliant mechanisms: a survey. Applied Mechanics Reviews, 72(3).

[38] Xu, Q. (2012). Design and development of a flexure-based dual-stage nanopositioning system with minimum interference behavior. IEEE Transactions on Automation Science and Engineering, 9(3), 554-563.

[39] Lee, J. W., Li, Y. C., Chen, K. S., & Liu, Y. H. (2016). Design and control of a cascaded piezoelectric actuated two-degrees-of-freedom positioning compliant stage. Precision Engineering, 45, 374-386.

[40] Xuerui, L., Weiqing, H., & Mengxin, S. (2018). A Novel 2D Piezo-Nanopositioning Stage Based on Triangle Amplifier Mechanism. Transactions of Nanjing University of Aeronautics & Astronautics, 34(1), 1-8.

[41] Pinskier, J., Shirinzadeh, B., Clark, L., Qin, Y., & Fatikow, S. (2016). Design, development and analysis of a haptic-enabled modular flexure-based manipulator. Mechatronics, 40, 156-166.

[42] Hao, G., & Yu, J. (2016). Design, modelling and analysis of a completely-decoupled XY compliant parallel manipulator. Mechanism and Machine Theory, 102, 179-195.

[43] Cai, K., Tian, Y., Wang, F., Zhang, D., & Shirinzadeh, B. (2016). Development of a piezo-driven 3-DOF stage with T-shape flexible hinge mechanism. Robotics and Computer-Integrated Manufacturing, 37, 125-138.

[44] Zhang, X., & Xu, Q. (2015, November). Design of a new decoupled compliant XYZ parallel-kinematic nanopositioning stage. In TENCON 2015-2015 IEEE Region 10 Conference (pp. 1-4). IEEE.

[45] Lai, L. J., Gu, G. Y., & Zhu, L. M. (2012). Design and control of a decoupled two degree of freedom translational parallel micro-positioning stage. Review of Scientific Instruments, 83(4), 045105.

[46] Ding, B., Li, Y., Xiao, X., Tang, Y., & Li, B. (2017). Design and analysis of a 3-DOF planar micromanipulation stage with large rotational displacement for micromanipulation system. Mechanical Sciences, 8(1), 117-126.

[47] Zhang, X., & Xu, Q. (2015, December). Design of a new flexure-based XYZ parallel nanopositioning stage. In 2015 IEEE international conference on robotics and biomimetics (ROBIO) (pp. 1962-1966). IEEE.

[48] Oba, Y., Yamada, Y., Igarashi, K., Katsura, S., & Kakinuma, Y. (2016). Replication of skilled polishing technique with serial–parallel mechanism polishing machine. Precision Engineering, 45, 292-300.

[49] Law, M., Ihlenfeldt, S., Wabner, M., Altintas, Y., & Neugebauer, R. (2013). Position-dependent dynamics and stability of serial-parallel kinematic machines. CIRP Annals, 62(1), 375-378.

[50] Tang, C., Zhang, M., & Cao, G. (2017). Design and testing of a novel flexure-based 3-degree-of-freedom elliptical micro/nano-positioning motion stage. Advances in Mechanical Engineering, 9(10), 1687814017725248.

[51] Cai, K., Tian, Y., Wang, F., Zhang, D., Liu, X., & Shirinzadeh, B. (2017). Design and control of a 6-degree-of-freedom precision positioning system. Robotics and Computer-Integrated Manufacturing, 44, 77-96.

[52] Zhang, Q., Zhao, J., Peng, Y., Pu, H., & Yang, Y. (2020). A novel amplification ratio model of a decoupled XY precision positioning stage combined with elastic beam theory and Castigliano's second theorem considering the exact loading force. Mechanical Systems and Signal Processing, 136, 106473.

[53] Zhu, W. L., Zhu, Z., Guo, P., & Ju, B. F. (2018). A novel hybrid actuation mechanism based XY nanopositioning stage with totally decoupled kinematics. Mechanical Systems and Signal Processing, 99, 747-759.

[54] Gan, J., Long, J., & Ge, M. F. (2021). Design of a 3DOF XYZ Bi-Directional Motion Platform Based on Z-Shaped Flexure Hinges. Micromachines, 13(1), 21.

[55] Xu, Q. (2014). Design of a large-range compliant rotary micropositioning stage with angle and torque sensing. IEEE Sensors Journal, 15(4), 2419-2430.

[56] Xu, Q. (2014). Design and testing of a novel multi-stroke micropositioning system with variable resolutions. Review of Scientific Instruments, 85(2), 025002.

[57] Polit, S., & Dong, J. (2010). Development of a high-bandwidth XY nanopositioning

stage for high-rate micro-/nanomanufacturing. IEEE/ASME Transactions on mechatronics, 16(4), 724-733.

[58] Dao, T. P., & Huang, S. C. (2017). Design and multi-objective optimization for a broad self-amplified 2-DOF monolithic mechanism. Sādhanā, 42(9), 1527-1542.

[59] Ling, M., Cao, J., Zeng, M., Lin, J., & Inman, D. J. (2016). Enhanced mathematical modeling of the displacement amplification ratio for piezoelectric compliant mechanisms. Smart Materials and Structures, 25(7), 075022.

[60] Yong, Y. K., Aphale, S. S., & Moheimani, S. R. (2008). Design, identification, and control of a flexure-based XY stage for fast nanoscale positioning. IEEE Transactions on Nanotechnology, 8(1), 46-54.

[61] Kim, H. Y., Ahn, D. H., & Gweon, D. G. (2012). Development of a novel 3-degrees of freedom flexure based positioning system. Review of Scientific Instruments, 83(5), 055114.

[62] Hu, X. Y., Jia, J. H., & Tu, S. T. (2012). Displacement amplifier design for an extensometer in high temperature deformation monitoring. Procedia Engineering, 29, 1872-1876.

[63] Nikoobin, A., & Niaki, M. H. (2012). Deriving and analyzing the effective parameters in microgrippers performance. Scientia Iranica, 19(6), 1554-1563.

[64] Wang, F., Liang, C., Tian, Y., Zhao, X., & Zhang, D. (2016). Design and control of a compliant microgripper with a large amplification ratio for high-speed micro manipulation. IEEE/ASME Transactions on Mechatronics, 21(3), 1262-1271.

[65] Chang, S. H., & Du, B. C. (1998). A precision piezodriven micropositioner mechanism with large travel range. Review of Scientific Instruments, 69(4), 1785-1791.

[66] Tang, H., Li, Y., & Xiao, X. (2013, May). Development and assessment of a novel hydraulic displacement amplifier for piezo-actuated large stroke precision positioning. In 2013 IEEE International Conference on Robotics and Automation (pp. 1409-1414). IEEE.

[67] Xu, Q. (2013, December). Structure design of a new compliant gripper based on Scott-Russell mechanism. In 2013 IEEE International Conference on Robotics and Biomimetics (ROBIO) (pp. 1623-1628). IEEE.

[68] W. Ai, W., & Xu, Q. (2014). New structural design of a compliant gripper based on

the Scott-Russell mechanism. International Journal of Advanced Robotic Systems, 11(12), 192.

[69] Lobontiu, N., & Garcia, E. (2003). Analytical model of displacement amplification and stiffness optimization for a class of flexure-based compliant mechanisms. Computers & structures, 81(32), 2797-2810.

[70] Ni, Y., Deng, Z., Wu, X., Li, J., Huang, W., & Li, L. (2013, December). Quasi-static and modal analysis of bridge-type compliant mechanism with flexure hinges. In 2013 Second International Conference on Robot, Vision and Signal Processing (pp. 102-106). IEEE.

[71] Yang, Y. L., Wei, Y. D., Lou, J. Q., Tian, G., Zhao, X. W., & Fu, L. (2015). A new piezo-driven microgripper based on the double-rocker mechanism. Smart Materials and Structures, 24(7), 075031.

[72] Xu, Q., & Li, Y. (2011). Analytical modeling, optimization and testing of a compound bridge-type compliant displacement amplifier. Mechanism and machine theory, 46(2), 183-200.

[73] Liu, P., & Yan, P. (2016). A new model analysis approach for bridge-type amplifiers supporting nano-stage design. Mechanism and Machine Theory, 99, 176-188.

[74] Ling, M., Cao, J., Zeng, M., Lin, J., & Inman, D. J. (2016). Enhanced mathematical modeling of the displacement amplification ratio for piezoelectric compliant mechanisms. Smart Materials and Structures, 25(7), 075022.

[75] Guo, F., Sun, Z., Zhang, S., Cao, R., & Li, H. (2022). Optimal design and reliability analysis of a compliant stroke amplification mechanism. Mechanism and Machine Theory, 171, 104748.

[76] Hricko, J., & Havlík, Š. (2019, June). Compliant mechanisms for motion/force amplifiers for robotics. In International Conference on Robotics in Alpe-Adria Danube Region (pp. 26-33). Springer, Cham.

[77] Chen, G., Ma, Y., & Li, J. (2016). A tensural displacement amplifier employing elliptic-arc flexure hinges. Sensors and Actuators A: Physical, 247, 307-315.

[78] Kota, S., Hetrick, J., Li, Z., & Saggere, L. (1999). Tailoring unconventional actuators using compliant transmissions: design methods and applications. IEEE/ASME Transactions on mechatronics, 4(4), 396-408.

[79] Ouyang, P. R., Zhang, W. J., & Gupta, M. M. (2005, January). Design of a new

compliant mechanical amplifier. In International Design Engineering Technical Conferences and Computers and Information in Engineering Conference (Vol. 47446, pp. 15-24).

[80] Broitman, E. (2017). Indentation hardness measurements at macro-, micro-, and nanoscale: a critical overview. Tribology Letters, 65(1), 1-18.

[81] Ling, M., Howell, L. L., Cao, J., & Chen, G. (2020). Kinetostatic and dynamic modeling of flexure-based compliant mechanisms: a survey. Applied Mechanics Reviews, 72(3).

[82] Nguyen, V. K., Pham, H. T., Pham, H. H., & Dang, Q. K. (2021). Optimization design of a compliant linear guide for high-precision feed drive mechanisms. Mechanism and Machine Theory, 165, 104442.

[83] Yu, Y. Q., Howell, L. L., Lusk, C., Yue, Y., & He, M. G. (2005). Dynamic modeling of compliant mechanisms based on the pseudo-rigid-body model.

[84] Koseki, Y., Tanikawa, T., Koyachi, N., & Arai, T. (2002). Kinematic analysis of a translational 3-dof micro-parallel mechanism using the matrix method. Advanced Robotics, 16(3), 251-264.

[85] Ling, M., Cao, J., Jiang, Z., & Lin, J. (2016). Theoretical modeling of attenuated displacement amplification for multistage compliant mechanism and its application. Sensors and Actuators A: Physical, 249, 15-22.

[86] Ling, M., Cao, J., & Pehrson, N. (2019). Kinetostatic and dynamic analyses of planar compliant mechanisms via a two-port dynamic stiffness model. Precision Engineering, 57, 149-161.

[87] Ryu, J. W., Gweon, D. G., & Moon, K. S. (1997). Optimal design of a flexure hinge based XYφ wafer stage. Precision engineering, 21(1), 18-28.

[88] Awtar, S., & Sen, S. (2010). A generalized constraint model for two-dimensional beam flexures: nonlinear load-displacement formulation.

[89] Midha, A., Bapat, S. G., Mavanthoor, A., & Chinta, V. (2015). Analysis of a fixed-guided compliant beam with an inflection point using the pseudo-rigid-body model concept. Journal of Mechanisms and Robotics, 7(3), 031007.

[90] Howell, L. L., & Midha, A. (1994). A method for the design of compliant mechanisms with small-length flexural pivots.

[91] Rakuff, S., & Cuttino, J. F. (2009). Design and testing of a long-range, precision fast

tool servo system for diamond turning. Precision Engineering, 33(1), 18-25.

[92] Qin, Y., Shirinzadeh, B., Tian, Y., Zhang, D., & Bhagat, U. (2013). Design and computational optimization of a decoupled 2-DOF monolithic mechanism. IEEE/ASmE Transactions on mechatronics, 19(3), 872-881.

[93] Boyle, C., Howell, L. L., Magleby, S. P., & Evans, M. S. (2003). Dynamic modeling of compliant constant-force compression mechanisms. Mechanism and machine theory, 38(12), 1469-1487.

[94] Wang, W. J., Bi, S. S., & Zhang, L. G. (2012). Dynamic modeling of compliant mechanisms based on 2R pseudo-rigid-body model. In Applied Mechanics and Materials (Vol. 163, pp. 277-280). Trans Tech Publications Ltd.

[95] Ling, M., Howell, L. L., Cao, J., & Jiang, Z. (2018). A pseudo-static model for dynamic analysis on frequency domain of distributed compliant mechanisms. Journal of Mechanisms and Robotics, 10(5), 051011.

[96] She, Y., Meng, D., Su, H. J., Song, S., & Wang, J. (2018). Introducing mass parameters to Pseudo–Rigid–Body models for precisely predicting dynamics of compliant mechanisms. Mechanism and Machine Theory, 126, 273-294.

[97] Huang, S. C., & Dao, T. P. (2016). Design and computational optimization of a flexure-based XY positioning platform using FEA-based response surface methodology. International Journal of Precision Engineering and Manufacturing, 17(8), 1035-1048.

[98] Reddy, B. S., Kumar, J. S., & Reddy, K. V. K. (2011). Optimization of surface roughness in CNC end milling using response surface methodology and genetic algorithm. International Journal of Engineering, Science and Technology, 3(8), 102-109.

[99] Tran, N. T., Le Chau, N., & Dao, T. P. (2020). A hybrid computational method of desirability, fuzzy logic, ANFIS, and LAPO algorithm for multiobjective optimization design of Scott Russell compliant mechanism. Mathematical Problems in Engineering, 2020.

[100] Garg, H., Ali, Z., & Mahmood, T. (2021). Generalized dice similarity measures for complex q-Rung Orthopair fuzzy sets and its application. Complex & Intelligent Systems, 7(2), 667-686.

[101] Barak, S., & Sadegh, S. S. (2016). Forecasting energy consumption using ensemble

ARIMA–ANFIS hybrid algorithm. International Journal of Electrical Power & Energy Systems, 82, 92-104.

[102] Güneri, A. F., Ertay, T., & Yücel, A. (2011). An approach based on ANFIS input selection and modeling for supplier selection problem. Expert Systems with Applications, 38(12), 14907-14917.

[103] Armstrong, R. A., Eperjesi, F., & Gilmartin, B. (2002). The application of analysis of variance (ANOVA) to different experimental designs in optometry. Ophthalmic and Physiological Optics, 22(3), 248-256.

[104] Friedman, M. (1937). The Use of Ranks to Avoid the Assumption of Normality Implicit in the Analysis of Variance. Journal of the American Statistical Association, 32(200), 675-701.

[105] Wilcoxon, F. (1992). Individual comparisons by ranking methods. In Breakthroughs in statistics (pp. 196-202). Springer, New York, NY.

[106] Dao, T. P., & Huang, S. C. (2017). Optimization of a two degrees of freedom compliant mechanism using Taguchi method-based grey relational analysis. Microsystem Technologies, 23(10), 4815-4830.

[107] Jiang, Y., Li, T., & Wang, L. (2016). Design, development, and application of a compact flexure-based decoupler with high motion transmission efficiency and excellent input decoupling performance. IEEE/ASME Transactions on Mechatronics, 22(2), 1071-1081.

[108] Kim, J. J., Choi, Y. M., Ahn, D., Hwang, B., Gweon, D. G., & Jeong, J. (2012). A millimeter-range flexure-based nano-positioning stage using a self-guided displacement amplification mechanism. Mechanism and Machine Theory, 50, 109-120.

[109] Lee, H. J., Kim, H. C., Kim, H. Y., & Gweon, D. G. (2013). Optimal design and experiment of a three-axis out-of-plane nano positioning stage using a new compact bridge-type displacement amplifier. Review of scientific instruments, 84(11), 115103.

[110] Li, Y., & Xu, Q. (2009). Design and optimization of an XYZ parallel micromanipulator with flexure hinges. Journal of Intelligent and Robotic Systems, 55(4), 377-402.

[111] Lin, S., Jia, Y., Lei, I. P., & Xu, Q. (2012, December). Design and optimization of a

long-stroke compliant micropositioning stage driven by voice coil motor. In 2012 12th International Conference on Control Automation Robotics & Vision (ICARCV) (pp. 1716-1721). IEEE.

[112] Liu, Y., Wu, K., Xu, D., & Xu, Q. (2014, July). Design of a microscope auto-focusing device based on multi-stage leaf spring. In 2014 IEEE International Conference on Information and Automation (ICIA) (pp. 1-6). IEEE.

[113] Tian, Y., Liu, C., Liu, X., Wang, F., Li, X., Qin, Y., ... & Shirinzadeh, B. (2015). Design, modelling and characterization of a 2-DOF precision positioning platform. Transactions of the Institute of Measurement and Control, 37(3), 396-405.

[114] Golpira, H., & Bevrani, H. (2011). Application of GA optimization for automatic generation control design in an interconnected power system. Energy Conversion and Management, 52(5), 2247-2255.

[115] Kaur, M., & Singh, D. (2021). Multi-modality medical image fusion technique using multi-objective differential evolution based deep neural networks. Journal of Ambient Intelligence and Humanized Computing, 12(2), 2483-2493.

[116] Chatterjee, S., Sarkar, S., Hore, S., Dey, N., Ashour, A. S., & Balas, V. E. (2017). Particle swarm optimization trained neural network for structural failure prediction of multistoried RC buildings. Neural Computing and Applications, 28(8), 2005-2016.

[117] Rao, R. V., Savsani, V. J., & Vakharia, D. P. (2012). Teaching–learning-based optimization: an optimization method for continuous non-linear large scale problems. Information sciences, 183(1), 1-15.

[118] Mirjalili, S. (2015). Moth-flame optimization algorithm: A novel nature-inspired heuristic paradigm. Knowledge-based systems, 89, 228-249.

[119] Aljarah, I., Faris, H., & Mirjalili, S. (2018). Optimizing connection weights in neural networks using the whale optimization algorithm. Soft Computing, 22(1), 1-15.

[120] Yang, X. S., & He, X. (2013), Firefly algorithm: recent advances and applications, Int. J. Swarm Intell, Vol. 1, No. 1, pp. 36--50.

[121] Sadollah, A., Sayyaadi, H., & Yadav, A. (2018). A dynamic metaheuristic optimization model inspired by biological nervous systems: Neural network algorithm. Applied Soft Computing, 71, 747-782.

[122] Lobontiu, N., Paine, J. S., Garcia, E., & Goldfarb, M. (2001). Corner-filleted flexure

hinges. J. Mech. Des., 123(3), 346-352.

[123] Dang, M. P., Le, H. G., Chau, N. L., & Dao, T. P. (2021). Optimization for a flexure hinge using an effective hybrid approach of fuzzy logic and moth-flame optimization algorithm. Mathematical Problems in Engineering, 2021.

[124] Henning, S., Linß, S., & Zentner, L. (2018). detasFLEX–A computational design tool for the analysis of various notch flexure hinges based on non-linear modeling. Mechanical Sciences, 9(2), 389-404.

[125] Yu, J., Xie, Y., Li, Z., & Hao, G. (2015). Design and experimental testing of an improved large-range decoupled XY compliant parallel micromanipulator. Journal of Mechanisms and Robotics, 7(4), 044503.

[126] Zhao, W., Wang, L., & Zhang, Z. (2019). Atom search optimization and its application to solve a hydrogeologic parameter estimation problem. Knowledge-Based Systems, 163, 283-304.

[127] Ho, N. L., Dao, T. P., Le, H. G., & Chau, N. L. (2019). Optimal design of a compliant microgripper for assemble system of cell phone vibration motor using a hybrid approach of ANFIS and Jaya. Arabian Journal for Science and Engineering, 44(2), 1205-1220.

[128] Le Chau, N., Nguyen, M. Q., Dao, T. P., Huang, S. C., Hsiao, T. C., Dinh-Cong, D., & Dang, V. A. (2019). An effective approach of adaptive neuro-fuzzy inference system-integrated teaching learning-based optimization for use in machining optimization of S45C CNC turning. Optimization and Engineering, 20(3), 811-832.

[129] Wei, L. Y. (2016). A hybrid ANFIS model based on empirical mode decomposition for stock time series forecasting. Applied Soft Computing, 42, 368-376.

[130] Dang, M. P., Le, H. G., Le Chau, N., & Dao, T. P. (2020). A multi-objective optimization design for a new linear compliant mechanism. Optimization and Engineering, 21(2), 673-705.

[131] Dao, T. P., Huang, S. C., & Le Chau, N. (2018). Robust parameter design for a compliant microgripper based on hybrid Taguchi-differential evolution algorithm. Microsystem Technologies, 24(3), 1461-1477.

[132] Dang, M. P., Le, H. G., Le, N. N. T., Le Chau, N., & Dao, T. P. (2021). Multiresponse optimization for a novel compliant Z-stage by a hybridization of response surface method and whale optimization algorithm. Mathematical Problems in

Engineering, 2021.

[133] Mirjalili, S., & Lewis, A. (2016). The whale optimization algorithm. Advances in engineering software, 95, 51-67.

[134] Gandomi, A. H., Yang, X. S., & Alavi, A. H. (2013). Cuckoo search algorithm: a metaheuristic approach to solve structural optimization problems. Engineering with computers, 29(1), 17-35.

[135] Dang, M. P., Le, H. G., Chau, N. L., & Dao, T. P. (2021). Optimization for a flexure hinge using an effective hybrid approach of fuzzy logic and moth-flame optimization algorithm. Mathematical Problems in Engineering, 2021.

[136] Yildiz, A. R. (2013). Hybrid Taguchi-differential evolution algorithm for optimization of multi-pass turning operations. Applied Soft Computing, 13(3), 1433-1439.

[137] Dinh, V. B., Chau, N. L., Le, N. T., & Dao, T. P. (2021). Topology-based geometry optimization for a new compliant mechanism using improved adaptive neuro-fuzzy inference system and neural network algorithm. Engineering with Computers, 1-30.

[138] Xu, Q. (2013). Design, testing and precision control of a novel long-stroke flexure micropositioning system. Mechanism and machine Theory, 70, 209-224.

[139] Xiaochen, L., & Yanling, T. (2013, August). The design and new controller of a 1-DOF precision positioning platform. In 2013 International Conference on Manipulation, Manufacturing and Measurement on the Nanoscale (pp. 190-194). IEEE.

[140] Le Chau, N., Tran, N. T., & Dao, T. P. (2021). An optimal design method for compliant mechanisms. Mathematical Problems in Engineering, 2021.

[141] Dang, M. P., Dao, T. P., & Le, H. G. (2018, November). Optimal Design of a New Compliant XY Micro positioning Stage for Nanoindentation Tester Using Efficient Approach of Taguchi Method, Response Surface Method and NSGA-II. In 2018 4th International Conference on Green Technology and Sustainable Development (GTSD) (pp. 1-6). IEEE.

[142] Martínez-Vargas, A., Domínguez-Guerrero, J., Andrade, Á. G., Sepúlveda, R., & Montiel-Ross, O. (2016). Application of NSGA-II algorithm to the spectrum assignment problem in spectrum sharing networks. Applied Soft Computing, 39, 188-198.

[143] Lu, K., Zhang, J., Chen, W., Jiang, J., & Chen, W. (2014, June). A monolithic microgripper with high efficiency and high accuracy for optical fiber assembly. In 2014 9th IEEE Conference on Industrial Electronics and Applications (pp. 1942-1947). IEEE.

[144] Yang, Y. L., Wei, Y. D., Lou, J. Q., Xie, F. R., & Fu, L. (2015). Development and precision position/force control of a new flexure-based microgripper. Journal of Micromechanics and Microengineering, 26(1), 015005.

[145] Dang, M. P., Le, H. G., Van, M. N., Chau, N. L., & Dao, T. P. (2022). Modeling and Optimization for a New Compliant 2-dof Stage for Locating Biomaterial Samples by an Efficient Approach of a Kinetostatic Analysis-Based Method and Neural Network Algorithm. Computational Intelligence and Neuroscience, 2022.

[146] Singh, D., Kumar, V., & Kaur, M. (2020). Classification of COVID-19 patients from chest CT images using multi-objective differential evolution–based convolutional neural networks. European Journal of Clinical Microbiology & Infectious Diseases, 39(7), 1379-1389.

[147] Pannu, H. S., Singh, D., & Malhi, A. K. (2019). Multi-objective particle swarm optimization-based adaptive neuro-fuzzy inference system for benzene monitoring. Neural computing and applications, 31(7), 2195-2205.

[148] Gupta, A., Singh, D., & Kaur, M. (2020). An efficient image encryption using non-dominated sorting genetic algorithm-III based 4-D chaotic maps. Journal of Ambient Intelligence and Humanized Computing, 11(3), 1309-1324.

[149] Tang, H., Li, Y., & Xiao, X. (2013, November). A novel flexure-based dual-arm robotic system for high-throughput biomanipulations on micro-fluidic chip. In 2013 IEEE/RSJ International Conference on Intelligent Robots and Systems (pp. 1531-1536). IEEE.

[150] Wu, Z., Li, Y., & Hu, M. (2018). Design and optimization of full decoupled micro/nano-positioning stage based on mathematical calculation. Mechanical Sciences, 9(2), 417-429.

[151] Zhu, W. L., Zhu, Z., Shi, Y., Wang, X., Guan, K., & Ju, B. F. (2016). Design, modeling, analysis and testing of a novel piezo-actuated XY compliant mechanism for large workspace nano-positioning. Smart Materials and Structures, 25(11), 115033.

[152] Lee, C., Stepanick, C. K., Lee, S. K., & Tarbutton, J. A. (2016). Cross-coupling effect of large range XY nanopositioning stage fabricated by stereolithography process. Precision Engineering, 46, 81-87.

[153] Wang, P., & Xu, Q. (2017). Design of a flexure-based constant-force XY precision positioning stage. Mechanism and Machine Theory, 108, 1-13.

[154] Wang, H., & Zhang, X. (2008). Input coupling analysis and optimal design of a 3-DOF compliant micro-positioning stage. Mechanism and Machine Theory, 43(4), 400-410.

[155] Dang, M. P., Dao, T. P., Chau, N. L., & Le, H. G. (2019). Effective hybrid algorithm of Taguchi method, FEM, RSM, and teaching learning-based optimization for multiobjective optimization design of a compliant rotary positioning stage for nanoindentation tester. Mathematical Problems in Engineering, 2019.

[156] Rao, R. V., Savsani, V. J., & Vakharia, D. P. (2011). Teaching–learning-based optimization: a novel method for constrained mechanical design optimization problems. Computer-aided design, 43(3), 303-315.

[157] Dao, T. P., Ho, N. L., Nguyen, T. T., Le, H. G., Thang, P. T., Pham, H. T., ... & Nguyen, T. T. (2017). Analysis and optimization of a micro-displacement sensor for compliant microgripper. Microsystem Technologies, 23(12), 5375-5395.

[158] Zimmerman, D. W., & Zumbo, B. D. (1993). Relative power of the Wilcoxon test, the Friedman test, and repeated-measures ANOVA on ranks. The Journal of Experimental Education, 62(1), 75-86.